HZDR-130

PLASMA DYNAMICS BETWEEN LASER-INDUCED BREAKDOWN AND RELATIVISTICALLY INDUCED TRANSPARENCY: AN INVESTIGATION OF HIGH-INTENSITY LASER-SOLID INTERACTIONS BY TIME-RESOLVED OFF-HARMONIC OPTICAL SHADOWGRAPHY

Constantin Bernert

Wissenschaftlich-Technische Berichte
HZDR-130 · 2023 · ISSN 2191-8708

WISSENSCHAFTLICH-
TECHNISCHE BERICHTE

HELMHOLTZ ZENTRUM
DRESDEN ROSSENDORF

Wissenschaftlich-Technische Berichte
HZDR-130

Constantin Bernert

PLASMA DYNAMICS BETWEEN LASER-INDUCED BREAKDOWN AND RELATIVISTICALLY INDUCED TRANSPARENCY: AN INVESTIGATION OF HIGH-INTENSITY LASER-SOLID INTERACTIONS BY TIME-RESOLVED OFF-HARMONIC OPTICAL SHADOWGRAPHY

HZDR
HELMHOLTZ ZENTRUM
DRESDEN ROSSENDORF

Druckausgabe: ISSN 2191-8708

Elektronische Ausgabe: ISSN 2191-8716

https://www.hzdr.de/publications/Publ-39006

urn:nbn:de:bsz:d120-qucosa2-910712

Die vorliegende Arbeit wurde sowohl als Dissertation an der Fakultät Mathematik und Naturwissenschaften der Technischen Universität Dresden sowie als Wissenschaftlich-Technischer Bericht des Helmholtz-Zentrum Dresden – Rossendorf mit der Berichtsnummer **HZDR-130** veröffentlicht.

2024

Herausgegeben vom

Helmholtz-Zentrum Dresden - Rossendorf

Bautzner Landstraße 400

01328 Dresden

Germany

TECHNISCHE UNIVERSITÄT DRESDEN

Fakultät Mathematik und Naturwissenschaften
Fachrichtung Physik

Plasma dynamics between laser-induced breakdown and relativistically induced transparency:
An investigation of high-intensity laser-solid interactions by time-resolved off-harmonic optical shadowgraphy

Constantin Andreas Bernert, M. Sc.
Born on May 24, 1991 in Dresden, Germany

Dissertation

to achieve the academic degree

Doctor rerum naturalium

Referee	Prof. Dr. Ulrich Schramm
	Prof. Dr. Thomas E. Cowan
	Prof. Dr. Jörg Schreiber
Supervisor	Dr. Karl Zeil

Submitted on: April 3, 2023
Defended on: March 25, 2024

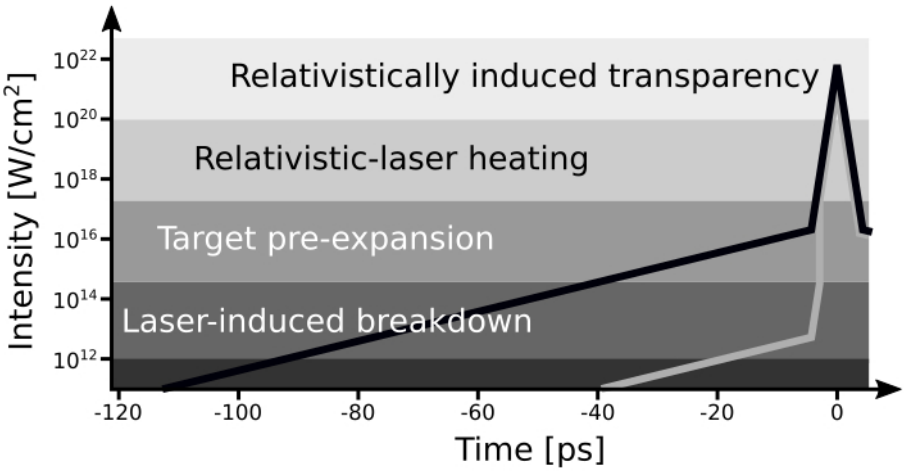
Relativistically induced transparency
Relativistic-laser heating
Target pre-expansion
Laser-induced breakdown
Intensity [W/cm^2]
10^{22}
10^{20}
10^{18}
10^{16}
10^{14}
10^{12}
-120
-100
-80
-60
-40
-20
0
Time [ps]

Abstract

Laser-plasma-based ion accelerators are becoming a versatile platform to drive different fields of applied research and life sciences, for example translational research in radiation oncology. To ensure stable accelerator performance, complete control over the ion source, i.e., the high-intensity laser-solid interaction, is required. However, idealized interaction conditions are almost impossible to reach, as the utilized high-power lasers always feature a non-negligible amount of light preceding the laser peak. This *leading edge* of the laser pulse usually exceeds the ionization potential of bound electrons much earlier than the arrival of the high-power laser peak and the solid-density target undergoes significant modifications even before the actual high-intensity laser-plasma interaction starts. Control over this so-called *target pre-expansion* is a key requirement to achieve quantitative agreement between numerical simulations and experiments of high-intensity laser-solid interactions.
This thesis investigates several aspects that are relevant to improve the capability of simulations to model realistic experimental scenarios. The corresponding experiments are conducted with cryogenic hydrogen-jet targets and the DRACO-PW laser at peak intensities between $10^{12}\,\mathrm{W/cm^2}$ and $10^{21}\,\mathrm{W/cm^2}$. The experimental implementation of time-resolved optical-probing diagnostics and technical innovations with respect to the technique of off-harmonic optical probing overcome the disturbances by parasitic plasma self-emission and allow for unprecedented observations of the target evolution during the laser-target interactions. The *laser-induced breakdown* of solids, i.e., the phase transition from the solid to the plasma state, can be considered as an heuristic starting point of high-intensity laser-solid interactions. As it is highly relevant to simulations of target pre-expansion, Chapter 3 of this thesis presents time-resolved measurements of laser-induced breakdown in laser-target interactions at peak intensities between $0.6 \cdot 10^{21}\,\mathrm{W/cm^2}$ and $5.7 \cdot 10^{21}\,\mathrm{W/cm^2}$. By increasing the peak intensity, a lowering of the applicable threshold intensity of laser-induced breakdown well below the appearance intensity of barrier-suppression ionization occurs. The observation demonstrates the relevance of the pulse-duration dependence of laser-induced breakdown and laser-induced damage threshold to the starting point of high-intensity laser-solid interactions. To apply the results to other laser-target assemblies, we provide a detailed instruction of how to pinpoint the starting point by comparing measurements of the laser contrast with a characterization study of the target-specific thresholds of laser-induced breakdown at low laser intensity. Chapter 4 of this thesis presents an example of how optical-probing diagnostics are able to estimate target pre-expansion as a starting condition for particle-in-cell simulations. The measurement allows to restrict the surface gradient of the pre-expanded plasma density to an exponential scalelength between 0.06 µm and 0.13 µm. Furthermore, the plasma-expansion dynamics induced by the ultra-relativistic laser peak are computed and post-processed by ray-tracing simulations. A comparison to the experimental results yields that the formation of the measured shadowgrams is governed by refraction in the plasma-density gradients and that the observed volumetric transparency of the target at 1.4 ps after the laser peak is not caused by *relativistically induced transparency* but by plasma expansion into vacuum instead. Chapter 5 of this thesis shows that a precise adjustment of the target density to the arrival of the ultra-relativistic laser peak by *all-optical target-density tailoring* in combination with the low solid density of the cryogenic hydrogen-jet target allows to explore the laser-target interaction in the nearcritical density regime. The chapter presents an experimental demonstration of all-optical target-density tailoring by isochoric heating via ultra-short laser pulses with a dimensionless vector potential $a_0 \sim 1$. A hybrid of hydrodynamics and ray-tracing simulations allows to determine the evolution of the full target-density distribution after isochoric heating. Finally, the utilization of the method as a testbed platform to experimentally benchmark collisional particle-in-cell simulations is proposed and an experimental exploration of future possibilities of all-optical target-density tailoring is given.

Zusammenfassung

Laser-Plasma-basierte Ionenbeschleuniger stellen einer vielseitigen Plattform für verschiedene Bereiche der angewandten Forschung und der Biowissenschaften dar, z. B. für die translationale Forschung in der Strahlentherapie. Um eine stabile Beschleunigerleistung zu gewährleisten, muss die Ionenquelle, d. h. die Wechselwirkung zwischen dem Hochintensitätslaser und einem Festkörper, vollständig kontrolliert sein. Idealisierte Wechselwirkungsbedingungen können jedoch fast nie erreicht werden, da die verwendeten Hochleistungslaser immer eine nicht zu vernachlässigende Lichtmenge vor der Spitze des Laserpulses aufweisen. Diese *vorangehende Flanke* des Laserpulses überschreitet Intensitäten, welche zur Ionisation gebundener Elektronen führen, in der Regel schon wesentlich eher als das die Spitze des Hochleistungslaserpulses eintrifft. Der Festkörper unterliegt deshalb noch vor der eigentlichen hochintensiven Wechselwirkung erheblichen Modifikationenen durch die vorangehende Flanke. Die Kontrolle dieser so genannten *Vorexpansion* ist eine wichtige Voraussetzung für die quantitative Übereinstimmung zwischen numerischen Simulationen und Experimenten von Wechselwirkungen zwischen hochintensiven Lasern und Festkörpern.
Diese Arbeit untersucht mehrere Aspekte, welche für die Verbesserung von Simulationen realistischer experimenteller Szenarien relevant sind. Die entsprechenden Experimente werden mit Festkörpern aus kryogenen Wasserstoff und dem DRACO PW Laser mit Intensitäten zwischen $10^{12}\,\mathrm{W/cm^2}$ und $10^{21}\,\mathrm{W/cm^2}$ durchgeführt. Die experimentelle Implementierung zeitaufgelöster optischer Mikroskopie und technische Innovationen für die Technik der optischen Untersuchung abseits der Harmonischen des Lasers (off-harmonic optical probing) überwinden Störungen durch parasitäre Selbstemission des Plasmas und ermöglichen bisher unerreichte Beobachtungen der Evolution des Plasmas. Die laserinduzierte Zerstörschwelle des Festkörpers, d.h. der Phasenübergang vom festen Aggregatzustand in den Plasmazustand, kann als heuristischer Anfangszeitpunkt der Wechselwirkung eines hochintensiven Lasers mit einem Festkörper betrachtet werden. Da dies für Simulationen der Vorexpansion von großer Bedeutung ist, werden in Kapitel 3 dieser Arbeit zeitaufgelöste Messungen der laserinduzierten Zerstörung von Festkörpern in Wechselwirkungen mit Laserpulsen, deren Spitzenintensität zwischen $0.6 \cdot 10^{21}\,\mathrm{W/cm^2}$ und $5.7 \cdot 10^{21}\,\mathrm{W/cm^2}$ liegt, präsentiert. Durch die Erhöhung der Spitzenintensität kommt es zu einer Absenkung der anwendbaren laserinduzierten Zerstörschwellintensität deutlich unter die Erscheinungsintensität (appearance intensity) der Ionisation mittels Absenkung des Coulomb Potentials (barrier-suppression ionization). Die Beobachtung demonstriert die Relevanz der Pulsdauerabhängigkeit von Messungen laserinduzierter Zerstörschwellen auch für den Anfangszeitpunkt von Wechselwirkungen zwischen Festkörpern und hochintensiven Laserpulsen. Um die Ergebnisse auf die Wechselwirkung anderer Kombinationen von Lasern und Festkörpern anwenden zu können, stellen wir eine detaillierte Anleitung zur Bestimmung des Anfangszeitpunkts der Vorexpansion dar, welche auf dem Vergleich der Messungen des Laserkontrasts mit einer Charakterisierungsstudie der spezifischen laserinduzierten Zerstörschwellen bei niedriger Laserintensität basiert. Kapitel 4 dieser Arbeit präsentiert ein Beispiel, wie mit Hilfe der zeitaufgelösten optischen Mikroskopie die Vorexpansion als Ausgangsbedingung für Teilchen-in-Zellen (particle-in-cell) Simulationen abgeschätzt werden kann. Die Messungen erlauben es, den Oberflächengradienten der vorexpandierten Plasmadichte auf eine exponentielle Skalenlänge zwischen 0.06 µm und 0.13 µm einzugrenzen. Darüber hinaus wird die Plasmaexpansionsdynamik, welche durch die hochintensive Spitze des Laserpulses induzierte wird, berechnet und durch Lichtstrahlverfolgungssimulationen (ray-tracing simulations) nachbearbeitet. Ein Vergleich mit den experimentellen Ergebnissen zeigt, dass die Erzeugung der gemessenen Schattenbilder durch Brechung in den Dichtegradienten des Plasmas bestimmt ist und, dass die beobachtete volumetrische Transparenz des Plasmas 1.4 ps nach der Spitze des Laserpulses nicht durch relativistisch induzierte Transparenz, sondern durch Plasmaexpansion in das umliegende Vakuum verursacht wird. Abschließend zeigt Kapitel 5 dieser Arbeit, dass eine präzise Anpassung der Plasmadichte zum Zeitpunkt des Eintreffens der hochintensiven Spitzenintensität durch eine gezielte optisch-induzierte Plas-

maexpansion in Kombination mit der niedrigen initialen Festkörperdichte des kryogenen Wasserstoffs die Untersuchung von Wechselwirkungen im nahkritischen Dichtebereich ermöglicht. Das Kapitel stellt eine experimentelle Demonstration der gezielten optisch induzierten Plasmaexpansion durch isochores Heizen mittels ultrakurzer Laserpulse mit einem dimensionslosen Vektorpotential $a_0 \sim 1$ vor. Ein Hybrid aus Hydrodynamik- und Lichtstrahlverfolgungssimulationen ermöglicht es, die zeitliche Entwicklung der gesamten Dichteverteilung des Plasmas nach dem isochoren Heizen zu bestimmen. Abschließend präsentiert das Kapitel ein Konzept, um die Methode als Testplattform für die experimentelle Überprüfung von kollisionalen Teilchen-in-Zellen Simulationen zu nutzen und es werden die Ergebnisse einer experimentellen Untersuchung zu zukünftigen Möglichkeiten der Methode dargelegt.

Most relevant publications

The following list shows publications by the author, which include relevant parts of this thesis.

- **Loeser et al. [117]:** M. Loeser, C. Bernert, D. Albach, K. Zeil, U. Schramm and M. Siebold. Compact millijoule $Yb^{3+} : CaF^2$ laser with 162fs pulses. *Opt. Express*, 29(6):9199-9206, 2021.
- **Bernert et al. [24]:** C. Bernert, S. Assenbaum, F.-E. Brack, T. E. Cowan, C. B. Curry, M. Garten, L. Gaus, M. Gauthier, S. Göde, I. Göthel, S. H. Glenzer, T. Kluge, S. Kraft, F. Kroll, M. Kuntzsch, J. Metzkes-Ng, M. Loeser, L. Obst-Huebl, M. Rehwald, H.-P. Schlenvoigt, C. Schoenwaelder, U. Schramm, M. Siebold, F. Treffert, T. Ziegler and K. Zeil. Off-harmonic optical probing of high intensity laser plasma expansion dynamics in solid density hydrogen jets. *Sci. Rep.*, 12:7287, 2022.
- **Bernert et al. [23]:** C. Bernert, S. Assenbaum, S. Bock, F.-E. Brack, T. E. Cowan, C. B. Curry, M. Garten, L. Gaus, M. Gauthier, R. Gebhardt, S. Göde, S. H. Glenzer, U. Helbig, T. Kluge, S. Kraft, F. Kroll, L. Obst-Huebl, T. Püschel, M. Rehwald, H.-P. Schlenvoigt, C. Schoenwaelder, U. Schramm, F. Treffert, M. Vescovi, T. Ziegler and K. Zeil. Transient Laser-Induced Breakdown of Dielectrics in Ultra-relativistic Laser-Solid Interactions. *Phys. Rev. Applied*, 19:014070, 2023.
- **Rehwald et al. [168]:** M. Rehwald, C. Bernert, F.-E. Brack, M. Bussmann, T. E. Cowan, C. B. Curry, F. Fiuza, M. Garten, L. Gaus, M. Gauthier, S. Göde, I. Göthel, S. H. Glenzer, L. G. Huang, A. Huebl, J. B. Kim, T. Kluge, S. Kraft, F. Kroll, J. Metzkes-Ng, M. Loeser, L. Obst-Huebl, M. Reimold, H.-P. Schlenvoigt, C. Schoenwaelder, U. Schramm, M. Siebold, F. Treffert, L. Yang, T. Ziegler and K. Zeil. Ultra-short pulse laser acceleration of protons to 80 MeV from cryogenic hydrogen jets tailored to near-critical density. Submitted, 2023.
- **Yang et al. [208]:** L. Yang, C. Bernert, et al. Time-resolved optical shadowgraphy of cryogenic hydrogen jets as a testbed platform to benchmark particle-in-cell simulations. In preparation, 2023.

Contents

1. Introduction

Nowadays, research of high-intensity laser-solid interactions with Petawatt-class lasers is mainly driven by two branches of technological development. The first branch is the investigation of high-energy-density matter to foster the development of inertial-confinement fusion [116, 45], in particular, the concept of fast ignition [175, 66], warm-dense-matter research [153, 64, 38, 209, 170, 130, 126, 69], secondary-source development [74, 115, 174, 44, 197, 85] and time-resolved studies of transient fields [29, 173]. The second branch is the infrastructure development of future laser-plasma-based ion accelerators [48, 124, 183, 13] for a variety of applications [28], e.g., translational research in radiation oncology [37, 108]. Full control of the laser-solid interaction is needed to achieve a stable operation of the laser-driven ion source. However, because of the small spatial and short temporal scales of the particle acceleration, numerical simulations are a key element to gain insight and control over the accelerator. Accompanied by the measurement of experimental boundary conditions, predictive power of computer simulations is anticipated to guide research and development strategies towards the envisioned applications.

In experiments, Petawatt-class lasers feature a non-negligible amount of light preceding the high-power laser peak [49]. This so-called *leading edge* is composed of singular prepulses and continuous pedestals. As the laser intensities of the leading edge usually exceed the ionization potential of bound electrons much earlier than the arrival of the high-power laser peak, the solid-density target undergoes significant modifications even before the actual high-intensity laser-plasma interaction starts. The target modifications by the leading edge are subsumed under the phrase *target pre-expansion*. Although the development of the laser technology is progressing towards minimization of the leading edge [98, 119] and dedicated methods of temporal pulse cleaning like second-harmonic generation [91] or plasma mirrors [194, 145] are available, quantitative agreement between experimental results and simulations of high-intensity laser-solid interactions is rare. This is mainly caused by the non-linear dependency of the final interaction products, e.g., the energy spectum of the accelerated ions, with respect to target pre-expansion [180]. Precise information on target pre-expansion is thus a key requirement of quantitative numerical modeling of experimental scenarios. On the one side, information on target pre-expansion can be inferred by experimental diagnostics, e.g., time-resolved microscopy by ultra-fast optical backlighters [30, 83, 111, 133, 99, 95, 134, 213, 50] and Bernert et al [24]. On the other side, numerical modeling of the laser-target interaction during the leading edge can provide reasonable initial conditions for the simulation of the ultra-relativistic laser-target interaction during the high-power laser pulse [132, 180, 141, 57] and Rehwald et al. [168].

Still, a consistent simulation of all parts of the laser-target interaction, i.e., a full *start-to-end simulation* that is initialized with a solid-state structure, models the ionization process and the phase transition to the plasma state, the subsequent regime of laser-plasma interaction with collisional and resonance absorption, up to the collisionless regime during the high-intensity laser peak, remains a challenge for the future. In the vicinity of the high-intensity laser peak, the electric field strengths of the laser and the generated charge-separation fields dominate the system and particle-in-cell (PIC) simulations are commonly used to model this kinetic regime of particle motion and thermal non-equilibrium. Adequate initial condition of the PIC simulations are usually derived from radiation-hydrodynamics simulations that capture longer timeframes and the more localized energy deposition of the lower laser intensities of the leading edge.

Currently, there are two challenges of the available modeling capabilities of start-to-end simulations. The first challenge is the combination of radiation-hydrodynamics simulations with computations of ionization, i.e., an approach to capture the phase transition from the solid to the plasma state, which is the actual starting point of the interaction of the laser with a plasma. Here, either the advancement of the simulative capabilities or heuristic approaches to pinpoint the temporal position of the phase transition are needed. The second challenge is the simulation of the transition regime between strongly

correlated plasmas at subrelativistic laser intensities and kinetic plasmas at ultra-relativistic laser intensities, i.e., laser intensities of a dimensionless vector potential $a_0 \sim 1$ ($\sim 10^{18}\,\mathrm{W/cm^2}$ for 800 nm light) and lower. Although the capabilities of today's PIC simulations develop toward the coverage of collisional plasma physics at subrelativistic laser-intensity levels together with the integration of atomic-physics models, theoretical predictions and experimental testbeds are needed to benchmark the implemented physics modules.

This thesis investigates three aspects that are relevant to improve the agreement of experimental results and start-to-end simulations of high-intensity laser-solid interactions. The results are derived by time-resolved optical microscopy of experiments with Petawatt-class laser pulses of 30 fs pulse duration and intensities between $10^{12}\,\mathrm{W/cm^2}$ and $10^{21}\,\mathrm{W/cm^2}$. All experiments utilize a micrometer-sized cryogenic hydrogen jet as a versatile target platform [104, 47]. The target features a comparably low solid density, simple ionization dynamics, as there is only one bound electron per atom, and it fosters experimental-data aquisition by it's free-standing and self-replenishing delivery in the experimental chamber.
Chapter 3 of this thesis issues the laser-induced breakdown of solid-density targets in interaction with ultra-relativistic Petawatt-class laser pulses, i.e., the phase transition from the solid to the plasma state. The experimental results demonstrate a high variation of the threshold intensity of breakdown for a varied slope of the leading edge. We provide detailed instructions of how to pinpoint the temporal position of the phase transition, i.e. the starting point of target pre-expansion, for other laser-target assemblies.
Chapter 4 presents measurements of target pre-expansion and by this provides reasonable initial conditions for a PIC simulation of the ultra-relativistic laser-target interaction, bridging the necessity of simulating target pre-expansion. The simulated plasma-expansion dynamics after the laser peak are compared to the experimental results and the contribution of relativistically induced transparency is investigated.
Chapter 5 introduces the opportunity to control the density distribution of the target to the arrival of the high-intensity laser peak by *all-optical target-density tailoring*. First, an experimental demonstration of the technique via isochoric heating by ultra-short laser pulses with a dimensionless vector potential of $a_0 \sim 1$ is presented. The results enable the quantitative comparison of experimental results of enhanced laser-driven proton acceleration and the corresponding PIC simulations of interactions of the cryogenic hydrogen-jet target and DRACO PW. In a second step, we show a concept of utilizing the technique as a testbed to experimentally benchmark collisional PIC simulations in the lasers-intensity regime between 10^{17} and $10^{19}\,\mathrm{W/cm^2}$. Finally, possible future realizations of all-optical target-density tailoring are demonstrated.

Before starting with the chapters 3, 4 and 5, chapter 2 provides an introduction to the scientific framework, the overarching research project in which this thesis is embedded and the experimental implementation and technical innovation that enabled the investigations.

2. Scientific framework, the overarching research project and experimental implementation

The first section 2.1 of this chapter provides an introduction to the relevant physics concepts and the available literature on high-intensity laser-solid interactions, with a special emphasis on laser-ion acceleration and optical probing of the respective interactions. The second section 2.2 presents the overarching research project in which this thesis is embedded. The section introduces the collaborative work on laser-ion acceleration from cryogenic hydrogen jets and presents the experimental infrastructure of the DRACO-laser facility. Most of the experimental results that are evaluated within this thesis are derived in an experimental campaign with the DRACO-PW laser in 2019. The evaluation is covered by three doctoral projects, which are Ref. [167], Ref. [79] and this thesis. The results are published in Ref. Rehwald et al. [168] and summarized at the end of section 2.2. The final section 2.3 give details on the experimental implementation and technical innovations that are realized within this thesis project and provides the groundwork to enable time-resolved optical probing of laser-solid interaction at laser intensities as high as $6 \cdot 10^{21}\,\mathrm{W/cm^2}$.

2.1. Scientific framework: High-intensity laser-solid interactions

Today, the term *high-intensity laser* refers to lasers with peak powers between tens of Terawatts up to several Petawatts. Generally, the choice of the active laser medium and the concept of laser pulse amplification are decisive for the specifications of an individual machine. The achievable parameters range from a pulse duration between tens of femtoseconds to single picoseconds and pulse energies between hundreds of Millijoule up to hundreds of Joule. Depending on the pulse energy, the repetition rate ranges from Kilohertz down to single shots per hour. All high-intensity lasers have in common that their finally focused electric field strength accelerates electrons up to relativistic energies during a single laser cycle. For lasers with about 1 µm central wavelength, this corresponds to intensities above $\sim 10^{18}\,\mathrm{W/cm^2}$. The corresponding electric field strength exceeds the binding forces of electrons in most atoms significantly. Therefore, all high-intensity laser-matter interactions are considered as laser-plasma interactions.

Plasma is the fourth thermodynamic state of matter. Generally, it is characterized by the separation of matter into mobile ions and electrons that interact via the Coulomb force. Because of the higher charge to mass ratio of the lighter electrons in comparison to the more heavy ions, the interaction of a plasma with electro-magnetic radiation is commonly described by the collective answer of the electron cloud to the external perturbation. On the timescale of an optical laser cycle, the quasi-static ionic background acts as restoring force and enables oscillations of the electrons. The plasma density of electrons n_e and the laser frequency ω_L define the characteristic response of the plasma.

The response function of the plasma is characterized by the *plasma frequency*

$$\omega_P = \sqrt{\frac{e^2 n_e}{\epsilon_0 m_e}} \tag{2.1}$$

with e, m_e and ϵ_0 being the electron charge, electron mass and vacuum permittivity. The electron gas of a plasma with a density n_e is able to follow a harmonic perturbation up to the plasma frequency. Perturbations with higher frequency are transmitted through the plasma.

The same physical behavior, but from the point of view of a laser beam, can be expressed by the *critical electron density*

$$n_c = \frac{\omega_L^2 \epsilon_0 m_e}{e^2} = \frac{4\pi^2 c^2 \epsilon_0 m_e}{e^2 \lambda_L^2} \tag{2.2}$$

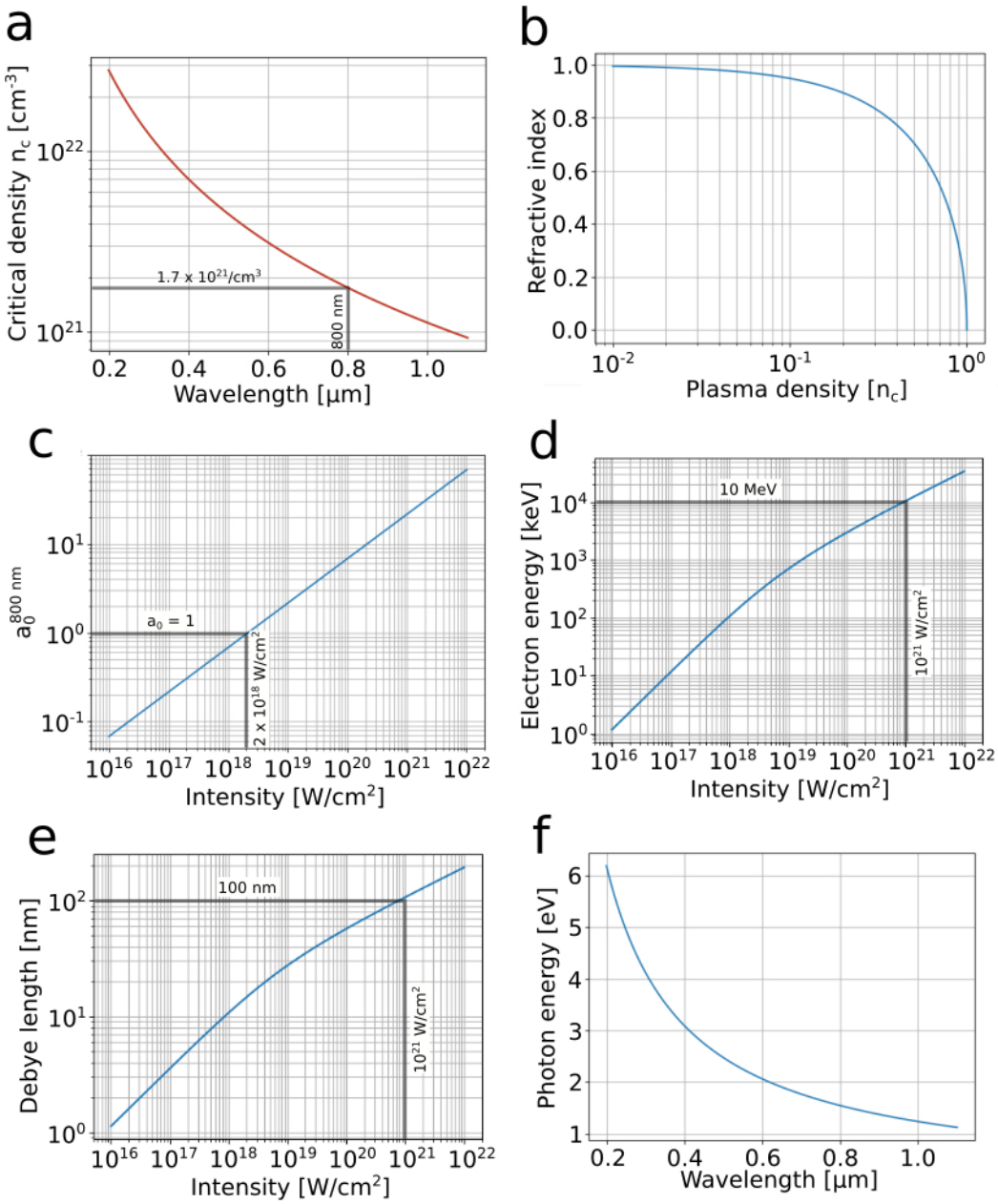

Figure 2.1.: The scaling of relevant physical quantities: **(a)** Critical plasma density versus laser wavelength, **(b)** Refractive index of a plasma versus plasma density, **(c)** Normalized vector potential a_0 versus laser intensity of 800 nm light. **(d)** Mean kinetic energy of laser-heated electrons versus laser intensity following the ponderomotive scaling [206], **(e)** Debye screening length versus laser intensity of a plasma with an electron density of $5.1 \cdot 10^{22}\,\mathrm{cm}^{-3}$ (for details see text) and **(f)** Photon energy versus photon wavelength.

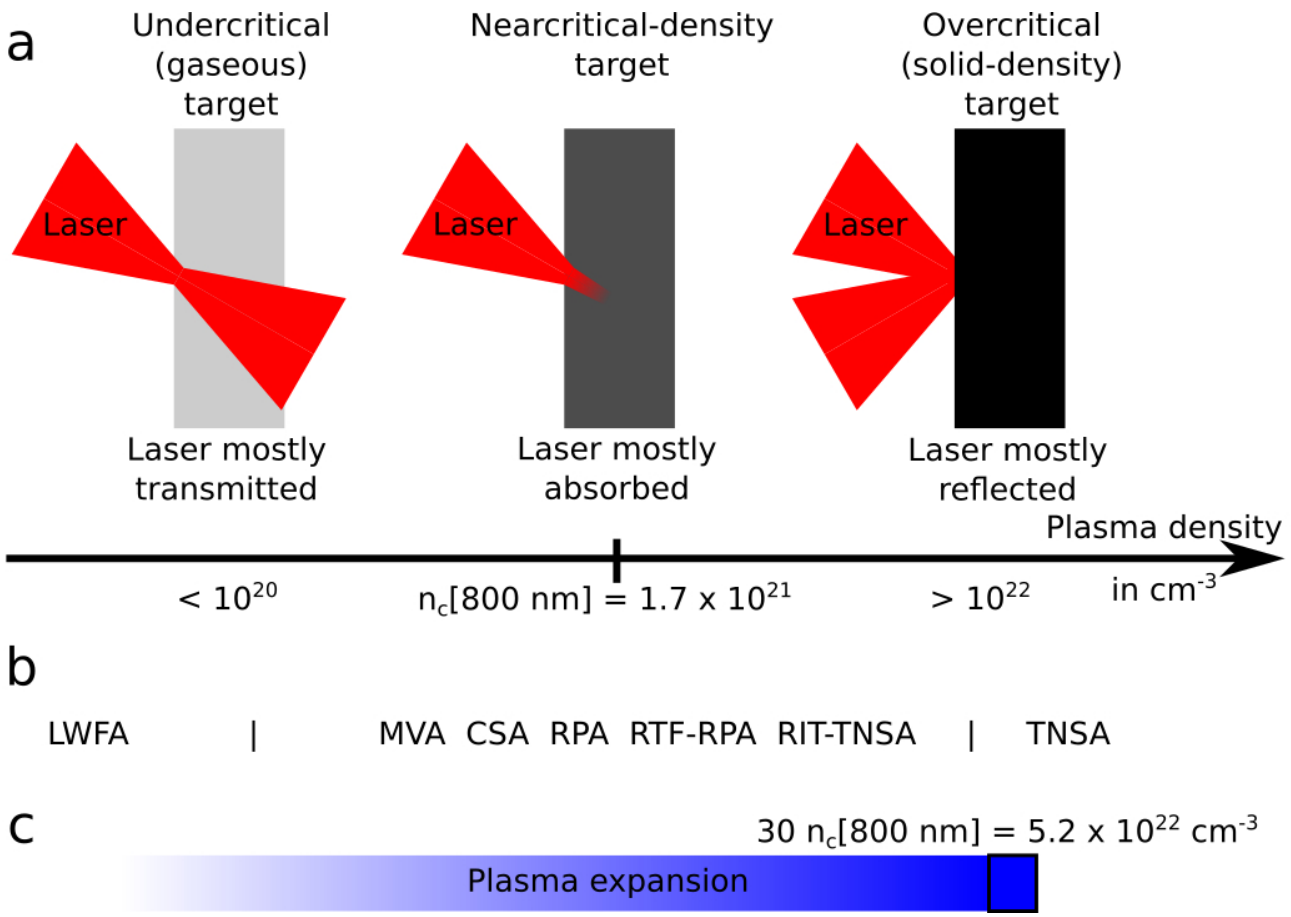

Figure 2.2.: **(a)** General overview of possible laser-target interactions and their dependence on target density. The central wavelength of the DRACO laser is 800 nm. **(b)** Different laser-particle-acceleration mechanisms in plasmas: *Laser wakefield acceleration* (LWFA) [60] for pure electron acceleration and several ion acceleration mechanisms: *Magnetic Vortex Acceleration* (MVA) [34, 138, 137, 152], *Collisionless Shock Acceleration* (CSA) [185, 68], *Radiation Pressure assisted Acceleration* (RPA) [61, 164], *Relativistic Transparency Front-RPA* (RTF-RPA) [81], which is also called *Synchronized Acceleration by Slow Light* (SASL) [32], *Relativistically Induced Transparency* enhanced TNSA (RIT-TNSA) [200, 52, 62] and *Target Normal Sheath Acceleration* (TNSA) [206]. **(c)** Density of the cryogenic hydrogen-jet target of $5.2 \cdot 10^{22}\,\mathrm{cm}^{-3}$. Lower densities close to or below the critical density are reached by plasma expansion into vacuum.

with the light speed c. A laser with constant frequency ω_L and wavelength λ_L is able to penetrate a plasma up to the critical electron density n_c only. For illustration, the critical density of wavelengths in the visible range is given in figure 2.1 (a). The electrons of a plasma with an electron density higher than n_c are able to collectively shield the inner plasma from the external perturbation. The oscillating electron gas reemits the light and because of momentum conservation, the laser light is reflected on the plasma-vacuum boundary. For electron densities below the critical density, the plasma acts as a refractive medium. The refractive index of a plasma depends on the electron density and the critical density:

$$\tilde{n} = \sqrt{1 - n_e/n_c}\,. \tag{2.3}$$

The equation is visualized in figure 2.1 (b) and shows that $\tilde{n} < 1$ for $n_e < n_c$.

In laser-plasma physics, the laser wavelength is usually a fixed quantity and plasmas are classified by their electron density in *undercritical plasmas* and *overcritival plasmas*. The critical density n_c marks the transition between the two regimes. For 800 nm light, which is the central wavelength of the DRACO laser, the critical density is $n_c^{800\,\mathrm{nm}} = 1.7 \cdot 10^{21}\,\mathrm{cm}^{-3}$. As plasmas with a density higher

then $10^{22}\,\mathrm{cm}^{-3}$ have a similar density like solid state matter, these plasmas are termed *solid-density plasmas*. Conversely, plasmas with a density below $10^{20}\,\mathrm{cm}^{-3}$ can be termed *gaseous plasmas* and plasmas with a density close to $10^{21}\,\mathrm{cm}^{-3}$ are referred to as *nearcritical plasmas*. In an experiment of a laser with a plasma, the plasma is commonly termed *target*.
The laser beam is usually focused down to the micrometer scale to achieve highest intensities. Figure 2.2 (a) shows that the induced laser-target interaction highly depends on the plasma density of the target. As visualized on the left-hand side, undercritical plasmas are mostly transmitting the laser light and the interaction is dominated by the refractive properties of the target. Nearcritical-density targets couple the laser energy very efficiently to the plasma electrons and most of the laser light is absorbed during the interaction (center). Solid-density targets mostly reflect the laser light and electrons gain energy on the target front surface only (right-hand side).
The interaction of the laser beam and the target not only depends on the plasma density but also on laser intensity. In high-intensity laser-plasma physics, the intensity of the laser is commonly expressed via the *normalized vector potential* [46]

$$a_0 = \sqrt{\frac{e^2\lambda_L^2 I_L}{2\pi^2\epsilon_0 m_e^2 c^5}} = \sqrt{\frac{2I_L}{n_c m_e c^3}} \approx 0.853 \cdot \lambda_L[\mu\mathrm{m}] \cdot \sqrt{I_L[10^{18}\,\mathrm{W/cm^2}]} \tag{2.4}$$

which is also called *laser-strength parameter*. I_L is the laser intensity. Figure 2.1 (c) show the relation for 800 nm light. $a_0 = 1$ marks the laser strength at which the rest-mass energy of an electrons equals the average kinetic energy of the electron within a single laser cycle (cycle-averaged quiver energy). A laser strength of $a_0 > 1$ describes the regime for which electrons become relativistic in their motion. Consequently, the corresponding laser intensities are termed *relativistic*. For 800 nm light, relativistic intensities are intensities higher than $2 \cdot 10^{18}\,\mathrm{W/cm^2}$. Laser intensities above about $10^{21}\,\mathrm{W/cm^2}$ are sometimes referred to as *ultra-relativistic*.
There are several text books that describe the fundamentals of high-intensity and high-power laser-matter interactions, see references [76] and [136]. In the relativistic regime, the kinetic energy of laser-heated electrons can be estimated via different scaling laws of laser-solid interactions [21, 206, 107]. For example, the *ponderomotive scaling* gives [206, 107]

$$k_B T_e = m_e c^2 (\sqrt{1 + a_0^2/2} - 1)\,. \tag{2.5}$$

k_B is Boltzmanns's constant. The electron temperature T_e does not describe a classical Maxwell-Boltzmann distribution of temperature. It rather describes the mean kinetic energy that is attributed to the laser-heated population of *hot electrons* at the laser plasma interface. Figure 2.1 (d) shows equation 2.5 for different laser intensities and $\lambda_L = 800\,\mathrm{nm}$. Ultra-relativistic intensities are expected to accelerate electrons up to the multi-MeV energies.
The electron density n_e and the temperature T_e enable the derivation of the *Debye screening length*

$$\lambda_D = \sqrt{\frac{\epsilon_0 k_B T_e}{n_e e^2}} \sim 69 \cdot \sqrt{\frac{T_e[K]}{n_e[1/m^3]}}\,. \tag{2.6}$$

It gives a characteristic spatial scale for charge neutrality in a plasma. On the spatial scale of the Debye screening length or below, the occurrence of strong electrical potential gradients is possible due to non-neutralized charge separation, e.g., in a *Debye sheath* on the surface of a solid. Considering a target of moderate solid density, like for example $5.1 \cdot 10^{22}\,\mathrm{cm}^{-3}$ (density of the cryogenic hydrogen-jet target), and the ponderomotive scaling of the electron temperature, the Debye screening length and its dependency on laser intensity are displayed in figure 2.1 (e). For laser intensities above $10^{21}\,\mathrm{W/cm^2}$, the Debye screening length approaches the hundreds of nanometer scale. The spatial parameters of the here discussed experiments like diameter of the focal spot, target dimensions and laser wavelength are on a similar order of magnitude. It follows, that the response of the here utilized target in experiments at ultra-relativistic laser intensity is expected to undergo high non-equilibrium stages of matter, i.e., strong charge-separation fields, and consequently allow for ultra-fast particle dynamics.

In fact, high-intensity laser-matter interactions are a unique tool to generate high-energy electron and ion beams by compact accelerator structures in plasmas. An overview and current status of plasma-based particle accelerators, including laser-driven approaches, and a variety of relevant references of the different branches of novel accelerator research can be found in Ref. [13]. In the following, we introduce two widely used branches of laser-particle acceleration and show some exemplary applications. On the one side, an extensively studied mechanism at undercritical target densities is the so called *laser wakefield acceleration* (LWFA) [60]. Here, a high-intensity laser pulse drives a collective motion of plasma electrons that formate a dynamic accelerating cavity and enables the acceleration of collimated, monoenergetic, high peak-current electron beams up to the GeV level within about a meter acceleration length. Today, developments point towards the staging of several acceleration units and preparing them for applications like compact injectors for particle-storage rings or as drivers for secondary sources like free-electron lasers [13]. On the other side, if the same high-intensity laser beam is used together with solid-density targets, the resulting interaction provides high-emittance broadband ion beams with particle energies of up to 100 MeV per nucleon. The laser-plasma-based ion sources are envisioned to enable different applications ranging from energy-relevant research like warm-dense matter investigations [153, 176, 38, 18, 170] or the concept of fast ignition for inertial-confinement fusion [175, 67] up to health-related applications like translational research for radiation oncology [31, 37, 108]. A collection of applications is presented in reference [28]. Today, the field of laser-ion acceleration faces several important challenges. Most important are renewable targetry, ion-beam transport from the source (laser-solid interaction) to the application, reproducibility and stability of the source and a boost of the achievable maximum energy of the ions to several hundreds of MeV [183]. This thesis tackles the topic of stabilization and optimization of the source by creating novel insight to the interaction of the high-intensity laser with solid-density targets.

2.1.1. High-intensity lasers and temporal laser contrast

There are many high-intensity lasers all over the world. *The international committee on ultra-high intensity lasers* (ICUIL) [6] lists the different laboratories as viewed in figure 2.3. A gathering of available laser systems, the state-of-the-art laser technology together with the history and envisioned future projects can be found in Ref. [49]. Today, lasers with a peak power in the Petawatt regime are readily availabe for research at ultra-relativistic laser intensities [151, 191, 181, 106, 121].
An important property of a high-power laser is the temporal *laser contrast*. It reflects the amount of light that preceds the actual main pulse and can be referred to as *leading edge*. A sketch of the relevant timescales and powers is shown in figure 2.4 (a). Generally, the parts of the leading edge can be divided into *prepulses*, the *nanosecond pedestal* and the *picosecond pedestal*. All parts have different origins in the laser-amplification chain and six principal mechanisms are listed in section 4.3.2 of Ref. [49]: The nanosecond pedestal consists of amplified spontaneous emission from the laser amplifiers and parametric fluorescence from optical parametric amplifiers. The main source of the 100 ps-scale pedestal is attributed to scattering on the stretcher and compressor gratings. A picosecond scale pedestal can be formed by imperfect compression or the quantum noise of the seed oscillator. Isolated prepulses are generated by back reflections in components that are used in a multipass configuration or by postpulses due to nonlinear mixing effects during amplification.
Especially for Petawatt-class high-intensity laser-solid interactions, the leading edge is of great importance. As the peak intensities approach values higher then $10^{21}\,\mathrm{W/cm^2}$, the inherently existing prepulses and pedestals surpass the relevant intensity scales of target manipulation at delays much earlier than the pulse duration of the main-laser peak, e.g., at tens of picoseconds before a 30 fs-laser pulse. This results in a significant modification of the target by heating and expansion (*preheating* and *preexpansion*) before the relativistic interaction during the high-intensity laser-peak.
The most common technique for measuring the laser contrast is scanning *third-order autocorrelation* (TOAC) [77, 179]. The measurement principle relies on sampling of the laser pulse with a replica of itself via a two-staged frequency conversion that allows to differentiate between prepulses and post-pulses in the measured signal. The delay between the signal pulse and the replica is scanned and a so-called *laser-contrast curve* is derived. A dynamic range between the laser peak and the detection limit of better than 10^{12} is possible [179]. An exemplary measurement is shown by the blue line in

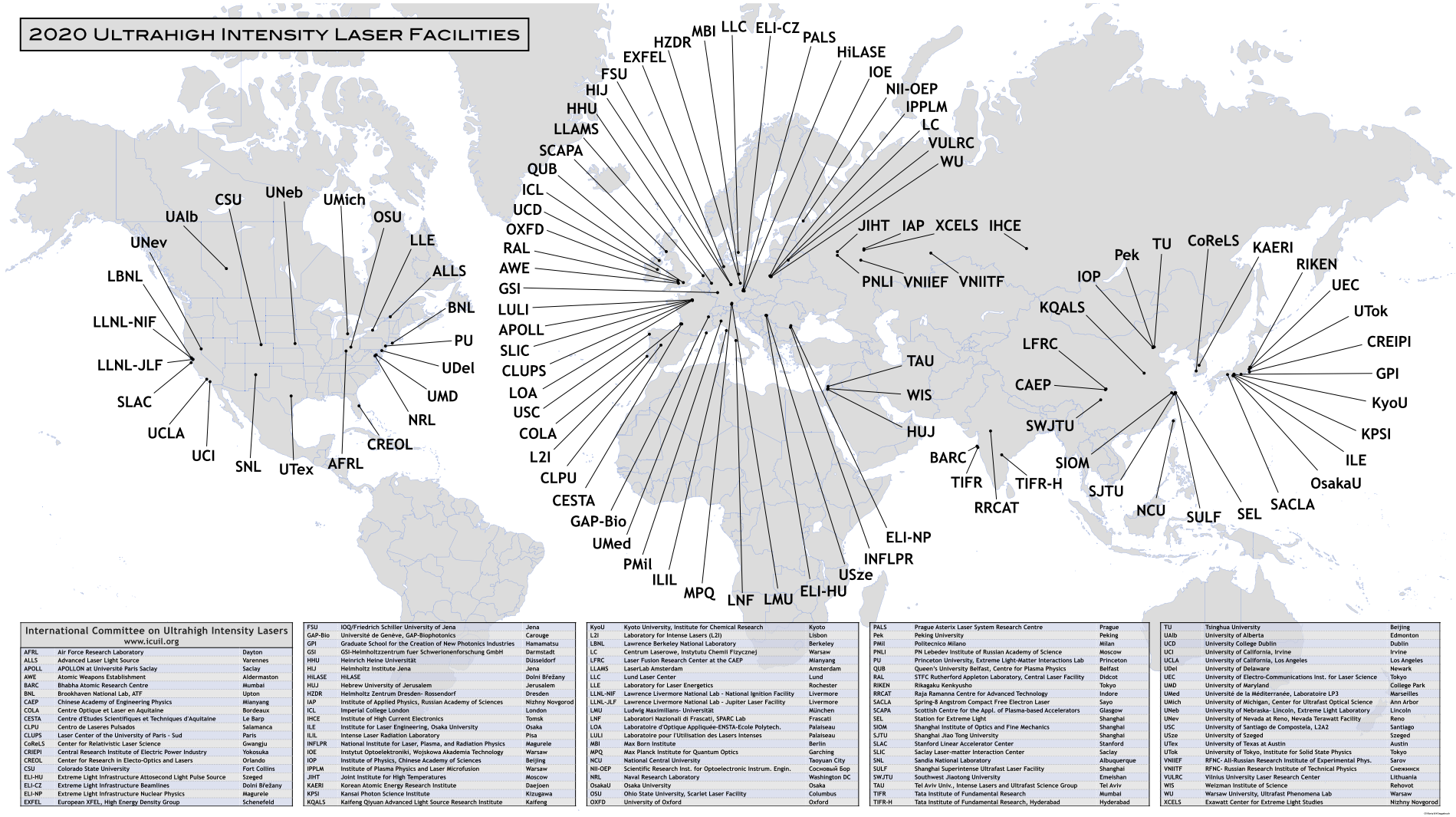

International Committee on Ultrahigh Intensity Lasers
www.icuil.org

AFRL	Air Force Research Laboratory	Dayton
ALLS	Advanced Laser Light Source	Varennes
APOLL	APOLLON at Université Paris Saclay	Saclay
AWE	Atomic Weapons Establishment	Aldermaston
BARC	Bhabha Atomic Research Centre	Mumbai
BNL	Brookhaven National Lab, ATF	Upton
CAEP	Chinese Academy of Engineering Physics	Mianyang
COLA	Centre Optique et Laser en Aquitaine	Bordeaux
CESTA	Centre d'Etudes Scientifiques et Techniques d'Aquitaine	Le Barp
CLPU	Centro de Laseres Pulsados	Salamanca
CLUPS	Laser Center of the University of Paris - Sud	Paris
CoReLS	Center for Relativistic Laser Science	Gwangju
CRIEPI	Central Research Institute of Electric Power Industry	Yokosuka
CREOL	Center for Research in Electo-Optics and Lasers	Orlando
CSU	Colorado State University	Fort Collins
ELI-HU	Extreme Light Infrastructure Attosecond Light Pulse Source	Szeged
ELI-CZ	Extreme Light Infrastructure Beamlines	Dolní Břežany
ELI-NP	Extreme Light Infrastructure Nuclear Physics	Magurele
EXFEL	European XFEL, High Energy Density Group	Schenefeld

FSU	IOQ/Friedrich Schiller University of Jena	Jena
GAP-Bio	Université de Genève, GAP-Biophotonics	Carouge
GPI	Graduate School for the Creation of New Photonics Industries	Hamamatsu
GSI	GSI-Helmholtzzentrum fuer Schwerionenforschung GmbH	Darmstadt
HHU	Heinrich Heine Universität	Düsseldorf
HIJ	Helmholtz Institute Jena	Jena
HiLASE	HiLASE	Dolní Břežany
HUJ	Hebrew University of Jerusalem	Jerusalem
HZDR	Helmholtz Zentrum Dresden- Rossendorf	Dresden
IAP	Institute of Applied Physics, Russian Academy of Sciences	Nizhny Novgorod
ICL	Imperial College London	London
IHCE	Institute of High Current Electronics	Tomsk
ILE	Institute for Laser Engineering, Osaka University	Osaka
ILIL	Intense Laser Radiation Laboratory	Pisa
INFLPR	National Institute for Laser, Plasma, and Radiation Physics	Magurele
IOE	Instytut Optoelektroniki, Wojskowa Akademia Technology	Warsaw
IOP	Institute of Physics, Chinese Academy of Sciences	Beijing
IPPLM	Institute of Plasma Physics and Laser Microfusion	Warsaw
JIHT	Joint Institute for High Temperatures	Moscow
KAERI	Korean Atomic Energy Research Institute	Daejoen
KPSI	Kansai Photon Science Institute	Kizugawa
KQALS	Kaifeng Qiyuan Advanced Light Source Research Institute	Kaifeng

KyoU	Kyoto University, Institute for Chemical Research	Kyoto
L2I	Laboratory for Intense Lasers (L2I)	Lisbon
LBNL	Lawrence Berkeley National Laboratory	Berkeley
LC	Centrum Laserowe, Instytutu Chemii Fizycznej	Warsaw
LFRC	Laser Fusion Research Center at the CAEP	Mianyang
LLAMS	LaserLab Amsterdam	Amsterdam
LLC	Lund Laser Center	Lund
LLE	Laboratory for Laser Energetics	Rochester
LLNL-NIF	Lawrence Livermore National Lab - National Ignition Facility	Livermore
LLNL-JLF	Lawrence Livermore National Lab - Jupiter Laser Facility	Livermore
LMU	Ludwig Maximilians- Universität	München
LNF	Laboratori Nazionali di Frascati, SPARC Lab	Frascati
LOA	Laboratoire d'Optique Appliquée-ENSTA-École Polytech.	Palaiseau
LULI	Laboratoire pour l'Utilisation des Lasers Intenses	Palaiseau
MBI	Max Born Institute	Berlin
MPQ	Max Planck Institute for Quantum Optics	Garching
NCU	National Central University	Taoyuan City
NII-OEP	Scientific Research Inst. for Optoelectronic Instrum. Engin.	Сосновый бор
NRL	Naval Research Laboratory	Washington DC
OsakaU	Osaka University	Osaka
OSU	Ohio State University, Scarlet Laser Facility	Columbus
OXFD	University of Oxford	Oxford

PALS	Prague Asterix Laser System Research Centre	Prague
Pek	Peking University	Peking
PMil	Politecnico Milano	Milan
PNLI	PN Lebedev Institute of Russian Academy of Science	Moscow
PU	Princeton University, Extreme Light-Matter Interactions Lab	Princeton
QUB	Queen's University Belfast, Centre for Plasma Physics	Belfast
RAL	STFC Rutherford Appleton Laboratory, Central Laser Facility	Didcot
RIKEN	Rikagaku Kenkyusho	Tokyo
RRCAT	Raja Ramanna Centre for Advanced Technology	Indore
SACLA	Spring-8 Angstrom Compact Free Electron Laser	Sayo
SCAPA	Scottish Centre for the Appl. of Plasma-based Accelerators	Glasgow
SEL	Station for Extreme Light	Shanghai
SIOM	Shanghai Institute of Optics and Fine Mechanics	Shanghai
SJTU	Shanghai Jiao Tong University	Shanghai
SLAC	Stanford Linear Accelerator Center	Stanford
SLIC	Saclay Laser-matter Interaction Center	Saclay
SNL	Sandia National Laboratory	Albuquerque
SULF	Shanghai Superintense Ultrafast Laser Facility	Shanghai
SWJTU	Southwest Jiaotong University	Emeishan
TAU	Tel Aviv Univ., Intense Lasers and Ultrafast Science Group	Tel Aviv
TIFR	Tata Institute of Fundamental Research	Mumbai
TIFR-H	Tata Institute of Fundamental Research, Hyderabad	Hyderabad

TU	Tsinghua University	Beijing
UAlb	University of Alberta	Edmonton
UCD	University College Dublin	Dublin
UCI	University of California, Irvine	Irvine
UCLA	University of California, Los Angeles	Los Angeles
UDel	University of Delaware	Newark
UEC	University of Electro-Communications Inst. for Laser Science	Tokyo
UMD	University of Maryland	College Park
UMed	Universite de la Méditerranée, Laboratoire LP3	Marseilles
UMich	University of Michigan, Center for Ultrafast Optical Science	Ann Arbor
UNeb	University of Nebraska- Lincoln, Extreme Light Laboratory	Lincoln
UNev	University of Nevada at Reno, Nevada Terawatt Facility	Reno
USC	University of Santiago de Compostela, L2A2	Santiago
USze	University of Szeged	Szeged
UTex	University of Texas at Austin	Austin
UTok	University of Tokyo, Institute for Solid State Physics	Tokyo
VNIIEF	RFNC- All-Russian Research Institute of Experimental Phys.	Sarov
VNIITF	RFNC- Russian Research Institute of Technical Physics	Снежинск
VULRC	Vilnius University Laser Research Center	Lithuania
WIS	Weizman Institute of Science	Rehovot
WU	Warsaw University, Ultrafast Phenomena Lab	Warsaw
XCELS	Exawatt Center for Extreme Light Studies	Nizhny Novgorod

Figure 2.3.: ICUIL World Map 2020 [6]

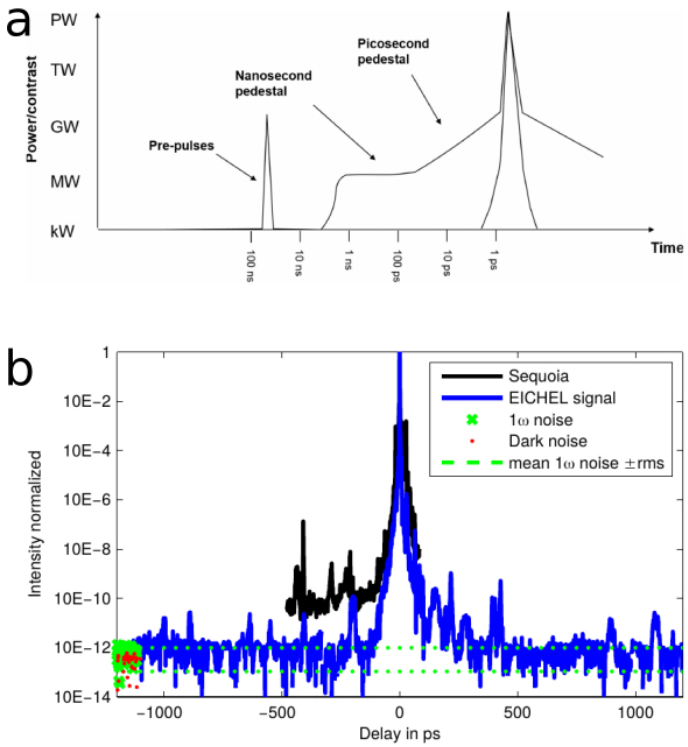

Figure 2.4.: **(a)** Figure copied from [49]: General sketch of the temporal contrast of a high-power laser. **(b)** Figure copied from [179]: Exemplary measurement of the *laser-contrast curve* (blue line) by scanning *third-order autocorrelation* (TOAC) and the detection limit of the method (green dots).

figure 2.4 (b). Negative delays correspond to times before the arrival of the laser peak at 0 ps. Several distinct prepulses at hundreds of picoseconds before the main peak as well as the triangular-shaped picosecond pedestal, which is placed symmetrically around the laser peak, are visible above the detection limit (green dots). The optical temporal resolution of a measurement is typically between 0.1 ps and 1 ps.
As target pre-expansion induces an unwanted amount of perturbation to the relativistic laser-target interaction, several techniques for the improvement of the laser contrast were developed. The introduction of double-CPA lasers [98] and a proper choice of the optical stretcher [119] are paramount examples. Furthermore, techniques like plasma mirrors [194, 145] or second-harmonic generation (SHG) [91, 26] after compression are frequently used to enhance the laser contrast by several orders of magnitude. A comprehensive summary of possible enhancement methods is given in section 4.3.2 of Ref. [49].

2.1.2. Plasma density as the decisive parameter for laser-ion acceleration

Nowadays, the reliable work-horse mechanism of ion acceleration by high-intensity lasers is *target normal sheath acceleration* (TNSA) [206]. It describes the acceleration of ions from a solid-density foil-like target. In a nutshell, the laser-to-ion energy transfer is mediated via a laser-heated population of hot electrons that generates a capacitor like acceleration structure on the rear side of the target. First and depending on the laser polarization, the laser generates a population of hot electrons via $J \times B$ heating [109, 205] and Brunel heating [33] on the front side of the solid target. Subsequently, the electrons traverse and circulate the target, while the ions initially stay at rest due to their higher mass. This generates a Debye-sheath on the rear side of the target, i.e., a quasi-static electric field. The electric field transfers the energy of the hot electrons to the ions. Especially light ions from the hydo-carbonic contaminant layers on the rear surface of the target are exposed to the highest accelerating fields. The step-by-step evolution of the Debye-sheath drives the acceleration of ions to their

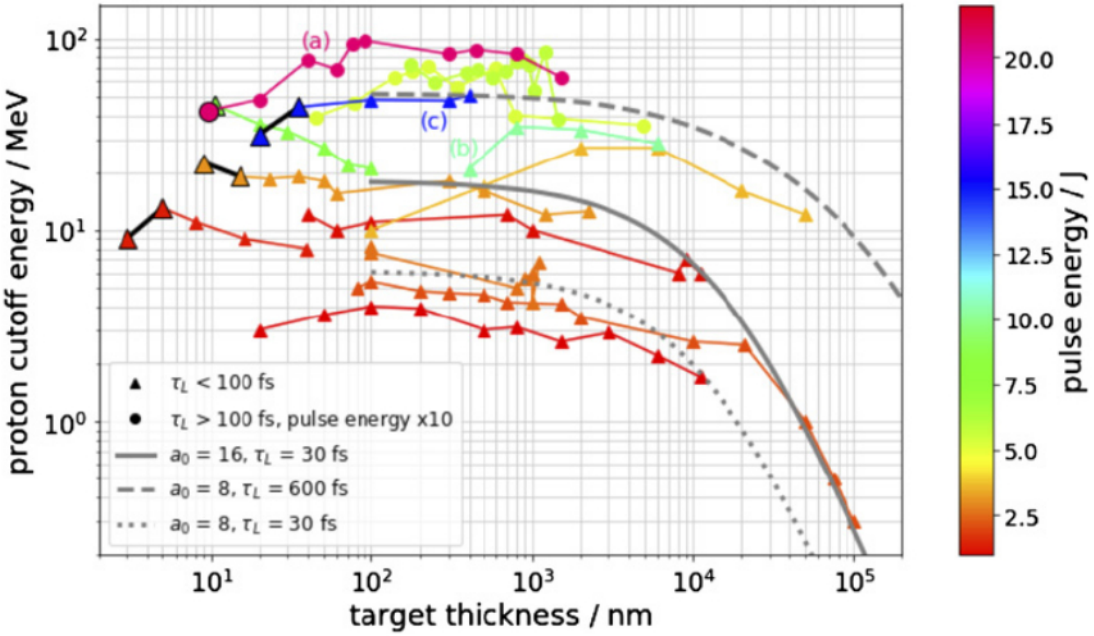

Figure 2.5.: Figure copied from [13]: Target-thickness scan for different laser systems: (a) data from Ref. [90], (b) from J-Karen laser and (c) DRACO-PW laser. Laser energy is color coded, a factor of 10 has to be applied for pulse durations $\tau_L > 100\,\text{fs}$. Gray lines are thickness-scan models from Ref. [48].

final energies (usually tens of MeV for laser intensities around $10^{21}\,\text{W/cm}^2$). An in-depth model of TNSA is described in different theoretical publications, see References [135] and [182].
Comprehensive summaries on laser-ion acceleration and the developments during the last two decades are gathered in several review publications [48, 124, 13]. In the following, only the most important key points for the context of this thesis are discussed and the focus lies on the acceleration of protons, which are the lightest ion species. The usual experimental procedure, for reaching highest proton energies, is the maximization of available laser intensity together with a search for the optimum target thickness, see figure 2.5. For all the different laser systems (different laser energies and pulse durations), the experimental data as well as the modeling (gray curves) feature the similar general trend of higher maximum proton energy or an optimum of maximum proton energy at lower target thickness. Generally, this increase of ion energy with lower target thickness is expected in the TNSA picture, because the density of electons in the sheath is increased for lower target thickness and the resulting accelerating fields are stronger [48].
However, this is only valid as long as a steep plasma-density gradient on the rear surface of the target is maintained. At this point, the dependency of laser-ion acceleration on the temporal laser contrast comes into play. The pre-expansion of a target by prepulses and the laser pedestal gains relevance with decreasing target thickness. Although this opens an opportunity for advanced acceleration schemes [57], it also limits the scalability of ion energy by target thickness for a given laser system in the TNSA picture. Because the temporal laser contrast varies from laser system to laser system, the pre-expansion of the target varies accordingly. This explains the different optimum target thicknesses for different laser systems. In other words, figure 2.5 does not only show a variation of target thickness. It shows a complicated variation of different target parameters, such as the front-side and rear-side plasma-density gradient, amount of target material and peak density. Especially in the regime of optimum proton acceleration, figure 2.5 can be interpreted as a scan of the target's peak density.
The so far published highest proton energies ($> 90\,\text{MeV}$) were measured in a hybrid acceleration regime with contributions by TNSA and *radiation pressure acceleration* (RPA) in the *relativistic induced transparency* (RIT) regime [90]. Figure 2.5 shows the experimental data points from reference [90] labeled by "(a)". The optimum acceleration performance is reached for an initial target thickness of about 100 nm. While the maximum proton energy is decreased for lower target thickness, the

amount of light that is transmitted through the target is increased up to 45 % of the initial laser light. The measurement of a significant amount of transmitted light nicely shows the volumetric nature of the laser-solid interaction within this regime. This is not considered in the original picture of TNSA and directly leads to a number of acceleration mechanisms that were proposed beyond TNSA [48, 124]. Figure 2.2 (b) lists a number of ion acceleration mechanisms, roughly sorted by the plasma density of the target. Note, that not the initial target density but rather the spatial distribution and absolute peak density shortly before the arrival of the ultra-relativistic laser peak is of relevance to the acceleration mechanism at play. TNSA dominates the acceleration at target densities of high solid density. RIT dynamically increases the number of electrons that are reachable by the laser pulse by laser-heating of the electrons themself. The relativistic Lorentz or gamma factor of the electrons γ reduces the critical densiy that is relevant for the reflection of the laser down to n_c/γ. Thus, RIT can yield an enhanced volumetric interaction with increased sheath fields (RIT-TNSA) [200, 52, 62]. At ultra-relativistic laser intensities, the light pressure (ponderomotive force) becomes significant and enables ion acceleration by *radiation pressure acceleration* (RPA). The contribution of this mechanism can be viewed as a laser piston that pushes the electrons out of the target and, in combination with RIT, can lead to very high proton energies, e.g., *hole-boring RPA* [61] or *light-sail RPA* [164]. A lowering of the target density into the nearcritical-density regime enables specialized mechanisms like *synchronized acceleration by slow light* (SASL) [32], which is also called *relativistic-transparency-front RPA* (RTF-RPA) [81], and *collisionless shock acceleration* (CSA) [185, 68]. For target densities below the critical density, several publications address *magnetic vortex acceleration* (MVA) [34, 138, 137, 152]. For MVA, the laser propagates through the target, formates a channel through the electrons and creates a strong electron current on the laser-propagation axis. The current follows the laser pulse into the rear-side plasma-density gradient and generate a magnetic vortex, which then induces an electric field pointing away from the target. The consecutive steps allow for *inductive acceleration*, which transfers energy from the relatively fast propagating laser driver into the plasma and subsequently to the slowly reacting ions via the generated electric field.

Finding and realizing acceleration mechanisms in addition to TNSA is motivated by the search for a stronger scaling of proton energy with laser power or the tuning of other particle-beam parameters like divergence, number or spectral distribution. Furthermore, the acceleration of light ion species like Helium could benefit from unconventional targetry approaches together with alternative schemes of acceleration. Although a target thickness scan in combination with the leading edge of a high-intensity laser intrinsically provides a scan of target density, the level of control over the spatial density distribution of the target is limited and the amount of material within the interaction changes for every target thickness. More control over the spatial profile and peak of the plasma density is desired to experimentally realize and explore the proposed acceleration mechanisms.
There exist two prerequisites to follow this path: First, a "high" temporal contrast of the laser, which avoids unwanted changes of the anticipated target-density distribution. As mentioned before, several experimental techniques are available for this purpose. Second, an experimental realization of advanced target manufacturing or target-density tailoring in the nearcritical-density regime ($\sim 10^{21}\,\mathrm{cm}^{-3}$). Most often, high-density gas jets are used [86, 39, 163, 186], but the surface-density gradients are long and it is technically challenging to reach nearcritical peak densities with pressurized gases [192, 89]. Another concept tries to reach the nearcritical-density regime from the opposite side of the density scale by starting with a solid-density target and subjecting it to controlled hydrodynamic plasma expansion, e.g., triggered by an optical laser pulse, see Ref. [143] and Rehwald et al. [168]. This approach is further detailed in section 2.2.5.

2.1.3. Reproducing high-intensity laser-solid interactions in start-to-end simulations

For high-intensity laser-ion acceleration, reaching quantitative agreement between simulation and experiment is still challenging and achieving a bijective mapping between all experimental measurements and a simulation remains a future challenge [13]. Today, simulations are usually used to exemplify the dominant acceleration mechanism for a rather general combination of target and laser parameters. The most important reason for this current status is that the envisioned *start-to-end simulations*

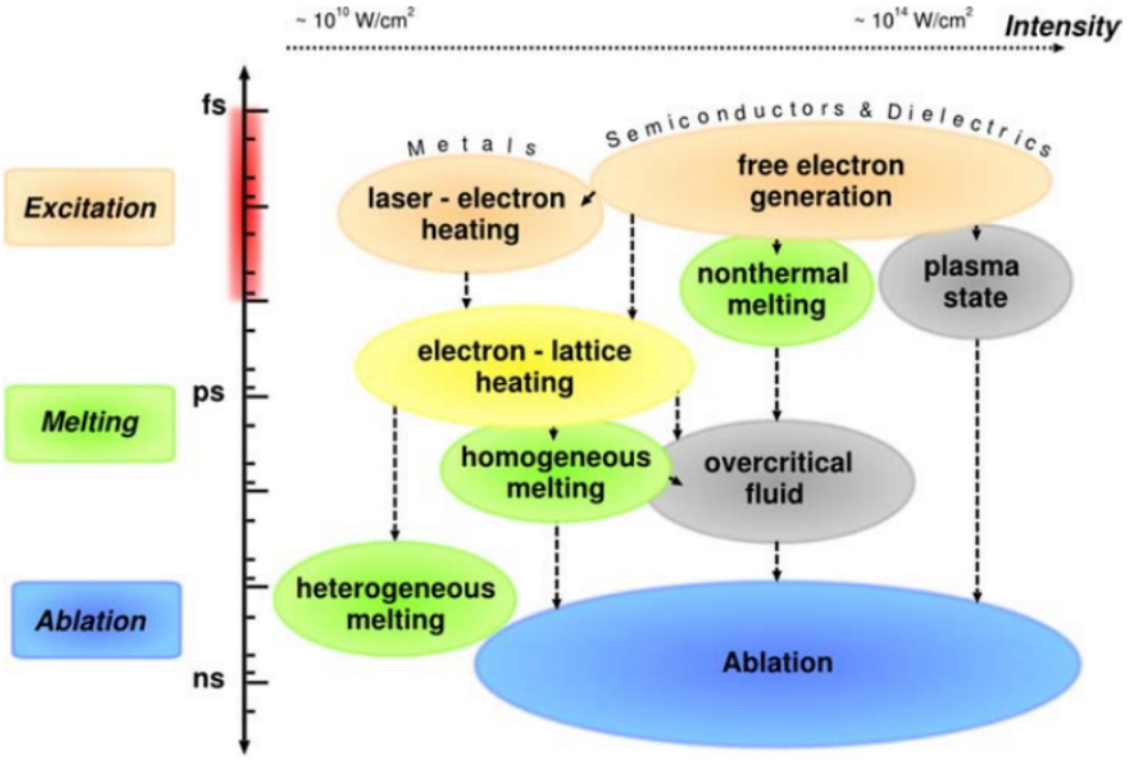

Figure 2.6.: Figure is copied from [172]: Relevant laser intensities and timescales together with the physical principles that initiate the breakdown of metals, semiconductors and dielectrics. In the context of high-intensity laser-solid interactions, the phrase *Ablation* can be associated with target pre-expansion.

need to include the relativistic laser-matter interaction *together* with the leading-edge-driven target pre-expansion and pre-heating. I.e., numerical modeling of different physical interaction mechanisms of laser radiation with matter on a broad range of temporal and spatial scales is required.
Generally, a high-intensity laser-solid interaction can be divided into three regimes of interaction mechanisms: First, the intensity range for which the laser can be modeled as a perturbation of the solid atomic system, i.e., for which the energy scales of the band structure dominate over the energy provided by the laser. Here, the energy transfer from the laser to the solid needs to be modeled until the *breakdown* of the solid, i.e., until the solid bonds get suspended and/or the energy deposition of the laser becomes localized at the critical-density surface of the quasi-free electron cloud. Second, after the breakdown of the solid, the matter can be modeled as a collective fluid of electrons and ions. The laser deposits energy mainly at the critical-density surface into the electronic system, e.g., by inverse bremsstrahlung and resonance absorption. Third, for relativistic prepulses and the ultra-relativistic laser peak, the laser field dominates the system. At these intensities, the ponderomotive force is strong and allows for a kinetic treatment of particles and electro-magnetic fields in particle-in-cell (PIC) simulations. A combination of all required modeling capabilities in a single simulation tool at full dimensionality is not available yet and a common approach is to make transitions between different simulation tools at different temporal and laser-intensity scales.

2.1.3.1. Breakdown of the solid

A classification of solids by their conductivity allows them to be separated into metals, semiconductors and dielectrics. For metals, the Fermi energy is located in the conduction band while, for dielectrics, the Fermi energy is located in the band gap between valence and conduction band. The optical properties of metals and dielectrics are consequently very different. The conduction-band electrons in a metal can absorb light from a continuous energy range and naturally show a collective plasma-like response that enables the reflection of optical light. Dielectrics with a band gap higher than the

incident photon energy, however, are mostly transmissive to incident radiation. The breakdown of both, metals and dielectrics, is connected to the removal of the solid bonds. Generally, this can be called melting. A detailed review in the context of laser ablation from solids can be found in Ref. [172].
Figure 2.6 gives an overview of the relevant laser intensities, timescales and physical mechanisms of laser-induced breakdown. In the context of high-intensity laser-solid interactions, the term *Ablation* can be associated with target pre-expansion. Metals usually show a lower intensity threshold of breakdown, starting already around $10^{10}\,\mathrm{W/cm^2}$. The melting of a metal is driven by the collision rate of laser-heated electrons with the lattice (electron-phonon collisions). The laser energy is first absorbed by the electron system and subsequently distributed to the lattice, which melts like in a classical description (left side of figure 2.6). Depending on the band gap, the breakdown of dielectrics usually occurs at higher intensities of up to $10^{14}\,\mathrm{W/cm^2}$ (right side of figure 2.6). The possible mechanisms that lead to breakdown are more diverse. Generally, the generation of quasi-free electrons in the conduction band occurs first by *strong-field ionization* , i.e. *multi-photon ionization* or *tunnel ionization*. The subsequent collisional generation of further quasi-free electrons (*avalanche ionization*, also called *impact ionization*) highly depends on laser intensity and pulse duration. The solid bonds are either removed directly by the excitation of electrons (*nonthermal melting*) or by collisions of the excited electrons with the lattice or bound electrons, which heats the lattice in a classical way. A more detailed description of the laser-induced breakdown of dielectrics is given in chapter 3.
The breakdown of the target is an important quantity for start-to-end simulation of high-intensity laser-solid interactions. It defines the starting point from which on the target can be modeled as a two temperature plasma-fluid and from which on laser energy deposition becomes highly efficient to drive significant target pre-expansion. Only recently, a publication raised the topic of target breakdown of different foil-target materials that are commonly used in laser-ion acceleration and discusses the implications to the laser contrast of different high-power laser systems [202]. Up to now, the topic of target breakdown received not much attention by the research community of high-intensity laser-ion acceleration. Today, most often dielectric targets, e.g., plastic foils or cryogenic hydrogen, are used to generate highest proton energies, see references [103, 201, 90, 211] and Rehwald et al. [168]. Chapter 3 of this thesis explores dielectric breakdown in experiments of ultra-relativistic laser-solid interactions and it's relation to the laser contrast.

2.1.3.2. Radiation-hydrodynamics modeling of the leading-edge-driven target pre-expansion

For laser intensities in the leading edge of a high-power laser, radiation-hydrodynamics simulations are commonly used to compute the comparably long timescales between target breakdown and the interaction of the target with the relativistic intensities close to the peak of the laser pulse. The plasma is treated as a fluid of electrons and ions and different models are implemented to calculate the deposition of laser energy to the electron fluid. Depending on the software, different spatial dimensionality and laser-intensity ranges can be simulated. *MULTI2D* [166], *Multi-fs* [165] and the *FLASH code* [71] are examples with different modeling capabilities.
In the following, the generally produced plasma dynamics are exemplified by a radiation-hydrodynamics simulation with the *Pollux* code in figure 2.7 (a) from Ref. [133]. An artificial laser pedestal of 0.5 ns (red solid line) and 3.5 ns (black solid line) duration with a constant intensity of $1 \cdot 10^{12}\,\mathrm{W/cm^2}$ impinges from the left onto a 25 µm-thick Copper-foil target and modifies the electron density in the presented way. Both cases represent the target density distribution at the time of the arrival of the ultra-relativistic laser pulse on target. The laser pedestal heats the front surface of the target at the position of the critical plasma density (horizontal blue line) and produces an exponential front-surface scalelength L_O of the plasma density by ablation. The ablation pressure on the front surface causes a material-compression wave that propagates into the target bulk. The compression wave is visible as a density peak of the black line in the inset of figure 2.7 (a). Between the position of the compression wave and the position of the critical plasma density, a reduction of the initial solid density with a ramp-like shape is produced. It can be approximated by a second exponential scalelength L_I of the plasma density.
The described mechanisms are well-known from the direct-drive approach of inertial-confinement fu-

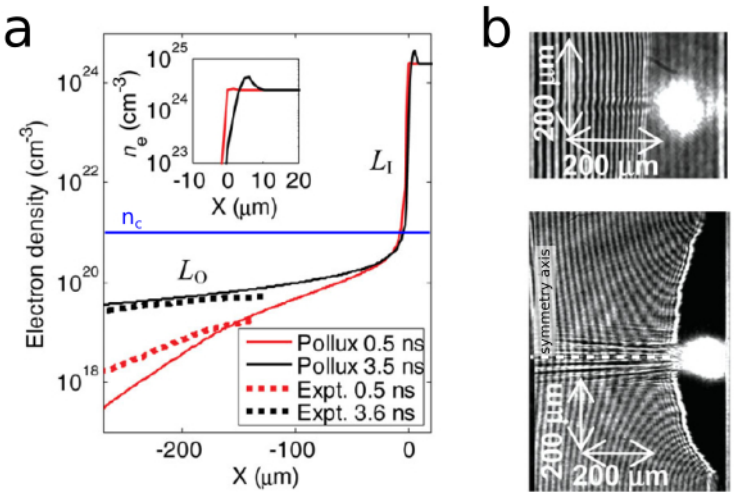

Figure 2.7.: Figure copied from [133]. **(a)** Results of radiation-hydrodynamic simulations: Electron density distributions on the front side of a Copper target after irradiation by an artificial laser pedestal of $1 \cdot 10^{12}\,\mathrm{W/cm^2}$ intensity with a duration of 0.5 ns (red solid line) and 3.5 ns (black solid line). For this experiment, the critical density is located at $1 \cdot 10^{21}\,\mathrm{cm^{-3}}$. Experimental measurements of the density are given as dotted lines. **(b)** Interferometry measurements by optical probing. Upper: 0.5 ns pedestal, Lower: 3.6 ns pedestal. The laser is entering the field of view from the left. Refraction by the solid target (black regions) and parasitic plasma self-emission (white spot) is visible on the right-hand side of each image. For both interferograms, the symmetric refraction around the horizontal axis shows the channeling of the laser pulse in the undercritical pre-plasma .

sion [45]. For high-intensity laser-solid interactions, the mechanisms are used to artificially preshape the target density by pre-pulses [120, 133, 82] or to take into account the intrinsically present leading edge of high-power lasers [132, 141, 57] in simulations.

Hydrodynamic simulations model the plasma dynamics in an equilibrium way via local temperatures, densities, heat capacity, conductivity, etc. The *equation of state* (EOS) defines the relationship between the thermodynamic quantities of the system, e.g., temperature, density, volume and pressure. The EOS is an important input parameter for hydrodynamic simulations. For two-temperature plasmas, e.g., plasmas with a different electron and ion temperature, the *Frankfurt equation of state* (FEOS) [63] can be used. Furthermore, a correct modeling of the heat-transfer rate is relevant.
The EOS defines how a material-compression wave propagates through the target and which thermodynamic state is generated during and after compression. The influence is coherently explained in Ref. [120]. In this reference, the reflection of a compression wave on the rear surface of the target and the subsequent generation of a rear-side plasma-density gradient is discussed together with other geometric effects that impact the directionality of ion acceleration in the TNSA regime. Depending on the target thickness and the duration of the laser pedestal, the compression wave is able to not only reach the rear surface and get reflected once. It can also be reflected back and forth between the rear and front side of the target and by this completely smear out all sharp density gradients of an initially box-shaped density profile of a solid target. Because of mass conservation, the generation of large front-side and rear-side plasma-density gradients is connected to a reduction of peak density. Depending on the intensity level and duration of the laser pedestal, target pre-expansion can cause a reduction of the peak density even down to the critical density, like it is presented in figure 2.8 from Ref. [132]. In this reference, a metal foil of 5 µm thickness is irradiated by a 1 ns pedestal of $1 \cdot 10^{13}\,\mathrm{W/cm^2}$ intensity, which corresponds to the intrinsically present nanosecond pedestal of the leading edge of the utilized high-power laser. The displayed line-out of density is taken along the laser axis and the blue line marks the critical plasma density. The line-out visualizes the generated large-scale front-side and rear-side plasma-density gradients together with the significant reduction of

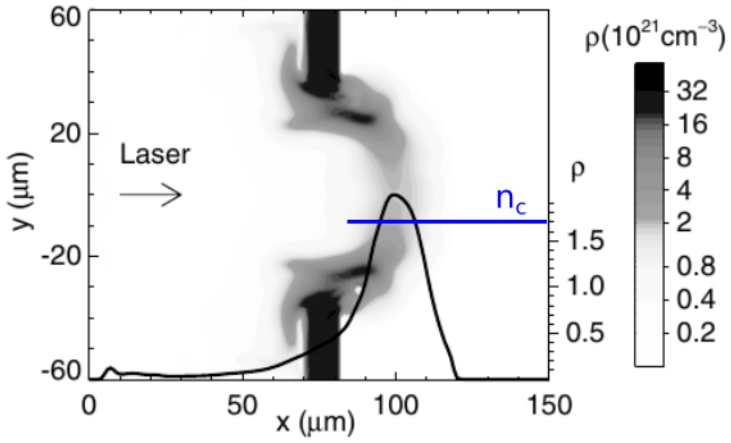

Figure 2.8.: Figure copied from [132]. Result of a radiation-hydrodynamics simulation: Two-dimensional electron-density distribution of a 5 µm-metal-foil target after irradiation by a laser pedestal of 1 ns duration with an intensity of $1 \cdot 10^{13}\,\mathrm{W/cm^2}$. The line-out of density is taken along the central laser axis. It shows a large-scale front-side and rear-side plasma-density gradient together with the reduction of the peak density down to the critical plasma density.

the peak density down to the critical density. For thinner metal targets, a lowering of the peak density even below the critical density is reported.
As shown, radiation-hydrodynamics simulations are a convenient tool to model the interaction of the leading edge of a high-power laser with a solid-density target on the timescale of nanoseconds down to picoseconds. The subsequent relativistic laser-plasma interaction around the laser peak highly depends on the generated plasma distribution by target pre-expansion. However, the limitations of each simulation tool with respect to the implemented heating mechanisms of electrons, reduced dimensionality and the negligence of ionization and recombination provides possible sources of errors and a comparison between different simulation tools with respect to their known limitations is requires for quantitatively valid results.

2.1.3.3. Modeling of the relativistic interaction by particle-in-cell simulations

The laser-plasma interaction at relativistic laser intensities is characterized by the generation of hot electrons. Laser-electron heating occurs by different mechanism, e.g., Brunel heating [33], $J \times B$ heating [109, 205] and the ponderomotive force. In first approximation, the generated plasma is collisionless and the electromagnetic field of the laser together with the generated charge-separation fields dominate the system. The regime is typically modeled by particle-in-cell (PIC) simulations.
In PIC simulations, the particles are grouped to *macro-particles*. They are able to move in a contiuous space according to the electromagnetic fields present. In contrast to that, Maxwell's equations are solved on a descrete and fixed grid and the local currents are calculated by the particle motion. Details on the general principle, the capabilities and applications in laser-plasma physics can be found for example in Ref. [14].
Several PIC-simulation tools are available, e.g., EPOCH [14], OSIRIS [70], Warp-X [198] and PIConGPU [35, 36]. Most of them are highly parallelized to manage the computational requirements. For high-intensity laser-solid interactions, most simulations are performed in one or two-dimensional space. Three-dimensional simulations are rare, because the computational expenses increase drastically and challenge the limits of the largest existing computer-clusters worldwide. Today, the available machines limit the computable scales of high-intensity laser-solid interactions to tens of micrometer in each spatial dimension and hundreds of femtoseconds in time (with respect to lasers at 800 nm wavelength). These limits hinder the simulation of the relativistic laser-solid interaction together with the leading-edge-driven target pre-expansion. Furthermore, physical interaction mechanisms that occur

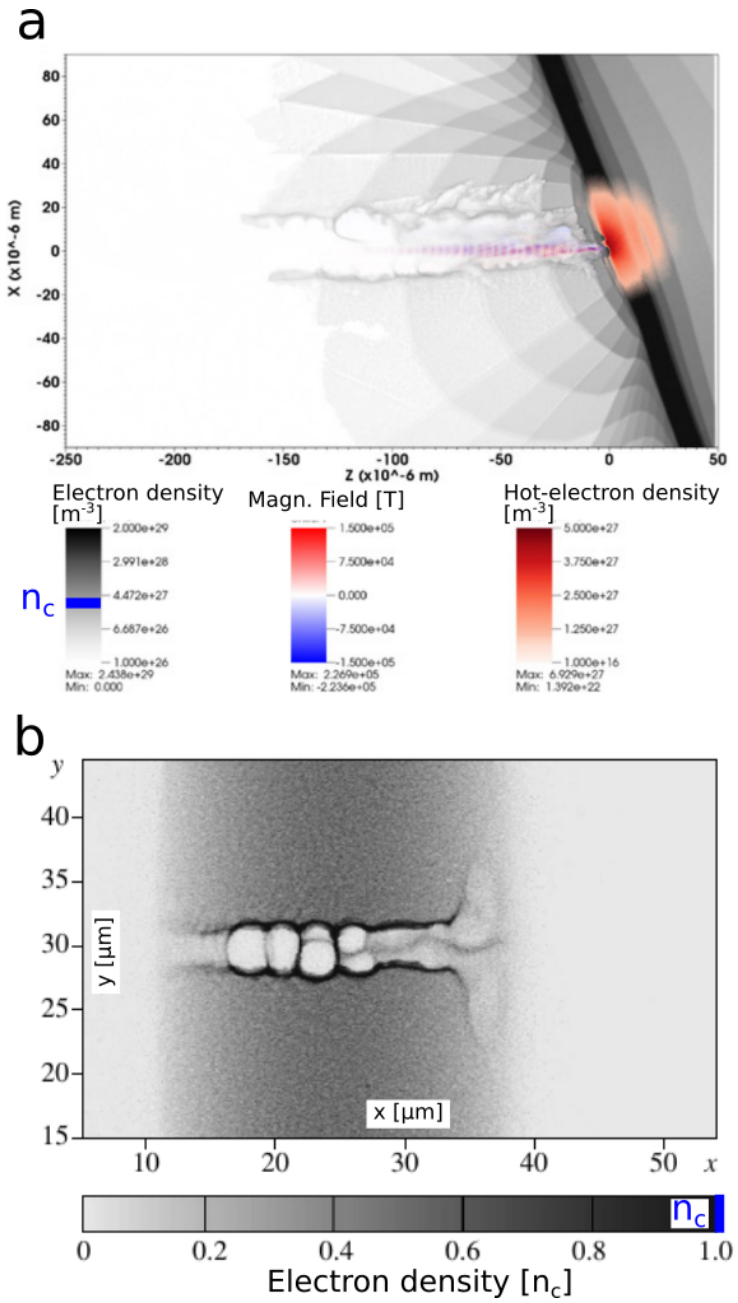

Figure 2.9.: **(a)** Figure copied from [14]. Snapshot of the electron density (gray) of a PIC simulation in which a relativistic laser pulse (oscillating field is visible in red-blue colorscale) is interacting with a solid-density foil target with pre-plasma on the front and on the rear side. The laser propagates from the left side towards the foil and generates a channel through the pre-plasma. At the front side of the foil, the laser heats electrons (red colorscale) that spread into the sourounding plasma. **(b)** Figure copied from [34]. Snapshot of the electron density (gray) of a PIC simulation in which a relativistic laser pulse propagates through a target of nearcritical density. The initial peak density of the target is $0.5\,n_c$ with a half-sinusoidal distribution from left to right. For the presented timestep, the laser already left the simulation box and created a channel through the entire target.

at lower laser intensities are only partially or not at all included in todays PIC-simulation tools, e.g., collisional plasmas, ionization and recombination, atomic-radiation processes and collective phenomena of solid-state physics. As the computational resources increase over the years, many possibilities for future improvements exist [13].
For the here described staged approach of start-to-end simulations, the results of the radiation-hydrodynamic modeling are transferred as initial conditions to the PIC simulation. Usually, a transition time at hundreds of femtoseconds or single picoseconds before the high-intensity laser peak is chosen [141, 57], i.e., a point at which the laser intensity approaches relativistic intensities. To generally illustrate the possible interactions, figure 2.9 presents two different scenarios.
In figure 2.9 (a), the target is modeled as a solid-density foil with pre-plasma on the front and on the rear surface. The electron density is shown by the gray colorscale. The laser (oscillating field is shown in red-blue colorscale) propagates from the left side into the plasma and creates a channel inside the pre-plasma. At the position where the targets becomes highly overcritical, the laser creates a cloud of hot electrons (red colorscale). Imagining zero pre-plasma on the rear side of the foil target, the hot electrons would generate a Debye-sheath with a strong charge-separation field that subsequently accelerates ions from the rear side of the target via TNSA. However, a large amount of pre-plasma on the rear side, like in the visualized example, suppresses this effect and minimizes the acceleration of particles into the surrounding vacuum.
Figure 2.9 (b) shows a scenario in which the initial target is completely undercritical (electron density in gray). The target is initialized as a half-sinusoidal distribution of plasma density with a peak at $0.5\,n_c$. The laser propagates from the left to the right and, for the presented timestep, already left the simulation box. The laser created a channel through the entire target and produced a complex and dynamic plasma structure. Charge separation is also present, but not in the same simple picture as in the TNSA description.
Both scenarios, together with the afore discussed target pre-expansion by compression waves that are driven by the intrinsically present leading edge, give an idea of the complexity of a target-thickness scan like it is presented in figure 2.5. As all high-power lasers feature an intrinsic leading edge, precise numerical modeling during all stages of the laser-target interaction is the contemporary challenge to disentangle different particle-acceleration mechanisms, especially in the RIT and nearcritical-density regime [132, 90, 57].

2.1.4. Comparison of experimental diagnostics and numerical modeling

In high-intensity laser-solid experiments and their simulations, the commonly followed procedure is the comparison of the ensamble of generated final or temporally-integrated reaction products. This includes, for example, x-ray spectra and x-ray yield [195, 129], charge state of accelerated ion species [141], spatial and temporal shape of the high-intensity laser beam after reaction [150, 207], electron temperature [56] and properties of the accelerated ion beam [187, 162]. Usually, there exist only two comparable end points between the simulation and the experiment: The final reaction products and the initial "cold" density distribution of the target together with the temporal and spatial properties of the laser beam. This circumstance is related to the ultra-fast timescale of the interaction itself. In most experiments, the pulse duration of the high-intensity laser is the shortest available quantity. The generation of the reactions products occurs on a similar or shorter timescale and it is challenging to find a sufficiently short probe for time-resolved experimental investigations. In contrast to that, numerical simulations give a detailed insight to the laser-plasma dynamics. Thus, PIC simulations are the common tool to visualize or illustrate the generation mechanism of reaction products today.
Time-resolved diagnostics for imaging the dynamics of strong electric fields via particle beams [29, 173] or for probing of the density and temperature evolution inside a solid target via x-ray free-electron lasers [73, 69] exists. However, they are challenging to implement or simply not available at every experimental facility. A more commonly followed approach is the implementation of time-resolved optical-microscopy techniques to characterize the evolution of the plasma density. Measurements can restrict the range of possible target parameters that are generated by the intrinsic or an artificial leading edge, e.g., shortly before the onset of the relativistic interaction. Figure 2.7 presents an example from Ref. [133]. Here, a short-pulse optical backlighter was used to benchmark the simulated pre-

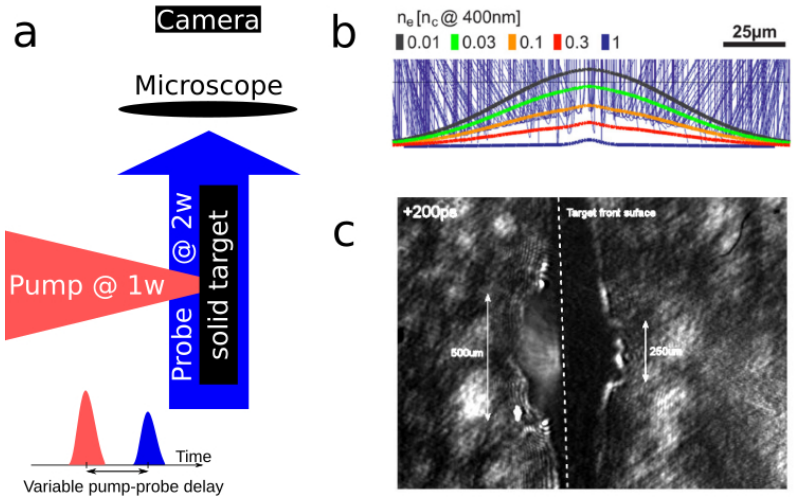

Figure 2.10.: **(a)** General setup of optical probing: The high-intensity pump laser is focused onto a solid-density target that is transversally probed by a short-pulse backlighter, e.g., a second harmonic ("2w") signal of the pump beam ("1w"). The probe beam is imaged to a camera via a microscope (objective or lens). The temporal resolution is given by the pulse duration of the backlighter and the delay between pump and probe is usually variable. **(b)** Figure copied from [134]: Ray-tracing results of a probe beam penetrating a surface gradient of plasma density (for details see text). Isolines of plasma density in units of the critical plasma density are given by different colors. The rays (blue lines) penetrate approximately up to $0.1 n_c$ **(c)** Figure copied from [111]: Shadowgram as derived by transverse optical probing of the interaction of a pump laser with a peak intensity of $5 \cdot 10^{20}\,\mathrm{W/cm^2}$ and 0.5 ps pulse duration with a 5 µm-Copper foil at 200 ps after the pump-laser peak. The dotted line marks the position at which the initially cold front surface of the target was located. Significant plasma expansion is visible on the front and rear side of the target.

expansion of the plasma via optical interferometry (figure 2.7 (b)). The calculated density distribution is shown as dotted lines in figure 2.7 (a) for both leading-edge durations (0.5 ns in red, 3.6 ns in black). Although only densities much lower than the critical density are accessible, the technique gives, in principle, a *temporally resolved* information and by this provides experimental boundary conditions to the sophisticated chain of numerical modeling of start-to-end simulations.

The breakdown of the solid target, the pre-plasma evolution and the plasma-expansion dynamics induced by the ultra-relativistic laser peak are all topics of scientific interest for a better understanding of high-intensity laser-solid interactions, i.e., to optimize the source of laser-accelerated particle. The three topics are ideally suited for an investigation via time-resolved optical-microscopy techniques. This thesis issues all three topics and demonstrates the dependency and relevance with respect to the leading edge of a high-power-laser system. Time-resolved optical microscopy is used to derive experimental boundaries and insight to specific parts of start-to-end simulations that are embedded in a larger project on the development of enhanced laser-driven ion sources from renewable targets.

Now, given that the scientific challenges are stated and a general literature background is provided, the following subsections give an overview on the technical aspects of optical probing in high-intensity laser-solid experiments. An introduction to the different methodologies and the challenge of parasitic plasma self-emission is provided. Finally, the specialized probing technique of *off-harmonic optical probing* is introduced.

2.1.5. Optical probing of high-intensity laser-solid interactions

The terminology "optical probing" usually refers to an experimental configuration in which the interaction of a high-intensity "pump laser" and a target is visualized using an optical "probe laser". The probe-laser pulses are used as a stroboscopic backlighter of the plasma dynamics of the target and a microscope magnifies the interaction either by a lens or by an objective. This allows to transport time-resolved amplitude damping and/or phase-shift information of the target density to a CCD or CMOS chip of a camera. The temporal resolution of the captured data is generally given by the pulse duration of the backlighter. A simplified setup is presented in figure 2.10 (a).
Commonly, the probe-laser beam is picked from the pump-laser system, for example by a beam splitter in the amplification chain and an individual compressor or by picking a signal from the pump beam after compression. Most often the probe signal is frequency converted via second-harmonic generation to achieve a better contrast to the scattered light from the pump beam via spectral filtering and to penetrate higher plasma densities (see the scaling of n_c with laser wavelength in fig. 2.1 (a)).

2.1.5.1. Refraction on solid-density targets

Time-resolved optical-probing diagnostics can infer target-density information at different temporal delays during the high-intensity laser-solid interaction. As the refractive index of a plasma drops to zero at the critical density n_c, probe rays are able to penetrate the undercritical densities of the target only. In this range, the refractive index is smaller than one and a strong density dependence especially for densities higher than $0.1n_c$ is observed (compare to scaling in figure 2.1 (b)). The peak density of solid-density targets is typically between tens and hundreds of n_c and the scalelength of the density gradients below n_c is typically between tens of nanometers and multiple tens of micrometers. Because of the strong refraction with increasing plasma density, the probe rays usually never reach the critical-density surface but get refracted beforehand. This is visualized in figure 2.10 (b) from Ref. [134]. Here, a ray-tracing simulation of an experiment with reflective optical probing at the rear side of a foil target is conducted. The angle of incidence of the probe is 53° to the target-normal direction. The high-intensity pump laser impinges the front surface of the solid target and creates a rear-side plasma expansion. This plasma expansion is modeled by a two-dimensional Gaussian plasma-density distribution and an exponentially decaying plasma density with a scalelength of 6.2 µm. The isolines of density are shown by different colors in figure 2.10 (b). The results of the ray tracing are shown as blue lines. Almost all rays do not reach the critical density surface but instead get refracted close to about $0.1n_c$.

2.1.5.2. Shadowgraphy

A technique to visualize refractive objects is *shadowgraphy*. It is commonly used to image disturbances or flows of transparent media. From a microscopy perspective, it can be considered as a type of bright field imaging of, most often three-dimensional, phase objects. However, absorption would also be visualized with this technique. An exemplary *shadowgram* is shown in figure 2.10 (c) from Ref. [111]. Here, a 5 µm-Copper foil is pumped by a 0.5 ps-laser pulse with a peak intensity of $5 \cdot 10^{20}\,\mathrm{W/cm^2}$. A probe laser, in a configuration like it is shown in figure 2.10 (a), is utilized as a backlighter for capturing shadowgrams of the target at 200 ps after the pump-laser pulse. The dotted line shows the position of the initial front surface of the target. The shadow shows target expansion on the front and on the rear side of the target. The comparison between the initial front side and the edge of the shadow illustrates the binary type of information that a shadowgraphy diagnostic is able to provide. Although the edge of the shadow is clearly visible, it is not straight forward to deduce properties of the density distribution from it. The shadow is the result of light deflection by propagation through a three-dimensional refractive-index distribution. The edge of the shadow marks the transition between rays that are captured by the numerical aperture (NA) of the microscope and rays that are deflected to higher angles than the NA of the microscope. In summary, shadowgraphy is a diagnostic that is selective to the deflection angle of the probe rays. Because of it's simplicity, the technique is often used for optical probing of high-intensity laser-solid experiments in different geometries, e.g., see references [30, 83, 128, 111, 134, 139].

2.1.5.3. Interferometry

An optical technique that is closer related to the derivation of the target density is interferometry. Most often, Mach-Zehnder or Nomarski-type interferometers are used [99, 133, 95]. The technique allows to record the phase shift of a light wave that is probing undercritical target densities by evaluation of the amount of fringe shift in the captured interferogram. The basic principles of interferometry can be found in text books about optics, e.g. in Ref. [88]. Exemplary interferograms from Ref. [133] are presented in figure 2.7 (b). The relevance of the derived target-density information as a benchmark for numerical modeling is already discussed in the previous section.
The main steps and required assumptions to calculate density information from an interferogram are as follows. To derive the amplitude-damping and phase-shift information, the interferogam is transformed into Fourier space. One of the two sidebands is cropped and an inverse Fourier transform is applied to the sideband only. The polar representation of the resulting complex-valued image directly gives the phase-shift and amplitude-damping information. Note, due to cropping in Fourier-space the spatial resolution is lower than in the original interferogram and the square of the amplitude damping information contains the same information as a shadowgram. However, an important prerequisite for an evaluation of a phase-shift map is the straight line of propagation through the target. This excludes the interpretation of phase-shift data in the vicinity of the shadow edge, as this edge specifically marks a region of non-straight propagation through the plasma-density distribution. To transform the phase-shift map to a map of refractive indices or electron density, further assumptions about the geometry of the target are required. For high-intensity laser-solid interactions, most often the high-intensity pump laser defines an axis of radial symmetry. This is nicely illustrated by the channeling of the pump-laser pulse in the preplasma of the solid target in the lower image of figure 2.7 (b). Here, the horizontal line in the middle of the laser channel is the symmetry axis of the preplasma. By inverse Abel transformation, the electron-density distribution of the plasma is derived in cylinder coordinates. The cylinder axis is given by the symmetry axis. Details about the Abel transform and the derivation of the electron density are available in Appendix A. For the interferograms in figure 2.7 (b), the resulting electron-density distribution along the symmetry axis is displayed in figure 2.7 (a) as dotted lines.

2.1.5.4. Other methods

Other methods of optical probing are for example polarimetry for the detection of magnetic fields [100] and few-cycle optical probing to visualize very fast processes [184]. Both techniques are usually used to investigate interactions of high-intensity lasers with undercritical targets. Furthermore, several techniques about the aquisition of multiple pump-probe delays in a single shot are demonstrated, e.g., probing with a double pulse of different color [99] or chirping of broadband laser pulses [125, 87]. Both techniques rely on the spectral discrimination by gratings or spectral bandpass filters before detection to discriminate between different pump-probe delays. In addition, polarization can be used for separation as well [50].

2.1.6. The challenge of parasitic plasma self-emission

A well-known source of noise for optical probing of high-intensity laser-solid interactions is plasma self-emission. It is often visible in published optical-probing data and appears as region of saturated signal on the camera (see central white spots in the images of figure 2.7 (b)). It is unwanted, as it shields the region of the highest pump-laser intensity on the target, i.e., the center of the interaction. Plasma self-emission is a generalized name for radiation that originates from light scattering and a diversity of mechanism during the high-intensity laser-plasma interaction. Figure 2.11 (a) shows a sketch and summarizes target parameters that influence the mechanisms at play. In the following, several generation mechanisms of plasma self-emission are highlighted and exemplary measurements are presented.
For undercritical plasmas, the high-intensity laser can experience self-phase modulation [203], spectral broadening [196] and depletion [60, 113]. The spectral properties of the laser beam after interaction are exemplified by figure 2.11 (b) from Ref. [113]. Here, a high-intensity laser with a peak intensity

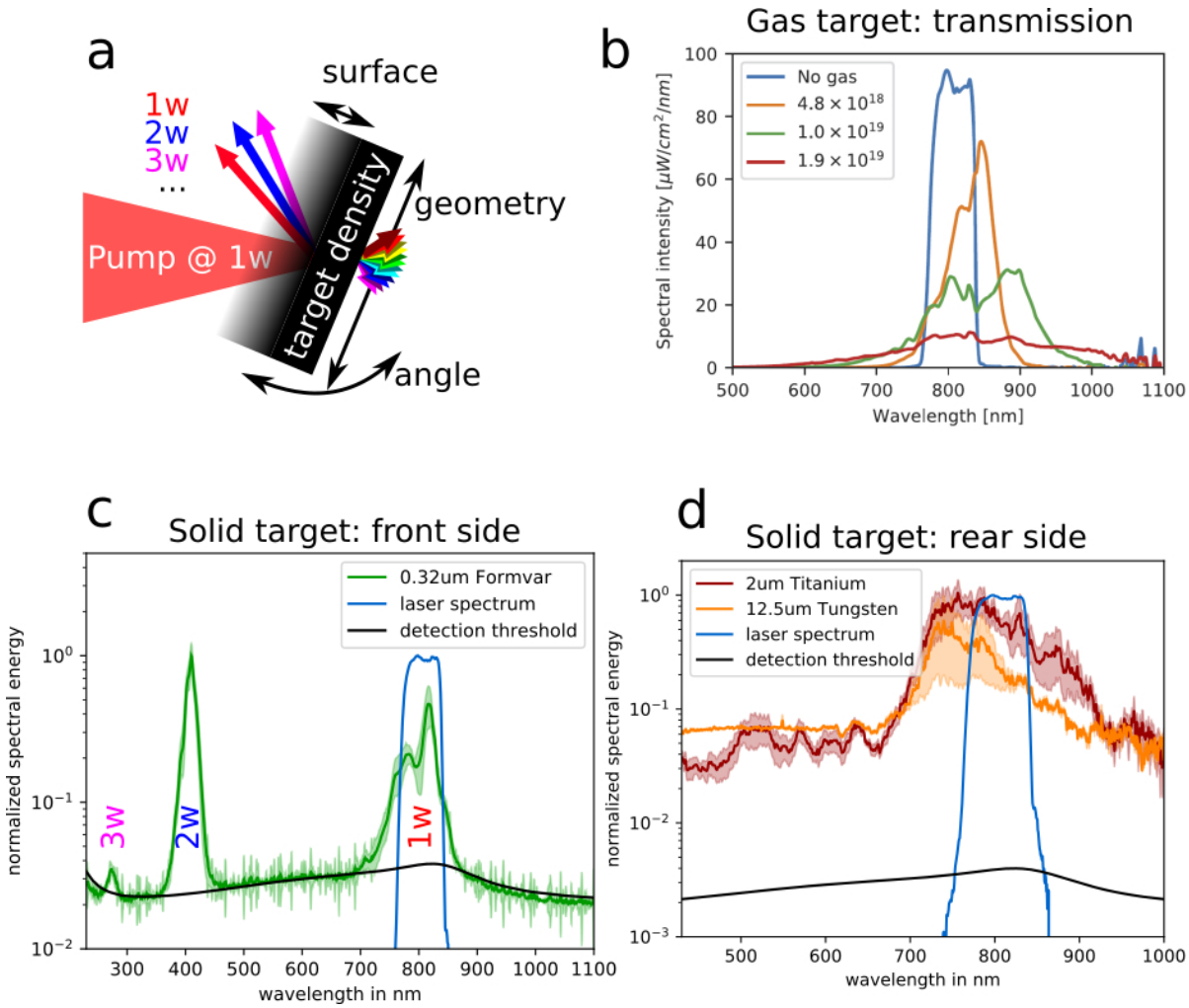

Figure 2.11.: Plasma self-emission: **(a)** General sketch of target properties that influence the occurrence and emission angle of self-emission. **(b)** Figure copied from [113]: High-intensity laser spectrum after propagation through a 500 µm-thick undercritical target with a varying peak density up to $\sim 1\,\% \, n_c$ ($I_\mathrm{L} \sim 3 \cdot 10^{19}\,\mathrm{W/cm^2}$). The initial laser spectrum is given in blue. **(c)** Second- and third-harmonic generation into specular direction from the front side of a 0.32 µm-thick Formvar-foil target ($I_\mathrm{L} \sim 5 \cdot 10^{21}\,\mathrm{W/cm^2}$). **(d)** Rear-side emission from a 2 µm-Titanium and a 12.5 µm-Tungsten-foil target ($I_\mathrm{L} \sim 5 \cdot 10^{20}\,\mathrm{W/cm^2}$). The solid lines in figures (c) and (d) show the mean over multiple shots and the shaded areas show the corresponding standard deviation of the mean. The approximate initial laser spectrum is given in blue and the detection threshold of the spectrometer setup is given in black.

of $\sim 3 \cdot 10^{19}\,\mathrm{W/cm^2}$ is propagating through a 500 µm-thick gas-jet target with peak densities up to $\sim 1\,\% \, n_c \approx 1.9 \cdot 10^{19}\,\mathrm{cm^{-3}}$. The initial laser spectrum (blue) is significantly broadened into the visible and into the near-infrared spectral region (see red spectrum). Viewing the spectra and their evolution with plasma density, an interpolation to further increased target density suggest a redistribution of the laser energy over a broad spectral range. This observation can also be transfered to high-intensity laser-solid interactions, given specific target parameters. For a significant amount of pre-expansion, e.g., with plasma-density scalelength of multiple tens up to hundreds of micrometers, or a peak density of the target in the nearcritical-density regime, the laser propagates in plasma with similar densities like in the presented measurements. Strong spectral shifts are thus expected in these cases.
The front side of solid-density targets can be used as an efficient source for attosecond pulses [204]. Their occurrence goes along with the generation of surface harmonics driven by high-intensity lasers [193]. The scalelength of the plasma density on the front surface and the laser intensity are defining parameters of the specific generation mechanisms of the harmonics (*relativistic oscillating mirror* or *coherent-wake emission*). In the optical spectral region, harmonic generation is usually present as the second- (2ω) and third-harmonic (3ω) of the pump-laser wavelength (1ω). Figure 2.11 (c) shows an exemplary spectrum of the specularly reflected light from a laser-solid interaction at $\sim 5 \cdot 10^{21}\,\mathrm{W/cm^2}$ peak intensity (DRACO-PW laser) and a 0.32 µm-thick Formvar-foil target at 45° angle of incidence. Spectral broadening of the fundamental beam together with the generation of a second- and third-harmonic beam are clearly visible. The fluctuating signal peaks near the detection threshold are caused by parasitic gamma rays that occasionally hit the semiconductor chip of the spectrometer. Note that the energy of the second harmonic signal is nearly equal to the residual energy of the fundamental beam. During equivalent laser-target interactions, usually the whole experimental chamber is dominated by blue light that is produced by second-harmonic generation.
The light emission from the rear side of solid-density targets depends on the material, thickness, peak density and spatial dimensions of the target. One source of light is given by optical transition radiation generated by laser-heated fast electrons that traverse the plasma-vacuum interface on the rear side of the target. Depending on the heating mechanism of the electrons, the emission occurs at the fundamental or the second hamonic of the laser beam [41]. Additionally, the laser-heated electrons cause return currents and produce a hot plasma that is radiating thermal emission. Both sources can be disentangled by time-resolved observations of the self-emission [178, 128]. For thin or strongly pre-expanded solid targets, the laser can leak through the target, e.g., by RIT, and is able to interfere with the transition radiation of electrons on the rear surface [207]. Figure 2.11 (d) shows spectra that are measured at the rears side of a 2 µm-thick Titanium and a 12.5 µm-thick Tungsten foil for a pump-laser peak intensity of $\sim 5 \cdot 10^{20}\,\mathrm{W/cm^2}$ (DRACO-150TW laser). The laser is incident at 45° to the target-normal direction and the observation angle is close to the laser-forward direction. In both cases, the measured signal shows spectral broadening of the initial laser spectrum and a significant amount of spectrally homogeneous emission is observed at wavelength lower than 650 nm. While there is shot-to-shot fluctuation of the homogeneous spectral emission for the thinner Titanium target, the homogeneous emission is highly stable for the thicker Tungsten target. In contrast to that, the spectral emission around the initial laser spectrum is fluctuating from shot to shot for both targets.
The different sources of optical emission from a high-intensity laser-solid interaction are challenging to disentangle, if the front and rear side of the target are not that well differentiable, e.g., for targets with small spatial scale and non-planar surfaces like rods, wires or spheres. Furthermore, the dominant generation mechanisms can change by changing the laser contrast, as this is known to change the target parameters significantly. Data of plasma self-emission from the cryogenic hydrogen-jet target is presented in section 2.3.4.

2.1.7. Off-harmonic optical probing

A shift the probe-laser wavelength away from the fundamental spectrum and the harmonics of the pump laser is a promising path to overcome parasitic plasma self-emission for optical-probing diagnostics of high-intensity laser-solid interactions. The method was first introduced as *frequency-shifted shearing interferometry* in Ref. [65]. For generality, in the following the technique is referred to as *off-harmonic optical probing*, as introduced in Ref. Bernert et al. [24].

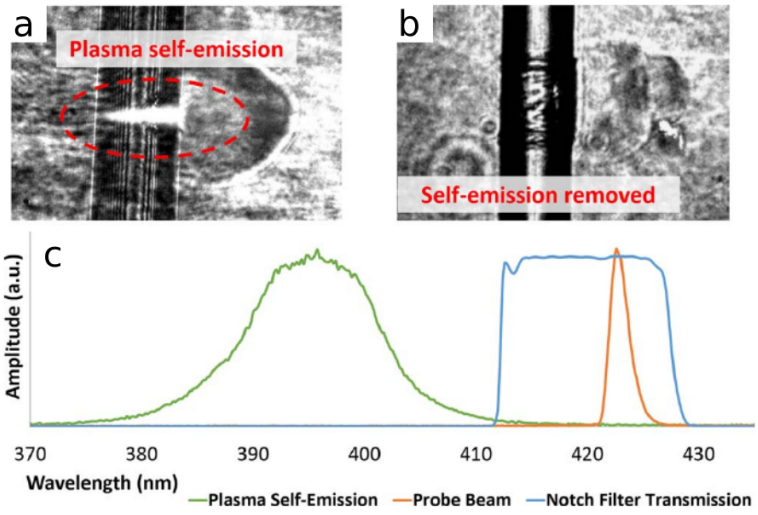

Figure 2.12.: Figure copied from [65]. Off-harmonic optical probing: **(a)** Shadowgram without spectral filtering. Parasitic plasma self-emission saturates the camera at the center of the laser-solid interaction. **(b)** Shadowgram with spectral filtering. The plasma self-emission is removed and plasma dynamics are visible. **(c)** Spectral distribution of the plasma self-emission (green), spectrum of the probe laser (orange) and spectral transmission function of the Notch filter utilized for spectral filtering (blue).

The principle of the technique is demonstrated in figure 2.12 from Ref. [65]. The corresponding experiments utilize a water-jet target and a 30 fs pump laser with a peak intensity of $5 \cdot 10^{18}\,\mathrm{W/cm^2}$. Figure 2.12 (a) shows a shadowgram in which the plasma self-emission saturates the camera in the center of the laser-solid interaction. In contrast, figure 2.12 (b) shows the shadowgram as derived by off-harmonic optical probing. The plasma self-emission is removed and modifications of the target are observed. The principle is demonstrated in figure 2.12 (c). As discussed previously, plasma self-emission can have a characteristic spectral distribution, like for example a strong second-harmonic emission of the fundamental pump-laser spectrum. In figure 2.12 (c), the spectrum of the second-harmonic is shown in green. If the backlighter spectrum (orange) is spectrally well separated from the plasma self-emission, spectral filtering can be used to differentiate between the parasitic signal and the probe signal. Here, spectral filtering is achieved by a Notch filter (blue).
Off-hamonic optical probing is demonstrated in several publications. For example in Ref. [20], the technique is utilzed at a pump-laser peak intensity of $4 \cdot 10^{19}\,\mathrm{W/cm^2}$. An ultra-short optical probe pulse with a broad spectral bandwidth [184] is used in combination with a narrow bandpass filter between microscope objective and camera. The bandpass filter transmits light in a narrow spectral band inbetween the fundamental and the second-harmonic spectrum of the high-intensity pump laser only. Note that the temporal resolution of a backlighter pulse at the position of the target is transported up to the camera, even if the bandwidth is clipped in the microscopy beamline [184]. In Ref. [213], off-harmonic optical probing is demonstrated at a pump-laser peak intensity of $5 \cdot 10^{20}\,\mathrm{W/cm^2}$. Different techniques of spectral filtering are tested to suppress the plasma self-emission on the camera, i.e., stacking of narrow-band dielectric interference filters, narrow-band high-reflection mirrors in transmission geometry and a reflective grating in the microscopy beamline. The attempts show success for a high temporal contrast of the pump laser. The authors conclude that the residual plasma self-emission is within the spectral band of the optical backlighter. A related experiment with detailed spectral analysis of the plasma self-emission and spectral-filter functions is performed at a pump-laser peak intensity of $5 \cdot 10^{21}\,\mathrm{W/cm^2}$ in Ref. Bernert et al. [24]. The reference is one pillar of this thesis and the content of Ref. [24] is presented in more detail in the following chapters.
In contrast to conventional probing techniques that rely on the fundamental or the second harmonic of the pump laser, the probe beam in the case of off-harmonic optical probing is usually not picked from the high-intensity pump beam after compression. Although a non-linear frequency conversion should, in principle, yield a variety of wavelength between the harmonics and the fundamental spectrum of the

pump laser, the usual fluctuation in spectral amplitude and phase at the spatial rim of a collimated high-intensity laser beam together with the non-Gaussian spatial beam profile that is generated by a pick-off mirror are disadvantageous as a seed for stable frequency conversion. Furthermore, changes in the settings of the pump beam would unavoidably induce changes in the probe-beam parameters and require readjustment or changes of the probing setup. Instead, a long-term implementation of an easily available, highly stable and comparably small laser system can be beneficial for a high-intensity laser-plasma laboratory. Such an implementation enables independent target alignment, synchronized probing of laser-plasma experiments and independent small-scale experiments, e.g., about targetry. Thus, it stimulates parallelized work in different target areas and enables time-consuming, detailed investigations.
Generally, two approaches for the generation of an off-harmonic optical probe beam are available. Either the seed of the probe beam is picked from the same oscillator like the pump beam and the seed is subsequently amplified to the desired power level [65], or the probe beam is generated by a secondary stand-alone laser system with an oscillator that is electronically synchronized to the oscillator of the pump laser [213] and Bernert et al. [24]. The first approach yields a minimum of temporal delay jitter between pump and probe in the experiment. However, under negligence of non-linear frequency shifts, the seed wavelength of the probe needs to be contained in the spectrum of the pump-laser oscillator. In contrast, wavelengths far away from each of the harmonics and the fundamental spectrum of the pump laser are easily reached by a laser system that is based on a completely different laser material. For this solution, a consideration of the temporal synchronization between the two laser oscillators is of major importance. In this thesis, the second option is chosen and details about the probe-laser system and the temporal synchronization are given in sections 2.3.1 and 2.3.2.

2.2. Laser-driven proton acceleration from cryogenic hydrogen jets

This section provides an overview about the research project of *laser-driven proton acceleration from cryogenic hydrogen jets* in which this thesis is embedded and highlights the contributions of the thesis to recent achievements of the project.

2.2.1. Introduction to the project

The mission of the research group on laser-ion acceleration at *Helmholtz-Zenter Dresden – Rossendorf* (HZDR) [8] in Dresden, Germany, is the development and optimization of a translational research-platform for radiation-oncology with laser-accelerated protons. This requires multi-disciplinary efforts in fundamental research, life science and engineering. The three main pillars are summarized in figure 2.13 (a), (b) and (c). Figure 2.13 (a) shows aspects of the optimization of the laser-target interaction to achieve highest spectral particle yield at maximized proton energy. This includes the development and implementation of laser metrology, concepts of renewable target production together with the development and application of plasma diagnostics. The combination of experimental diagnostics and advanced numerical modeling enables insights to the acceleration process and fosters reliability and control of the particle source. Figure 2.13 (b) displays aspects of the transport beamline of laser-accelerated protons. The required developments include particle-beamline concepts [131], individual beamline components [31] and dosimetry [169], all adapted to the characteristic properties of laser-accelerated proton beams. Figure 2.13 (c) illustrates the required developments of radio-biological models, treatment concepts and the conduction of comparative studies with existing technologies in radiation-oncology [101, 25, 108]. An overview of the international state-of-the-art of radiobiological experiments with laser-accelerated protons can be found in Ref. [37].
This thesis is placed in part (a) of the research platform of figure 2.13 and provides insight to the high-intensity laser-solid interaction from experimental plasma diagnostics, specifically, data that is retrieved by optical probing. The experiments are part of a collaborative project on laser-proton acceleration from cryogenic hydrogen-jet targets. For the development of the target and it's utilization in experiments on laser-proton acceleration, the HZDR group regularly joins collaborative experiments with the research group on *High Energy Density Science* (HEDS) from the *SLAC National Accelerator*

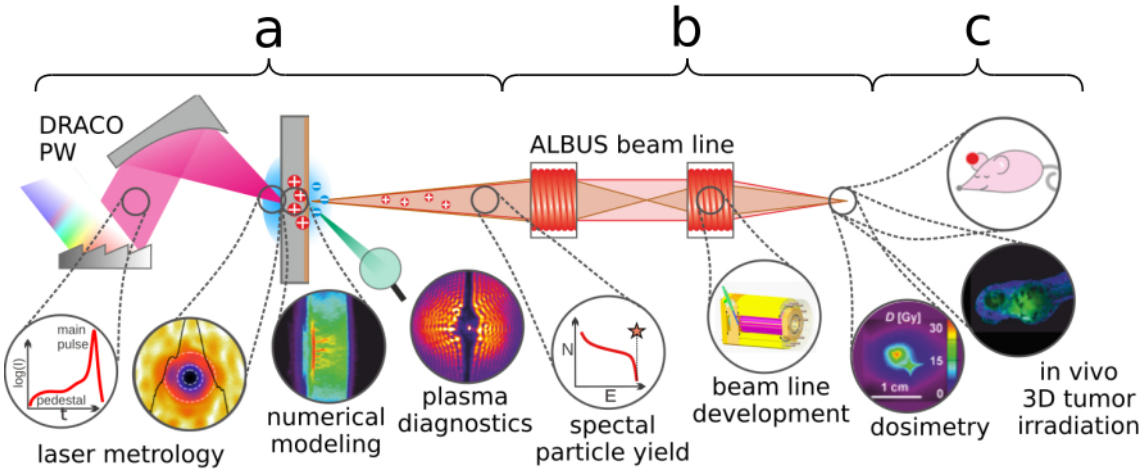

Figure 2.13.: Mission of the research group on laser-ion acceleration at Helmholtz-Zentrum Dresden – Rossendorf: development and optimization of a platform delivering laser-accelerated protons for translational research in radiation-oncology. This comprises: **(a)** Optimization of the laser-target interaction towards high spectral particle yield with maximum-achievable proton energies via the development and implementation of laser metrology, plasma diagnostics, renewable target production and numerical modeling. **(b)** Particle transport requires the development of specialized particle-beamline concepts and components together with dosimetry methods that are adapted to the characteristics of the laser-driven particle source. **(c)** The utilization of laser-accelerated particles in radiobiological studies requires the development of biological models, treatment concepts and the conduction of comparative studies with existing technologies in radiation-oncology.

Laboratory [5] and Sebastian Göde, scientist at the high-energy-density instrument at *European XFEL* [4].
Several collaborative achievements are published, see references [75, 74, 78, 144, 146, 213], Bernert et al. [24], Rehwald et al [168] and Bernert et al. [23]. To provide the specific background of this thesis, the most prominent and recent results that are achieved in an experiment at the DRACO-PW laser in 2019 are presented in the following section 2.2.5. Before that, the general properties of the cryogenic hydrogen-jet target (section 2.2.2), the DRACO-laser infrastructure (section 2.2.3) and the experimental setup (section 2.2.4) are summarized.

2.2.2. The cryogenic hydrogen-jet target

Cryogenic hydrogen jets are a common target in laser-driven proton acceleration, see references [127, 159] and Rehwald et al. [168]. Because of the self-replenishing and continuous target delivery that, in principle, allows for high-repetition-rate experiments [104] and laser-driven proton beams at 1 Hz [75], it is a highly attractive target. The target is constituted by protons and electrons only. It overcomes the pollution of optics in the target chamber by target debris and the beam of accelerated particles contains only a single ion species. For target production, the hydrogen is cooled down to liquid temperatures by a cryostat. After liquefaction, the hydrogen is pressed through a micrometer-sized aperture into the vacuum [104]. The aperture shape defines the spatial shapes of the jet, e.g., cylindrical or sheet-like. The technical aspects of target production are sumarized in Ref. [47]. The continuous liquid jet propagates with a speed of about 100 m/s into the vaccum of the experimental chamber, solidifies after about one millimeter of propagation by evaporative cooling and forms a hydrogen ice with a random mixture of face-center-cubic (fcc) and hexagonal-close-packed (hcp) crystal domains [110]. Figure 2.14 (b) from Ref. [110] gives an overview of the propagation of the jet into the vacuum. The solidification process stops the hydrodynamic motion of the liquid and enables a target delivery at tens of millimeters below the nozzle with a spatial jitter on the micrometer scale [144], i.e., a spatial dimension comparable with the focal-spot size of the high-intensity laser. A measurement of the

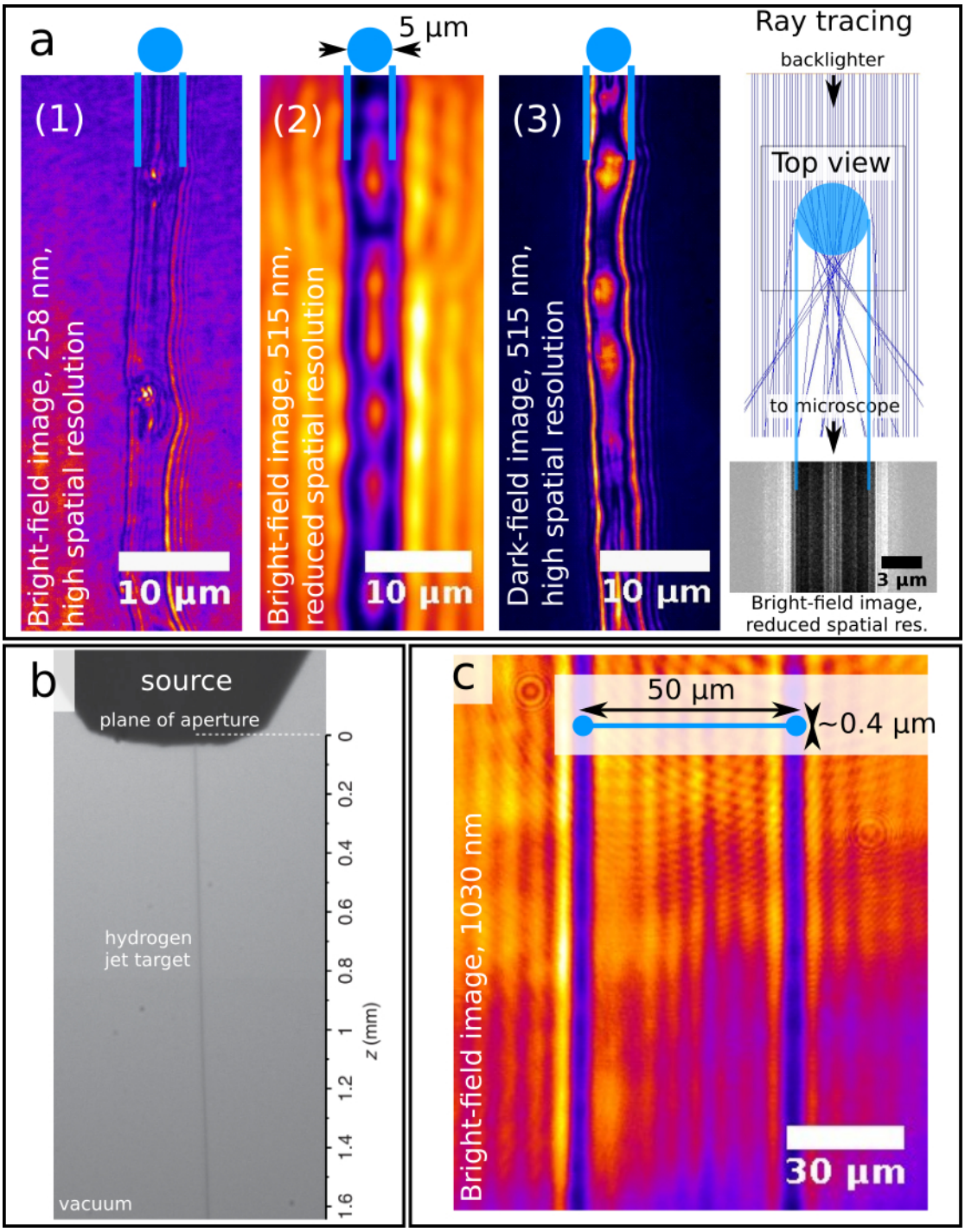

Figure 2.14.: **(a)** Bright-field images (1, 2) and dark-field image (3) of the cylindrical hydrogen-jet target of 5 µm diameter at backlighter wavelength of 258 nm and 515 nm. All images show a different position of the jet target. High and reduced spatial resolution corresponds to a measured spatial resolution limit of ~ 0.3 µm and 1.5 µm, respectively. Right-hand side: A ray-tracing simulation with an idealized hydrogen rod and a virtual microscopy setup similar to the microscope that is utilized for image (2). The top view shows the refraction of the dark-blue rays by the hydrogen rod (light-blue circle). The synthetic bright-field image on the bottom shows a darkening of the jet rims and light transmission in the center part. **(b)** Figure copied from [110]: Overview image with the bottom part of the source of the target on the top and the hydrogen jet propagating into the vacuum below. **(c)** Bright-field image of the hydrogen sheet-jet target with a backlighter wavelength of 1030 nm and a measured spatial resolution limit of 4 µm. The sheet-jet target features a thin planar area between two cylindrically shaped rims.

hydrogen flow and the size of the aperture allows to calculate the average density of electrons in the target bulk to $5.2 \cdot 10^{22}\,\mathrm{cm}^{-3}$ [167]. This corresponds to 30 times the critical density of 800 nm light ($30\,n_c[800\,\mathrm{nm}]$), i.e., a moderate solid density that is convenient for the modeling via PIC simulations even in three-dimensions.
The ranking of the target density on the density axis of figure 2.2 (c) on page 5 directly suggests TNSA as a dominant acceleration mechanism of protons from experiments of high-intensity lasers with the target. This is verified by PIC simulations together with the role of target shape, i.e., cylindrical or sheet-like, for the proton emission characteristic in Ref. [144]. Compared to other solid-density targets like metal foils, the initial density of cryogenic hydrogen is already close to the nearcritical density regime. This regime of advanced particle-acceleration mechanisms beyond TNSA is reachable directly by RIT with ultra-intense lasers or by plasma pre-expansion, either artificially via controlled prepulses or by target pre-expansion via the intrinsically present leading edge of a high-power laser. More details are discussed in the following section 2.2.5.
The isolated positioning in the experimental chamber, the reduced dimensions, the self-replenishing delivery and a low spatial jitter make the target a particularly well-suited platform to study high-intensity laser-solid interactions, e.g., via optical probing diagnostics [213], Bernert et al. [24], Yang et al. [208] and Bernert et al. [23]. Exemplary microscopy images with backlighters of 258 nm, 515 nm and 1030 nm wavelength are given in figure 2.14 (a) and (c). Here, *bright-field image* is just a different name for *shadowgram* that is more commonly used in conventional microscopy. Figure 2.14 (a) shows images of the cylindrical hydrogen jet with 5 µm diameter. The two highly magnified bright-field images (1) and (2) demonstrate that the center part of the jet is transparent to 515 nm and 258 nm light. A comparison of (1) and (2) shows that the size of the dark rim on both sides of the jet depends on the NA of the microscope. While the measured spatial resolution is $\sim 0.3\,\mu\mathrm{m}$ for (1), it is only 1.5 µm for (2). The dark rims of the jet target is caused by refraction of rays to angles outside the NA of the microscope. The effect is illustrated by a ray-tracing simulation on the right-hand side of figure 2.14 (a). The hydrogen jet is idealized by a cylindrical rod with a refractive index of 1.14. The top view shows that the rod acts like a cylinder lens and focuses the incident rays (dark-blue lines) behind the rod. Rays that propagate close to the rim get refracted to higher angles than rays that enter the rod close to the central axis. By ray tracing through a microscope with an equivalent NA like in case (2), the synthetically generated shadowgram shows the same signature of transmitted light in the center of the jet and darkened rims like in the measured bright field image (2). Additionally, the effect is experimentally visualized by backlighting the hydrogen jet from an angle that is not covered by the NA of the microscope in figure 2.14 (a) (3). Consequently, the microscopy image shows the refracted rays only. The strong refraction on the rims produces a bright signal along both sides of the jet target.
All three images in 2.14 (a) show that the micro-structure of the hydrogen jet can be inhomogeneous. Especially the images (1) and (3) at highest resolution evidence that the jet has a slightly varying diameter and, connected to that, slight changes of the target normal direction. Furthermore, there are regions where the material has a high optical quality (no disturbance of transmission, no scattered light from the target bulk) in contrast to regions with grains that strongly scatter or refract the light from a straight line of propagation.
The observation of light transmission at 258 nm wavelength demonstrates that the cryogenic hydrogen-jet target is a dielectric material with a bandgap of at least 4.8 eV (photon energy of 258 nm light). Although the measured bandgap of single crystalline solid hydrogen is 10.9 eV [94], the observation of scattering grains in the bright- and dark-field images together with the measured random mixture of fcc and hcp crystal structure by Ref. [110] suggests the occurrence of intraband energy levels due to grain boundaries. Up to now, a more precise description of the band structure of the cryogenic hydrogen jet is missing and we assume a bandgap of 10.9 eV in the following.
Changing the aperture of the source from cylindrical to a slit profile enables the production of different sheet-jet targets [144, 47]. Especially tapered slit nozzles enable the production of wide and thin sheet jets with a dumbbell-like cross section. The actual process of the generation and freezing of the jets is still under investigation [167]. A sketch of the cross section and an exemplary bright-field image is shown in figure 2.14 (c). The bright-field image shows the two prominent cylindrical rims of the sheet.

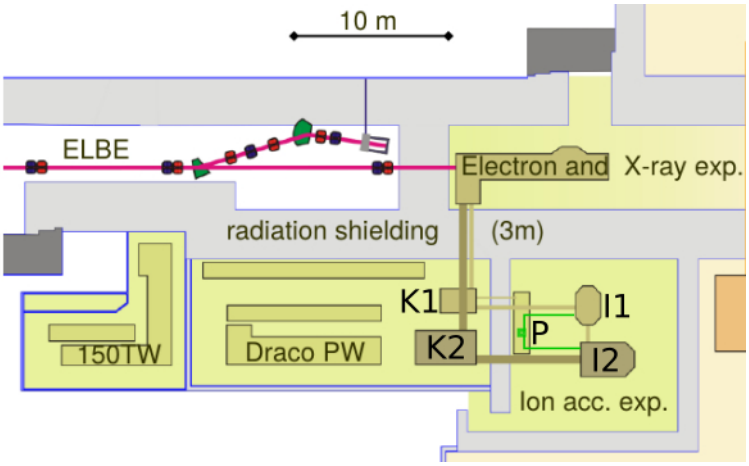

Figure 2.15.: Figure copied from [181]: High-intensity laser DRACO and experimental laser-plasma laboratories at HZDR. "K1" and "K2" are the DRACO 150TW and DRACO PW compressor chambers. Laser beams can be delivered to two experimental areas: "Electron and X-ray experiments" and "Ion acceleration experiments". Two experimental chambers are available for laser-ion acceleration: "I1" with DRACO 150TW only and "I2" with DRACO 150TW and DRACO PW. The position of the probe-laser system is labeled by "P". The probe beam is available in I1 and I2.

The flat central part shows no evidence of irregularities like grains or other structures. Measurements in Ref. [167] show that the flat part of the sheet jet has a thickness of about 400 nm.

2.2.3. The DRACO laser system

2.2.3.1. Infrastructure and provided laser beams

The high-intensity laser utilized in this thesis is the *Dresden laser acceleration source* (DRACO) at HZDR. DRACO is a Ti:Sapphire-based laser system and details can be found in Ref. [181]. It provides two high-power beams: the DRACO 150 Terawatt (150TW) and the DRACO Petawatt (PW). Both beams have a nominal final pulse duration of 30 fs and a central wavelength of 800 nm. The systems are designed to deliver 4.5 J and 30 J energy after compression with a repetition rate of up to 10 Hz and 1 Hz, respectively. The experiments of this thesis mostly used the DRACO PW laser with up to 23 J on target (32 J before compression).
Both DRACO beams are frequently used for laser-electron and laser-ion acceleration. A layout of the experimental infrastructure is shown in figure 2.15. From the compressor chambers "K1" (DRACO 150TW) and "K2" (DRACO PW) the laser beam is distributed to the experimental areas. Two experimental chambers "I1" and "I2" are available for laser-ion acceleration. I2 offers the possibility of combined experiments with DRACO 150TW and DRACO PW. In I1, the DRACO 150TW beam is available only. The location of the stand-alone probe-laser system is labeled by "P". The probe beam is available in I1 and I2.

2.2.3.2. Temporal laser contrast

As introduced in section 2.1.1, the temporal contrast of a high-power laser is a unique characteristic of each specific laser system and it is commonly measured via third-order autocorrelation (TOAC). The temporal contrast depends on many system-specific parameters and the overall laser design. A variation of beam alignment, setup changes or exchange of optical components can lead to subtle changes of the laser contrast. For experiments of laser-ion acceleration, the laser contrast is an important and regularly measured quantity to estimate the amount of target pre-expansion (refer section 2.1.3).
In this work, we utilize the *Sequoia HD* device by *Amplitude* for TOAC measurements. A measurement of the device features a dynamic range $> 10^{13}$, a temporal-scan resolution < 16 fs and an optical

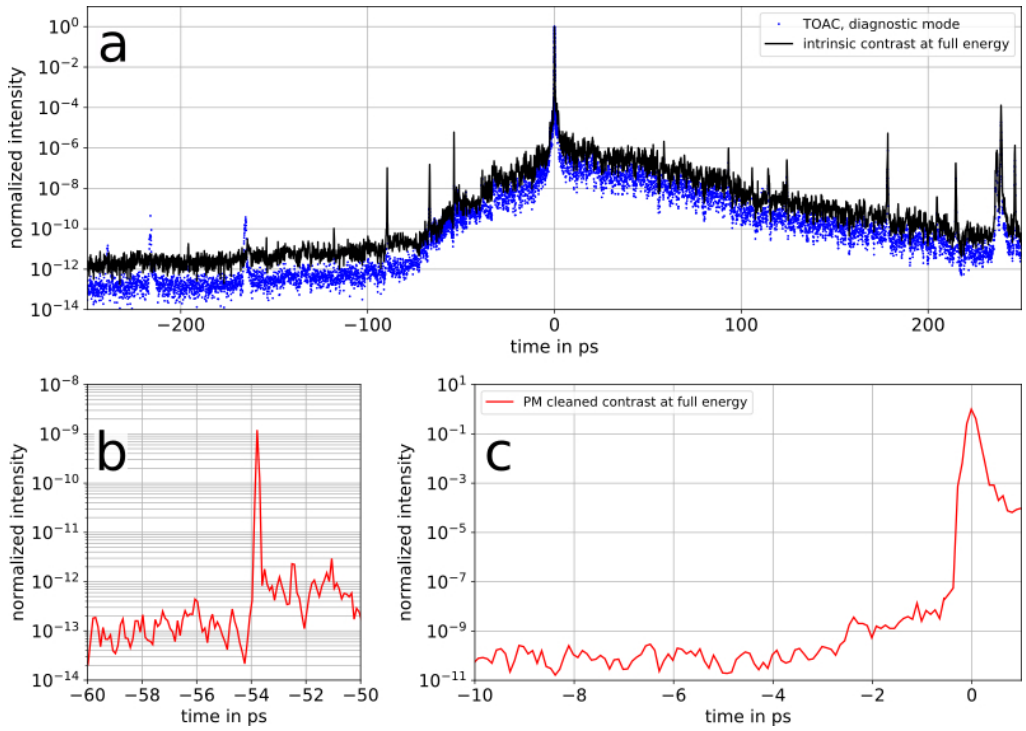

Figure 2.16.: **(a)** Intrinsic temporal contrast of DRACO PW: The black line shows the laser contrast at full laser energy (32 J before compression), calculated from a measurement in diagnostic mode (blue dots, 0.27 J before compression). Details of the calculation can be found in Appendix B. **(b,c)** Plasma mirror (PM) -cleaned laser contrast of DRACO PW at full energy (32 J before compression): Fig. (b) shows a pre-pulse at −54 ps and fig. (c) shows the single-picosecond pedestal.

temporal resolution < 100 fs. A TOAC-measurement trace usually features hundreds to thousands of laser shots. Therefore, the laser contrast is commonly measured in a "diagnostic mode", i.e., at reduced laser energy, to avoid degradation of the compressor gratings. The diagnostic-mode measurement (0.27 J before compression) of the DRACO-PW laser contrast from the experimental champaign in 2019 is displayed in figure 2.16 (a) by blue markers. The final amplification stage of the laser amplifiers is known to induce time-delay-dependent changes of the leading edge and to manipulate the height of individual short prepulses [105]. TOAC measurements from 2021 at different laser-amplification levels (part of a different doctoral project, Ref. [212]) allow to calculate a laser-systems-specific conversion function and to transform the diagnostic-mode measurement to the laser contrast at full energy (32 J before compression). Details are presented in Appendix B. The calculated *intrinsic laser contrast* of the DRACO-PW laser at full energy is displayed as black line in figure 2.16 (a).
For both DRACO-laser beams, a recollimating single-plasma-mirror (PM) setup is available [145, 211]. The improvement factor of the laser contrast is $2 \cdot 10^{-4}$ and the switching point is located between -0.3 ps and -0.2 ps before the high-intensity peak. Details are presented in Appendix B. The relevant timescales of the *PM-cleaned laser contrast* of DRACO PW at full energy are given in figures 2.16 (b) and (c). Note that the optical temporal resolution of the TOAC device is not sufficient to resolve the pulse duration of the DRACO-laser peak or the pulse duration of the prepulse at -54 ps.
The laser-contrast curves in figure 2.16 represent the status during the high-intensity experiments with the cryogenic hydrogen-jet target in 2019. It is not the current status of the contrast of the DRACO-PW laser. The chronological development and improvement of the laser contrast is continuing and more recent data is given in another doctoral project, see Ref. [212].

2.2.4. Experimental set-up

The interactions of the DRACO-PW laser and the cryogenic hydrogen-jet target are generated in experimental chamber I2. The relevant setup and diagnostics of this thesis are shown in figure 2.17.

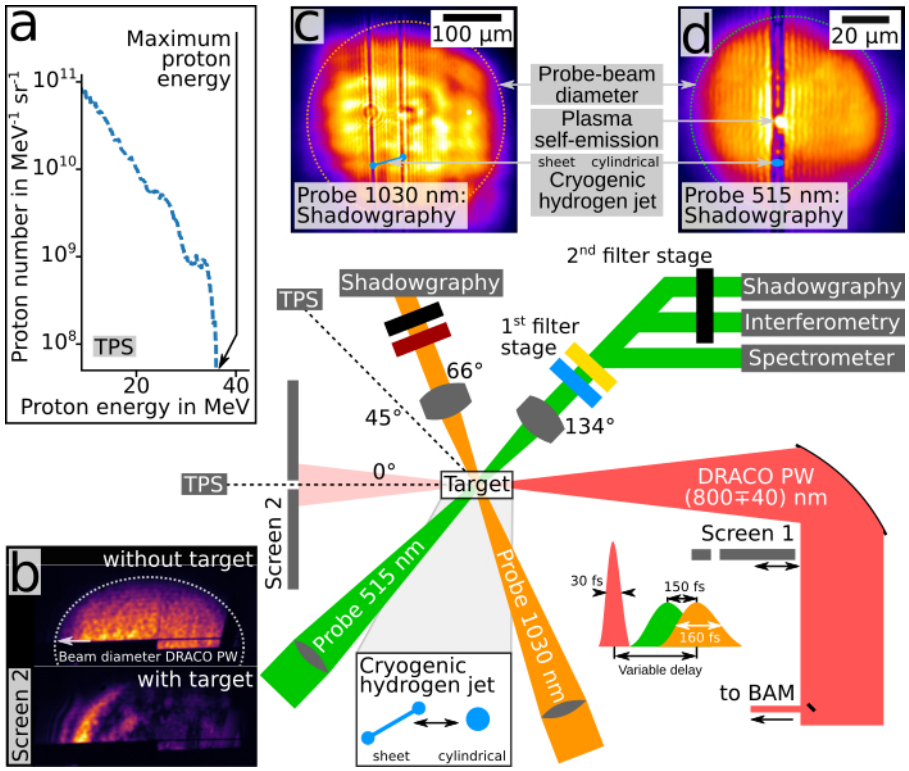

Figure 2.17.: Experimental setup: The DRACO-PW laser is focused via an f/2.3 off-axis parabolic mirror onto the cryogenic hydrogen-jet target (cylindrical or sheet-jet) with intensities of up to $6 \cdot 10^{21}\,\mathrm{W/cm^2}$. Residual laser light behind the target is captured by "Screen 2" (exemplary data in figure (b)) and accelerated protons are measured by Thomson parabola spectrometers ("TPS") in 0° and in 45° direction (exemplary proton spectrum in fig. (a)). Two backlighter pulses (central wavelength of 515 nm and 1030 nm) are focused close to the target and allow for off-harmonic optical probing at 66° and 134° with two long-working-distance objectives for imaging. Both backlighters have a pulse duration of 160 fs, a fixed time delay of 150 fs to each other and a variable delay to the DRACO-PW laser. A two-staged approach of spectral filtering (1^{th} and 2^{nd} filter stage) allows to record shadowgraphy and interferometry data with a low level of plasma self-emission (exemplary shadowgrams of the sheet-jet and the cylindrical hydrogen-jet target in figures (c) and (d)). An optical spectrometer measures the plasma self-emission behind the first filter stage. Screen 1 enables to block the entire DRACO-PW laser or to transmit only a fraction of the beam through a hole in the screen. A half-inch mirror is used to pick a signal from the collimated DRACO-PW laser and to send in to the *beam arrival monitor* (BAM).

The central part of the setup is placed in vacuum of at least $1 \cdot 10^{-4}$ mbar. The DRACO-PW laser (800 nm central wavelength, $\sim$ 50 nm spectral full width at half maximum (FWHM), 30 fs pulse duration, in the following refered to as *pump laser*) enters the experimental chamber with a maximum energy of 23 J (19 J) after compression without (with) temporal contrast cleaning by a recollimating PM setup. A half-inch pick-off mirror is placed in the collimated beam to pick a signal for the *beam arrival monitor* (BAM) (details in section 2.3.2.2) and an optional ceramic screen "screen 1" can be used to block the entire beam or to transmit just a fraction onto the target. The DRACO-PW laser is focused via an f/2.3 off-axis parabola (OAP) to a spot size of 2.6 µm FWHM. This results in a peak intensity of $6.5 \cdot 10^{21}$ W/cm^2 for the intrinsic and $5.4 \cdot 10^{21}$ W/cm^2 for the PM-cleaned laser contrast. A measurement of the pump-laser spectrum and the focal spot is given in figures 2.18 (c) and (d). Artificial short prepulses with $\sim 10^{-4}$ times lower peak intensity than the fully pumped laser beam can be introduced by a half-inch pick-off-mirror (POM) in front of the last folding mirror before the OAP, see figure 2.18 (e). The prepulse delay is tunable between $\sim$ 5 ps and $\sim$ 200 ps before the pump-laser peak and because of spectral-phase accumulation in the POM substrate, the pulse duration of the artificial prepulse is about 55 fs.
The target is either the cylindrical hydrogen-jet target with 5 µm diameter or the hydrogen sheet-jet target (for details see section 2.2.2). Residual light behind the laser-target interaction is captured by the ceramic screen "screen 2" in laser forward direction (0° in figure 2.17). Exemplary data is shown in figure 2.17 (b). The upper image shows the laser beam on the screen without a target in the laser focus. Only part of the laser beam is visible, as other devices block the line of sight to the screen. The dotted line indicates the full beam diameter. The lower image shows an example in which the cylindrical hydrogen jet is placed centrally in the focal spot of the laser. The overall signal level is much lower and, because of the comparable size of focal spot and target diameter, Fresnel-diffraction rings are partially visible. The inherently present spatial-positioning jitter of the target and the laser focus cause a non-constant laser-target overlap from shot to shot, see Ref. [144]. The fraction of the integrated transmitted light on screen 1 is used to sort out shots with low laser-target overlap.
The spectra of accelerated protons are measured by two Thomson parabola spectrometers (TPS) in 0° and 45° direction. An exemplary spectrum of the TPS 0° as measured from the cylindrical hydrogen-jet target interacting with the fully amplified and PM-cleaned DRACO-PW laser is shown in figure 2.17 (a). The significant drop of particle number at around 38 MeV is referred to as *maximum proton energy*. In this thesis, the maximum proton energy is used as a secondary sorting criterion for high spatial laser-target overlap.
Although more diagnostics for particle detection were present during the experiment, they are not required for this thesis and not shown in figure 2.17. Another doctoral project adresses the proton-acceleration performance and mechanisms of the very same experimental campaign, see Ref. [167]. As the experimental data evaluated and interpreted in this thesis is mostly derived by optical probing, the general parameters of the corresponding optical diagnostics are presented in the following subsection and more specific properties are issued in section 2.3.

2.2.4.1. Optical-probing diagnostics

Two backlighter pulses with a central wavelength of 515 nm and 1030 nm and a pulse duration of 160 fs are focused close to the target and allow for off-harmonic optical probing at two different angles. The generation of the probe pulses is presented in section 2.3.1. Both probe pulses have a fixed time delay of 150 fs to each other and a variable *pump-probe delay* to the DRACO-PW laser (details on the temporal synchronization in section 2.3.2). The pulse energy of the 515 nm probe is 100 μJ and it is focused to a field of view (FOV) of 60 µm FWHM. This yields a fluence of about 4 J/cm^2 and an intensity of about $2 \cdot 10^{13}$ W/cm^2 in the target plane. The pulse energy of the 1030 nm probe is 200 μJ and it is focused to a FOV of about 280 µm FWHM. This yields a fluence of about 0.3 J/cm^2 and an intensity of about $2 \cdot 10^{12}$ W/cm^2 in the target plane.
The evolution of the target is imaged by two microscopy objectives, one for each backlighter (custom-made, finite conjugate, apochromatic, working distance of 80 mm, numerical aperture NA = 0.28, magnification of 30.5). The 1030 nm probe allows for target inspection under 66°. The created image is recorded by a CCD camera (*pco.pixelfly usb*, 6.45 µm pixel size, 1392 × 1040 pixels) outside the

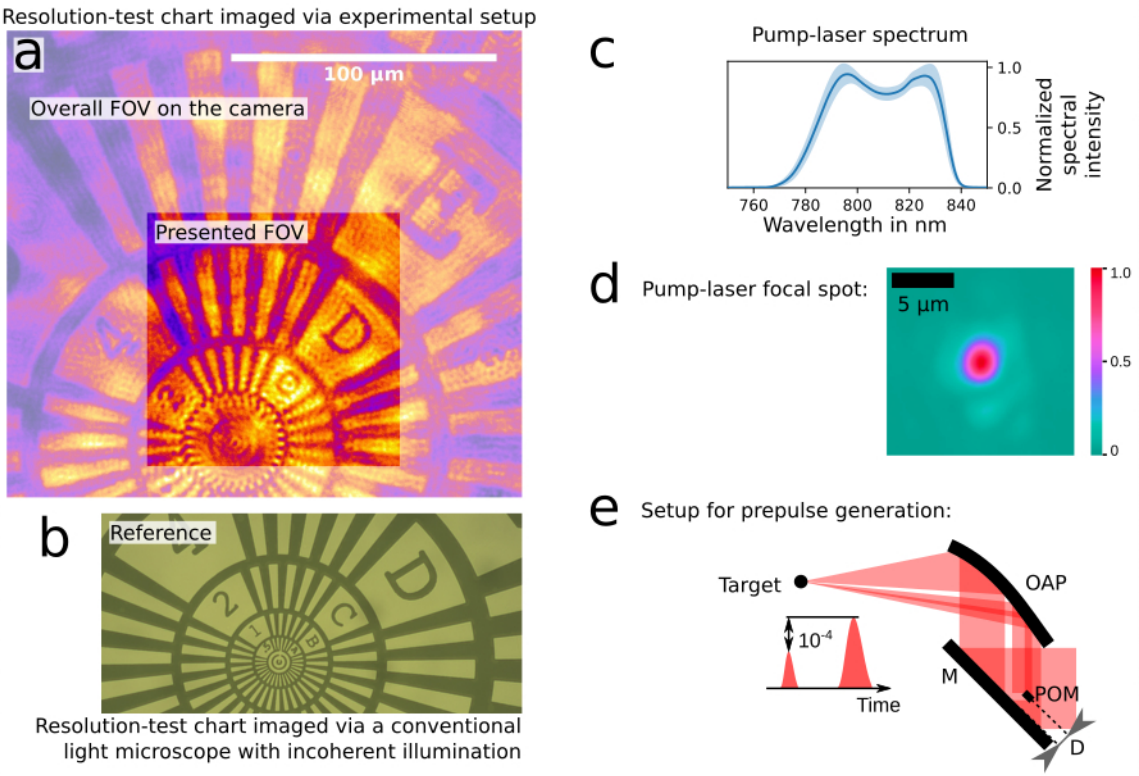

Figure 2.18.: Figure copied from the supplementary information of Ref. Bernert et al. [24]. **(a)** Resolution test chart illuminated by the probe 515 nm and captured by the shadowgraphy camera (refer figure 2.17). The overall field of view (FOV) on the camera and the presented FOV are shown. A structure size as small as 1.5 µm is resolved into all directions and no image distortion is visible within the overall FOV. **(b)** The same resolution test chart imaged by a conventional light microscope in bright-field operation and with incoherent illumination. The spatial scale is equivalent to figure (a). **(c)** Spectrum of the fully amplified DRACO-PW laser before compression. The spectrum shows the mean and standard deviation over 37 days of laser operation. **(d)** Pump-laser focal spot measured with the attenuated pump-laser beam. Instead of the anti-reflection coating of the PM substrate, a reflective part of the same substrate is used to emulate the reflective PM surface during a high-power laser shot. **(e)** Setup for artificial prepulse generation. The pump-laser beam with 18 cm beam diameter is reflected by the last folding mirror (M) to the off-axis parabola (OAP) and focused onto the target. A pick-off mirror (POM) with half-inch diameter is inserted before the last folding mirror and generates a prepulse with defined delay (D).

vacuum chamber. An exemplary shadowgram of the hydrogen sheet-jet target is shown in figure 2.17 (c). The 515 nm probe allows for target inspection under 134° and the created image is split outside the vacuum chamber by two non-polarizing cube beam splitters. One image is recorded directly by a CCD camera (*Allied Vision Prosilica GT1600*, 4.4 µm pixel size, 1600 × 1200 pixels). An exemplary shadowgram is shown in figure 2.17 (d). The image shows residual plasma self-emission (central white spot), because the image is captured during a high-power laser shot on target. Another image is send into a Nomarski-type interferometer [22] and the resulting interferogram is recorded by a CMOS camera (*pco.edge 4.2*, 6.5 µm pixel size, 2048 × 2048 pixels). The third image is projected onto a thin ceramic plate (cosine corrector, *CCSA1* by *Thorlabs Inc.*) in front of a calibrated spectrometer (*Avantes AvaSpec-ULS2048CL-EVO*) with a sensitive range between 200 nm an 1100 nm. It allows to measure spectra of the plasma self-emission. To reduce the parasitic plasma self-emission to a minimum on all three cameras, a two-staged approach of spectral filtering is used and presented in detail in section 2.3.3. All mirrors in the microscopy beamline are enhanced-aluminum mirrors with sufficient diameter to avoid clipping in the microscope and the vacuum windows are coated by an anti-reflection coating for both probing wavelength.
The spatial resolution of both microscopes is measured by a resolution test chart with structure sizes down to 0.5 µm. A reference image is given in figure 2.18 (b). For the microscope of the 515 nm and the 1030 nm probe, the smallest resolvable spacing is 1.5 µm and 4 µm, see exemplary shadowgram of the test chart in figure 2.18 (a). The overall field of view (FOV) of the probe-515 nm shadowgraphy camera is 200 µm × 180 µm and only 100 µm × 100 µm FOV is presented in this thesis. For the probe-1030 nm shadowgraphy camera, the maximum FOV is 390 µm × 390 µm. Comparing shadowgrams of the resolution test chart from both microscopes to the reference image in figure 2.18 (b), no image distortions are found within the overall FOV. No change in imaging quality is observed, if the test chart is moved by 10 µm along the optical axis of each microscope. The temporal resolution of a time-delay scan is 175 fs and observations are blurred by the probe-laser pulse duration (details in section 2.3.2.4).

In conclusion, the temporal and spatial resolution of both microscopes is sufficiently precise to scan the high-intensity laser-solid interaction within hundreds of fs around the pump-laser peak and to observe target modifications on the micrometer scale.

2.2.5. Recent results of the project

2.2.5.1. Ultra-short-pulse laser acceleration of protons to 80 MeV from cryogenic hydrogen jets tailored to nearcritical density

The main achievement of the collaborative experiment on laser-proton acceleration from cryogenic hydrogen-jet targets at the DRACO-PW laser in 2019 is the acceleration of 80 MeV protons by artificially tailoring the target density into the nearcritical-density regime and thereby using advanced acceleration mechanisms beyond TNSA. The results are published in Ref. Rewald et al. [168]. In the following, a summary of the results of reference Rehwald et al. [168] is intended to give an accurate classification and meaning of the results presented later in different chapters of this thesis.
The main result of the experiment is shown in figure 2.19 (a). The figure presents three experimentally measured proton-energy spectra (TPS 0°). Each spectrum is derived by tailoring the density of the cylindrical hydrogen jet to a different spatial distribution with different absolute plasma densities. Experimental control over the target density is given by three aspects. First, a minimization of uncontrolled target pre-expansion by using the DRACO PW laser with PM-cleaned laser contrast. Second, the artificial induction of a well-predictable hydrodynamic plasma expansion by an artificial prepulse with $5 \cdot 10^{17}\,\mathrm{W/cm^2}$ peak intensity at a defined delay before the peak of DRACO PW. With this, the target density is a continuous function of the prepulse delay. Third, the on-shot measurement of the target diameter d by off-harmonic optical shadowgraphy to the time of the arrival of the peak of the DRACO-PW laser. A doubling of the maximum proton energy from 38 MeV to 80 MeV is achieved by tuning the target from an initial diameter of $d = 5\,\mu\mathrm{m}$ (spectrum "(1)") to $d = 11\,\mu\mathrm{m}$ (spectrum "(2)"). A further increase of the target diameter to $d = 28\,\mu\mathrm{m}$ yields a reduced maximum proton energy (spectrum "(3)").

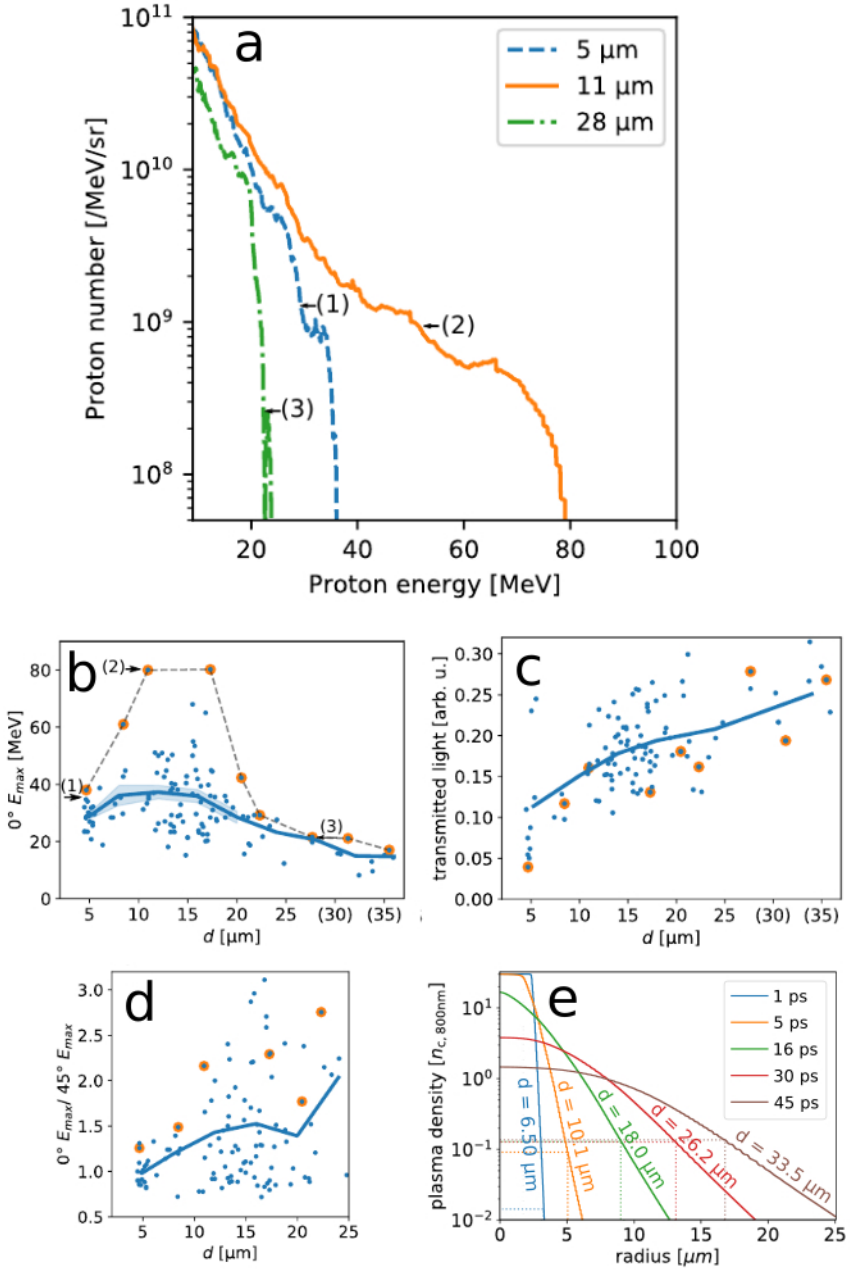

Figure 2.19.: Figure copied from Rehwald et al. [168]. Experimental results of proton acceleration from density-tailored cylindrical hydrogen-jet targets. **(a)** Proton-energy spectra for three different target diameters d. Diameters are measured for every laser shot by off-harmonic optical shadowgraphy to the time of the DRACO-PW laser-peak arrival. **(b)** Maximum proton energy in the 0° TPS versus target diameter d. The orange markers show the best shots and the blue line gives the average of all shots. **(c)** Residual laser light behind the target as recorded by screen 2. **(d)** Fraction of maximum proton energy in the 0° TPS and the 45° TPS. **(e)** Result of a hydrodynamics simulation of artificial target pre-expansion that is used to tailor the plasma density of the target before the arrival of the DRACO-PW laser pulse. The different colors give the corresponding delay of the artificially introduced prepulse. The conversion of each density profile to the target diameter as measured by shadowgraphy is calculated by ray-tracing simulations (for details see text).

The overall scan of maximum proton energy versus target diameter d is given in figure 2.19 (b). The figure shows that not only the best shots (orange) but also the mean of the shots (blue line) displays an enhancement of maximum proton energy compared to the non-pre-expanded hydrogen jet (data with $d = 5\,\mu m$). The range of highest proton energies spans from diameters of about $d = 8\,\mu m$ to $d = 18\,\mu m$. Further experimental signatures at increased target diameters are an increased amount of transmitted light (figure 2.19 (c)) and a more forward-directed proton beam (fraction of maximum proton energy of 0° and 45° TPS in figure 2.19 (d)).
Generally, an increased target diameter suggests a lowering of the target density. Because of the initially low density of the non-pre-expanded target of $30\,n_c$, a tripling of the target diameter can already be sufficient to enter the nearcritical-density regime. This regime is known to allow for enhanced particle-acceleration mechanism beyond TNSA and an interpretation of the experimental findings should be possible by PIC simulations. However, as todays three-dimensional PIC simulations are limited to a comparably small timewindow around the main peak of the high-intensity laser pulse, the target interaction with the artificial prepulse at tens of picoseconds before to the main peak cannot be captured in the same simulation. As an alternative, the target-density distribution at a delay shortly before the ultra-relativistic peak is given as a starting condition to the PIC simulation. This starting condition is found by combining numerical modeling of the target pre-expansion via hydrodynamics simulation with ray-tracing simulations and the experimentally measured shadowgraphy data. As this is a contribution of this thesis to reference Rehwald et al. [168], chapter 5 presents the method in detail. The results are presented in figure 2.19 (e). The figure shows the full target-density distribution for different prepulse delays and the corresponding shadow diameters. The data allows to initialize PIC simulations with the target-density distribution that corresponds to the experimentally measured target diameter as starting condition. Furthermore, the PIC simulations rely on the fact that the target-density tailoring by the artificial prepulse is not altered significantly by the leading edge of the DRACO-PW laser. The assumption is verified by a time-delay scan of shadowgraphy, which shows that, for the PM-cleaned laser contrast of DRACO PW, dielectric breakdown of the target occurs not until $-3.9\,ps$ before the pump-laser peak and target pre-expansion at $-0.2\,ps$ delay is at a negligible level. Both of these contributions to reference Rehwald et al. [168] are presented in chapter 3 and 4 of this thesis.

The results of the PIC simulations are compared to the best-performing shots of the experiment in figure 2.20 (a). Like the experimental data, the mean of the simulated maximum proton energy (black-dashed line) increases to about twice the energy of the non-pre-expanded target at an optimum diameter d between $12\,\mu m$ and $20\,\mu m$. Further reduction of the initial peak density of the target (upper axis of the figure) down to the classical critical density n_c still allows to accelerate protons up to a significant energy level. To get an estimate of the regime of the laser-target interaction, the blue line in the lower panel shows the dynamically piled-up maximum density of the target during laser propagation into the target on the central laser axis. While in the non-pre-expanded case the laser piles up the density to $80n_c$, the global maximum of proton energy is observed when the dynamically piled-up density approaches the theoretical threshold of RIT $\gamma \cdot n_c$, with $\gamma \approx \sqrt{1 + a_0/2}$ [124]. For lower plasma densities, the laser is able to propagate through the plasma. The estimation via $\gamma \cdot n_c$ is confirmed by an increased amount of transmitted laser energy at target diameters above $22\,\mu m$ (red line). The general trend of higher laser transmission at higher target diameters d is in agreement to the experimental observation in figure 2.19 (c). This suggests the occurrence of RIT at large target diameters in the experiment.
Figures 2.20 (b), (c) and (d) show simulated proton spectra, resolved by the emission angle ϕ. Each figure corresponds to a characteristic region of target density in figure 2.20 (a): figure 2.20 (b) ("Sim. B") exemplifies the non-pre-expanded solid-density target, figure 2.20 (c) ("Sim. C") exemplifies the pre-expanded target with initial peak densities close to the theoretical threshold of RIT and figure 2.20 (d) ("Sim. D") exemplifies the pre-expanded target that is well within the RIT regime with initial peak densities close to the classical critical density. While the emission characteristic of Sim. B is more isotropic, both cases of the pre-expanded target in Sim. C and Sim. D show a clear directionality of the proton beam into the laser-propagation direction. Although the emission characteristic of Sim. C and Sim. D have a different shape, both support the experimental observation of a more forward-directed

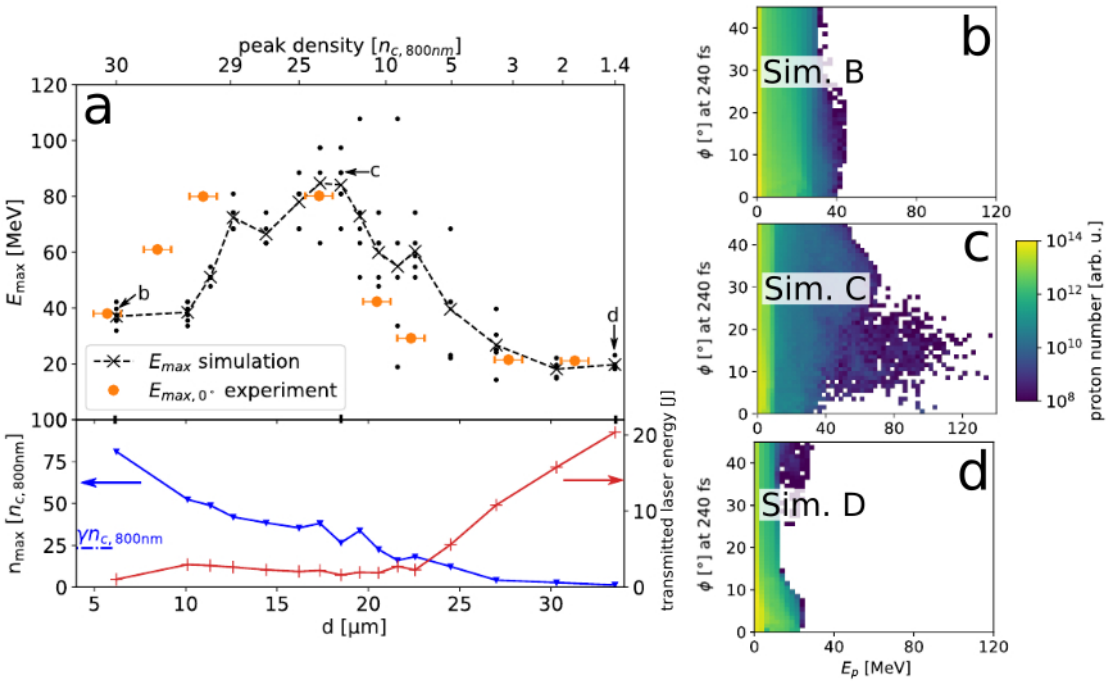

Figure 2.20.: Figure copied from Rehwald et al. [168]. PIC-simulation results of proton acceleration from density-tailored cylindrical hydrogen-jet targets. **(a)** Upper graph: Maximum proton energy as derived by individual PIC simulations (black dots) versus target diameter d (lower axis) and peak density (upper axis) of the target as initialized in the PIC simulation (compare to figure 2.19 (e)). The mean of the simulated maximum proton energy is given by the dashed line and the highest measured proton energies of the experiment are given by the orange markers. Lower graph: Dynamically piled-up maximum target density during laser propagation into the target on the central laser axis (blue line) and amount of transmitted laser energy behind the target (red line). **(b)**, **(c)** and **(d)**: Simulated proton-energy spectra versus emission angle ϕ of (b) the non-pre-expanded hydrogen jet with overcritical solid density, (c) the pre-expanded hydrogen jet at the onset of RIT and (d) the pre-expanded hydrogen jet in the RIT regime with an initial peak density close to the classical critical density. The corresponding maximum proton energy of the individual simulations (b), (c) and (d) are labeled in figure (a).

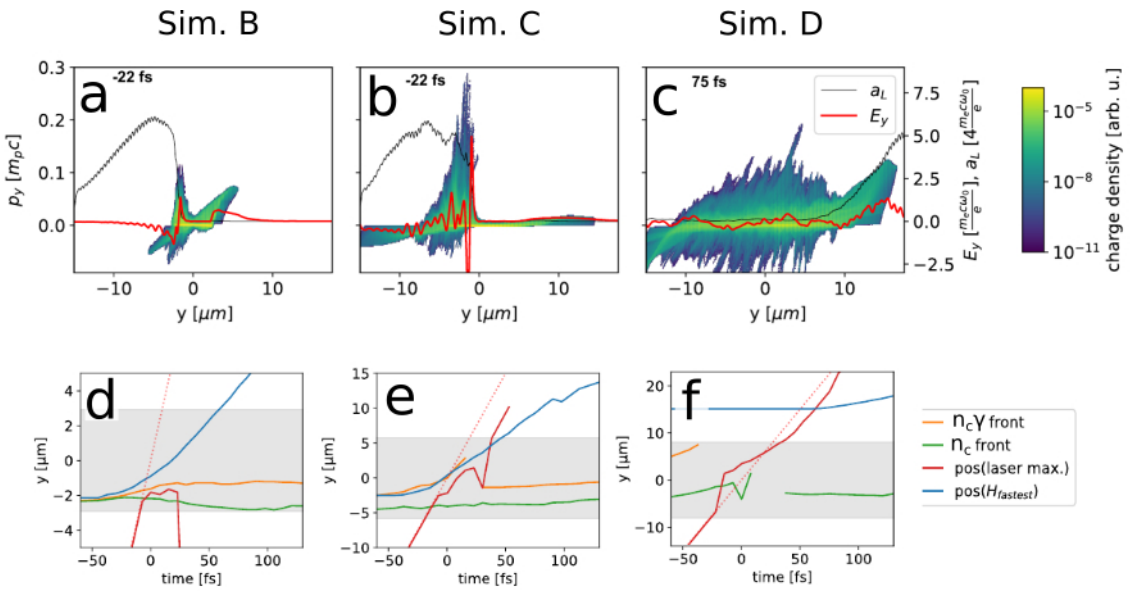

Figure 2.21.: Figure copied from Rehwald et al. [168]. Details of the PIC simulations Sim. A, B and C (refer fig. 2.20). **(a)**, **(b)** and **(c)**: Phase space of the protons (colormap), laser strength a_L (black line) and electric field into the laser-propagation direction E_y (red line) for representative times of each of the acceleration mechanism at play. **(d)**, **(e)** and **(f)**: Time versus position of the maximum laser intensity (red), the fastest proton (blue), the classical critical density n_c at the front surface (green) and the relativistic-transparency front $n_c \cdot \gamma$ (orange). The gray-shaded background corresponds to the initial shadow diameter d.

proton beam in figure 2.19 (d).

The PIC simulations enable an identification of three regimes with different acceleration mechanisms in transition of different target densities. Complementary to the proton-emission characteristics in figure 2.20 (b) to (d), more-detailed insight to the particle acceleration of each regime is depicted in figure 2.21. Figures 2.21 (a), (b) and (c) show the phase space of the protons (colormap), the laser-strength parameter a_L (black) and the electric-field components into the laser-propagation direction E_y (red) for different time steps, each characteristic of the respective acceleration regime. Figure 2.21 (d), (e) and (f) show the time-dependent position of the maximum intensity of the laser (red), the fastest proton (blue), the classical critical density n_c at the front surface (green) and the relativistic-transparency front $n_c \cdot \gamma$ (orange). The gray-shaded background corresponds to the initial shadow diameter d.

A general classification of the Simulations B, C and D can be given by viewing the laser propagation through the plasma. For Sim. B, the laser is reflected on the front surface (red line in figure 2.21 (d)). RIT allows the laser to penetrate the target slightly deeper than the critical-density surface and *hole-boring RPA* (HB-RPA) of protons occurs. At the same time, electron heating on the front surface of the target causes TNSA on the rear side of the target (phase space and E_y in figure 2.21 (a)). The fastest proton (blue line in figure 2.21 (d)) is first accelerated by HB-RPA on the front side and subsequently injected into the rear-side TNSA field. The overall isotropic emission characteristic of protons (figure 2.20 (b)) is characteristic for TNSA that accelerate protons into the target-normal direction of the wire-like target.

In Sim. C, the laser is able to propagate deeply into the target (red line in figure 2.21 (e)) and to deplete a significant amount of energy into the plasma. Between -10 fs and 20 fs, the relativistic-transparency front (orange) coincides with the position of the fastest proton and both follow the movement of the maximum laser intensity through the target. The synchronized movement of the laser and the relativistic-transparency front generates a peaked charge-separation field at the foremost front of the laser pulse (E_y in figure 2.21 (b)) that continuously accelerates protons to very high kinetic energies (view phase space in figure 2.21 (b)). For matched conditions, the laser front pushes onto

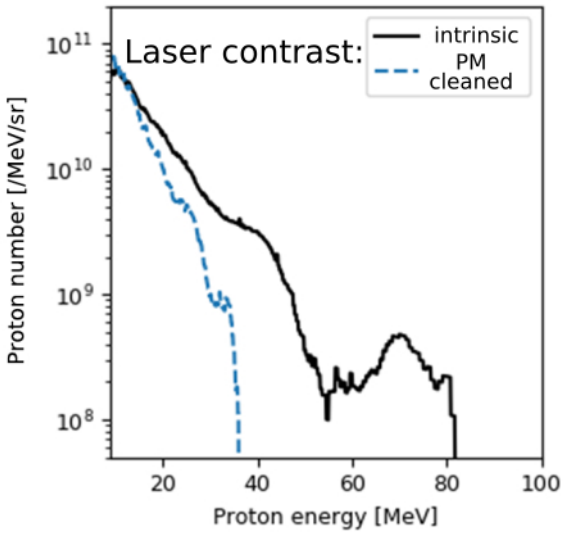

Figure 2.22.: Proton-energy spectrum of the highest maximum proton energy that is measured from an interaction of the DRACO-PW laser with intrinsic laser contrast and the cylindrical hydrogen-jet target (black line). The proton-energy spectrum of an interaction of DRACO PW with PM-cleaned laser contrast and the cylindrical hydrogen-jet target (blue-dashed line) is copied from fig. 2.19 (a).

the electron front that simultaneously experiences RIT. This allows for a continuous preservation of the charge-separation field with a slow enough velocity, such that the protons can follow the charge-separation field. The acceleration mechanism is termed *optimized RPA at the relativistic-transparency front* or *relativistic-transparency-front RPA* (RTF-RPA) and the mechanism is studied in detail for optimized initial-density distributions of the target in Ref. [81].
The initial density distribution of the target in Sim. D shows a peak density close to the classical critical density n_c. Because of RIT, the laser propagates though the whole target (red line in figure 2.21 (f)) and a significant amount of laser intensity leaves the target on the rear side (a_L in figure 2.21 (c)). Here, the prominent field structure of RTF-RPA rushes too fast trough the target and protons cannot catch up in a synchronized way. Instead, the acceleration mechanism of *magnetic-vortex acceleration* (MVA) occurs. The laser drives a non-linear wakefield structure that accelerates a strong electron current behind the laser pulse. When entering the down ramp of the plasma density, the electron current induces a toroidal magnetic field, which creates a longitudinal electric field (red line in figure 2.21 (c)) that accelerates protons to moderate maximum energies. Figure 2.20 (d) shows that a significant amount of protons is accelerated prodominantly into the laser-forward direction. Furthermore, the scattering of the simulated maximum proton energy is reduced compared to the RTF-RPA regime of Sim. C (see black dots in figure 2.20 (a)). The scattering of the simulation results occurs because of the sensitivity of the mechanism to small changes in the initialized microscopic plasma conditions. Details are discussed in another doctoral project, see Ref. [79].

Overall, the identification of one of the described acceleration mechanism with an individual experimental measurement is challenging. It is likely that a hybrid scheme between the different mechanisms is observed in the experiment. Although reference Rehwald et al. [168] demonstrates the experimental realization of enhanced laser-driven proton acceleration in the nearcritical-density regime, the identification and measurement of decisive experimental signatures of one of the suspected acceleration mechanism remain as a future task.

2.2.5.2. Enhanced proton acceleration by target pre-expansion via the intrinsic leading edge

In addition to the controlled target-density tailoring via artificial prepulses and the excellent proton-acceleration performance retrieved in combination with the DRACO-PW laser with PM-cleaned laser contrast, another striking acceleration result is measured during the experiments in 2019. Figure

2.22 shows a proton-energy spectrum with a maximum energy of 80 MeV, which is measured from the interaction of the cylindrical hydrogen-jet target and the DRACO-PW laser with intrinsic laser contrast. For reference, the spectrum of the best-performing shot as derived for the PM-cleaned laser contrast and the non-pre-expanded cylindrical hydrogen-jet target is copied from figure 2.19 (a). The measurement is a paramount result for envisioning laser-plasma accelerators for future applications, as the self-replenishing target delivery and the repetition rate of the DRACO-PW laser, in principle, allow for the generation of similar particle beam at repetition rates of up to 1 Hz. An identification of the laser parameters of the leading edge that cause the optimized pre-expanded target-density distribution of the specific shot together with the overcoming of the shot-to-shot jitter of the laser-target overlap is highly desired in the future.
The high-energy part of the proton spectrum in figure 2.22 shows a characteristic spectral distribution. Similar distributions are observed in a number of comparable shots, although not with the same maximum proton energy. The investigation of the underlying acceleration mechanism is not as developed as for the case of target-density tailoring presented before. The different spectral shape in comparison to the spectra in figure 2.19 (a) suggests different particle-acceleration dynamics at play. Currently, more data analysis together with start-to-end simulations of the intrinsic temporal-contrast setting of DRACO PW are needed to derive the key target parameters that lead to the optimized performance. Section 3.4 of this thesis includes results that prepare the way towards the required evaluation.

2.3. Implementation of off-harmonic optical probing at DRACO PW

The following sections describe results that are achieved within this thesis project. Most of the content and figures of this section are published by the author in Ref. Bernert et al. [24].

The long-term optical-probing capability of a laser-plasma laboratory profits from the implementation of a dedicated laser system for optical probing. The alignment of the target and the probe beam is completely independent from the high-intensity-laser settings and it's availability. In addition, if different laser media are used for both laser systems, the possibility of off-harmonic optical probing is intrinsically given. The presentation of the utilized laser system for optical probing is given in section 2.3.1. An important aspect of two lasers within one experiment is their temporal synchronization. In the here presented implementation, the probe-laser oscillator is electronically synchronized to the high-intensity pump-laser oscillator and the pump-probe delay is controlled via a beam-arrival monitor. Details are given in section 2.3.2. Off-harmonic optical probing features a discrimination of the probe signal from the parasitic plasma self-emission via spectral filtering in the microscopy beamline. In section 2.3.3 the developed approach of two-staged spectral filtering is presented and quantified. The resulting filter efficiency and the dependency of the plasma self-emission on the high-intensity-laser contrast are shown and discussed in section 2.3.4.

2.3.1. Stand-alone laser system

For off-harmonic optical probing of high-intensity laser-solid experiments, a high spectral separation of the probe-laser and the pump-laser wavelengths is desired to ease the requirements on spectral filtering. Furthermore, a laser material with a broad amplifier bandwidth is needed to guarantee femtosecond pulse duration and thus sufficient temporal resolution of the probing data. Figure 2.23 (a) illustrates that a combination of Ti:Sapphire and Yb:Calcium-fluoride lasers is particularly well suited. The fundamental spectrum as well as the second harmonic (2ω) of the Yb:Calcium-fluoride laser are well separated from the fundamental spectrum and the second harmonic of the Ti:Sapphire laser. For both laser systems, optical components for the fundamental and the second-harmonic wavelengths are commercially available.

2.3.1.1. Oscillator and regenerative amplifier

Compact design and robustness are desired properties of a stand-alone laser system that is operated in the experimental area of a high-power-laser system (location in the cave is highlighted by "P" in

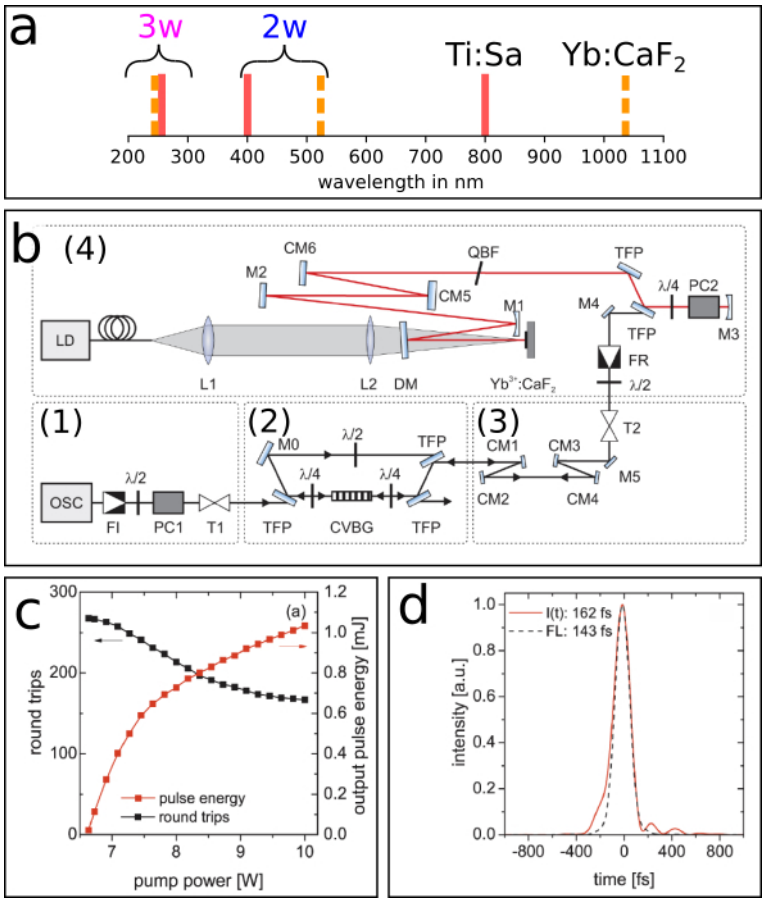

Figure 2.23.: **(a)** The spectral positions of the fundamental wavelengths of femtosecond Ti:Sapphire ($\sim 800\,\mathrm{nm}$) and femtosecond Yb:Calcium-fluoride ($\sim 1030\,\mathrm{nm}$) lasers are well separated. The same applies to the second-harmonic wavelengths (2ω) of both lasers. The large spectral separation eases the requirements on spectral filtering for off-harmonic optical probing. **(b)** Figure copied from Loeser et al. [117]: Setup of the probe-laser system. (1) Laser oscillator (OSC), (2) Hybrid stretcher-compressor unit, (3) "Extra-cavity" dispersion compensation, (4) laser cavity. Optical components: Mirror (M), Faraday isolator (FI), lambda-halve waveplate $\lambda/2$, Pockels cell (PC), telescope (T), thin-film polarizer (TFP), chirped-volume Bragg grating (CVBG), chirped mirror (CM), Faraday rotator (FR), Quartz-birefringent filter (QBF), dichroic mirror (DM), lens (L), laser diode (LD), laser medium $Yb^{3+} : CaF_2$ on a mirror (active mirror). **(c)** Figure copied from Loeser et al. [117]: Cavity round trips and output energy before compression versus power of the pump-laser diode. **(d)** Figure copied from Loeser et al. [117]: Pulse shape (red-solid line) measured by a *Wizzler* device and theoretical Fourier limit (black-dashed line).

figure 2.15). The stand-alone laser system is placed on a dedicated optical table with a housing for laser safety, reduction of air turbulences, temperature changes, pollution and accidental misalignment. A laser design with little demands on realignment helps to focus on the utilization in the experiment. The demands are achieved by a solid-state laser material and by avoiding adjustment-sensitive optical components like a grating stretcher and a grating compressor or non-linear optical processes in the amplifier. The stand-alone laser system consists of a laser oscillator and a regenerative amplifier based on chirped-pulse amplification, which is constructed within this thesis project. The setup details and laser parameters of the system are published in Ref. Loeser et al. [117]. In the following, only a concise overview is given.
The four basic components of the laser are presented in figure 2.23 (b). The commercially available oscillator (*Flint* by *Light Conversion* [9]) delivers 60 fs pulses at a center wavelength of 1033 nm. The laser pulses propagate through a Faraday isolator, a pulse-picker Pockels cell, a prism for pulse selection and a telescope for collimation of the beam ((1) in fig. 2.23 (b)). All following amplifier components are placed in a sealed Aluminum housing. The pulses are stretched in a hybrid stretcher-compressor unit ((2) in fig. 2.23 (b)). A *chirped-volume Bragg grating* (CVBG) reflects wavelengths between 1019 nm and 1041 nm in different depth of the device and stretches the pulses to a duration of about 480 ps. Via polarization coupling, the stretched pulses are inserted into an "extra-cavity" dispersion-compensation unit ((3) in fig. 2.23 (b)) consisting of four chirped mirrors and a telescope for mode matching in the subsequent regenerative amplifier ((4) in fig. 2.23 (b)). The pulses enter a Faraday rotator for isolation and are captured in the cavity during the on-time of the second Pockels cell. The laser mode is nearly collimated in the beam path between M1 and M3 and the focus of the cavity is located in the laser medium (active mirror). The "intra-cavity" dispersion compensation by two chirped mirrors allows to balance the accumulation of spectral phase by hundreds of paths through the cavity components. A quartz plate is used for artificial linear spectral broadening of the amplified spectrum. After switching off the second Pockels cell, the amplified pulse is sent through the extra-cavity dispersion compensation again and reenters the hybrid stretcher-compressor unit. By polarization coupling, the pulses are guided into the chirped volume Bragg grating from the other side. The different length of propagation of each wavelength during stretching is reversed and by this the reflected pulses are compressed. Polarization coupling enables the isolation of the amplified pulses for the application.
The utilization of chirped mirrors and a chirped-volume Bragg grating reduces the complexity of the setup, enable a compact footprint of $900 \times 600\,\mathrm{mm}^2$ and reduces the demands for realignment of the system. For the utilization as a backlighter in an experiment, the most relevant properties of the laser pulses are energy and pulse duration. A measurement of both quantities is given in figures 2.23 (c) and (d). The red curve in figure 2.23 (c) demonstrates the ability of tuning the output energy continuously up to 1 mJ before compression (0.91 mJ after compression) by changing the power of the pump-laser diode. Figure 2.23 (d) shows a measured pulse duration of 162 fs with a little amount of residual third-order dispersion. Further reduction of dispersion to a minimum pulse duration of 143 fs (*Fourier limit* (FL)) is not required for an application as optical backlighter.

2.3.1.2. Probe-beam generation and splitting for the experiments

For the utilization as backlighter in the experiment, the probe-laser system is operated with a pulse energy of 300 µJ after compression, a pulse duration of 160 fs and a repetition rate of 10 Hz. A spectrum of the amplified pulses is shown in figure 2.24 (b). The generation and splitting of the two backlighter beams *515 nm probe* and *1030 nm probe* is visualized in figure 2.24 (a). The pulses of the probe-laser system are sent into an LBO crystal for type-one second-harmonic generation (SHG). The LBO crystal is cut with theta = 90° and phi = 13.8° to a thickness of 3.7 mm and features an anti-reflection (AR) coating for 515 nm and 1030 nm light on both surfaces. The frequency conversion results in a pulse energy of 100 µJ for the 515 nm probe and 200 µJ for the 1030 nm probe. A calculation with the software *SNLO* [12] and the specific LBO-crystal properties yields a maintained pulse duration of 160 fs of the 515 nm probe. The measured spectral bandwidth of the beam in figure 2.24 (c) yields an even lower pulse duration of the Fourier-transform limit and by this supports the calculation by SNLO.

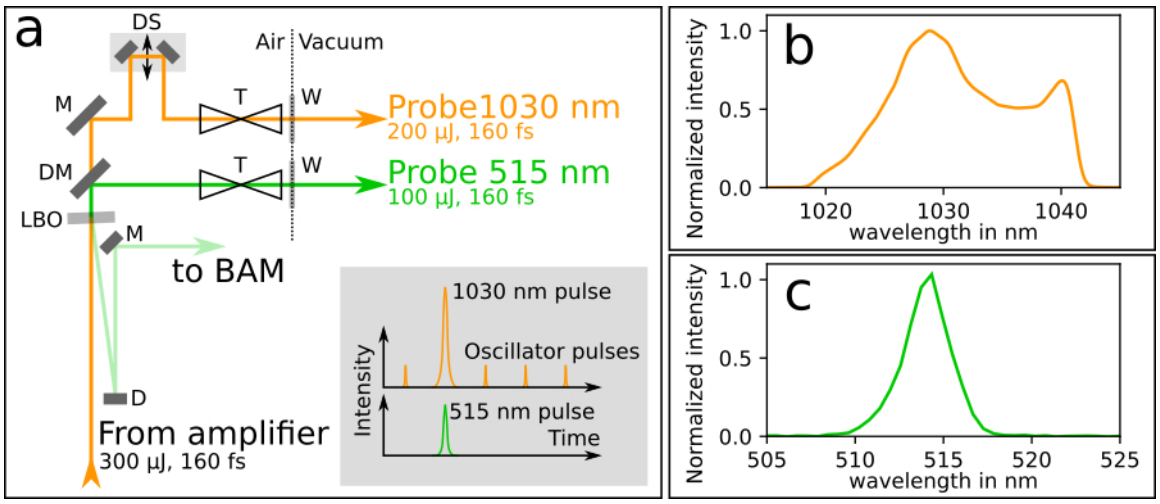

Figure 2.24.: **(a)** Probe-beam generation and spitting for the experiments in chamber I2. Optical components: LBO crystal for second-harmonic generation (SHG), mirrors (M) with low-group-delay dispersion, dichroic mirror (DM) for splitting of the SHG beam at 515 nm wavelength from the fundamental beam at 1030 nm wavelength, delay stage (DS) to compensate for temporal delay by different beam paths towards the experiment. The telescope (T) magnifies each probe beam by a factor of two and enable fine tuning of the focal position behind final focusing in the experiment, windows (W) for entering the experimental chamber, D-shaped mirror (D) for picking the signal of the beam-arrival monitor (BAM). Inset: Sketch of the temporal structure of both probe beams. The 1030 nm probe features residual signal of the laser-oscillator pulses at 78 MHz. **(b)** Spectrum of the 1030 nm-probe beam. **(c)** Spectrum of the 515 nm-probe beam.

Both generated probe beams have perpendicular polarization and are spatially separated by a dichroic mirror. For matching the delay between both pulses at the position of the high-intensity laser-solid interaction in the experiment, a manual delay stage is placed in the beam path of the 1030 nm probe. Before entering the target chamber, a telescope magnifies each probe beams by a factor of two. For each telescope, one of the two lenses is mounted on a manual stage for tuning the distance between the lenses. This enables high-precision spatial shifts of the focal spot of each probe beam behind final focusing in the experimental setup (refer to setup-figure 2.17). All utilized lenses are planoconvex and made from fused silica (UVFS) with an AR coating for 515 nm and 1030 nm light on both sides. All mirrors in the beamline up to the experiment are optimized for low group-delay dispersion of the respective wavelength. The vacuum windows are one-inch-diameter optics made from UVFS with a thickness of 3.05 mm and an AR coating for 515 nm and 1030 nm light on both sides.
The probe-beam signal of the *beam-arrival monitor* (BAM) is generated by turning the angle of the LBO crystal by 2° and picking the reflection of the converted 515 nm signal from the rear-side AR coating by a D-shaped Silver mirror close the the beam path of the incoming 1030 nm beam (see sketch in figure 2.24 (a)).
The temporal structure of both probe beams is sketched in the inset of figure 2.24 (a). While the 515 nm probe is a singular pulse, the 1030 nm probe features a continuous background of weak non-amplified pulses of the laser oscillator at 78 MHz.

2.3.2. Temporal synchronization

Utilizing two laser systems within a single experimental platform places high demands on temporal synchronization. Two options are commonly used. Either pump and probe laser share the same laser oscillator [65] or a stand-alone laser oscillator of the probe-laser system is electronically synchronized to the pump-laser oscillator [213] and Bernert et al. [24]. Here, the second option by utilizing commercially available lock-electronics together with a single centralized clock for both laser oscillators is followed.

In general, the temporal synchronization is based on three pillars. The first pillar is the high-frequency synchronization at the level of the laser-oscillator frequency or higher. It determines the temporal shot-to-shot stability of the pump-probe delay in the experiment and is desired to be close to the laser-pulse duration. The second pillar is the low-frequency synchronization on the level of the laser-amplifier repetition rate. It is realized by a gate trigger of the pump-laser trigger electronics that dictates the starting point of the trigger electronics of the probe laser. The third pillar is the active synchronization control via a *beam-arrival monitor* (BAM). The BAM is a tool that allows for on-shot measurement of the timing between both amplified laser pulses. Furthermore, a method of defining the absolute timing in the experiment is needed. Most of the results that are presented in this section are part of reference Bernert et al. [24].

2.3.2.1. Opto-electronic synchronization of the two laser oscillators

A schematic of the temporal-synchronization setup is given in figure 2.25 (a). The core of the high-frequency-synchronization control is a highly stable external *optical-master oscillator* (OMO), which is provided by the ELBE-accelerator infrastructure at HZDR. The OMO signal is distributed to the DRACO oscillator and to the probe-laser oscillator (each located in a different experimental cave) via actively stabilized fiber links to compensate drifts (e.g. thermal, vibrations). The stabilization of the fiber length is realized by a feedback loop, which is fed by a balanced cross-correlator signal between the OMO pulses and the partially back-reflected laser pulses from the end of each fiber link. The synchronization electronics of the DRACO-laser and probe-laser oscillators are a commercially available solutions by *Menlo Systems* [10] that consists of *balanced optical-to-microwave phase detector* (*BOM-PD*), *digital phase shifter* (*DDS 120*), *mixer-detector unit* (*MDU*) and a lock electronic (*RRE Syncro*). The BOM-PD converts the OMO laser pulses into an RF-signal with very low timing jitter. It corresponds to the 25th harmonic (1950 MHz) of the fundamental repetition rate of both lasers of 78 MHz. The oscillators are locked at the 26th harmonic that is detected from the optical signal of the respective laser oscillator by the MDU. The differential frequency between the BOM-PD and the 26th harmonic of 78 MHz is given to a phase detector by the DDS120. The error signal of the phase-lock loop with the 78 MHz signal from the laser oscillator is used to adapt the cavity length of the respective laser oscillator by changing the voltage of a piezo stage, which positions a mirror inside the laser cavity. This minimizes the temporal jitter between the OMO and the respective laser oscillator (DRACO or probe-laser). The DDS120 can be used to change the phase between the OMO and each oscillator. For a pump-probe time-delay scan, the device enables software-controlled sub-10 fs steps and overcomes the necessity of one motorized optical-delay stage in the DRACO or the probe-laser beampath.
To benchmark the temporal stability of each oscillator, noise measurements with a stable external clock (*FSWP* by *Rohde-Schwarz* [2]) are conducted. The figures 2.25 (c) and (d) show the single-sideband phasenoise (solid gray - free running and solid blue - synchronized) and the calculated integrated squared RMS jitter (dashed-blue line) of both oscillators. The covered frequency range of the piezo stage in each oscillator is seen in the reduction of phase noise up to a frequency of about 1 kHz. The temporally integrated RMS jitter between 1 Hz and 20 kHz is measured to be 119 fs for the DRACO oscillator and 152 fs for the probe-laser oscillator.

2.3.2.2. Beam-arrival monitor

The *beam-arrival monitor* (BAM) is designed to enable an on-shot measurement of the time delay between a pump-laser and a probe-laser pulse versus a reference. In general, this is realized by picking a small part of the DRACO-laser beam before final focusing (*DRACO leakage*, refer to setup figure 2.17 in section 2.2.4) and overlapping it in space and time with a small part of the probe-laser beam (*probe leakage*, see "to BAM" in figure 2.24 (a)). To bring the two laser pulses in interaction, we use the well-characterized mechanism of laser self-guiding in air [102]. Outside the experimental chamber, the DRACO leakage is focused to intensities between $10^{14}\,\mathrm{W/cm^2}$ and $10^{16}\,\mathrm{W/cm^2}$. Guiding of the laser pulse causes a transient localized perturbation of the refractive index that lasts up to nanoseconds, i.e., the pulse is followed by a filament of refractive-index perturbation. By transversal stroboscopic

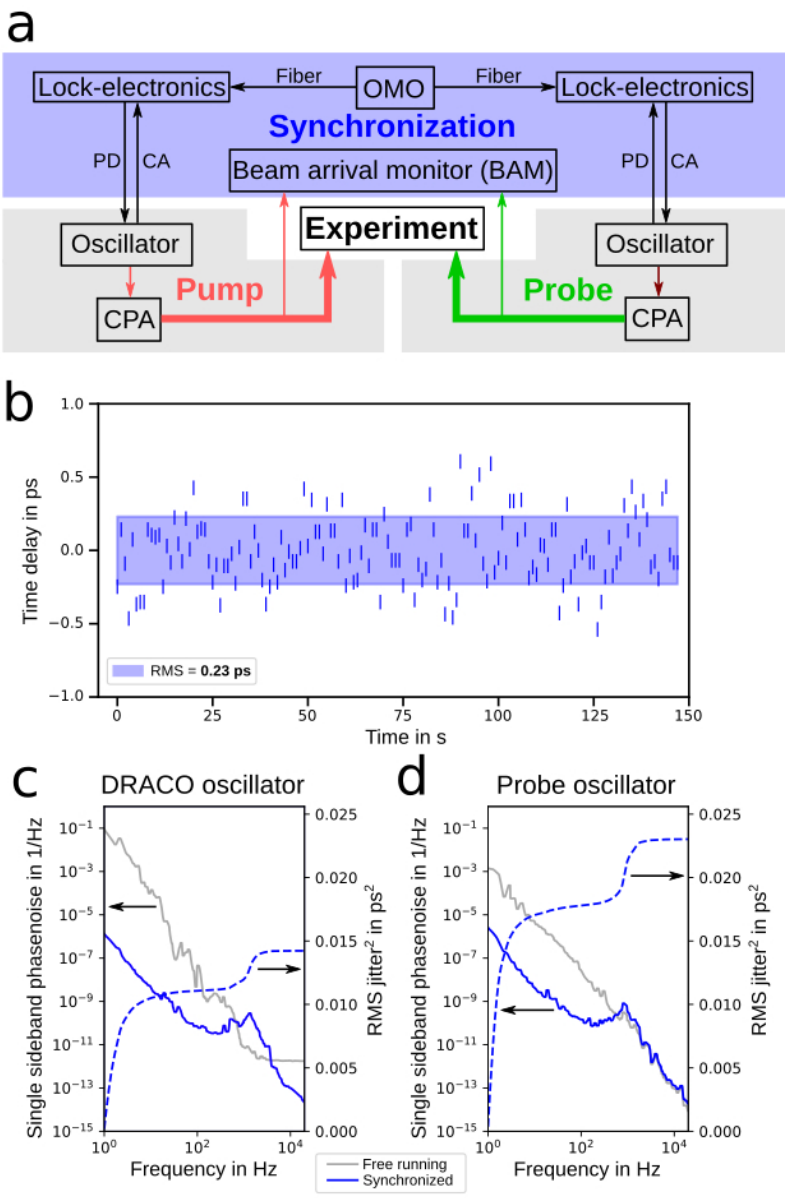

Figure 2.25.: Figure copied from supplement of Bernert et al. [24]. **(a)** Schematic of the synchronization control between the pump-laser (DRACO) and the probe-laser system. OMO - optical-master oscillator, PD - photo diode, CA - cavity adjustment, CPA - chirped-pulse amplification. **(b)** Measurement of the shot-to-shot time delay via the BAM. The height of each marker gives the uncertainty of a single BAM measurement. **(c), (d)** Measurement of the single-sideband phase noise with an external clock and the calculated square of the temporal RMS-jitter of (c) the DRACO-laser oscillator and (d) probe-laser oscillator.

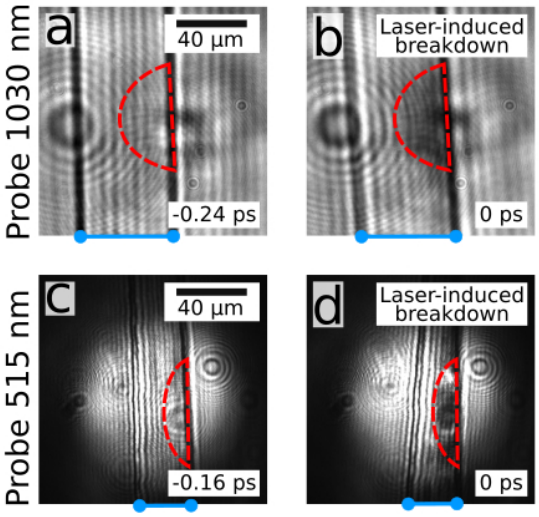

Figure 2.26.: The absolute temporal reference is the pump-laser-peak arrival on target. Exemplary shadowgrams of the hydrogen sheet-jet target at reduced pump-laser-peak intensity: **(a), (b)** probe 1030 nm and **(c), (d)** probe 515 nm. At 0 ps pump-probe delay, first laser-induced breakdown of the target is observed as large-scale blackened target region (encircled by the red-dashed line). With an accuracy of $\sim$ 170 fs, the delay correspond to the pump-laser-peak arrival.

illumination of the filament with the probe leakage, a time-resolved shadowgram of the filament is recorded. The spatial position of the leading edge of the filament follows the temporal position of the DRACO-leakage pulse. It is used to measure shifts of the time-delay for each shot versus a previously defined reference position. As reference, we use the leading-edge position of the filament at which the pump-laser peak of the full DRACO-laser beam arrives on target in the experimental chamber (details in section 2.3.2.4). Details about the optical setup, the alignment procedure and the derivation of time delays from the BAM are presented in Appendix C.

2.3.2.3. Measurement of the overall timing stability

The overall timing stability accumulates all electronic and optical jitters of the whole synchronization chain up to the experiment. A measurement of 150 consecutive shots at 1 Hz via the BAM is presented in figure 2.25 (b). The timing uncertainty of each BAM measurement is given by the length of the vertical lines. From this data, we retrieve an RMS pump-probe-delay stability of 230 fs. Quadratic subtraction of the measured integrated RMS jitter of the DRACO oscillator (119 fs) and the probe-laser oscillator (152 fs) yields 125 fs. The origin of this residual RMS jitter is attributed to jitter in optical-path length between the two oscillators and the experiment ($\sim$ 0.5 km). The value can serve as lower limit of achievable delay stability for further improved techniques of temporal synchronization of both laser oscillators. The overall timing stability underlines the necessity of the BAM to achieve control over the pump-probe delay on a scale of 100 fs in the experiment.

2.3.2.4. Absolute timing in the experiment

The relative timing between different shots is determined via the BAM. To transform the relative time delays of different shots to an absolute time delay, the arrival of the pump-laser peak on target is used as a reference and the corresponding pump-probe delay is set to zero. To determine the pump-laser-peak arrival on target, the ionization response of the dielectric target, i.e., the laser-induced breakdown, is used. During breakdown, the absorptive and reflective properties strongly change and the corresponding areas occur as blackened regions within the otherwise transparent target (for details see chapter 3). To ensure that the laser-induced breakdown is triggered by the laser peak and not by the leading edge of the pump laser, the pump-laser-peak intensity should be reduced below about 10^{15} W/cm^2 without changing the optical-path length. This is achieved by blocking most part of the

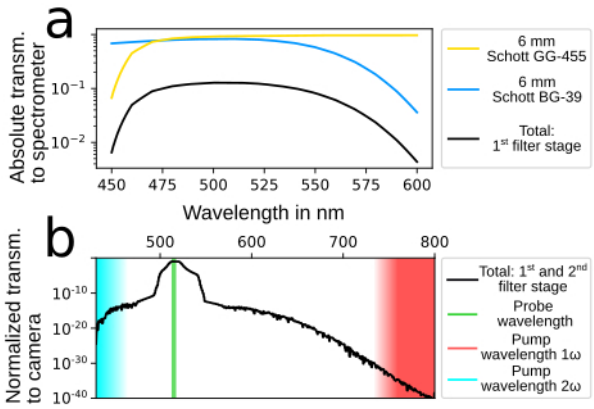

Figure 2.27.: Figure copied from Bernert et al. [24]. **(a)** Calculated absolute spectral-transmission function from the target up to the spectrometer together with the individual transmission of the two colored-glass filters as provided by the manufacturer (refer to setup-figure 2.17). **(b)** Normalized transmission function up to the shadowgraphy camera of probe 515 nm (combined first and second filter stage). The graph is calculated from the manufacturers data of all microscopy-beamline components of probe 515 nm.

high-power beam with a ceramic screen before the final focusing optics (screen 1 in setup-fig. 2.17) and transmitting just a small portion of the beam through a hole in the screen onto the target. By continuously changing the pump-probe delay and capturing shadowgrams of the target together with the corresponding timing on the BAM, the earliest timing of the shadowgram with an observed laser-induced breakdown is found. It defines the arrival time of the pump-laser peak on target. Exemplary shadowgrams are presented in figure 2.26.
For the experiments presented in this thesis and the shadowgrams in figure 2.26, however, the pump-laser-peak intensity is not reduced down to $10^{15}\,\mathrm{W/cm^2}$. As the size of the hole in screen 1 was fixed, the peak intensity on target was reduced to $\sim 10^{17}\,\mathrm{W/cm^2}$ only and the recollimating plasma mirror is used to suppress the leading edge instead. Considering the contrast enhancement ($2 \cdot 10^{-4}$) and the trigger point of the plasma mirror ($\sim -0.2\,\mathrm{ps}$, refer to Appendix B), the generation of laser-induced breakdown for this configuration is expected to occur between $-50\,\mathrm{fs}$ and $-100\,\mathrm{fs}$ before the laser peak, which is smaller than the blurring that is induced by the probe-laser pulse duration of 160 fs. To account for this uncertainty, the accuracy of determining the pump-laser-peak arrival on target is estimated over the blurring by the probe laser pulse duration and the uncertainty of the BAM measurement of the corresponding shot to $\sim 170\,\mathrm{fs}$. Furthermore, for referencing a specific shots with respect to the pump-laser-peak arrival, the accuracy of the BAM measurement of the specific shots needs to be included. It follows, that the temporal resolution of a time delay scan is 175 fs.

In conclusion, the temporal synchronization stability and control of the pump-probe setup is sufficiently precise to scan the high-intensity laser-solid interaction within hundreds of fs around the pump-laser peak.

2.3.3. Two-staged approach of spectral filtering

Off-harmonic optical probing features two main aspects of a successful implementation in a high-intensity laser-solid experiment. One part is the appropriate choice of backlighter wavelength and the other part is the discrimination of the probe signal from the plasma self-emission. High spectral fluence of the probe on target as well as sufficient spectral filtering in the microscopy beamline are needed. Furthermore, dielectric coatings on vacuum windows, mirrors and spectral-bandpass filters most often have low damage thresholds and require protection against high fluences, in particular against the ultraviolet light of the 3$^{\mathrm{rd}}$ and 4$^{\mathrm{th}}$ harmonic of the pump laser. This is solved by a two-staged approach of spectral filtering, which is published in Ref. Bernert et al. [24]. The first filter stage is placed directly behind the objective and the second filter stage is placed in front of the

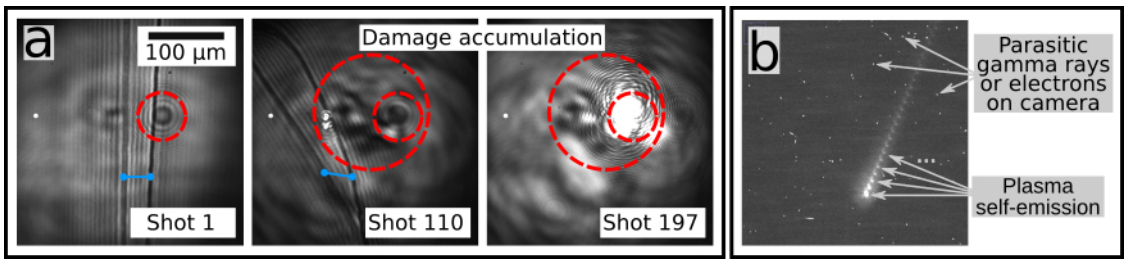

Figure 2.28.: **(a)** Damage accumulation in the microscopy beamline of probe 1030 nm by plasma self-emission during a single experimental day. The small red circle marks a damage on the dielectric bandpass filter on the camera (*FLH1030-10* by *Thorlabs Inc.*) that transformed from a small spot (shot 1) to a large transparent hole (shot 197) by accumulation over ∼ 200 DRACO-laser shots at varied pulse energy (∼ 50 shots at full energy). The large red circle marks a permanent damage of the AR coating of the vacuum-window that suddenly occurred by accumulating two consecutive shots at full energy. The vacuum-window is positioned roughly in the middle between objective and camera. For this specific day, the vacuum window is exposed to a broadband optical range of wavelengths of plasma self-emission, because the first filter stage (6 mm *Schott*-glass *RG-1000*) was positioned behind the vacuum-window. Placing the first filter stage inside the experimental chamber directly behind the objective prevents damage accumulation. **(b)** Plasma self-emission is trapped between the front- and rear-side dielectric coating of a bandpass filter (*FB400-40* by *Thorlabs Inc.*). It causes multiple equally spaced spots of plasma self-emission on the camera.

camera. The position of both filter stages is sketched in the microscopy beamline of probe 515 nm in the setup-figure 2.17. Note that the second filter stage is not used for the spectrometer, but for the shadowgraphy and interferometry camera only.
The first filter stage of the microscope of probe 515 nm consists of two different layers of *Schott*-glasses (*GG-455* and *BG-39*), each with 6 mm total thickness. They restrict the transmission of the microscopy beamline to the spectral band between 450 nm and 600 nm, as shown by the black line in figure 2.27 (a). The line is calculated from the respective nominal transmission function given in the data sheet of each glass (blue and yellow line). The position of the first filter stage directly behind the objective protects all following components in the microscopy beamline. Furthermore, the position minimizes the risk of intensity-driven nonlinearities in the glass filter that can cause permanent damage or optical image distortion (shot-to-shot variation of the image quality). These occur, if the filter stage or another optical component, e.g., a window or beamsplitter, is placed close to a position at which a particularly strong wavelength of the plasma self-emission is focused by the chromatic objective, e.g., the 4^{th} harmonic of the pump laser. An example is given in figure 2.28 (a).

The second filter stage is placed directly in front of the cameras of probe 515 nm. It consists of two spectrally narrow dielectric bandpass filters. One filter is centered around 520 nm with a spectral FWHM of 40 nm (*FBH520-40* by *Thorlabs Inc.*) and the other filter is centered around 514.5 nm with 10 nm FWHM (*FL514.5-10* by *Thorlabs Inc.*). Both are centered around the probe wavelength and give a combined optical density ≥ 10 for all other wavelength. To avoid reflections between the bandpass filters, the more narrow-band filter is stacked closer to the camera. In figure 2.27 (b), which shows the calculated transmission function from the target position up to the shadowgraphy camera of probe 515 nm, the broadband spectral-transmission characteristic of the first filter stage is well separated from the more sharp spectral transmission characteristic of the second filter stage (between 500 nm and 540 nm).The calculated transmission includes all microscopy-beamline elements except the objective. The transmission of the objective is measured to vary less than 10 % between 450 nm and 750 nm. This would effect the overall transmission curve by less than 1 %.
To quantify the expected filter efficiency of the combined first and second filter stage, figure 2.11 (b) shows the spectral band of probe 515 nm in green, the band of the pump (1ω) in red and the band of the second harmonic of the pump (2ω) in turquoise. The transmission ratio between the probe

spectrum and the spectral band of the fundamental and second harmonic of the pump is calculated to be better than 10^{32} and 10^{15}, respectively. The calculation does not take into account transient effects like saturated absorption in the colored glass. Thus, within the strongly absorbing bands of the glasses, the attenuation may be lower.
For the microscope of probe 1030 nm, a similar approach of two-staged optical filtering is used. Here, the first filter stage consist of the long-pass *RG1000 Schott*-glass with 6 mm total thickness and the second filter stage consists of one dielectric long-pass (*FELH1000* by *Thorlabs Inc.*) and one dielectric bandpass filter (*FLH1030-10* by *Thorlabs Inc.*).
In summary, dielectric bandpass filters and colored glasses have different advantages and disadvantages. Dielectric bandpass filters provide a wavelength-dependent fixed transmission with sharp spectral edges. However, stacking of these filters creates the risk of trapping light that was transmitted through the first dielectric-coating layer. Usually, this is the case if multiple spots of plasma self-emission with equal spacing are observed on the camera, see figure 2.28 (b). Glass filters, however, provide more smooth and broadband spectral-transmission characteristics, but can be manufactured with different thicknesses. In principle, thick glasses are able to provide a very high spectral-contrast ratio between the probe-laser and pump-laser wavelengths. For a sufficient spectral separation of pump and probe, a combination of the advantages of both kinds of spectral filters in a two-staged approach results in a very high transmission ratio between the specific wavelengths.

2.3.4. Plasma self-emission at ultra-relativistic pump-laser-peak intensity

An introduction to plasma self-emission, exemplary measurements of plasma self-emission for different types of targets and an overview of the generation mechanisms is given in the introductory section 2.1.6 and figure 2.11. The intention of the following section is the quantification of the specific plasma self-emission of the cylindrical hydrogen-jet target in interaction with the DRACO-PW laser. The presented data, evaluation and discussion is published in Ref. Bernert et al. [24]. In connection to the previous section, the first subsection 2.3.4.1 is dedicated to the experimental demonstration of the filter efficiency of the two-staged approach of spectral filtering. In the second subsection 2.3.4.2, spectral measurements of the plasma self-emission of different laser-contrast settings are presented and discussed. Finally, the third subsection 2.3.4.3 discusses the implications of the spectral-emission characteristics on the applicability of off-harmonic optical probing and an outlook on possible future developments of the probing technique is given.
All data that is presented in this section is measured with a pump-laser energy of 19 J on target, i.e., with a peak intensity of about $6 \cdot 10^{21}\,\mathrm{W/cm^2}$. High temporal contrast (PM-cleaned contrast) is used and occasionally, an artificial prepulse at varied delay is introduced before the pump pulse to emulate a low-temporal-contrast setting of the interaction. The prepulse has an intensity that is about 10^{-4} times lower than the peak of the pump laser and a pulse duration of about 55 fs. It is generated via an optical shortcut, as sketched in figure 2.18 (e) in section 2.2.4. The spectrometer data is measured in the image plane of the microscopy beamline of probe 515 nm (refer to setup-fig. 2.17).

2.3.4.1. Efficiency of spectral filtering

The spectrometer behind the first filter stage of probe 515 nm is used to demonstrate the filter efficiency of the two-staged approach of spectral filtering. The raw data in the spectral band between 200 nm and 1100 nm is presented in figure 2.29. The graphs show the light distribution right before the second filter stage for three different settings of the pump-laser contrast. The blue graph represents the high temporal-contrast setting, the orange and purple graph represent a low temporal-contrast setting that is generated by an artificial prepulse at -20 ps or -40 ps delay. All graphs show the mean and the standard deviation of the mean for consecutive shots. For each setting, the variation of the spectra is mainly caused by slight variations in the pump-laser-target overlap. Probe 515 nm is simultaneously used as a backlighter for time-resolved shadowgraphy and therefore all spectra show the spectrum of probe 515 nm (green line) as additive signal. The black line shows the detection threshold as provided by the vendor. Secondary gamma rays are generated by the high-intensity laser-solid interaction and it's reaction products and causes random high signal peaks in singular spectra, although the spectrom-

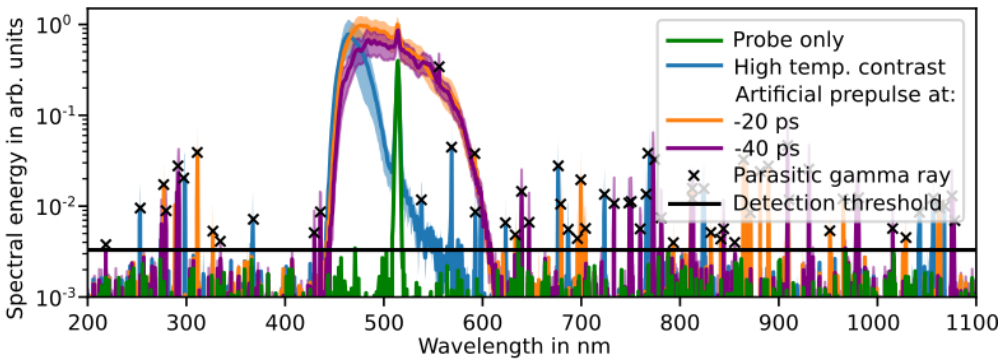

Figure 2.29.: Raw data as measured by the spectrometer behind the first filter stage of probe 515 nm for different pump-laser-contrast settings (blue, orange, purple). All graphs are scaled equally. The pump-laser energy is 19 J and the cylindrical hydrogen jet is used as a target. A high number of gamma rays causes localized parasitic signal peaks on the CCD of the spectrometer (black crosses). The green line shows the spectrum of probe 515 nm (pump laser off). The detection threshold is specified by the vendor (black line).

eter is shielded by lead bricks of multiple cm thickness. The mean of the spectra is raised accordingly and the corresponding peaks are marked by black crosses in figure 2.29. The parasitic signals need to be excluded from the evaluation.
Independent on the laser-contrast setting, optical light is measured within the spectral band from 450 nm to 600 nm only. This demonstrates the filter efficiency of the first filter stage (refer to transmission function in fig. 2.27 (a)). The first, second, third and fourth harmonic of the pump laser are successfully shielded. For each laser-contrast setting, a comparison of the plasma self-emission with the signal height of the probe 515 nm spectrum (green) demonstrates that the suppression of light outside the spectral range of probe 515 nm is easily achieved by the second filter stage with a combined optical density of ≥ 10 (compare to transmission curve in fig. 2.27 (b)). It follows, that only the amount of light in the spectral band of the probe is transmitted to the cameras behind the second filter stage. All residual plasma self-emission on the cameras is within the same spectral band like probe 515 nm.

2.3.4.2. Laser-contrast dependence of plasma self-emission

The correction of the spectrometer raw data (fig. 2.29) by the transmission function of the first filter stage (fig. 2.27 (a)) enables the spectral characterization of the plasma self-emission between 450 nm and 600 nm. For all three different laser-contrast settings, the results are displayed in figure 2.30. The spectra are calibrated to an absolute scale in mJ/nm by the known amount of energy in the spectrum of probe 515 nm (green line). The spectra show the emitted spectral energy into the solid angle that is captured by the objective.
The spectral energy of the measured data is in the range of ~ 0.1 mJ/nm and can be compared to estimates from the pump-laser energy (19 J) and the covered solid angle of the objective ($\sim 0.1\,\pi$sr). Assuming an isotropic emission of the pump-laser energy from the focal spot without any spectral shifts (800 nm central wavelength, 50 nm spectral FWHM), about 10 mJ/nm spectral energy within the spectral FWHM of the pump laser are expected. In contrast, assuming strong spectral broadening to a box-like spectrum between 200 nm and 1100 nm gives a spectral energy of about 0.5 mJ/nm. As expected, the spectral energies in figure 2.30 are below both estimates. Further drains of energy like fast particles, bulk-plasma expansion, radiation in the non-visible spectral range and reflection of the laser lower the expected amount of spectral energy even more.
The spectrum of the high temporal-contrast setting in figure 2.30 shows the falling tail of the second harmonic of the pump laser between 450 nm and about 500 nm. The spectra that are measured for the setting with an artificial prepulse show that the tail vanishes and a close to homogeneous spectral emission over the whole displayed spectral range emerges. The different spectral characteristics can

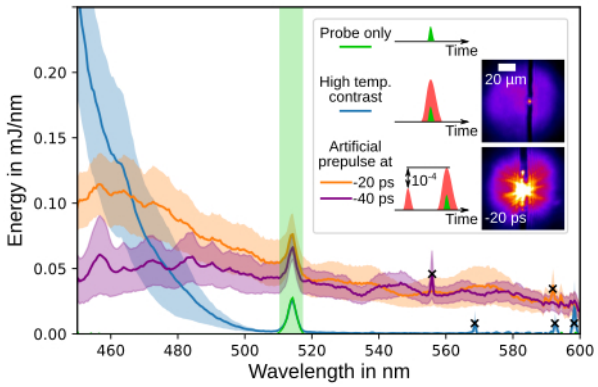

Figure 2.30.: Figure copied from Bernert et al. [24]. Spectral measurement of the plasma self-emission for three different laser-contrast settings: High temporal contrast (blue) and artificial ultra-short prepulse at −20 ps (orange) and −40 ps delay (purple). Each setting shows the mean over consecutive shots and the corresponding standard error of the mean as shaded area. The probe-515 nm wavelengths (green line) are highlighted by the green-shaded area. Parasitic gamma ray signals on the detector are marked by black crosses. Exemplary shadowgrams of the high temporal-contrast and the −20 ps-prepulse setting are shown in the legend.

be explained as follows. Highest conversion efficiency of second-harmonic generation on solid-density targets is achieved for surface scalelengths of the plasma density shorter than the pump-laser wavelength [189, 55, 72]. As measured by time-resolved optical shadowgraphy and presented in section 4.1, the scalelengths in the high temporal-contrast setting to the arrival of the pump-laser peak is between 60 nm and 130 nm, i.e., far below the pump-laser wavelength. From measurements of the prepulse-induced plasma-expansion dynamics that are presented in chapter 5, the generated surface scalelength for the prepulse delays of −20 ps and −40 ps varies between ∼ 1 µm and ∼ 5 µm, i.e., single to multiple pump-laser wavelengths. It follows that a strong second-harmonic signal in the high temporal-contrast setting and a reduction of the second-harmonic signal with increasing prepulse delay are expected.
The homogeneous spectral emission for both prepulse settings in figure 2.30 can be attributed to an interplay between several mechanisms. First, the generation of a surface scalelength of the plasma density increases the coupling efficiency of laser energy into hot electrons that heat the plasma by collisions or via return currents [157, 92]. The electrons of the laser-heated plasma produces a high number of photons in a broad energy range by Bremsstrahlung [133, 43, 82]. Second, pre-expanded targets features a larger surface area to emit radiation. Third, the increased amount of undercritical plasma together with the lowering of the peak density of the target close to or below the relativistically corrected critical plasma density n_c/γ (compare to target density profiles in figure 2.19 (e) in section 2.2.5) act as a nonlinear medium to the incident pump laser and spectral broadening and self-phase modulation occur [196, 203, 113].

Reference [199] reports on the generation of 3/2-harmonic generation on solid-density targets by a two-plasmon decay. The authors utilized a pump-laser-peak intensity around $10^{17}\,\mathrm{W/cm^2}$, a pulse duration of 135 fs and surface scalelengths of the plasma density of several hundred micrometers. The generation of the emission, i.e., at 534 nm for a pump-laser wavelength of 800 nm, could be unfavorable for off-harmonic optical probing at a backlighter wavelength of 515 nm. However, the emission is never observed as isolated spectral emission for all laser-contrast settings. There are at least two plausible reasons why this emission is not observed. The generation of a surface scalelength of several hundred micrometers is neither given for the high temporal-contrast setting nor for the prepulse timings of −20 ps and −40 ps. Furthermore, the intensity range around $10^{17}\,\mathrm{W/cm^2}$ corresponds to a contrast range of $\sim 2 \cdot 10^{-5}$ for the here discussed peak intensity. Viewing the laser contrast of the PM-cleaned DRACO-PW laser in figure 2.16 (c), this intensity range is located in the steep-rising edge before the laser peak and not in the more slowly rising picosecond pedestal. It follows, that during the

laser-target interaction the regime between $5 \cdot 10^{16}\,\mathrm{W/cm^2}$ and $5 \cdot 10^{17}\,\mathrm{W/cm^2}$ is exceeded rapidly in approximately 60 fs. The estimate is consistent with a measurement of the laser contast at higher temporal resolution (fig. 1 (d) in Ref. [211]). For the investigated settings, the 3/2 harmonic emission is either less important compared to other mechanisms that generate optical emission or the the generation process is disturbed, e.g., by the pile up of electron density on the front surface of the target by the ponderomotive force that increases with the rapidly rising leading edge.

2.3.4.3. Implications on the potential of off-harmonic optical probing

The technical implications of the quantified plasma self-emission (fig. 2.30) to the implementation of off-harmonic optical probing in similar experiments, with the prospect of low image disturbance by plasma self-emission, can be evaluated by comparing the signal heights of the self-emission to the signal height of the backlighter spectrum. Because the probe spectrum is occurring as additive spectral energy for all three spectra of plasma self-emission, not the peak but rather the measured values at the edges of the green interval represent the amount of plasma self-emission around the probe wavelength and thus need to be compared to the "probe only" spectrum.
For the high temporal-contrast setting, the spectral energy of plasma self-emission at the edges of the green interval is close to zero and the probe energy is much higher. For the two low temporal-contrast settings, however, the probe energy is much lower than the level of plasma self-emission. The probe energy is thus not expected to be sufficient for outshining the plasma self-emission on the camera.
To quantitatively estimate the required amount of backligther energy for these settings, an additional spatial factor needs to be taken into account. The plasma self-emission mostly originates from a small region while the probe beam illuminates a larger spot, i.e, the field of view. This is illustrated by two exemplary shadowgrams in the legend of figure 2.30. For the prepulse-contrast setting, the addition of defined attenuation via neutral-density filters on the camera yields a required amount of attenuation of 100 to restrict the self-emission to the same spatial extent like in the high temporal-contrast setting. It follows, that a shadowgram without disturbance by plasma self-emission requires a factor 100 higher backligther energy. This is a factor of ~ 20 higher than what is estimated solely from the spectral data. The estimation is in agreement with the five times larger field of view that is illuminated by the probe compared to the source size of the plasma self-emission.

In the following, a generalization of the findings and possible prospects for the technique of off-harmonic optical probing are given. Provided that the spectral filtering is sufficient and plasma self-emission on the camera occurs only within the spectral band of the probe with a given pulse energy, the only parameter left to outshine the self-emission is spectral fluence. As the fluence scales with the square of the beam diameter, a clever choice of focusing is key to find a good compromise between plasma self-emission and field of view.
Considering the non-spatial parameters of the probe beam, i.e., pulse duration and energy, it is important to recall that Fourier-limited laser-pulse duration is inherently linked to spectral bandwidth by the time-bandwidth product. Shorter pulses require a broader bandwidth and the pulse energy is always distributed over the whole spectrum of the pulse. Thus, at constant pulse energy, short pulses have a lower spectral energy per unit wavelength than longer pulses. For a good-quality probing image without saturation of the camera, the probe beam is required to be spectrally brighter than the plasma self-emission. Simultaneously, the probe should be noninvasive, i.e., it should not cause laser-induced breakdown.
For the current setup of probe 515 nm, an increased pulse energy by a factor of ten would shift the backlighter intensity to $\sim 2 \cdot 10^{14}\,\mathrm{W/cm^2}$. As presented in section 3.1.2, this is already above the target's threshold of laser-induced breakdown of a 160 fs laser pulse. In the current implementation, probe 515 nm is already pushing the limits of noninvasive diagnostics. It follows that for a spectrally strong and broadband plasma self-emission, e.g., the -40 ps-prepulse setting, a concentration of the probe-pulse energy into a narrow bandwidth can be beneficial. A picosecond backlighter in combination with narrow bandpass filters probably outshines the self-emission and at the same time keeps the intensity of the backlighter below the threshold of laser-induced breakdown. However, this comes at the price of lower temporal resolution.

Very short and broadband backlighter pulses require at least a part of their spectral bandwidth to be brighter than the plasma self-emission. This is possible in the high temporal-contrast setting for which the emission characteristic of the plasma shows spectral gaps. Here, the technique of off-harmonic optical probing could evolve towards higher temporal resolution in the future. This will be enabled by a spectral characterization of the plasma self-emission and a clever choice of spectral filters. A prerequisit of this approach is that spectral filtering behind the investigated interaction does not diminish temporal resolution of the probing data, which is demonstrated in Ref. [184]. For high-intensity laser-solid interactions, the approach is already used at a pump-laser-peak intensity of $4 \cdot 10^{19}\,\mathrm{W/cm^2}$ in Ref. [20].

3. Dielectric breakdown in high-intensity laser-solid interactions

Most of the content and figures of this chapter are published by the author in Ref. Bernert et al. [23].

Start-to-end simulations of high-intensity laser-solid interactions are envisioned to guide experiments towards improved properties of the desired interaction products, e.g., maximized particle energy. Section 2.1.3 provides an overview of the status and the challenges that have to be tackled to stengthen the predictive power of start-to-end simulations. Generally, particular attention should be given to high-intensity-laser interactions with dielectric targets, as they yield highest proton energies in experiments, see references [201, 103, 90, 211] and Rehwald et al. [168].
Several stages of the interaction of a high-intensity laser pulse with a dielectric solid can be defined, sorted by the increasing laser-intensity level up to the laser peak. In this chapter, the temporal starting point of the laser-plasma interaction is investigated. This point during the leading edge of a high-power laser can be considered as a classification into relevant and negligible laser intensities of target pre-expansion.
With the generation of a quasi-free electron density above the critical plasma density and a removal of the lattice bonds, the breakdown of the dielectric solid constitutes a reasonable onset of a plasma-hydrodynamics modeling of target pre-expansion. One the one hand, it marks the transition from a volumetric interaction with propagation of the laser in the transparent target bulk to a localized laser-energy deposition at the critical-density surface, at which most of the subsequent laser light is reflected. On the other hand, the removal of the lattice bonds allows for a fluid description of the system. However, radiation-plasma-hydrodynamics simulations usually do not include ionization dynamics. Commonly, the process of dielectric breakdown is omitted by the simulation and a simple estimate of the starting point of target pre-expansion is retrieved from the intersection point of the measured laser contrast and a threshold intensity like the *appearance intensity* I_{app}, e.g., see Ref. [210]. The apprearance intensity corresponds to the critical field of *barrier suppression ionization* (BSI threshold) [16]. At this intensity, the ionization potential of a bound electron of the target atoms is balanced by the electric field strength of the laser. A classical treatment gives

$$I_{\mathrm{app}}[\mathrm{W/cm^2}] \approx 4 \cdot 10^9 \times E_{\mathrm{ip}}[\mathrm{eV}]^4/(Z_{\mathrm{eff}}^2), \tag{3.1}$$

with Z_{eff} being the charge state of the atom after ionization and E_{ip} the ionization potential of the $Z_{\mathrm{eff}} - 1$ charge state, e.g., tabulated in [11]. A quantum mechanical treatment yield somewhat higher values of the critical field [19]. For atomic hydrogen, the approximation via equation 3.1 gives $I_{\mathrm{app}} \approx 1 \cdot 10^{14}\,\mathrm{W/cm^2}$, while the exact quantum-mechanical treatment calculates $I_{\mathrm{app}} \approx 8 \cdot 10^{14}\,\mathrm{W/cm^2}$.
I_{app} is usually used to describe the ionization of gases or underdense plasmas. A utilization for the description of highly-correlated matter like solids is somewhat artificial, because the binding energy of electrons, especially the outer electrons, is not given by a single-atomic Coulomb potential, but rather by a superposition of Coulomb potentials of the correlated atoms, i.e., the band structure. The so-called *laser-induced breakdown of solids* is an extensively studied field and the occurrence of different melting mechanisms leads to a significant variation of the *laser-induced damage threshold (LIDT)* well below the BSI threshold for varied laser parameters. For metallic solids, laser energy is directly absorbed by quasi-free electrons and the energy is subsequently transferred to the lattice by collisions. It follows, that a broad range of laser parameters induces a phase transition similar to classical melting. Dielectric solids, however, are transparent to the incident laser light and a single photon is insufficient to bridge the band gap between valence and conduction band. They generally exhibit higher LIDT intensities than metals.

LIDT intensity and fluence are commonly measured by target fracture, e.g., hole diameter, and represent time-integrated measurements. For high-intensity laser-solid interactions, however, the breakdown is a transient effect and accounts for only a specific part of the overall interaction. In a start-to-end simulation, the transient formation of a quasi-free electron density above the critical plasma density and the abruptly occuring change of the optical properties [97] is the relevant parameter. In the following, we call this formation *transient laser-induced breakdown (LIB)*. LIB can be considered as part of the temporal evolution towards LIDT. In fact, exceeding the critical plasma density is one of the ways to define LIDT in rate-equation models for simulating dielectric breakdown [17].
Because of technical limitations in the amplification chain of a Petawatt-class laser system, the leading edge of an amplified pulse typically exhibits distinct short prepulses, a subjacent continuous *pedestal* of varying slope and a *steep-rising edge* towards the *laser peak* (see section 2.1.1). It is well known that LIDT intensity varies with laser-pulse duration and similar dependencys should apply to LIB. Therefore, it is expected that different parts of the leading edge could trigger dielectric breakdown by exceeding different threshold intensities [202].

In this chapter, we demonstrate the impact of the pulse-duration dependence of LIB on high-intensity laser-solid interactions. For demonstration, we use the interaction between high-contrast laser pulses of the DRACO-PW laser with peak intensities from $0.6 \cdot 10^{21}\,\mathrm{W/cm^2}$ to $5.7 \cdot 10^{21}\,\mathrm{W/cm^2}$ and the dielectric hydrogen sheet-jet target. As hydrogen has only a single bound electron per atom, it is a particularly basic example for the investigation of ionization effects.
The chapter is structured as follows. Section 3.1 introduces LIB by illustrating the physical picture of the different ionization mechanisms from the literature in section 3.1.1 and by presenting quantitative measurements of LIB of the hydrogen sheet-jet target at low laser intensities and different pulse durations in section 3.1.2. In section 3.2, the experimental shadowgraphy results of experiments with ultra-relativistic laser-peak intensities between $0.6 \cdot 10^{21}\,\mathrm{W/cm^2}$ and $5.7 \cdot 10^{21}\,\mathrm{W/cm^2}$ are presented and compared to measurements of the laser contrast in section 3.3. The comparison can be viewed from two different perspectives. Section 3.3.1 discusses the implication of the slope of the leading edge to the starting point of LIB, i.e., the starting point of target pre-expansion, and section 3.3.2 discusses the prospects of LIB as a diagnostic tool to investigate the spatio-temporal properties of high-intensity laser pulses in the position of the final focus. To give an instruction of how to derive the starting point of LIB in other laser-target assemblies, a demonstration example using the intrinsic laser contrast of DRACO PW is given in section 3.4. Finally, section 3.5 discusses the observation of dielectric breakdown, which is not directly caused by laser light, but instead by relativistic electrons that traverse the target as soon as the laser intensities of the leading edge become relativistic.

3.1. Transient Laser-Induced Breakdown (LIB)

3.1.1. Physical picture of the mechanism

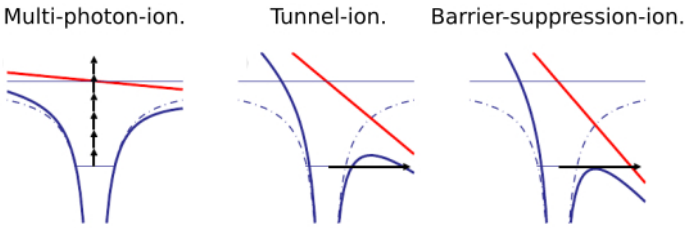

Figure 3.1.: Figure copied from [17]. Illustration of the *strong-field ionization* processes (*Multi-photon ionization* and *Tunnel ionization*) and *barrier-suppression ionization*.

The following subsection is intended to provide insight to the physical mechanisms that lead to LIB of a dielectric solid. The content of the subsection was developed on the basis of the research articles [190, 19, 188, 171, 97, 118, 59, 158, 42, 40, 149, 202, 51] and the review articles [160, 112, 17, 161, 172].

All figures of this subsection 3.1.1 are copied from the literature.

LIDT measurements with femtosecond and picosecond lasers show a significant variation of the LIDT fluence with laser-pulse duration, target material and thickness [112, 17, 172]. Furthermore, not only the laser fluence but also the specific temporal envelope of the intensity is relevant [188, 118, 59, 149]. The variation of thresholds results from an interplay of several ionization mechanisms in different intensity and pulse-duration regimes. Figure 3.1 pictures the three fundamental ionization processes on the basis of which an electron in a dielectric solid can be excited to the conduction band, purely by the presence of a laser field. The Coulomb potential of a bound atom (dashed line) is superimposed with the electric potential of the laser field (red) and results in a deformed effective potential (blue line). To achieve excitation to the conduction band, either a bound electron absorbs multiple photons (*Multi-photon ionization*, left image), or the bound electron tunnels through the finite potential wall of the effective potential (*Tunnel ionization*, center image), or the atomic Coulomb potential is reduced such that the electron can classically escape (*Barrier-suppression ionization*, right image). Barrier-suppresion ionization occurs at intensities above the BSI threshold [19], i.e., for very rapidly rising laser envelopes. Below the BSI-threshold intensity and for most practical scenarios, the Keldysh theory descibes ionization rates of tunnel and multi-photon ionization (see references [160, 161]). Both ionization mechanisms can be viewed as a limiting case, either for a slowly varying laser field compared to the characteristic orbital period of a bound electron (multi-photon ionization) or for a fast varying laser field compared to the characteristic orbital period of a bound electron (Tunnel ionization). For the laser wavelengths and intensities relevant to LIB and LIDT of the here discussed dielectrics and pulse-duration regime, both ionization mechanisms contribute and a full treatment via Keldysh's theory is required [17]. Both mechanisms are subsumed under the term *strong-field ionization*.

Another important ionization mechanism causing LIB and LIDT in the regime of picosecond to femtosecond pulses is the so-called *avalanche ionization* (also termed *impact ionization*). The process is pictured in figure 3.2 (ii). In a first step, several seed electrons are excited to the conduction band by strong-field ionization. As the conduction band allows for a continuous spectrum of electron energies, the electrons in the conduction band are able to absorb energy from the laser field directly via inverse Bremsstrahlung. For these electrons, the absorption of energy is not restricted to the processes of strong-field ionization, which means that an electron can in principle absorb a single photon like in a metal. The laser heats the conduction-band electrons to high kinetic energies. Electrons with an energy higher than the band gap are able to excite valance-band electrons by collision, i.e., they produce two low-energy electrons in the conduction band. As long as the laser field is applied, it provides energy to the conduction-band electrons. Once initialized, the process causes a non-linear increase of quasi-free electrons, which is an *electron avalanche*, with recombination counteracting.
Simulations of the ionization dynamics are usually based on single- or multiple-rate equations and nowadays provide quantitative agreement with experimental LIDT results over a wide range of laser-pulse durations. An overview and details about the different mathematical models can be found in the review articles [17] and [172]. A recently demonstrated dynamic-rate-equation model shows computational effectiveness and by this promises to be a convenient approach for an implementation in large-scale electro-magnetic simulations like PIC approaches [51]. Commonly, there are two ways to define LIDT in a simulation. Either the laser fluence is high enough to produce a conduction-band-electron density higher than the critical plasma density or the integrated absorbed energy by the conduction-band electrons reaches the energy threshold of material ablation [17]. The first criterion corresponds to the generation of LIB.

Fused silica is a dielectric solid with a high band gap of about 9 eV and LIDT of this material is thoroughly investigated. Figure 3.3 shows exemplary simulation data and experimental data of the pulse-duration regime from tens of picoseconds down to a few femtoseconds. Figure 3.3 (a) is copied from Ref. [190]. The authors demonstrate a transition from the conventional diffusion-dominated regime of thermal damage at pulse durations $\gtrsim 50\,\mathrm{ps}$ (*square root law*) to the regime of pulse durations $\lesssim 10\,\mathrm{ps}$, in which strong-field ionization and avalanche ionization are the main driving mechanisms that lead to LIDT. The calculated data termed "Multiphoton Ionization Limit" demonstrates

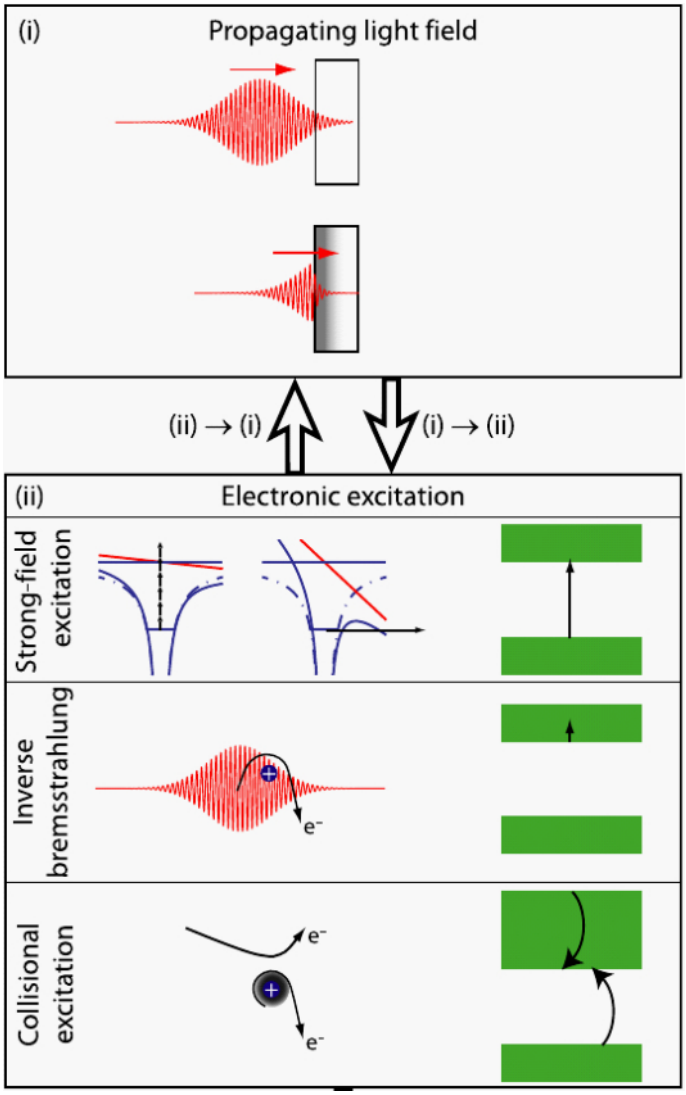

Figure 3.2.: Figure copied from [17]. **(i)** Optical properties of the dielectric solid before (upper sketch) and after laser-induced breakdown (LIB, lower sketch). **(ii)** Basic interaction mechanisms that lead to LIB. Each sketch on the right side shows the conduction and valance band as upper and lower green bar together with the energy gain of electrons as black arrow. Upper panel: Strong-field ionization enables direct ionization of valence-band electrons to the conduction band. Middle panel: Conduction-band electrons gain energy from the laser by inverse Bremsstrahlung. Lower panel: Conduction-band electrons with sufficiently high kinetic energy ionize valence-band electrons collisionally and by this generate two conduction-band electrons with low kinetic energy.

that strong-field ionization alone is insufficient to describe the scaling trend of the experimental data, especially in the regime of picosecond pulses. In this regime, the authors conclude that avalanche ionization is strongly contributing to LIDT (see the other two solid lines in fig. 3.3 (a)).
Since the last decade, the relative contribution of strong-field and avalanche ionization to LIDT in the sub-picosecond regime is under debate [17]. Figure 3.3 (b) is copied from the recently published reference [51]. The figure gathers experimental LIDT data for pulse durations between single femtoseconds and single picoseconds with a scaling trend of $F_{th}^{\mathrm{FS}} \propto \tau^{0.30}$ (dotted gray line). $F_{th}^{\mathrm{FS}}[\tau]$ is the LIDT fluence of fused silica and τ is the laser-pulse duration. As demonstrated by the blue dash-dotted line, strong-field ionization alone would yield a pulse-duration scaling proportional to $\tau^{0.73}$. Similar results are derived, if strong-field ionization together with laser-heating of conduction-band electrons is included (green dashed line). Only the inclusion of collisional ionization of valence-band electrons by laser-heated conduction-band electrons (red line) enables a fit of the experimental scaling trend

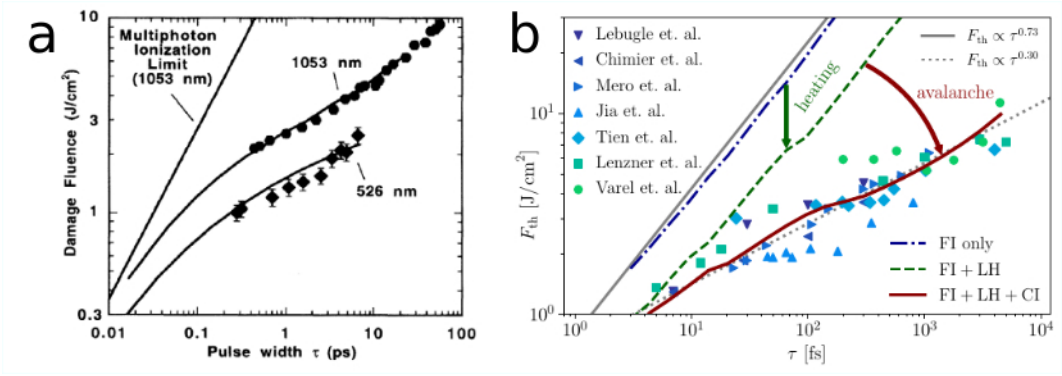

Figure 3.3.: **(a)** Figure copied from [190]. Experimental data (markers) and calculations (lines) of LIDT fluences of fused silica versus pulse duration for two different pump-laser wavelength. **(b)** Figure copied from [51]. Experimental data (markers) of LIDT fluences of fused silica for a pump-laser wavelength of 800 nm. Calculated LIDT fluence by rate equations (lines) for: "FI only"- strong-field ionization only, "FI + LH": Strong-field ionization and laser heating of conduction-band electrons, "FI + LH + CI": Strong-field ionization, laser heating of conduction-band electrons and collisional ionization of valence-band electrons.

$\tau^{0.30}$. The authors of Ref. [51] conclude that even for pulse durations down to tens of femtoseconds, the consideration of avalanche ionization in the rate-equation model is required to explain the experimental data quantitatively. The findings are supported by earlier work at pulse durations between 7 fs and 300 fs [40]. Therein the authors conclude that avalanche ionization is predominant at pulse durations $\gtrsim 50$ fs and increases in relevance with pulse duration .
In summary, LIDT of fused silica for laser-pulse durations in the femtosecond up to the tens-of-picosecond regime includes mutually relevant contributions of avalanche and strong-field ionization.

LIDT and LIB of a dielctric solid are accompanied by an increase of the conduction-band electron density above the critical plasma density. As the quasi-free electron density increases, the optical properties of the solid undergo significant changes. The common approach is the derivation of the dielectric function $\epsilon(\omega)$ from a superposition of the Drude-model of a free-electron gas, which describes the response of the conduction-band electrons, with the refractive index $\tilde{n}_0$ of the unperturbed solid, which takes the response of the bound electrons into account. Γ is the scattering rate of conduction-band electrons with the other constituents of the solid (electron-phonon, electron-ion, electron-neutral atom, electron-electron). The complex refractive index $\tilde{n}$ is given by [17]

$$\sqrt{\epsilon(\omega)} = \Re(\tilde{n}) + i\Im(\tilde{n}) \approx \sqrt{\tilde{n}_0^2 - \frac{\omega_p^2}{\omega^2 + i\omega\Gamma}}\,. \tag{3.2}$$

More advanced approaches include the contribution of the emptied valence band to the unperturbed refractive index $\tilde{n}_0$ [84]. To illustrate the optical properties of a dielectric after LIB, the reflectivity and the absorption coefficient of fused silica that undergoes LIDT is given in figure 3.4 (b). At the time the electron density in the conduction band increases above the critical density (compare to solid line in figure 3.4 (a)), the reflectivity increases strongly with a step-like function and the absorption coefficient increases with increasing electron density.

An illustration of the dynamics of the process is given in figure 3.5. The graphs display the laser field E_y, the conduction-band electron density n_e and the electron temperature T_e versus the spatial coordinate of the laser-propagation direction at different simulation-time steps. The simulated material is fused silica with a band gap of 9 eV and the laser properties are 800 nm wavelength and 26.7 fs-FWHM pulse duration. Figure 3.5 (a) shows a case with $3 \cdot 10^{13}\,\mathrm{W/cm^2}$ peak intensity, which is below the threshold of breakdown. Here, part of the laser pulse is reflected at the vacuum-dielectric interface, according to Fresnel's coefficients. As soon as the laser pulse enters the material, it excites electrons to the conduction band. The number of electrons increases until the end of the pulse is reached (refer to

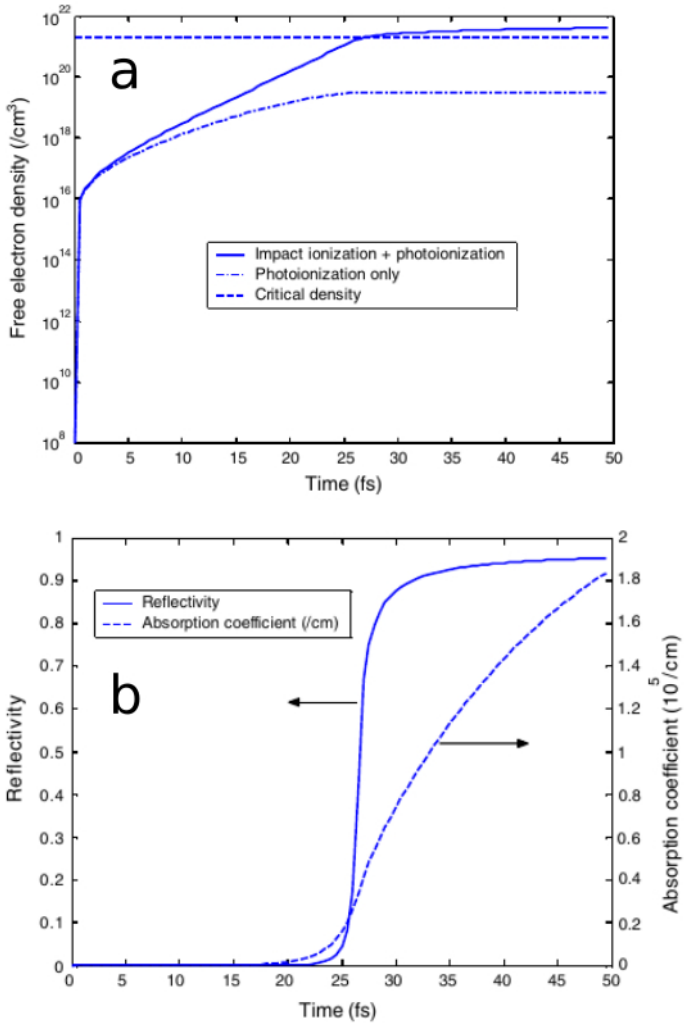

Figure 3.4.: Figures copied from [97]. The simulated material is fused silica (9 eV band gap, LIDT-fluence threshold of 3.15 J/cm^2). The laser-pulse properties are 780 nm wavelength, 50 fs FWHM-pulse duration and 5 J/cm^2 fluence. **(a)**: Electron-density evolution in the conduction band (solid line). **(b)**: Evolution of the reflectivity and the absorption coefficient.

$t = 60$ fs) and decreases afterwards by recombination (refer to $t = 160$ fs). The electron temperature T_e peaks at the position of the laser-peak intensity and quickly decreases behind the laser pulse.
At a laser intensity of $2 \cdot 10^{14}$ W/cm^2, which is above the threshold of LIB, the laser-propagation dynamics are more involved and presented in figure 3.5 (b). The laser increases the electron density until it surpasses the critical plasma density at the vacuum-solid interface (refer to $t = 40$ fs). An increased absorption of light is visible by comparing the laser light field at $t = 20$ fs and $t = 40$ fs. The leading edge of the pulse is reflected and transmitted, as in the case in figure 3.5 (a). Close to the regions where the electron density surpasses the critical density, the amplitude of the light field is strongly damped, which is visible especially in the falling flank of the transmitted laser pulse at $t = 60$ fs. Until the end of the simulation the electron density remains strongly peaked at the vacuum-solid interface and the remaining part of the transmitted light increases the electron density throughout the entire bulk. Note that up to the end of the simulation the effect of recombination is not directly visible due an ongoing strong absorption of the falling flank of the laser pulse and according to that, a significant excitation of electrons. However, an overshooting of the critical density is observed only on the vacuum-solid interface, which acts like a "plasma-shutter" and prevents light from entering the bulk. The evolution of the electron temperature is similar to figure (a).

In summary, LIB is characterized by an overshooting of the conduction-band electron density above

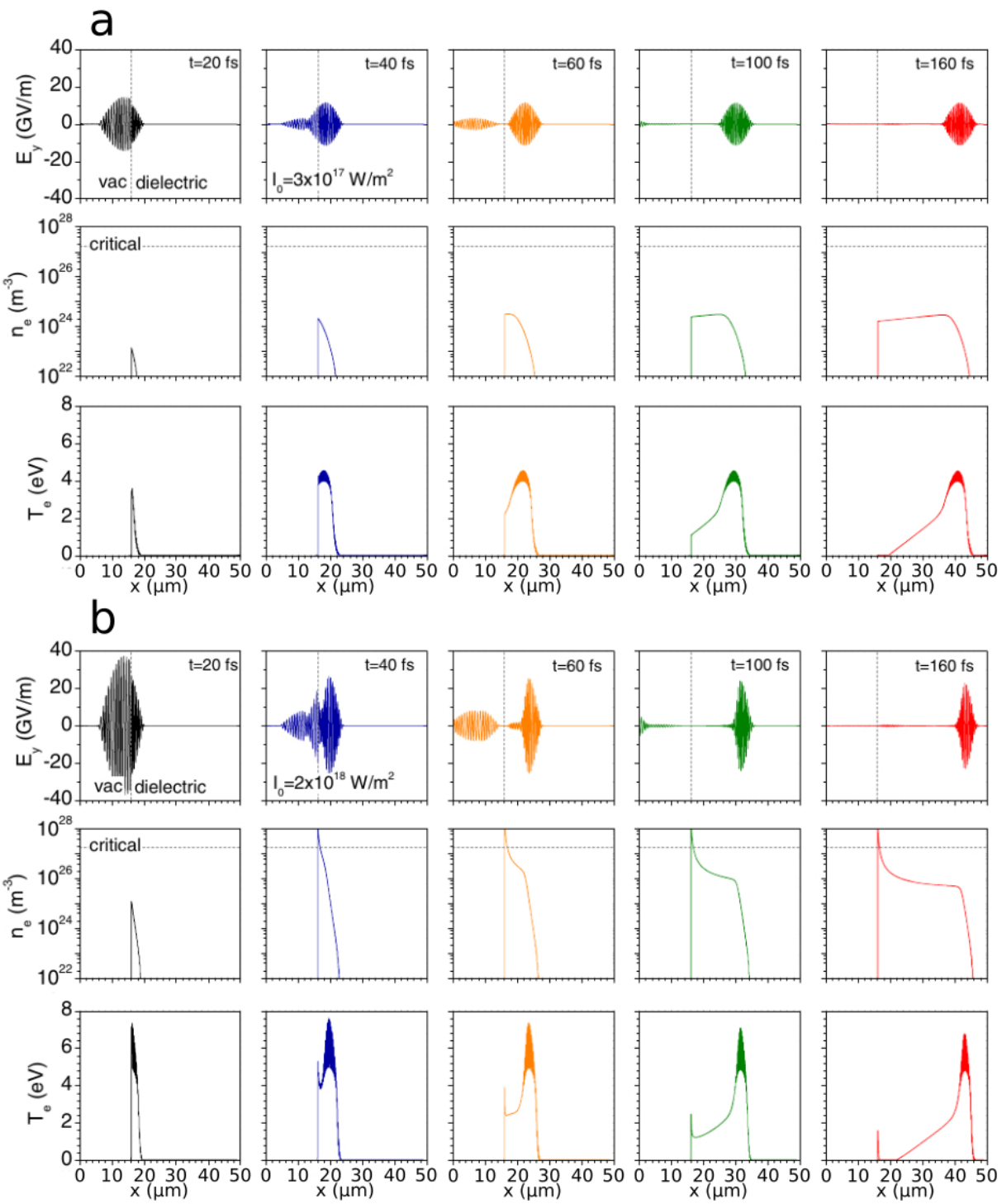

Figure 3.5.: Figures copied from [158]. The simulated material is fused silica (9 eV band gap) and the laser-pulse properties are 800 nm wavelength and 26.7 fs-FWHM pulse duration. The x axis of each graph corresponds to the laser-propagation direction. The first row of each figure shows the electric field E_y. The vacuum-solid interface is marked by the vertical dashed line. The second row shows the electron density in the conduction band n_e. The critical plasma density is marked by the horizontal dashed line. The third row shows the electron-temperature distribution T_e. **(a)** The laser-peak intensity is $3 \cdot 10^{13}\,\mathrm{W/cm^2}$, which is below the threshold of LIB. **(b)** The laser-peak intensity is $2 \cdot 10^{14}\,\mathrm{W/cm^2}$, which is above the threshold of LIB.

the critical plasma density of the pump-laser wavelength. For femtosecond pulses as well as for picosecond pulses, LIB is caused by strong-field ionization in combination with avalanche ionization.

LIB can be understood as a part of the process leading to LIDT. With respect to the time-resolved optical-shadowgraphy diagnostics that are used in this work, LIB occurs as blackened regions within the otherwise transparent dielectric target. As the change of reflectivity during LIB occurs rapidly with a step-like function, blackened regions correspond to regions with a conduction-band electron density that equals or is above the critical plasma density of the backlighter wavelength. Because of the variation of the absorption coefficient with electron density, the observation of different opacities is correlated to different electron densities in the conduction band.

3.1.2. Laser-pulse-duration dependence of LIB - A characterization study

The individual segments of the leading edge of a high-intensity pump laser can be characterized by their temporal slope. For high-intensity lasers with a pulse duration of a few tens of femtoseconds, such as the DRACO laser, the intensity within the *steep-rising edge* typically increases by an order of magnitude in less than 100 fs. The intensity in the *picosecond pedestal*, however, increases more slowly, by an order of magnitude in single to tens of picoseconds.
As the literature neither provides data of LIDT and LIB of the cryogenic hydrogen-jet target nor the relevant microscopic properties for simulating LIB, an experimental characterization study of the LIB thresholds of the cryogenic hydrogen-jet target using reduced laser-peak intensity and laser-pulse durations between 29 fs and 6.3 ps is conducted. Although none of the temporal envelopes of the utilized pulses exactly matches with individual segments of the leading edge, pulses with tens-to-hundreds-of-femtoseconds duration can approximate the steep-rising edge or singular prepulses. Pulses of multiple-picoseconds duration with a more super-Gaussian envelope can approximate the slowly rising picosecond pedestal.

3.1.2.1. Setup

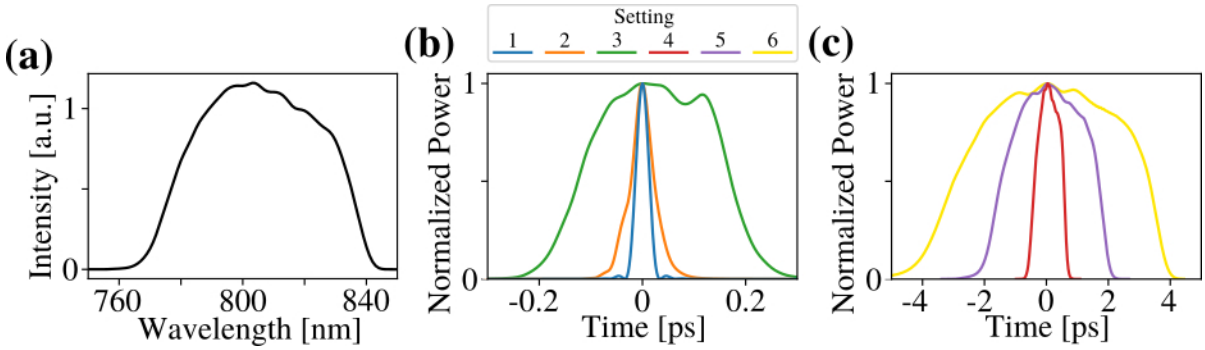

Figure 3.6.: Figure copied from Bernert et al. [23]. Pump-laser properties for the measurement of the pulse-duration dependence of LIB. **(a)** Spectrum, **(b)** temporal pulse envelope of the settings 1, 2, 3 and **(c)** of the settings 4, 5, 6 (refer to table 3.1).

The goal of the characterization study is the measurement of the threshold fluences F_{th} and threshold intensities I_{th} of LIB of the cryogenic hydrogen sheet-jet target for different laser-pulse durations. For this purpose, a dedicated pump-probe experiment is set up in the experimental chamber I1 as part of a master-thesis project, see Ref. [15]. The laser energy of the DRACO-150 TW beam is attenuated by about six orders of magnitude. The attenuation is achieved by multiple wedges and a reduction of the beam diameter by a circular aperture in front of the OAP. This generates an Airy-pattern focus with a 14 µm FWHM of the central disk on target. The residual pump-laser energy can be scanned between 10 % and 100 % via the rotation of a waveplate and pairs of thin-film polarizers in the beampath before compression. The temporal pulse characteristics of the pump laser are preserved during attenuation. Six different settings of pulse duration are realized by introducing defined chirp via an acousto-optic programmable dispersive filter (settings 1, 2, 3, 4) and an SF6 glass block (settings

5, 6) in the stretched beampath of the laser system. For all settings, the temporal pulse shape (figure 3.6 (b) and (c)) and the peak intensity are inferred from the measured laser spectrum (figure 3.6 (a)), the artificially introduced spectral phase, the laser energy and a measurement of the focal spot (refer to Appendix G). The peak fluence is calculated using the laser energy and the measurement of the focal spot only. For setting 1 (zero spectral phase), the pulse duration is verified by measurements with a *Wizzler* device by Fastlite. The different settings are summarized in table 3.1.
The repetition rate of the pump laser and the self-replenishing target delivery of the cryogenic hydrogen jet allow to generate laser-target interactions at a repetition rate of 1 Hz. Each interaction is visualized by time-resolved optical shadowgraphy with a 515 nm backlighter. The specific imaging properties of the setup are equivalent to the setup that is described in Appendix G. The probe delay is fixed to 1 ps after the falling flank of the pump pulse. Time-delay scans for different pulse-duration settings show that the influence of recombination is negligible at this delay.

Setting	GDD [fs^2]	TOD [fs^3]	τ[ps]	F_{th}[J/cm^2]	I_{th}[W/cm^2]
1	0	0	0.0285	3.4 ± 0.4	$(1.1 \pm 0.2) \cdot 10^{14}$
2	500	0	0.0445	4.1 ± 0.7	$(7.2 \pm 1.2) \cdot 10^{13}$
3	2000	0	0.296	5.4 ± 0.7	$(1.8 \pm 0.3) \cdot 10^{13}$
4	6000	0	0.954	8.3 ± 0.7	$(9.3 \pm 0.8) \cdot 10^{12}$
5	19 536	12 320	3.17	8.6 ± 1.9	$(2.9 \pm 0.6) \cdot 10^{12}$
6	38 612	24 290	6.33	14 ± 2	$(2.4 \pm 0.4) \cdot 10^{12}$

Table 3.1.: Measured threshold fluence F_{th} and threshold intensity I_{th} of LIB of the hydrogen sheet-jet target for the different settings of group-delay dispersion (GDD) and third-order dispersion (TOD). The FWHM of the laser-pulse duration τ is derived from the calculated pulse envelopes (figure 3.6 (b) and (c)).

3.1.2.2. Evaluation

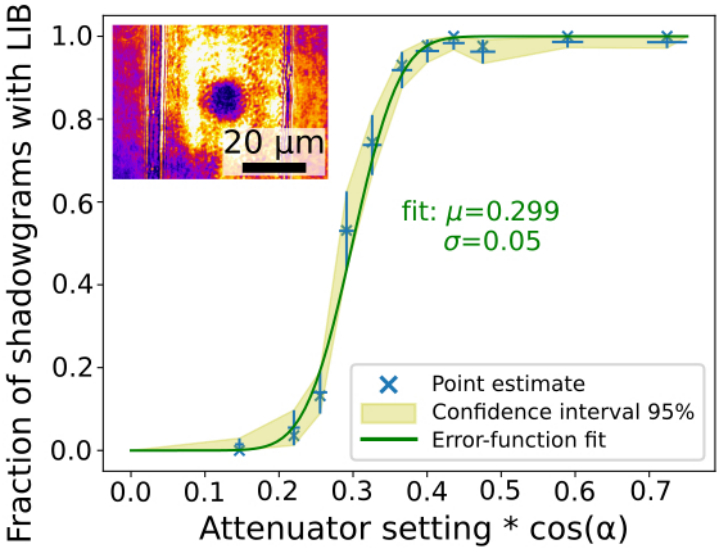

Figure 3.7.: Fluence scan of the pump laser (x-axis), which is given by to the waveplate-attenuator setting multiplied by the cosine of the target-rotation angle, versus the fraction of shadowgrams with LIB and the full number of captured shadowgrams (y-axis). The calculated confidence intervals are fitted by an error function (green line) that corresponds to the cumulative distribution function of a normal distribution with a mean value $\mu = 0.299$ and a standard deviation $\sigma = 0.05$. The inset shows an exemplary shadowgram with LIB occurring as blackened target region.

For each pulse-duration setting, the threshold intensity I_{th} and threshold fluence F_{th} are derived by a laser-energy scan. The transmission of the waveplate attenuator is reduced stepwise from 100 % down to 10 %. The pulse energy before the transmission attenuator is adjusted such that for the 100 % setting LIB is assured and it can be ruled out for the 10 % setting. Thousands of shots at 10 to 14 transmission-attenuator settings are acquired for each pulse-duration setting. A secondary optical-probing axis allows to sort the data by target-rotation angle. The approach allows to use hundreds of shots for a statistical evaluation of the laser-energy scan and with that enables an averaging over the fluctuation of the pump-laser peak power (refer to Appendix B). The resulting point estimates and 95 %-confidence intervals of setting 2 are shown in figure 3.7. Assuming an underlying normal distribution of fluctuations in the laser and target properties, the distribution function of the fraction of shots with LIB as a function of laser fluence is an error function (green line). The threshold of LIB is given by the laser energy at which the error function reaches 50 %, i.e., the mean μ of the underlying normal distribution. The standard deviation σ of the threshold value is given by the width of the error function. The resulting mean and standard deviation of I_{th} and F_{th} for all pulse-duration settings are given in table 3.1.

3.1.2.3. Results

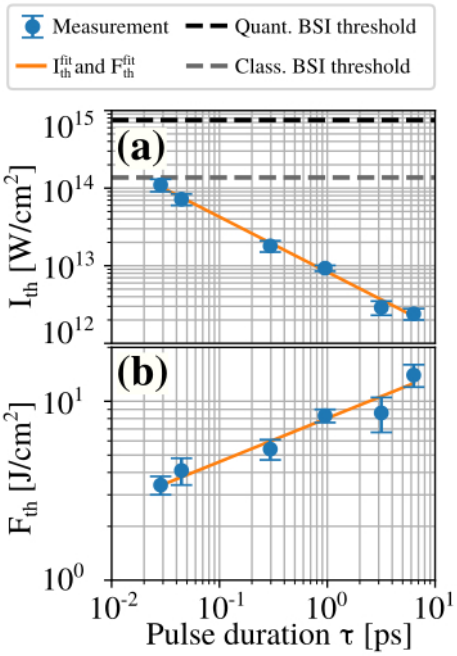

Figure 3.8.: Figure copied from Bernert et al. [23]. **(a)** Measured intensity thresholds I_{th} and **(b)** fluence thresholds F_{th} of LIB of the hydrogen sheet-jet target versus FWHM-laser-pulse duration τ (blue dots). The pump-laser settings of each measurement are given in table 3.1. A power-law fit to the data yields $I_{th}^{\text{fit}} \propto \tau^{-0.71 \pm 0.03}$ (orange line in figure (a), equation 3.3) and $F_{th}^{\text{fit}} \propto \tau^{0.24 \pm 0.02}$ (orange line in figure (b), equation 3.4). The quantum-mechanical BSI threshold (black) and the classical BSI threshold (gray) are given by dashed–horizontal lines in figure (a).

As the main result of the characterization study, the intensity and fluence thresholds of LIB, I_{th} and F_{th}, are presented in figure 3.8. I_{th} and F_{th} mark the thresholds at which a transiently blackened target area, i.e., an area undergoing LIB, is observed by using time-resolved optical shadowgraphy with a 515 nm backlighter. Thus, the measured thresholds compare particularly well with the time-resolved measurements at ultra-relativistic peak intensity in the next section. The thresholds show a high dependence on the FWHM-laser-pulse duration τ. Power-law fits to the thresholds of intensity I_{th} and fluence F_{th} (orange lines) yield the scalings

$$I_{th}^{\text{fit}}[\text{W/cm}^2] = (8.3 \pm 0.5) \cdot 10^{12} \times \tau[\text{ps}]^{-0.71 \pm 0.03} \tag{3.3}$$

and

$$F_{th}^{\mathrm{fit}}[\mathrm{J/cm^2}] = (8.0 \pm 0.4) \times \tau[\mathrm{ps}]^{0.24 \pm 0.02}. \tag{3.4}$$

To estimate the contribution of the different underlying ionization mechanisms, in the following the results are compared with the literature on LIDT of fused silica (FS), which is introduced in section 3.1.1. FS has a band gap of about 9 eV, which almost reaches that of solid hydrogen (~ 10.9 eV [94]). Recently, a dynamical rate-equation model was used to investigate the contribution of avalanche ionization and strong-field ionization to the scaling of the damage fluence of fused silica $F_{th}^{\mathrm{FS}}[\tau]$ for pulse durations between 10 fs and 4 ps, see Ref. [51]. Their results in figure 3.3 (b) show that strong-field ionization alone yields a too strong pulse-duration scaling of LIDT ($\propto \tau^{0.73}$) and that the inclusion of avalanche ionization is required to support a scaling that fits the experimental data ($\propto \tau^{0.30}$). They conclude that the entire avalanche sequence (laser heating of conduction-band electrons and collisional ionization) is important for the explanation of breakdown not only at pulse durations in the picosecond regime (e.g. see fig. 3.3 (a) from [190]) but even at pulse durations shorter than 100 fs. The findings are supported by earlier work at pulse durations between 7 fs and 300 fs, where it is concluded that avalanche ionization is predominant at pulse durations $\gtrsim 50$ fs and increases in relevance with pulse duration [40].
The pulse duration scaling of fused silica $F_{th}^{\mathrm{FS}} \propto \tau^{0.30}$ is similarly weak as the scaling we find for LIB of solid hydrogen $F_{th}^{\mathrm{fit}} \propto \tau^{0.24}$. From this and taking into account the comparable band gap, we derive that LIB of solid hydrogen in the presented pulse-duration regime is also caused by strong contributions of avalanche ionization, similar to fused silica. More quantitative conclusions would require detailed numerical modeling, which is, however, not needed for the subsequent analysis.

For the laser parameters used in this study, the BSI threshold can serve as an upper estimate of possible threshold intensities of LIB. The appearance intensity of atomic hydrogen $I_{app}^{H} = 1.37 \cdot 10^{14}\,\mathrm{W/cm^2}$ ("classical BSI threshold") is shown as gray-dashed line in figure 3.8 (a). However, a non-simplified quantum-mechanical treatment of the hydrogen atom yields a higher critical field of barrier suppression ionization and a corresponding appearance intensity of $7.58 \cdot 10^{14}\,\mathrm{W/cm^2}$ ("quantum-mechanical BSI threshold", black-dashed line in figure 3.8 (a)) [19].

3.2. Experimental results at ultra-relativistic laser-peak intensities

To test the relevance of the pulse-duration dependence of I_{th} and F_{th} to the starting point of LIB in high-intensity laser-solid interactions, this section experimentally investigates the occurence of LIB in experiments of the PM-cleaned DRACO-PW laser and the hydrogen sheet-jet target. The results are published in Bernert et al. [23]. The details of the experimental setup are introduced in section 2.2.4 and an illustrative sketch of the setup is given in figure 3.9 (a). The FWHM-pulse duration of the pump laser is 30 fs and the laser-peak intensity of $5.7 \cdot 10^{21}\,\mathrm{W/cm^2}$ can be tuned between 10 % and 100 % by changing the amplification of the final laser amplifier. The laser contrast is $> 10^{-8}$ at -2 ps, $> 10^{-10}$ at -10 ps and a singular prepulse with 10^{-9} occurs at -54 ps (see section 2.2.3). Details about the hydrogen sheet-jet target are given in section 2.2.2. The total width of the jet in this experiment is 60 µm. As sketched in figure 3.9 (a), the planar sheet-like part with a thickness of approximately 400 nm is formed between two prominent cylindrical rims. The experiment is conducted at target-rotation angles between 65° and 80° (target normal to pump-laser-propagation axis) and the probe 515 nm propagates at 134° relative to the pump-laser axis (see top-view inset in figure 3.9 (a)). Probe 1030 nm at 69° guarantees control over the target-rotation angle for each shot. The observable general structures in the recorded shadowgraphy images are illustrated in the inset of figure 3.9 (a). A pump-probe delay of 0 ps corresponds to the arrival of the pump-laser peak on target and negative delays represent earlier times.
Figure 3.9 (b) shows the typical temporal properties of the leading edge of the pump laser. The *peak* is preceded by a *steep-rising edge* and a more shallow *picosecond pedestal*.

For four different peak intensities of the pump-laser, time-delay scans of shadowgraphy are shown in figure 3.10. Each setting shows shadowgrams without and with blackened target areas, i.e., areas

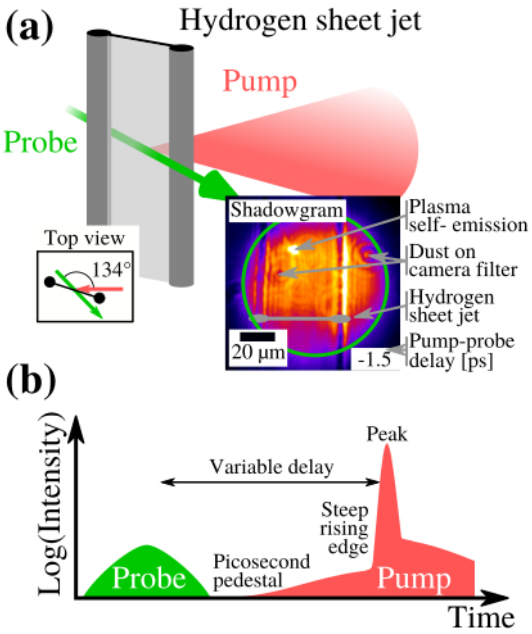

Figure 3.9.: Figure copied from Bernert et al. [23]. **(a)** Experimental setup (not to scale): High-intensity pump laser is focused onto the hydrogen sheet-jet target. Optical probe pulses enable time-resolved shadowgraphy. **(b)** Temporal schematic of the setup, with the probe-laser pulse preceding the pump-laser pulse. The specific characteristics of the leading edge of the high-intensity pump laser are explicitly labeled.

where the target experiences dielectric breakdown. The pump-probe-delay intervals within which LIB occurs (*onset interval of LIB*) are given in table 3.2. The upper boundary of the interval is given by the delay of the earliest shadowgram with an area of dielectric breakdown and the lower boundary is given by the closest delay of a shadowgram without such observation. Note that the width of the onset interval is mainly limited by the available number of shadowgrams and their respective pump-probe delay. As illustrated by the green line and gray-shaded background in figure 3.10, we observe a clear shift of the onset interval of LIB to earlier pump-probe delays with increasing peak intensity.
Depending on the intensity setting and the pump-probe delay, the areas with dielectric breakdown have different contours and patterns. Generally, with increasing delay the spatial extent of the area grows until it fills the whole field of view (FOV = 100 µm × 100 µm) close to zero delay. Up to a delay of about −0.4 ps, the areas with dielectric breakdown show sharp contours with larger width than height, exemplified by the shadowgam labeled "α". For this and similar shadowgrams, the contour represents the spatial distribution of light with intensities exceeding the threshold of LIB during the leading edge [87]. The aspect ratio of width and height of the area resembles the projected shape of the focal spot on the rotated target to the time of the pump-probe delay. Further details are discussed in section 3.3.2.
For pump-probe delays between −0.4 ps and zero, an additional large-scale contour with spatially varying opacity is observed (e.g. shadowgram labeled "β"). The additional contour is most likely caused by relativistic electrons that are generated when the pump-laser intensity surpasses $\sim 10^{18}\,\mathrm{W/cm^2}$ [107]. For the peak intensities and laser-contrast settings discussed here, this occurs a few hundred femtoseconds before the pump-laser peak reaches the target [211]. Section 3.5 discusses the observation in more detail.

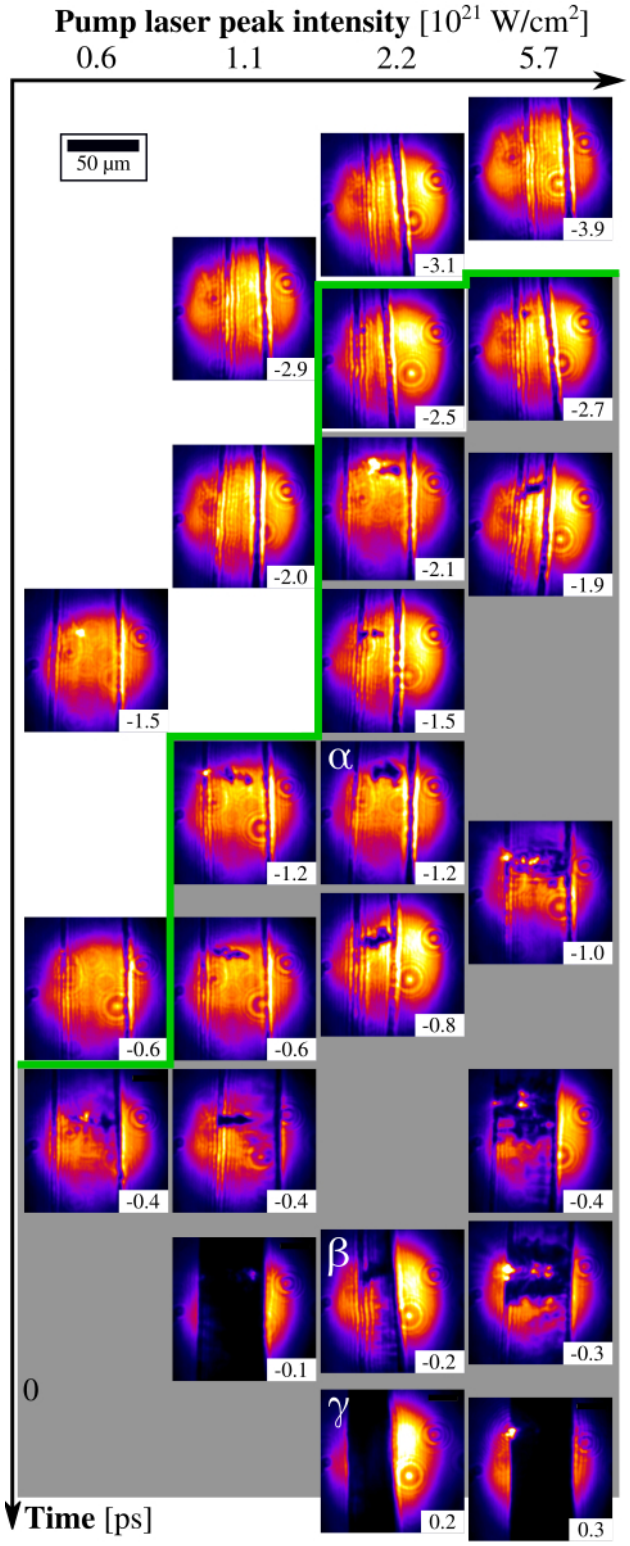

Figure 3.10.: Figure copied from Bernert et al. [23]. Shadowgraphy images (consistent colorscale) captured at different pump-probe delays and pump-laser-peak intensities. Shadowgrams without dielectric breakdown (white background) are separated from shadowgrams with dielectric breakdown (gray background) by the green line.

Peak intensity [W/cm^2]	Onset interval [ps]
$0.6 \cdot 10^{21}$	$[-0.6, -0.4]$
$1.1 \cdot 10^{21}$	$[-2.0, -1.2]$
$2.2 \cdot 10^{21}$	$[-3.1, -2.5]$
$5.7 \cdot 10^{21}$	$[-3.9, -2.7]$

Table 3.2.: Measured onset intervals of LIB versus pump-laser-peak intensity as adopted from figure 3.10. The pump-laser-pulse duration is 30 fs FWHM.

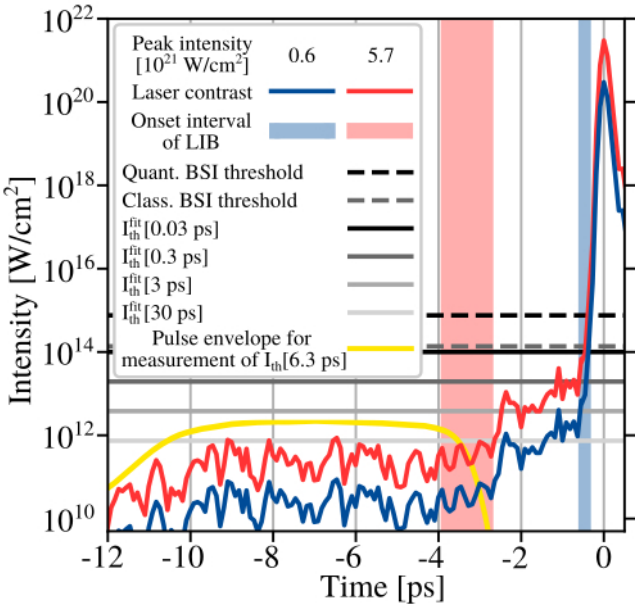

Figure 3.11.: Figure copied from Bernert et al. [23]. Laser-contrast measurement of the leading edge normalized to the highest (red) and the lowest (blue) peak intensity on target versus the respective onset interval of LIB. The quantum-mechanical and classical BSI thresholds are given together with the fitted intensity thresholds of LIB $I_{th}^{\mathrm{fit}}[\tau]$ for four different pulse durations τ (horizontal lines). The yellow line gives the temporal envelope of the laser pulse utilized for the measurement of $I_{th}[6.3\,\mathrm{ps}]$. The temporal position is chosen for comparability with the laser contrast in the highest peak-intensity setting.

3.3. Comparison to the laser contrast

3.3.1. Relevance of the pulse-duration dependence of LIB

3.3.1.1. Onset interval versus threshold intensity

The comparison of the measured onset intervals of LIB (table 3.2) to the laser-contrast measurement of the leading edge is presented in figure 3.11. The laser contrast of the highest ($5.7 \cdot 10^{21}\,\mathrm{W/cm^2}$) and the lowest peak-intensity setting ($0.6 \cdot 10^{21}\,\mathrm{W/cm^2}$) is given in red and blue color, respectively. Details about the measurement of the laser contrast are given in section 2.2.3. Taking the mean target-rotation angle into account, the laser contrast is scaled to the respective peak intensity of each setting. The steep-rising edge is visible between -0.4 ps and zero, while the actual temporal shape is smeared out by the temporal resolution of the measurement (~ 100 fs). The more slowly rising picosecond pedestal is shown between -12 ps and about -1 ps. The relative intensities of the measurement are commonly used to compare different high-power laser systems [49].
For the highest peak-intensity setting, the measured onset interval of LIB (red shaded) lies within the picosecond pedestal. Between about -10 ps and about -3 ps the picosecond pedestal includes a plateau with intensities fluctuating from about $10^{11}\,\mathrm{W/cm^2}$ to about $10^{12}\,\mathrm{W/cm^2}$. The onset interval of LIB is located at the end of the plateau and no standout signature of intensity is observed during the interval. In particular, the prepulse at ~ -2.3 ps is well separated from the observation of LIB

at $-2.7\,\mathrm{ps}$. For the lowest peak-intensity setting, the measured onset interval of LIB (blue shaded) is located within the foot of the steep-rising edge.
To discuss both settings along with the results of the characterization study of LIB (section 3.1.2), the quantum-mechanical and classical BSI threshold and the values of $I_{th}^{\mathrm{fit}}[\tau]$ for different pulse durations τ between 0.03 ps and 30 ps are given as horizontal lines of different style.
In the lowest peak-intensity setting, the intersection points of the laser contrast with the quantum-mechanical BSI threshold, the classical BSI threshold, the threshold intensity $I_{th}^{\mathrm{fit}}[0.03\,\mathrm{ps}]$ and $I_{th}^{\mathrm{fit}}[0.3\,\mathrm{ps}]$ are all located close to each other between $-0.32\,\mathrm{ps}$ (quantum-mechanical BSI threshold) and $-0.43\,\mathrm{ps}$ ($I_{th}^{\mathrm{fit}}[0.3\,\mathrm{ps}]$). Within the errorbars, the whole cluster of intersection points is in agreement with the experimental observation and the intensities of the laser contrast suggest a minimum applicable threshold intensity of $4 \cdot 10^{12}\,\mathrm{W/cm^2} = I_{th}^{\mathrm{fit}}[2.8\,\mathrm{ps}]$. The agreement between the shadowgraphy measurement and the intersection point of the laser contrast with the classical BSI threshold demonstrates that the appearance intensity I_{app} can be a convenient estimate to determine the starting point of LIB in interactions with similar target properties and similar or lower absolute intensities of the leading edge. This changes as the peak intensity is increased by a factor of ten to $5.7 \cdot 10^{21}\,\mathrm{W/cm^2}$. For the corresponding leading edge, the intersection of the laser contrast with the classical BSI threshold at $-0.44\,\mathrm{ps}$ overestimates the starting point of LIB substantially. The same applies to the intersection with the threshold intensities $I_{th}^{\mathrm{fit}}[0.3\,\mathrm{ps}]$ at $-1.14\,\mathrm{ps}$ and $I_{th}^{\mathrm{fit}}[3\,\mathrm{ps}]$ at $-2.48\,\mathrm{ps}$. The observation reveals that for this setting the simple BSI threshold cannot be used as a criterion for estimating the starting point of LIB based on the laser-contrast measurement. Instead, the setting demonstrates that LIB is reached by accumulation of intensity on target and not by crossing a specific intensity level. In the plateau of the picosecond pedestal between $-10\,\mathrm{ps}$ and $-3\,\mathrm{ps}$, the intensities are close to the thresholds of LIB for picosecond pulses. Comparing $-10\,\mathrm{ps}$ and $-3\,\mathrm{ps}$, there is no significant difference in the intensity level, except for the amount of temporally "accumulated intensity", which corresponds to the fluence. As argued in section 3.1.2, the contribution of avalanche ionization to LIB of the target increases with pulse duration. It follows that the described scenario is most likely an illustrative example for which avalanche ionization during the picosecond pedestal of the leading edge contributes to LIB.

3.3.1.2. Quantitative comparison to the characterization study

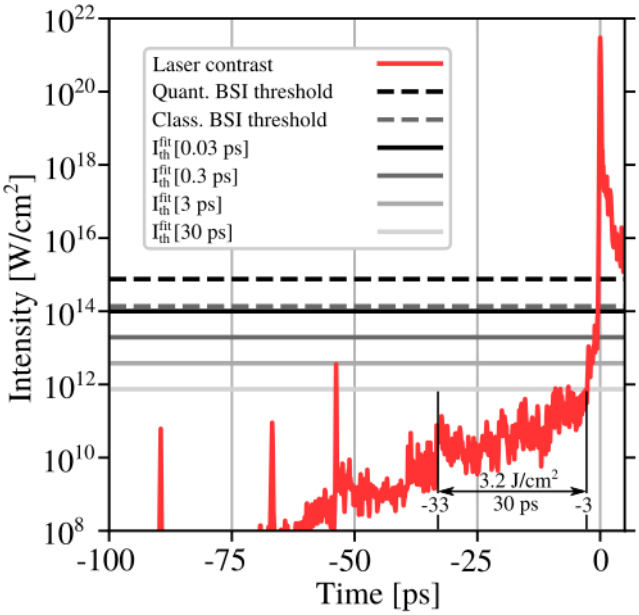

Figure 3.12.: Figure copied from Bernert et al. [23]. Leading edge of the pump laser (laser contrast) in the highest peak-intensity setting (red line). The quantum-mechanical and classical BSI thresholds are given together with the fitted intensity thresholds of LIB $I_{th}^{\mathrm{fit}}[\tau]$ for four different pulse durations τ (horizontal lines).

To quantitatively compare the results at $5.7 \cdot 10^{21}\,\mathrm{W/cm^2}$ peak intensity with the characterization study of LIB (section 3.1.2), the temporal pulse envelope of a 6.3 ps pulse as used in the characterization study is plotted by a yellow line in figure 3.11. For illustration purposes, the pulse is placed before the measured onset of LIB. The peak intensity of the pulse is scaled to $I_{th}[6.3\,\mathrm{ps}] = (2.4 \pm 0.4) \cdot 10^{12}\,\mathrm{W/cm^2}$, ensuring that a similar pulse induces LIB of the target *after* interaction. The area under the curve corresponds to the threshold fluence $F_{th}[6.3\,\mathrm{ps}] = (14 \pm 2)\,\mathrm{J/cm^2}$. An integration of the laser-contrast measurement between -12 ps and -3 ps yields a fluence of $2.2\,\mathrm{J/cm^2}$ with a highest intensity of $9 \cdot 10^{11}\,\mathrm{W/cm^2}$. It follows that the fluence of the laser-contrast measurement is a factor of six and the maximum intensity is a factor of three lower than the measured thresholds of the 6.3 ps pulse.
To also consider contributions of the leading edge earlier than -12 ps, a larger window of the laser contrast is displayed in figure 3.12. The graph shows a prepulse with a peak intensity of $3.6 \cdot 10^{12}\,\mathrm{W/cm^2}$ at -54 ps delay. The pulse duration of the prepulse is limited by the temporal resolution of the TOAC measurement to $\tau < 100$ fs. The intensity threshold of LIB of a 100 fs pulse is $I_{th}^{\mathrm{fit}}[100\,\mathrm{fs}] = 4.3 \cdot 10^{13}\,\mathrm{W/cm^2}$ and shorter pulses feature a higher threshold intensity. Even assuming an uncertainty of one order of magnitude for the intensity level of the laser contrast, the prepulse is insufficient to initiate LIB, in agreement with the time-resolved optical-shadowgraphy measurements. Furthermore, temporal integration of the laser contrast between -33 ps and -3 ps yields a fluence of $3.2\,\mathrm{J/cm^2}$ (figure 3.12). This is about a factor of six lower than the fitted damage fluence $F_{th}^{\mathrm{fit}}[30\,\mathrm{ps}] = 18.1\,\mathrm{J/cm^2}$, similar to the case of the plateau between -10 ps and -3 ps. However, this implies that the picosecond pedestal between -33 ps and -12 ps contains only $1\,\mathrm{J/cm^2}$, which is more than a factor of 16 below the fluence threshold $F_{th}^{\mathrm{fit}}[21\,\mathrm{ps}] = 16.6\,\mathrm{J/cm^2}$. The observation of LIB in the highest peak-intensity setting is thus most likely caused by accumulation of intensity around $I_{th}[6.3\,\mathrm{ps}]$ during the plateau of the picosecond pedestal between -10 ps and -3 ps, although the absolute intensities of the laser contrast are slightly below the characterized threshold $I_{th}[6.3\,\mathrm{ps}]$.

3.3.1.3. Discussion

The scaling of laser-contrast measurements to absolute intensity, however, has to be considered with caution. In principle, the pulse shape in the focal spot where the plasma dynamics are induced could be different from the laser-pulse characteristics measured from the non-focused laser beam, e.g., due to spatio-temporal couplings [96]. In view of this, the presented comparison to the characterization study shows surprisingly good agreement. The comparison demonstrates the methodology of how the starting point of LIB can be derived from a laser-contrast measurement. The starting point of LIB is not triggered by the first intersection with a specific threshold intensity, but by a continuous temporal accumulation of intensity at a specific level for a specific duration. If the accumulated intensity, i.e., the deposited fluence, reaches the threshold fluence $F_{th}[\tau]$ of a comparable pulse duration τ within an order of magnitude, the subsequent onset of LIB must be expected. To exemplify this methodology, a demonstration example with the intrinsic laser contrast of DRACO PW is presented in section 3.4. Furthermore, the comparison between the lowest and the highest peak-intensity setting demonstrates the relevance of the pulse-duration dependence of LIB to the starting point of LIB in ultra-relativistic laser-solid interactions. As laser-peak intensity increases, the intensities in the leading edge also increase. The simplified assumption of a fixed intensity threshold of LIB, for example the classical BSI threshold, would shift the starting point of LIB only slightly to earlier times, depending on the leading-edge intensity evolution. However, if the slowly rising picosecond pedestal enters the relevant intensity range of LIB, the starting point of LIB is actually shifted to earlier times by a lowering of the applicable threshold intensity. Figure 3.8 (a) shows that the relevant intensity range varies significantly with pulse duration, i.e., pedestal duration.

3.3.1.4. Requirements for future laser metrology

An important prerequisite of the described analysis is a temporally well-resolved and quantitatively valid laser-contrast measurement. To capture the strong-field-ionization effects, single-femtosecond

temporal resolution is desired, especially for short pre-pulses. The picosecond-pedestal-induced avalanche ionization imposes the measurement of intensities lower than $\sim 10^{11}\,\mathrm{W/cm^2}$, which is a required dynamic range higher than 10^{11} for current Petawatt-class laser systems. Considering the intrinsic leading edge of these laser systems without any temporal-contrast cleaning, a time window of at least 100 ps is needed.
Several commercial products based on third-order autocorrelation are available and the development is progressing towards higher dynamic range [179] and operation at single shot [123, 122]. However, an exploration of the limitations of existing technology is desired [27] and the design of additional techniques like self-referenced spectral interferometry with extended time excursion (SRSI-ETE) [147, 148] is promising to reliably quantify absolute intensity levels in the leading edge that are highly relevant to LIB, target pre-expansion and pre-heating in high-intensity laser-solid experiments.

3.3.2. LIB as a diagnostic tool

Recently, a technique for temporal and spatial intensity characterization of high-intensity laser pulses via time-resolved optical probing was proposed and termed *temporally resolved intensity contouring (TRIC)*, see Ref. [87]. The appeal of the technique lies in the characterization of the laser properties in the final focal spot, i.e., directly on target. The authors of Ref. [87] present optical-shadowgraphy data captured at pump-laser-peak intensities of up to $\sim 10^{19}\,\mathrm{W/cm^2}$. They compare the evaluation of the data via TRIC to conventional methods of spatial and temporal laser characterization. In the following, TRIC is applied to the here presented optical shadowgraphy data at two orders of magnitude higher pump-laser-peak intensity. In the first subsection, the technique is used to characterize the temporal laser contrast and in the second subsection it is used to derive the spatial distribution of laser intensity in the final focal plane. Furthermore, the first subsection includes a discussion of the hurdles that the laser-pulse-duration dependency of LIB imposes to the implemetation of TRIC.

3.3.2.1. Characterization of the laser contrast

TRIC uses the target's threshold of LIB I_{th} to sample the spatio-temporal laser-intensity distribution in the focal spot. The appoach of the technique is as follows. Considering the temporal evolution of the laser-target interaction during the leading edge of a high-power laser, the optical shadowgraphy diagnostic shows first LIB at a delay when the spatial peak of the pump laser surpasses I_{th}. Subsequently, the target area with LIB increases with the rate of the increasing intensity in the leading edge, because a larger spatial extend of the pump-laser focal spot grows above I_{th}. For rotated targets and circular focal spots, the shape of the area with LIB appears stretched, according to the projection of the focal spot.
Following TRIC, a scan of the pump-laser-peak intensity can be used to sample the leading edge of a high-power laser in a discrete way. By assuming a roughly constant I_{th}, the temporal starting point of LIB of a specific peak-intensity setting samples the laser contrast at the very same point in time. For a slighly decreased or increased peak intensity, the leading edge is decreased or increased accordingly. Consequently, the temporal starting point of LIB shifts. Considering many sampling points, the whole leading edge of the laser can be scanned. For each starting point of LIB, the corresponding intensity of the laser contrast is given by I_{th} times the ratio between the set and the full peak intensity.
However, as shown and discussed in section 3.1.2, I_{th} can not be assumed to be roughly constant. For an unknown intensity distribution of the leading edge, it is not clear which $I_{th}[\tau]$ is relevant to the optically diagnosed starting point of LIB. Section 3.3.1 proves that, for well-controlled laser-contrast conditions of a Petawatt-class laser system, a change of the applicable threshold intensity I_{th} occurs by changing the laser-peak intensity by only a factor of ten. It follows that, for an unknown leading edge, the characterization of the leading edge via TRIC cannot be performed without further assumptions. Assuming that the leading edge includes intensities that are relevant to LIB only in the last 30 ps before the laser peak, the interval of possible threshold intensities is between $I_{th}^{\mathrm{fit}}[30\,\mathrm{ps}] = 7.4 \cdot 10^{11}\,\mathrm{W/cm^2}$ and $I_{th}^{\mathrm{fit}}[30\,\mathrm{fs}] = 1.0 \cdot 10^{14}\,\mathrm{W/cm^2}$. Figure 3.13 (a) shows the laser contrast of the pump laser (red line) together with the interval between $I_{th}^{\mathrm{fit}}[30\,\mathrm{ps}]$ and $I_{th}^{\mathrm{fit}}[30\,\mathrm{fs}]$ (gray-shaded). The interval is slightly shifted to lower contrast levels according to the mean rotation angle of the target. In the highest peak-

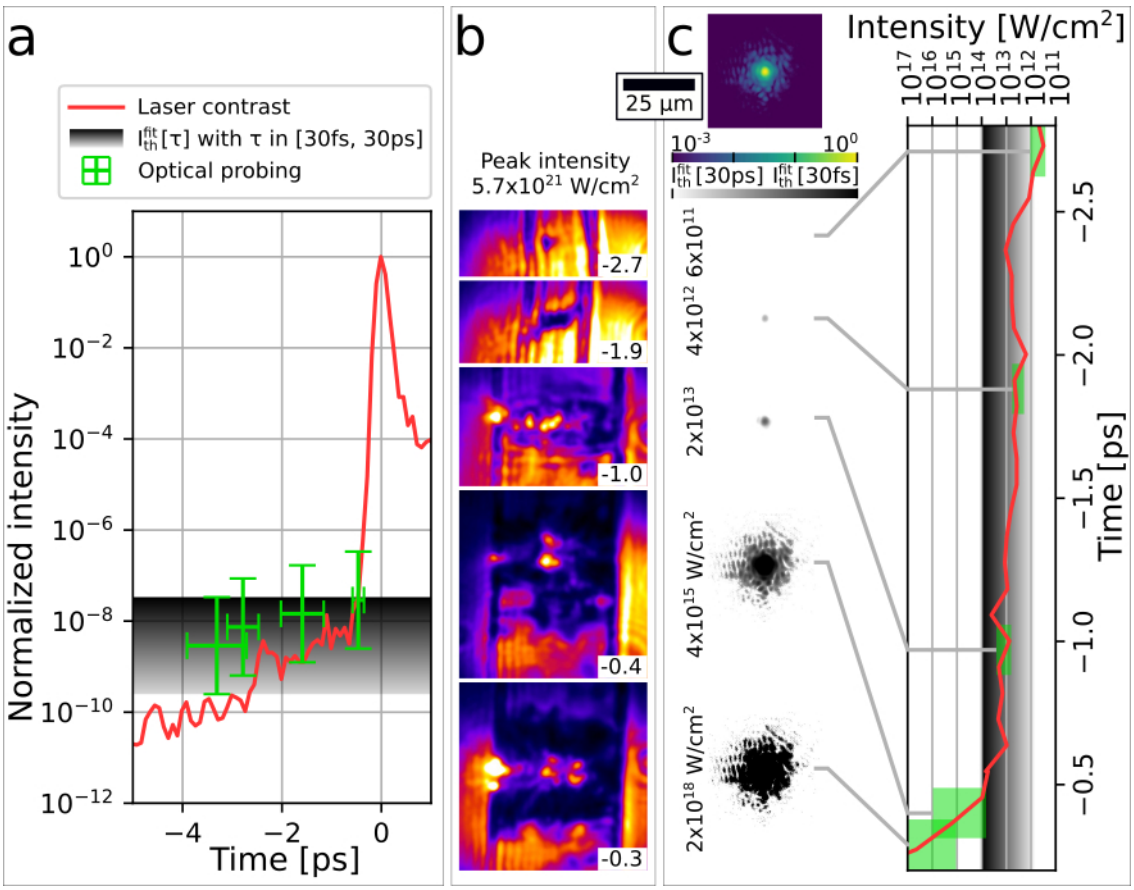

Figure 3.13.: *Temporally resolved intensity contouring (TRIC)*: **(a)** Temporal aspect of TRIC: Laser contrast (red curve) and range of possible threshold intensities of LIB $I_{th}^{\mathbf{fit}}[\tau]$ with τ in the interval between 30 fs and 30 ps (gray-shaded area). By utilizing the measured onset interval of LIB (table 3.2)for different pump-laser-peak intensities, the TRIC methodology suggests discrete measurements of the laser contrast (green markers, for details see text). **(b)** Close-ups of shadowgrams as copied from figure 3.10 for a peak intensity of $5.7 \cdot 10^{21}\,\mathrm{W/cm^2}$. The pump-probe delay is given in the lower-right corner of each image. **(c)** Spatial aspect of TRIC: The image on the top shows a measurement of the focal spot in logarithmic colorscale. The graph on the right side shows a detail of the laser contrast as adopted from figure 3.11 for a peak intensity of $5.7 \cdot 10^{21}\,\mathrm{W/cm^2}$. For each pump-probe delay in figure (b), the peak of the focal-spot measurement is scaled to the mean intensity of the laser contrast within the green interval and displayed in gray colorscale next to the corresponding shadowgram (for details see text). The logarithmic colorscale is restricted to intensities between $I_{th}^{\mathrm{fit}}[30\,\mathrm{ps}] = 7.4 \cdot 10^{11}\,\mathrm{W/cm^2}$ and $I_{th}^{\mathrm{fit}}[30\,\mathrm{fs}] = 1.0 \cdot 10^{14}\,\mathrm{W/cm^2}$.

intensity setting and as measured by optical shadowgraphy, the starting point of LIB occurs between −3.9 ps and −2.7 ps pump-probe delay. According to TRIC, this corresponds to a measurement of the laser contrast as given by the left-most green marker. The horizontal errorbar is given by the measured onset interval of LIB (table 3.2) and the vertical error bar is given by the possible variation of I_{th}. Each of the lower peak-intensity settings gives another green marker by the respective onset interval and the range of possible I_{th} multiplied by the ratio between the highest intensity ($5.7 \cdot 10^{21}\,\mathrm{W/cm^2}$) and the set intensity (5.7, 2.2, 1.1 and $0.6 \cdot 10^{21}\,\mathrm{W/cm^2}$).

Although the laser contrast in figure 3.13 (a) and the green markers derived by TRIC seem to agree quite well, another argument suggests that this is more or less a coincidence. As discussed in section 3.3.1 for the peak-intensity setting of $5.7 \cdot 10^{21}\,\mathrm{W/cm^2}$, LIB of the target is caused by the accumulation of intensity on target, specifically by the plateau of intensity in the leading edge between

$-10\,\mathrm{ps}$ and $-3\,\mathrm{ps}$. According to this, the left-most green marker in figure 3.13 (a) can actually not be placed between $-3.9\,\mathrm{ps}$ and $-2.7\,\mathrm{ps}$, i.e., at the measured starting point of LIB. The corresponding $I_{th} \approx I_{th}[6.3\,\mathrm{ps}]$ would rather need to be distributed between $-10\,\mathrm{ps}$ and $-3\,\mathrm{ps}$. With this, however, TRIC implies a fallacy. Considering an unknown leading edge, the observation of the starting point of LIB neither allows to attribute a specific value of I_{th} nor to specify the temporal window of how long this intensity impacts the target. The only information the starting point of LIB provides is that LIB *is* initiated at the specific delay.

The reason for the agreement of the results of TRIC with a measurement of the laser contrast by a third-order autocorrelator in figure 4 of Ref. [87] may be given by the fact that, in this case, the leading edge is sampled only during the steep-rising edge, i.e., the leading edge features a rather constant slope. As soon as changes in the slope of the leading edge occur, e.g., by the picosecond pedestal, the results in section 3.3.1 demonstrate that it becomes challenging to quantitatively characterize the leading edge via TRIC.

3.3.2.2. The spatial distribution of light in the final focus

The following paragraph discusses the spatial aspect of TRIC. Despite simplified assumptions of the TRIC methodology about I_{th}, the basic consideration that the target areas with dielectric breakdown show properties of the pump-laser focal spot is confirmed by the here presented investigations. Figure 3.13 (b) shows close-ups of shadowgrams that are captured in the highest peak-intensity setting ($5.7 \cdot 10^{21}\,\mathrm{W/cm^2}$). The spatial extend of the area with dielectric breakdown grows for delays that are closer to the pump-laser peak. To compare the experimental observation with theoretically expected patterns following the TRIC methodology, figure 3.13 (c) shows a measurement of the focal spot (top-most image, logarithmic colorscale) and a detail of the laser contrast as adopted from figure 3.11 for the highest peak-intensity setting (red graph on the right side). In the simplest case, the spatial light distribution of the focal spot at different delays can be estimated by scaling the peak of the time-integrated focal-spot measurement to the intensity of the laser contrast at the respective delay. For each pump-probe delay and to take the finite temporal resolution of the time-delay scan by shadowgraphy into account, the specific peak intensity is calculated by averaging the laser contrast over 175 fs (green boxes in the graph). The resulting value is given in each row on the left side of figure 3.13 (c). The measurement of the focal spot, scaled to the respective peak intensity, is given as a grayish pattern in each row. The gray colorscale shows intensities between $I_{th}^{\mathrm{fit}}[30\,\mathrm{ps}] = 7.4 \cdot 10^{11}\,\mathrm{W/cm^2}$ and $I_{th}^{\mathrm{fit}}[30\,\mathrm{fs}] = 1.0 \cdot 10^{14}\,\mathrm{W/cm^2}$ on a logarithmic scale. The images show the blackened target pattern that are expected following the TRIC methodology (*synthetic TRIC patterns*). For the synthetic pattern at $-0.3\,\mathrm{ps}$ delay, the dynamic range of the focal-spot measurement is not sufficient to show intensities down to $I_{th}^{\mathrm{fit}}[30\,\mathrm{ps}]$. As the target-rotation angle is not considered for the synthetic TRIC patterns, only the vertical extend of each pattern can be compared to the respective shadowgram in figure 3.13 (b).
The comparison of the experimental and the synthetic TRIC patterns in figures 3.13 (b) and (c) directly shows that the synthetic TRIC patterns are smaller than the pattern in the shadowgraphy measurement. This indicates that the laser-contrast measurement underestimates the intensities of the actual leading edge, which is in agreement to the quantitative comparison in section 3.3.1. At $-1.0\,\mathrm{ps}$ delay, the measured shadowgram in figure 3.13 (b) shows concentric rings at the rim of the blackened target area. The rings are not visible in the focal spot measurement (top-most image in figure 3.13 (c)), but their existence is plausible by considering the finite aperture of optical components in the laser beamline or reflexions in lenses that subsequently propagate with a different collimation than the main beam and are consequently out-of-focus in the nominal focal plane. Small amounts of light with sharply contoured near-field profiles are sufficient to cause Airy-patterns in the focal plane that could be associated to the observed ring structures. It follows that the shadowgram enables the visualization of light that is not visible in a simple camera image of the focal spot. This underlines the capability of TRIC to provide qualitative information on the spatial distribution of light in the focal spot. Another application of this aspect is given in the next paragraph.
The shadowgrams at $-0.4\,\mathrm{ps}$ and $-0.3\,\mathrm{ps}$ delay show larger areas of dielectric breakdown with different

contours than what would be expected from the more confined synthetic TRIC patterns. These shadowgrams correspond to the laser-intensity regime for which the applicability of TRIC ends. Here, the origin of local dielectric breakdown is not given by the fluence or intensity of the local light distribution only, but rather by the presence of relativistic electrons. To the time the leading-edge intensities become relativistic ($\sim 10^{18}\,\mathrm{W/cm^2}$), the mean free-path length of the generated hot electrons can exceed the spatially confined blackened patterns that are caused by TRIC. The hot electrons cause collisional ionization and field ionization by generating charge-separation fields. More details are discussed in section 3.5.

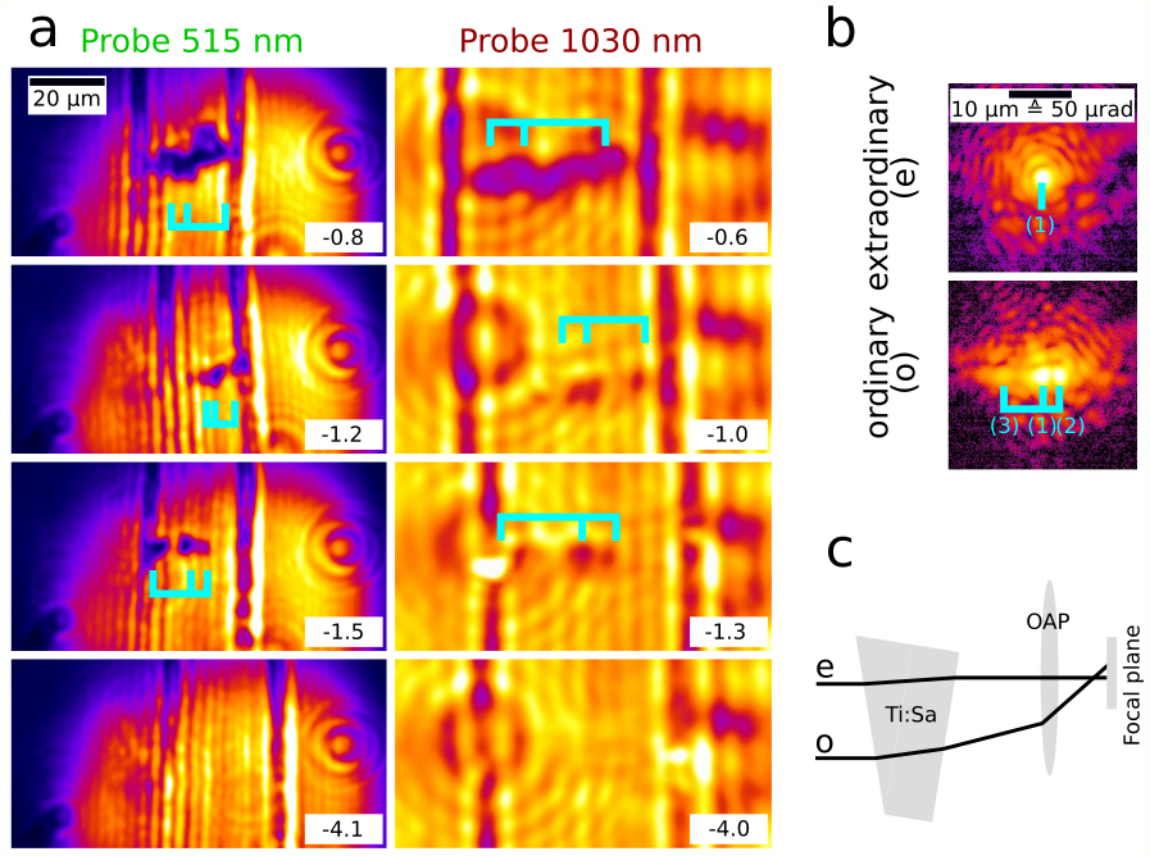

Figure 3.14.: **(a)** Shadowgrams that are captured at $2.2 \cdot 10^{21}\,\mathrm{W/cm^2}$ pump-laser-peak intensity with probe 515 nm and probe 1030 nm. The pump-probe delay is given in picoseconds in the lower-right corner of each shadowgram. The data shows several focal spots on the target. **(b)** Magnified camera image of the pump-laser focal spot (logarithmic colorscale), the final laser amplifier is switched of. The seed beam into the final amplifier is tuned to extraordinary (nominal setting) or ordinary polarization with respect to the c-axis of the amplifier crystals. For ordinary polarization, a generation of multiple focal spots occurs. The distance between the three brightest spots (1), (2), (3) is indicated by the cyan markers. The same marker is displayed in each shadowgrams of figure (a), corrected for the specific rotation angle of the target. **(c)** The extraordinary (e) and ordinary (o) beam are deflected to different angles due to the non-parallelism of the Titanium-Sapphire (Ti:Sa) crystal surfaces. The short focal length of the $F/2$ OAP visualizes the angular separation in the focal plane.

At nine to seven orders of magnitude below the pump-laser-peak intensity and single-picosecond delay before the pump-laser peak, the light distribution in the focal spot is expected to show influences from various mechanism that occur during laser-pulse amplification, like for example B-integral mixing of post- to pre-pulses [105] and spatio-temporal couplings [96]. Furthermore, the alignment of optical beamline elements and amplifier components is practical only up to the accuracy of the available diagnostics, e.g., polarizing beamsplitters with an extinction ration of about 1 : 1000, and

trade-offs between practical feasibility and laser-beam quality must be made. Figure 3.14 shows an example of how TRIC provides qualitative insight to the spatio-temporal light distribution on target, encouraging deeper investigation of specific properties of the pump-laser beam that would otherwise likely be overlooked.

The shadowgrams in figure 3.14 (a) demonstrate that neither a round nor an oval shape of the patterns with dielectric breakdown is observed, which is what would be expected according to the synthetic TRIC data and the time-integrated focal-spot measurement in figure 3.13 (c). Instead, the experimental data shows multiple focal spots that are roughly aligned along a horizontal line. The focal spots are observed for different delays and synchronously in two optical probe beams (each line in fig. 3.14 (a) corresponds to the same pump-laser shot).

The alignment of the spots along a single axis and the occurrence of multiple spots with similar shape suggest that the phenomenon is caused by several laser beams from a common source with equivalent collimation, which propagate the beampath off the laser with different angles towards the OAP. As almost all laser-beamline elements in the final amplifiers, the compressor and the beam-transport system are reflective, they cannot be the origin of several beams with slightly different propagation angle. Ti:Sapphire crystals, however, are birefringent and are the non-avoidable transmissive optical elements in the final laser amplifier. This motivates the hypothesis that, because of the alignment of the Ti:Sapphire crystals in the final laser amplifier (two crystals, each in a multipass configuration), an ordinary beam co-exists or is generated in addition to the nominal extraordinary laser beam. Geometric optics calculations demonstrate that a wedge of a Ti:Sapphire crystal between 1° and 0.1°, which is below the specifications of the vendor, would be sufficient to induce a difference of the propagation angle between an ordinary and an extraordinary beam of single micro radians up to hundreds of micro radians (see sketch in figure 3.14 (c)). According to the different beampaths of the individual passes of the multi-pass amplifier, a variation of the angle of incidence between 0° and 5° is considered for the calculation.

To experimentally prove the hypothesis, we insert a waveplate before the final laser amplifier, tuned the seed from extraordinary (nominal) to ordinary polarization and simultaneously measured the focal spot after the final OAP with $\sim 30\times$ magnification. During the measurement the laser beam (1 Hz, ~ 2 J before compression) traverses the final laser amplifier (not pumped), a wedge attenuator (two fused-silica wedges with 45° angle of incidence) and the compressor chamber. The top image of figure 3.14 (b) shows the nominal setting with extraordinary polarization of the seed and the lower image shows the setting with ordinary polarization of the seed. The latter shows several focal spots with an angular distance of several tens of micro radians. To compare the spacing between the spots with the shadowgraphy measurements in figure 3.14 (a), the cyan marker with the numbering (1), (2) and (3) is stretched or compressed according to the respective target-rotation angle and displayed in each shadowgram. There is remarkable correlation between the shadowgraphy measurements at ultra-relativistic peak intensity and the focal-spot measurement with ordinary polarization of the seed. The results suggest that the spacing between the focal spots in the shadowgraphy measurements is explained by a wedge of the Ti:Sapphire crystals in combination with different angles of incidence for each individual pass in the final multi-pass amplifiers. Still, for nominal laser operation, the effect should only occur if an ordinary-polarized laser beam is seeded into the final laser amplifier or is generated in the final laser amplifier.

Two possible scenarios of the origin of an ordinary-polarized beam in the final amplifier exist. Either the seed already has ordinary polarization components or the components are generated within the final amplifier. The first option is unlikely, as the polarization is cleaned by several thin-film polarizers before the amplifier. Therefore, Appendix D explores the second option. The results show that the final amplifier generates an ordinary-polarized beam that co-propagates with the nominal extraordinary-polarized laser beam. For a focal spot with a peak intensity of $5 \cdot 10^{21}\,\mathrm{W/cm^2}$ on target, a neighboring focal spot with an intensity of about $1 \cdot 10^{18}\,\mathrm{W/cm^2}$ is thus expected.

According to the current status of the investigation, a final confirmation of the initial hypothesis about the origin of multiple focal spots on target that are caused by polarization mixing in the final laser amplifier lacks the explanation of why the spots initiate LIB to the same time as the leading edge of the main extraordinary-polarized laser pulse. The difference of the ordinary and extraordinary refractive

index of Ti:Sapphire calculate a maximum delay of 6.9 ps between both beams (4 passes per amplifier crystals). However, the ordinary beam should arrive later than the nominally polarized extraordinary beam. Furthermore, the ordinary beam has a lower peak intensity and the corresponding leading edge should be lowered accordingly.
Polarization mixing in the large amplifier crystals and the multi-pass configuration of the amplifier can generate more complicated scenarios than just a single ordinary and a single extraordinary beam. Amongst others, the amplifier crystal cannot be considered as a perfect single crystal. The crystals suffers from thermal load and the associated local changes of the refractive-index ellipsoid during pumping. Dielectric mirrors introduce spectrally and angularly dependent rotations of the beam polarization. Furthermore, the accumulated spectral phase and the compressed pulse duration of an ordinary laser beam is different from the nominal extraordinary-polarized beam.

In summary, the investigation of the origin of multiple focal spots on target needs further consideration in the future. Still, the experimental observation is an illustrative example of how TRIC enables qualitative insights to the intensity distribution of a high-power laser in the final focal spot.

3.4. Determining the starting point of LIB from the laser contrast

The determination of the starting point of LIB is essential for all simulations of high-intensity laser-solid interactions that aim to achieve quantitative agreement to experimental results by accurately modeling target pre-expansion and pre-heating. Moreover, the predictive power of computer simulations depends on modeling realistic experimental scenarios [180]. Most experiments of high-intensity laser-solid interactions, however, do not feature optical-probing diagnostics to infer the onset point of LIB experimentally. The following section is intended to use the insights gained in section 3.3.1 and to provide guidance on how to derive the starting point of LIB for other laser-target platforms. The prerequisites are a quantitatively valid measurement of the leading edge and a characterization study of the target-specific LIB thresholds versus laser-pulse duration. A demonstration example based on the intrinsic leading edge of the DRACO-PW laser and the LIB thresholds of the cryogenic hydrogen-jet target is given below.

Figure 3.15 (a) and (b) show the accumulated-fluence and intensity representation of the leading edge as calculated from a third-order-autocorrelator measurement of the intrinsic laser contrast of DRACO PW (figure 2.16 (a)). For the accumulated-fluence representation, the laser energy of 22.4 J is distributed over the area under laser contrast and stepwise integrated starting from −250 ps. The fluence at a given time corresponds to the accumulated fluence on target within the FWHM of the pump-laser focal spot. The step-like increase of fluence between the colored time intervals corresponds to the arrival of short prepulses at −90 ps, −67 ps and −54 ps, which becomes clear by a the comparison to figure 3.15 (b). Figure 3.15 (b) shows the laser contrast scaled to the pump-laser-peak intensity of $6.7 \cdot 10^{21}\,\mathrm{W/cm^2}$.
The discussion in section 3.3.1 yields that not the overshooting of a specific threshold intensity, but rather the accumulation of fluence in a specific duration is causing the generation of LIB. With respect to measurement data that features a finite temporal resolution, e.g., as recorded by third-order autocorrelators, this statement needs more detailed consideration. As long as the temporal resolution of the measurement device is sufficient to sample the intensity envelope of the leading edge, the comparison of the accumulated fluence during a specific temporal interval can be compared to a characterized LIB-threshold fluence. This is examplified by the red, yellow and blue time intervals that are depicted in figure 3.15 (c) on the left side. Note that the y-axis is in linear scale. The intervals correspond to time delays between the three short prepulses. Each interval features a specific pulse duration and a fluence that is calculated from the difference between the accumulated fluence at the end and at the beginning of the colored interval. Each colored interval is represented by a marker in the graph on the right side of figure 3.15 (c). The accumulated fluence is compared to the characterized threshold fluence of LIB, which is given as orange line (adopted from figure 3.8). The comparison shows that the accumulated fluences between −90 ps and −67 ps and between −67 ps and −54 ps are not sufficient to trigger LIB. However, the leading edge between −54 ps and −39 ps

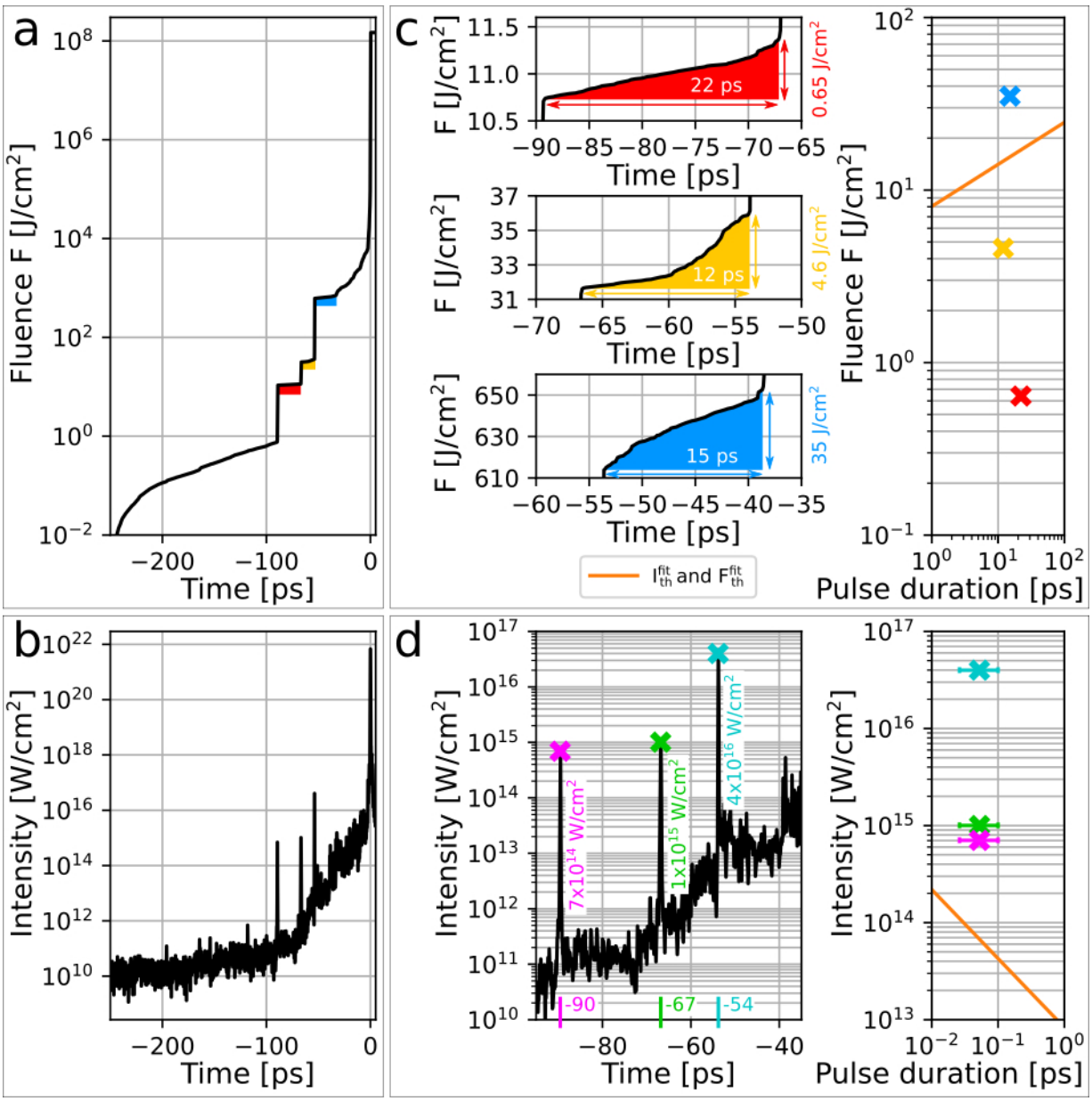

Figure 3.15.: **(a)** Accumulated fluence versus time as calculated from the intrinsic laser contrast of DRACO PW. **(b)** Intensity representation of the intrinsic laser contrast of DRACO PW. **(c)** Three details of the accumulated fluence from fig. (a). The increase of fluence during each colored time interval is compared to the threshold fluence of LIB (orange line) in the graph in the right side. **(d)** Detail of the graph in fig. (b). The intensity of the three short prepulses is compared to the threshold intensity of LIB (orange line) in the graph on the right side. The pulse duration of each prepulse is below the optical resolution of the third-order autocorrelator. In consequence, a pulse duration between $\sim 30\,\mathrm{fs}$ and $\sim 100\,\mathrm{fs}$ is estimated (error bar of the markers in the graph on the right side).

surpasses the characterized threshold and LIB is expected to occur not later than $-39\,\mathrm{ps}$.
Up to this point, the short prepulses at $-90\,\mathrm{ps}$, $-67\,\mathrm{ps}$ and $-54\,\mathrm{ps}$ are not considered in the comparison. The temporal resolution of the measurement device ($\sim 100\,\mathrm{fs}$) is not sufficient to sample their envelope. Here, a heuristic approach is the usage of the intensity representation of the leading edge. The three short prepulses are depicted in figure 3.15 (d). Their peak intensity cannot be allocated to a specific pulse duration, therefore the corresponding marker in the graph on the right side of figure 3.15 (d) features a horizontal errorbar between 30 fs and 100 fs (pulse duration of the main pulse and temporal resolution of the measurement). All three peak intensities are above the characterized

intensity threshold of LIB (orange line). It follows that, in an interaction of the cryogenic hydrogen-jet target and DRACO PW with intrinsic laser contrast, LIB is most likely initiated by the short prepulse at $-90\,\mathrm{ps}$.

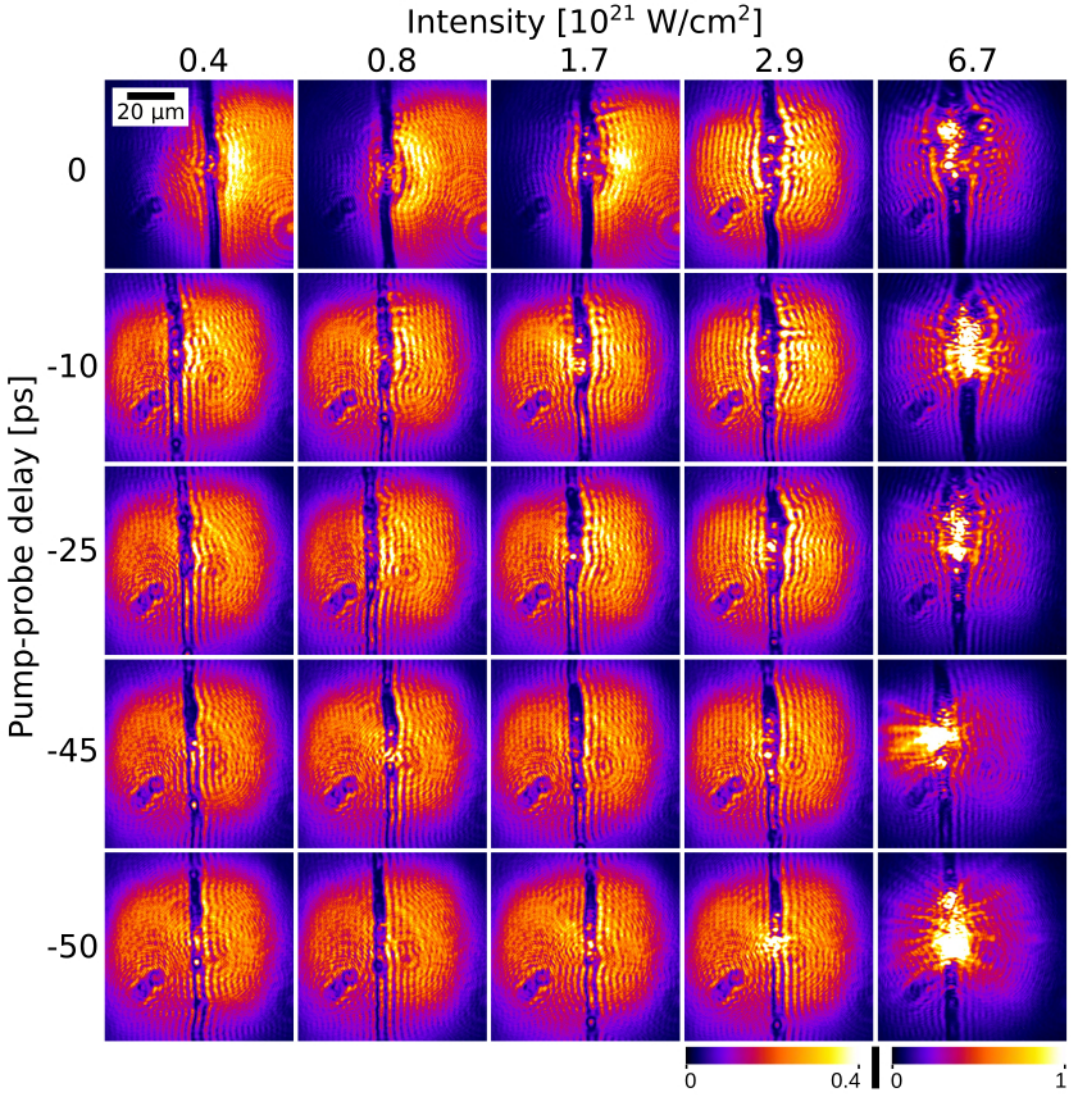

Figure 3.16.: Shadowgrams (probe 515 nm) of target pre-expansion for different peak-intensity settings of DRACO PW with intrinsic laser contrast. The accuracy of the pump-probe delay is $\sim 1\,\mathrm{ps}$ for this figure. The shadowgrams at $6.7 \cdot 10^{21}\,\mathrm{W/cm^2}$ pump-laser-peak intensity are given in a different colorscale.

An experimental validation of the result is partially possible by time-resolved optical shadowgraphy of interactions of the cylindrical hydrogen-jet target and the DRACO-PW laser with intrinsic laser contrast. The data set is displayed in figure 3.16. The columns correspond to a scan of pump-laser energy, yielding peak intensities between $0.4 \cdot 10^{21}\,\mathrm{W/cm^2}$ and $6.7 \cdot 10^{21}\,\mathrm{W/cm^2}$ on target. Each line corresponds to a specific pump-probe delay before the arrival of the pump-laser peak. The precision of the pump-probe delay is about 1 ps for this specific data set. Because of plasma self-emission, the shadowgrams recorded in the highest-peak-intensity setting are given in a different colorscale.
The first line of figure 3.16 directly shows that there is significant target pre-expansion for all pump-laser-intensity settings (horizontally increased shadow diameter in the center of each image). This underlines the importance of the aforementioned consideration of target pre-expansion by the leading edge of Petawatt-class lasers in similar experiments and their simulations. For each displayed delay, target pre-expansion gradually grows with pump-laser-peak intensity. For a peak intensities $\leq 2.9 \cdot 10^{21}\,\mathrm{W/cm^2}$ and pump-probe delays $\leq -10\,\mathrm{ps}$, the vertical extend of the area featuring LIB and target pre-expansion is spatially confined to a diameter of about $40\,\mu\mathrm{m}$. Outside this area, the

target is still transparent, i.e., it is still in the unperturbed initial state. At −50 ps delay, the horizontal extent of target pre-expansion is below the spatial-resolution limit of the microscope. LIB, however, is still observed as blackened target area for all peak intensity settings.
As no data with earlier pump-probe delays is available, a direct discrimination between the three short prepulses and their impact on the starting point of LIB is not possible. Still, the comparison of the observation of LIB at −50 ps and at one order of magnitude lower peak intensity ($0.4 \cdot 10^{21}$ W/cm^2) than the maximum peak intensity ($6.7 \cdot 10^{21}$ W/cm^2) shows that at least one of the three short prepulses exists and induces LIB of the target. This is supported by the fact that, for the lowest peak-intensity setting, all three intervals of the fluence representation (red, yellow and blue in figure 3.15 (c)) are well below the fluence threshold of LIB. A lowering of the intensity of the short prepulses (figure 3.15 (d)) by an order of magnitude shows that the intensity of the −67 ps and the −54 ps prepulse are still well above the LIB threshold. The prepulse at −90 ps, however, is very close to the threshold and the exact pulse duration is of relevance. Furthermore, the quantitative validity of the scaling of the laser contrast needs to be considered in detail.
Another detail that is not considered in the presented comparison between laser contrast and LIB thresholds is the separate treatment of short prepulses and the continuous pedestal. It is possible that a single short prepulse is not sufficient to trigger LIB on its own. However, as it excites a large amount of electrons to the conduction band, the subsequent continuously impacting light of the pedestal may drive efficient avalanche ionization and cause LIB shortly after the short prepulse.

The comparison of figure 3.16 and figure 3.15 shows that the discussed methodology of finding the onset of LIB from a laser-contrast measurement is not in conflict with the time-resolved optical-probing results. Consequently and with respect to the starting point of LIB, the presented absolute intensities and fluences in figure 3.15 do not overestimate the experimental settings significantly.
In conclusion, the DRACO-PW laser with intrinsic-temporal contrast and a peak intensity of $6.4 \cdot 10^{21}$ W/cm^2 in interaction with the cryogenic hydrogen-jet target is expected to trigger LIB by a short prepulse at −90 ps delay. Because of the change of optical properties during LIB, the subsequent deposition mechanism of laser energy is changed from a volumetric to a localized deposition on the front side by inverse Bremsstrahlung. A start-to-end simulation of such an interaction should simulate target pre-expansion in a radiation-hydrodynamics framework starting from the −90 ps prepulse on. Looking ahead, we state that the simulation of future experiments will benefit from the implementation of an artificial short prepulse with an intensity well above a characterized LIB threshold in the experiment. This defines the starting point of the laser-plasma interaction and fosters comparability to the accompanying start-to-end simulations.

3.5. Dielectric breakdown induced by relativistic electrons

A hitherto not discussed aspect of the shadowgraphy measurements of the interactions of the PM-cleaned DRACO-PW laser and the hydrogen sheet-jet target in figure 3.10 is the large-scale dielectric breakdown, which is observed for delays greater than about −0.4 ps. Figures 3.17 (a) to (d) show exemplary shadowgrams that are captured by probe 515 nm and probe 1030 nm at a pump-laser-peak intensity of $2.2 \cdot 10^{21}$ W/cm^2. The field of view (FOV) of probe 1030 nm is larger than the FOV of probe 515 nm. While LIB is not observed in figure 3.17 (a), figure 3.17 (b) shows the regime of TRIC that applies to the sub-relativistic laser intensities of the leading edge. Figure 3.17 (c), however, shows the large-scale dielectric-breakdown patterns that are discussed in this section. The patterns feature a different contour than the confined TRIC-patters in figure 3.17 (b). Interestingly, for the shadowgram of probe 1030 nm in figure 3.17 (c), the area of dielectric breakdown is more pronounced above the laser-target-interaction point that is positioned in the center of the shadowgram. The direction corresponds to the closest distance to an electrical grounding, which is the source of the target. Figure 3.17 (d) shows that the target experiences dielectric breakdown on a large spatial scale after the laser peak impinged on the target.
The laser contrast in figure 3.11 shows that, from about −0.4 ps on, the picosecond pedestal transitions into the steep-rising edge, i.e., the intensities rapidly increase towards the ultra-relativistic

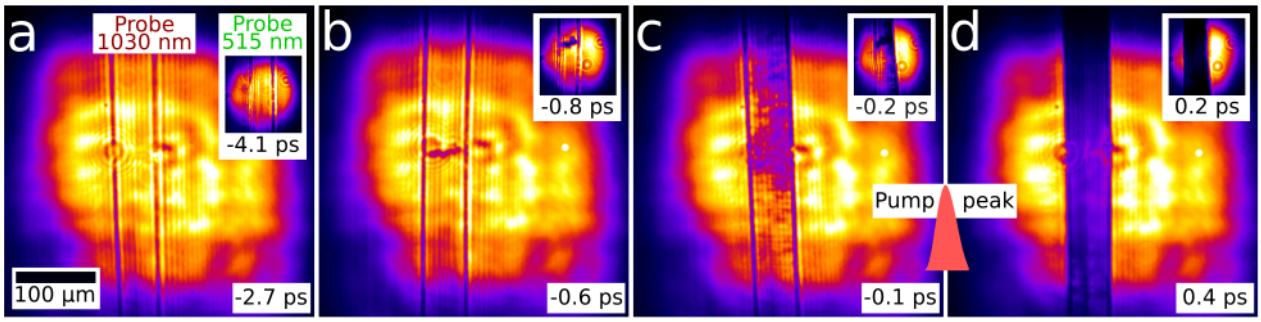

Figure 3.17.: Dielectric breakdown of the target at $2.2 \cdot 10^{21}\,\mathrm{W/cm^2}$ pump-laser-peak intensity. Three different regimes are identified. **(a)**: Onset of LIB (for both delays, LIB is not observed yet), **(b)**: TRIC in the sub-relativistic-intensity regime, **(c)** and **(d)**: Large-scale dielectric breakdown that is induced by laser-heated relativistic electrons. The shadowgraphy data of probe 515 nm and probe 1030 nm are shown with the same spatial scale. The pump-probe delay is given in the lower-right corner of each shadowgram.

laser peak. As soon as the intensities in the focal spot surpass $\sim 10^{18}\,\mathrm{W/cm^2}$, electrons are heated to relativistic velocities and the mean free-path length of the electrons increases accordingly (refer to *ponderomotive scaling*, eq. 2.5). The relativistic electrons traverse the target into all directions, induce return currents and charge-separation fields. Via collisional ionization and field ionization they induce dielectric breakdown of the surrounding target. Recently, Ref. [139] demonstrated a blackened target area with about 0.2 mm diameter of a water sheet-jet target by utilizing a peak intensity of only $5 \cdot 10^{18}\,\mathrm{W/cm^2}$ (5 mJ pump energy, 40 fs pulse duration). The authors investigate the dynamics of the laser-heated electrons that transversally stream through the target and discuss their interaction with colder return currents. In our work, the intensity of $5 \cdot 10^{18}\,\mathrm{W/cm^2}$ is surpassed already tens of femtoseconds before the pump-laser peak [211] and a much larger extent of the area with dielectric breakdown is expected to occur after the impact of the pump-laser peak. As the available FOV of the shadowgraphy diagnostic is limited, only a lower bound of the diameter of the blackened target area of 0.39 mm can be given here (figure 3.17 (d)).
The spatially varying opacity of the blackened areas in figure 3.17 (c) is caused by differences in the local conduction-band electron density close to the critical plasma density of the probe wavelength $n_c^{515\,\mathrm{nm}} = 4.2 \cdot 10^{21}\,\mathrm{cm^{-3}}$. In contrast, shadowgrams that are captured very close to or later than zero delay (figure 3.17 (d)) show a high opacity within the whole FOV. For probe 515 nm, the FOV corresponds to an area with a diameter about 40 times larger than the FWHM of the focal spot. Here, the amount of quasi-free electrons equals or is above $n_c^{515\,\mathrm{nm}}$, i.e., the ionization degree of the target is above $\sim 8\,\% = n_c^{515\,\mathrm{nm}}/n_e^{\mathrm{jet}}$. Probe 1030 nm shows the high opacity within an area greater than 0.39 mm. The ionization degree of the target within this area is above 2 % accordingly. This experimental observation can be used as a boundary condition for initial condition in calculations and simulations that model physical process, which are associated to electron conductivity outside the region of the high-intensity laser peak, e.g., magnetic-field generation by return currents [93], *electromagnetic pulse* (EMP) generation [44] and Terahertz generation [115] by high-intensity lasers.
In general, the growth rate of the area undergoing dielectric breakdown possibly includes information on the number and kinetic energy of the laser-heated electrons. Comparing the size of the area that features dielectric breakdown with the corresponding pump-probe delays, a spatial growth rate of about the speed of light is found. Unfortunately, the available data of the discussed experiment is too limited to yield more quantitative information. To nevertheless explain the principle concept of such a measurement, the following paragraph demonstrates similar results of an experiment at lower peak intensity and different laser-contrast settings.

Figure 3.18 shows shadowgraphy results (probe 515 nm) of an interaction of a planar hydrogen sheet-jet target (details on the target in Ref. [47]) with the DRACO-PW laser at a peak intensity of $4 \cdot 10^{19}\,\mathrm{W/cm^2}$, a laser energy of 0.5 J and intrinsic laser contrast. The arrival time of the pump-

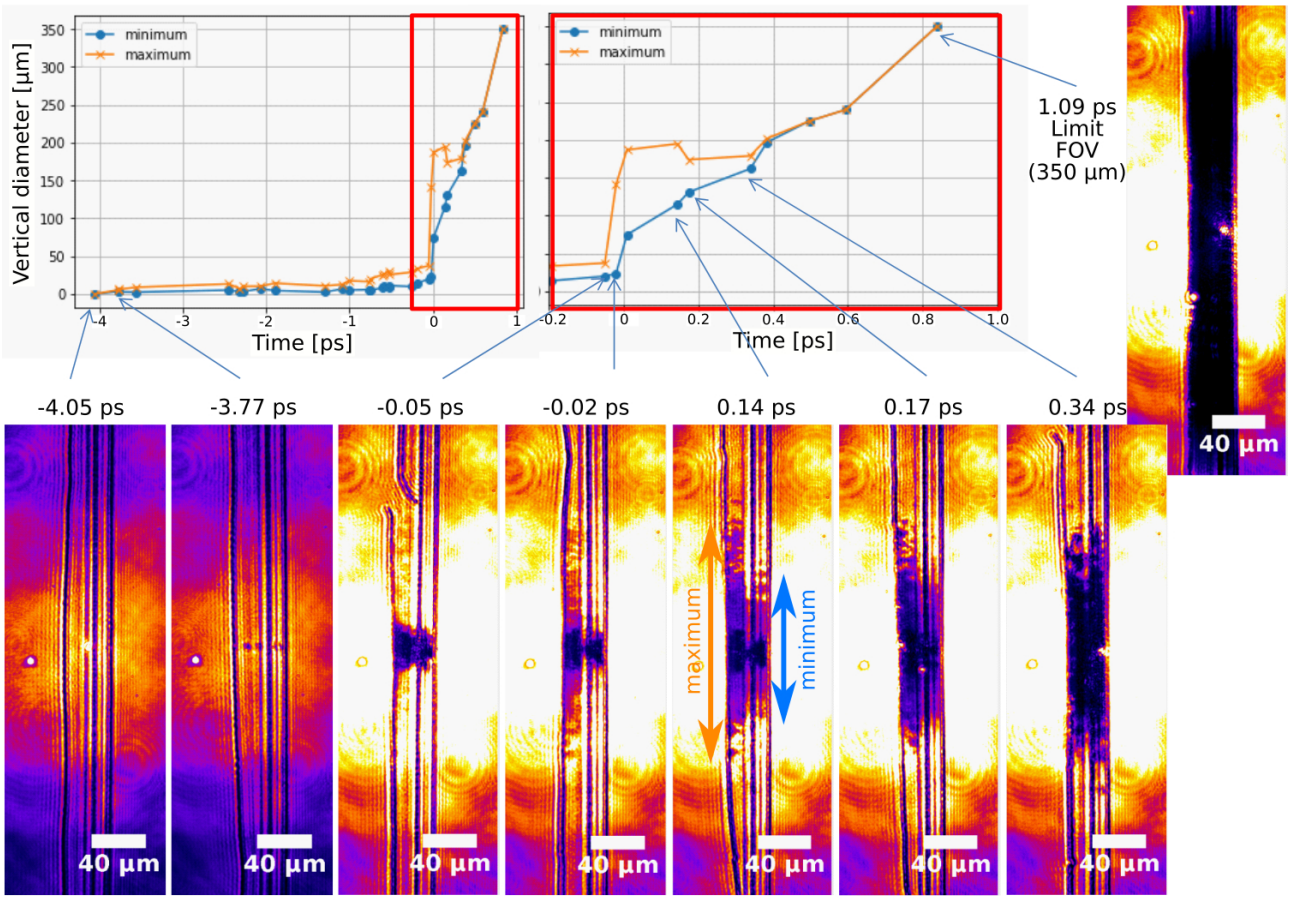

Figure 3.18.: Measurement of relativistic-electron-driven dielectric breakdown via time-resolved optical shadowgraphy (probe 515 nm) at a pump-laser-peak intensity of $4 \cdot 10^{19}$ W/cm^2 (DRACO PW, 0.5 J laser energy, intrinsic laser contrast). The minimum and maximum vertical diameter of the area with dielectric breakdown is shown in the graphs on the top. To visualize the different shades of blackened target areas, the colorscale of the shadowgrams captured at a delay ≥ -0.05 ps is different from the shadowgrams at earlier delay.

laser peak is not explicitly measured for this specific experiment. Because of the low peak-intensity level, short prepulses in the relativistic regime can be excluded by laser contrast measurements. In consequence, the laser peak is presumed to impact the target to a pump-probe delay for which the first large-scale pattern of dielectric breakdown is observed (0 ps in figure 3.18). The two shadowgrams on the left side of figure 3.18 demonstrate that the starting point of LIB is located between -4.05 ps and -3.77 ps. Up to 0 ps, TRIC patterns like in the shadowgrams captured at -3.77 ps and -0.05 ps are observed. The graph on the top of figure 3.18 shows that the vertical diameter of the area with dielectric breakdown slowly increases towards the laser peak, which is expected following TRIC. Starting from -0.02 ps on, a large-scale area of dielectric breakdown is observed, most likely because of the generation of relativistic electrons and the subsequent ionization of the surrounding matter (as described above). The opacity as well as the vertical maximum and minimum diameter of the area increase with increased delay until the whole target experienced dielectric breakdown at 1.09 ps (limited by FOV). The growth of the vertical diameter is depicted in the red-framed inset of the graph in figure 3.18. Between -0.05 ps and 0.84 ps the average radial-growth rate is calculated to $2 \cdot 10^8$ m/s, i.e., 66 % of the speed of light.

In summary, this chapter reports on the time-resolved observation of transient laser-induced breakdown (LIB) of dielectric hydrogen sheet-jet targets during the leading edge of high-contrast Petawatt-class laser pulses with peak intensities between $0.6 \cdot 10^{21}\,\mathrm{W/cm^2}$ and $5.7 \cdot 10^{21}\,\mathrm{W/cm^2}$. By switching from the lowest to the highest peak intensity, a shift of the starting point of LIB from the foot of the steep-rising edge into the picosecond pedestal of the leading edge occurs. The temporal shift is attributed to an increased absolute-intensity level in the picosecond pedestal, which lowers the applicable threshold intensity of LIB well below the appearance intensity I_{app} of barrier-suppression ionization. The observation clearly demonstrates that the laser-pulse-duration dependence of LIB and LIDT affect the starting point of LIB in high-intensity laser-solid experiments.
To generalize the observation to other laser-target systems, we present an approach to infer the starting point of LIB from laser-contrast measurements compared to a characterization study of target-specific thresholds of LIB at low laser intensity.
The pulse-duration dependence of LIB and its coupling to the leading-edge-intensity evolution requires careful consideration of the target-specific breakdown thresholds to determine the correct starting point for modeling target pre-expansion in start-to-end simulations of high-intensity laser-solid interactions.

4. Plasma expansion dynamics

The starting point of target pre-expansion is given by the laser-induced breakdown (LIB) of the solid target. Although this starting point is well defined, modeling of the residual laser-target interaction with a single simulation tool is still challenging. This is because of the variety of target-heating mechanisms for the different laser intensities of the leading edge. From the initially localized energy deposition (collisional and resonance absorption), the interaction becomes more volumetric by the generation of fast electrons as the leading-edge intensities rise above the relativistic limit of about $10^{18}\,\mathrm{W/cm^2}$. The fast electrons deposit their energy in the target bulk and drive collisional processes either directly or via return currents. For intensities well above the relativistic limit and close to the peak intensity of petwawatt-class lasers, particle motion is highly kinetic, i.e., non-collisional.
Today, the kinetic regime of relativistic laser-plasma interactions is captured by particle-in-cell (PIC) simulation tools. For the leading-edge-driven target pre-expansion, most often radiation-hydrodynamics simulations are used. For a comprehensive summary of the state-of-the-art of corresponding *start-to-end simulations* of high-intensity laser-solid interactions refer to section 2.1.3.
A possible approach to bridge or benchmark the simulation of the leading-edge-driven target pre-expansion is the utilization of time-resolved optical diagnostics. In the following, plasma expansion dynamics that occur in laser-solid interactions with peak intensities of up to $5.4 \cdot 10^{21}\,\mathrm{W/cm^2}$ are investigated by time-resolved optical shadowgraphy. Section 4.1 derives the amount of target pre-expansion from the experimental data to use it as a starting condition of a PIC simulation of the interaction between the plasma and the ultra-relativistic pump-laser peak. In section 4.2, the experimental observations subsequent to the laser-peak arrival on target are compared to the simulated plasma-expansion dynamics by post-processing the PIC-simulation results with ray-tracing simulations. The speeds of the simulated and measured plasma expansion are compared and the role of relativistically induced transparency (RIT) to the measured volumetric transparency of the target at 1.4 ps after the laser peak is investigated.
Most of the presented results are published in Ref. Bernert et al. [24].

4.1. Target pre-expansion by the leading edge

Figure 4.1 presents a collection of shadowgrams of probe 515 nm, which show the interaction of the DRACO-PW laser with a peak intensity of $5.4 \cdot 10^{21}\,\mathrm{W/cm^2}$ and PM-cleaned laser contrast with the cylindrical cryogenic hydrogen-jet target. The respective pump-probe delays are given in the lower-right corner of each shadowgram. Figure 4.1 (a) shows pump-probe delays before the pump-laser peak and figure 4.1 (b) shows pump-probe delays after the pump-laser peak. The generally visible features of each shadowgram are explained in the legend on the left side of figure 4.1 (a). Residual plasma self-emission occurs occasionally and it is limited to a small spot. For better visualization of the onset of LIB and the subsequent plasma dynamics, the colorscales are different in figures 4.1 (a) and (b) (continuity is given at −0.2 ps).
For all shadowgrams that are captured earlier than −1.8 ps, the hydrogen target is transparent throughout the whole field of view (see transmitted probe light along the entire target). The target acts like a cylindrical lens and rays that are close to the edge of the target get refracted outside the objective (details in section 2.2.2). Except for the residual plasma self-emission at the pump-laser-target interaction point, the shadowgrams are equivalent to images for which no pump laser is interacting with the target (e.g. figure 2.14 (a2) in section 2.2.2). For −1.6 ps delay, the target shows a small darkened volume at the position where the pump-laser peak is focused on the target. The spatial extent of the darkened volume grows with increased pump-probe delay. For a better visualization, the dark volume is highlighted by two horizontal white bars in all shadowgrams between −1.6 ps and −0.2 ps. The darkening indicates target regions that feature dielectric breakdown. From the data alone it cannot

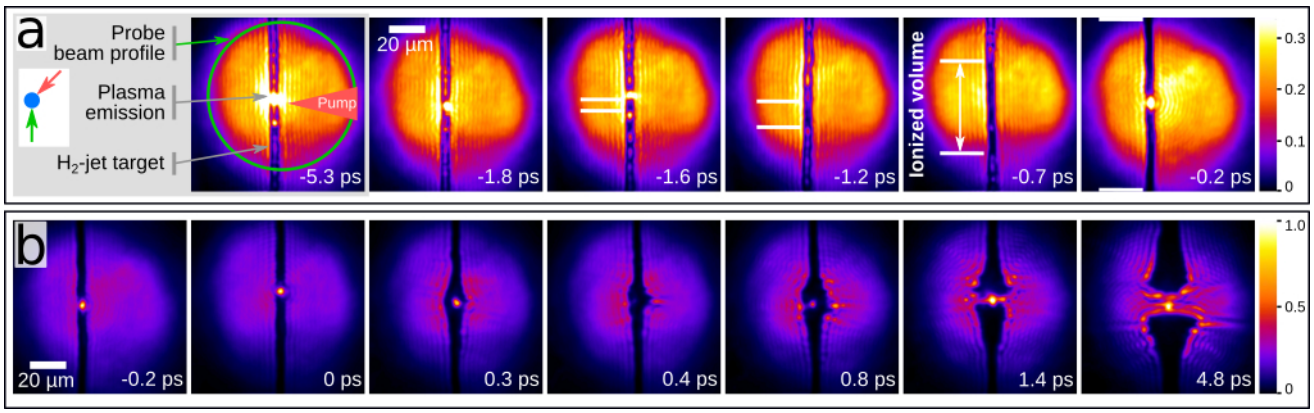

Figure 4.1.: Figure copied from Bernert et al. [24]. Shadowgraphy images at different pump-probe delays for a pump-laser-peak intensity of $5.4 \cdot 10^{21}\,\mathrm{W/cm^2}$. **(a)** Laser-induced breakdown and pre-expansion of the target. The area of dielectric breakdown occurs between the horizontal white bars. **(b)** Plasma expansion after the pump-laser peak. The pump-laser and probe-laser settings are equivalent for all images.

be distinguished whether dielectric breakdown is present on the cylindrical surface only or also in the target bulk. Because of the probing angle (see icon in the legend of figure 4.1 (a)), it is possible that the front side of the target shows LIB even earlier than it is observable in this geometry.
The time-dependent increase of opaque target volume is identified as an interplay between two sources. First, the spatial extent of the pump-laser focus in combination with the temporally rising intensity on target (refer to section 3.3.2) and, second, by the dissipation of hot electrons from the center of the interaction as soon as the pump-laser intensity becomes relativistic (refer to section 3.5). To disentangle the direct optical- and electron-driven contributions to dielectric breakdown, the hydrogen sheet-jet constitutes a more feasible target testbed. The corresponding results are presented in chapter 3. The following subsection 4.1.1 is intended to shed light on the relevance of the target geometry to the onset of LIB in high-intensity laser-solid interactions, in specific for the cylindrical hydrogen-jet target. Subsequently, subsection 4.1.2 estimates the target-density distribution from the shadowgraphy measurement at $-0.2\,\mathrm{ps}$ delay as a starting condition for a PIC simulation of the ultra-relativistic interaction.

4.1.1. LIB of the cylindrical hydrogen-jet target

The influence of the cylindrical target shape on the generation of LIB is investigated as part of a detailed characterization study of the laser-induced plasma dynamics at sub-relativistic laser intensities in Appendix G. The relevant results about LIB are displayed in figure 4.2. In figure 4.2 (a), the target is pumped by a 28.5 fs laser pulse at four different peak intensities I_p. The shadowgrams are recorded by a 258 nm backlighter in a 90° geometry at 20 ps (left row) and 1.206 ns (right row) delay after the pump pulse. For $3.5 \cdot 10^{14}\,\mathrm{W/cm^2}$ and 20 ps delay, the front side of the target shows a blackened area (white arrow). For $1.4 \cdot 10^{14}\,\mathrm{W/cm^2}$ and 20 ps delay, however, the blackened area is visible on the rear side of the target only (white arrow). For $7.1 \cdot 10^{13}\,\mathrm{W/cm^2}$ and $3.5 \cdot 10^{13}\,\mathrm{W/cm^2}$ and 20 ps delay, the target features no blackened areas. The pump-probe delay of 1.206 ns shows, whether the solid structure of the target was altered by the pump laser or not. If so, the target is dispersed by fluid-dynamic motion after the phase transition. For the intensities above $10^{14}\,\mathrm{W/cm^2}$ and independent on the front- or rear-side position of the blackened target area, the target is dispersed volumetrically (between the two white bars). For $7.1 \cdot 10^{13}\,\mathrm{W/cm^2}$, the rear side of the target undergoes a stronger expansion than the front side and produces a highly asymmetric target shape at 1.206 ns. Although no blackened target area is observed at 20 ps delay, the absorbed laser energy is high enough to induce the phase transition from the solid to the fluid state. The observation is explained by the three-times shorter probe wavelength compared to the pump wavelength. Assuming that the electron density in the conduction band at the rear side of the target constitutes a critical-density surface for the pump light

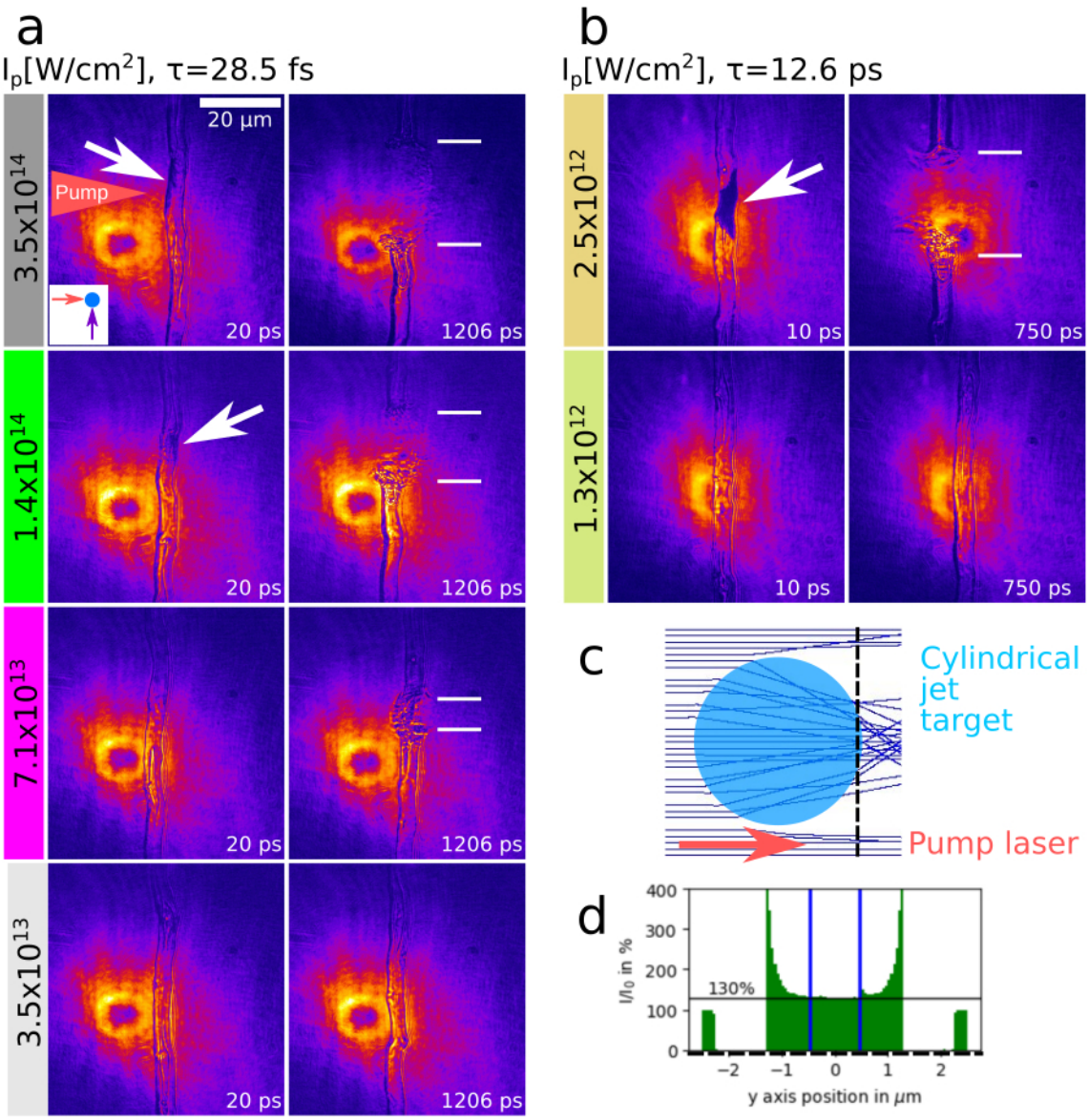

Figure 4.2.: Characterization study of the laser-induced breakdown of the cylindrical hydrogen-jet target for different laser-peak intensities I_p of **(a)** 28.5 fs pulses and **(b)** 12.6 ps pulses. The backlighter wavelength is 258 nm, the spatial resolution is better than 0.5 µm and the pump-probe geometry is 90°. More details on the specific setup and the characterization study can be found in Appendix G. **(c)** Top view of a ray-tracing simulation with an idealized cylindrical hydrogen-jet target. **(d)** Figure copied from [15]: Normalized intensity distribution I/I_0 at the rear side of the target (dotted line in fig. (c)).

during the interaction, a release of the solid bonds and an expansion into vacuum on long timescales is generated. For the 258 nm probe, however, an electron density of $n_c^{800\,\mathrm{nm}}$ is just $\sim 1/9$ of the critical density $n_c^{258\,\mathrm{nm}}$, i.e., just a disturbance of the local refractive index. The probe light propagation is consequently not altered much and no blackened target area is observed. Furthermore, recombination between 0 ps and 20 ps may already be relevant. For $3.5 \cdot 10^{13}\,\mathrm{W/cm^2}$, no modifications of the target are observed on all timescales.
From the measurement of the LIB thresholds of the hydrogen sheet-jet target in section 3.1.2, a LIB threshold of $I_{th}(28.5\,\mathrm{fs}) = (1.1 \pm 0.2) \cdot 10^{14}\,\mathrm{W/cm^2}$ is derived. The value agrees with the observation of a blackened target and a dispersion of the target volume on long timescales for $1.4 \cdot 10^{14}\,\mathrm{W/cm^2}$ and $3.5 \cdot 10^{14}\,\mathrm{W/cm^2}$. The intensity $7.1 \cdot 10^{13}\,\mathrm{W/cm^2}$ is well below the LIB threshold and the dispersion of the target on long timescales can be attributed to a refocusing effect of the light inside the target by the cylindrical geometry. The effect is illustrated in figure 4.2 (c) and quantified in figure 4.2 (d), which is copied from a master-thesis project, see Ref. [15]. The cross-section of the target acts like a cylindrical lens to the pump light and increases the intensity on the target-rear side at least to 130 % above the nominal intensity. Close to the rim of the target, the intensity increases above 200 % of the nominal intensity. As a lower bound, the calculation $130\,\% \times 7.1 \cdot 10^{13}\,\mathrm{W/cm^2}$ yields $9.2 \cdot 10^{13}\,\mathrm{W/cm^2}$, which is already in the one sigma error margin of $I_{th}(28.5\,\mathrm{fs})$. The focusing effect inside the target explains the observation of a stronger hydrodynamic expansion on the target-rear side at $7.1 \cdot 10^{13}\,\mathrm{W/cm^2}$ peak intensity and 1.206 ns delay. Furthermore, the argumentation explains the observation of a blackened target area only on the rear side of the target for a peak intensity of $1.4 \cdot 10^{14}\,\mathrm{W/cm^2}$ and 20 ps delay. For $3.5 \cdot 10^{14}\,\mathrm{W/cm^2}$ peak intensity, however, the shadowgram at 20 ps demonstrates that an intensity above I_{th} initializes LIB on the target-front side and by this causes a shielding of the residual target bulk from trailing pump-laser light. Consequently, the target bulk experiences less excitation of electrons to the conduction band on the target rear side. The nevertheless arising volumetric dispersion of the target on long timescales with a much higher spatial extend than the blackened target area at 20 ps is either caused by the difference in pump- and probe-laser wavelength or by the energy transport via electrons, holes and phonons through the target bulk. Both arguments should also explain the observation at $1.4 \cdot 10^{14}\,\mathrm{W/cm^2}$, for which the blackened target area occurs on the target rear side only, i.e., the conduction-band electron density is higher on the target rear side, and still, the phase transition occurs throughout the whole target bulk.
To experimentally investigate the refocusing effect of the cylindrical target for longer pulse durations, i.e., in reference to the multiple-picosecond-long leading edge of the laser pulse with a peak intensity of $5.4 \cdot 10^{21}\,\mathrm{W/cm^2}$, figure 4.2 (b) shows a similar study of LIB that is conducted with a pump laser of 12.6 ps pulse duration. In this case, LIB is observed at $2.5 \cdot 10^{12}\,\mathrm{W/cm^2}$ peak intensity and no disturbance of the target is observed at $1.3 \cdot 10^{12}\,\mathrm{W/cm^2}$. The values agree to the LIB measurements in section 3.1.2, for which an interpolation of the measured data yields $I_{th}^{\mathrm{fit}}(12.6\,\mathrm{ps}) = 1.4^{+0.4}_{-0.8} \times 10^{12}\mathrm{W/cm^2}$. For $2.5 \cdot 10^{12}\,\mathrm{W/cm^2}$ and 10 ps delay, close to the end of the 12.6 ps-long pump pulse, the refocusing of the pump light in the cylindrical target is clearly visible from the greater extend of the blackened target area on the rear side compared to the front side of the target (white arrow). The peak of the pump laser is sufficient to induce LIB on the front side of the target, while the outer parts of the pump-laser focal spot get refocused inside the target and cause LIB only on the rear side. Taking into account the lower bound of 130 % intensity increase at the rear side of the target by the cylindrical shape, the actual peak intensity of the $1.3 \cdot 10^{12}\,\mathrm{W/cm^2}$ setting is at least $1.7 \cdot 10^{12}\,\mathrm{W/cm^2}$ on the target-rear side. As no disturbance of the target is observed in this setting, the comparison to $I_{th}^{\mathrm{fit}}(12.6\,\mathrm{ps})$ suggests an actual threshold intensity of LIB of a 12.6 ps pulse that is slightly higher than the fitted scaling. This is in agreement to other LIB measurements of dielectrics in references [202] and [190], in which the authors show that, for pulse durations τ in the regime of several tens of picoseconds, the power-law scaling of LIB in the femtosecond and picosecond regime transitions to the $\sqrt{\tau}$ scaling of the nanosecond regime. Referring to the observation of LIB of the cylindrical hydrogen target at a peak intensity of $5.4 \cdot 10^{21}\,\mathrm{W/cm^2}$ and -1.6 ps delay (fig. 4.1 (a)), the occurrence of residual plasma self-emission, the spatial-resolution limit of 1.5 µm and the probing angle of 134° to the pump laser complicate a detailed analysis of the starting point of LIB in this experiment. The cylindrical target geometry implies corrections to the threshold intensity of LIB between about 130 % and 200 % of the nominal

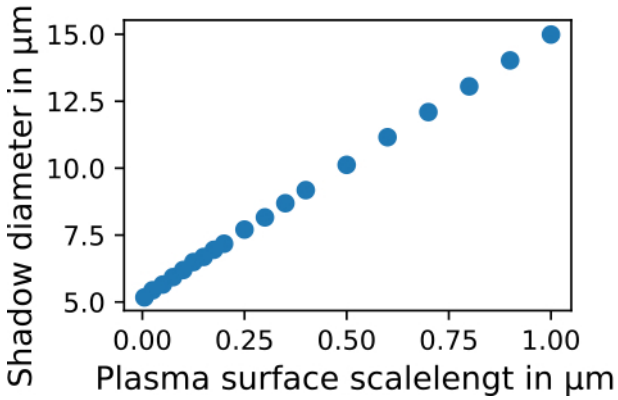

Figure 4.3.: Simulated shadow diameter in the image plane of the microscopy system of probe 515 nm for a plasma cylinder with 5 µm diameter and a surface gradient with different exponential scalelengths.

intensity.

4.1.2. Estimating target pre-expansion

As introduced in the beginning of the chapter, the recorded time-resolved shadowgraphy data at a pump-laser-peak intensity of $5.4 \cdot 10^{21}\,\mathrm{W/cm^2}$ can be used to bridge a simulation of the leading-edge-driven target pre-expansion by providing reasonable initial conditions for a PIC simulation of the ultra-relativistic laser-target interaction. For pump-probe delays between −1.6 ps and −0.7 ps, the shadowgrams in figure 4.1 (a) show no deviation of the shadow diameter from the cold target diameter of 5 µm (diameter at the source). For −0.2 ps delay (fig. 4.1 (a), right side) the target features LIB throughout the whole field of view (0.1 mm × 0.1 mm). The target shape is generally unchanged and small-scale changes are partially masked by plasma self-emission. The shadow diameter at −0.2 ps delay is measured to be between 5.77 µm and 6.52 µm.
As there is no target pre-expansion observed at −0.7 ps and only little target pre-expansion at −0.2 ps, the target-density distribution at −0.2 ps is expected to be similar to the box-like cold-target-density distribution. For convenience, the amount of pre-expansion is modeled by a short exponential scalelength on the plasma surface, as it is often done in similar experiments (compare section 2.1.3). To find the best-fitting scalelength, ray-tracing simulations of a plasma cylinder with 5 µm diameter and various surface scalelength are conducted. The simulated shadow diameters in the image plane of the virtual microscopy system of probe 515 nm are given in figure 4.3. Given the experimentally measured shadow diameter at −0.2 ps pump-probe delay, the best-fitting scalelength is between 0.06 µm and 0.13 µm.

4.2. Plasma expansion after the laser peak

4.2.1. Experimental findings

Figure 4.1 (b) shows the plasma expansion of the target between −0.2 ps and 4.8 ps. Prominent plasma dynamics are observed between 0.3 ps and 0.8 ps. For later pump-probe-delays (> 1.4 ps), the shadow of the plasma shows a more symmetric shape and the probe laser is able to penetrate the entire central volume of the plasma, i.e., the target is fully transparent.
Three characteristic transient target states are identified, each in a different time domain. Close-ups of representative shadowgrams are depicted in figures 4.4 (a), (b) and (c). Figure 4.4 (a) represents the ionization process and target pre-expansion by the leading edge of the pump laser, figure 4.4 (b) shows the fast expansion of the target after the pump-laser peak and figure 4.4 (c) shows the *full transparency* of the target. As sketched in figure 4.4 (b), a front- and a rear-side shadowradius can be measured from each shadowgram. The central axis of the target is determined by the undisturbed

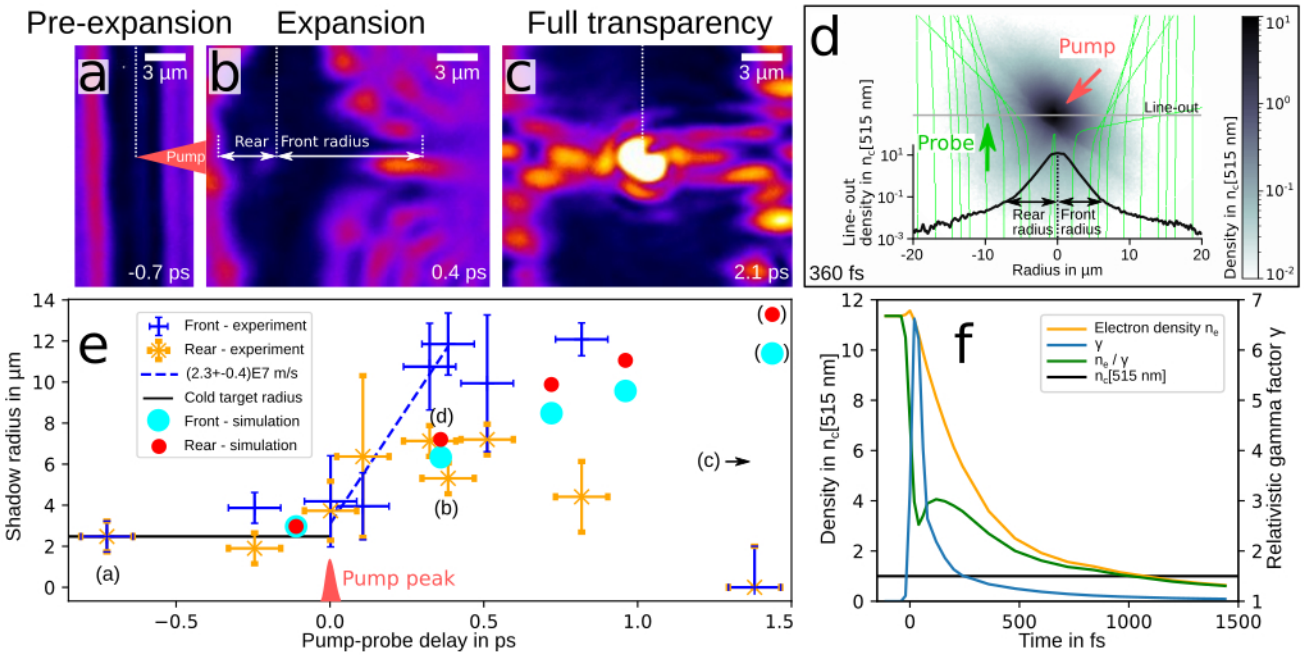

Figure 4.4.: Figure copied from Bernert et al. [24]. Close-up of three shadowgraphy images, each representative for one of the three characteristic transient target states: **(a)** ionization and target pre-expansion by the leading edge of the pump laser; **(b)** rapid plasma expansion after the pump-laser peak; **(c)** full transparency of the target after single picoseconds. The colorscale is consistent in all images. **(d)** Ray tracing of the PIC-simulation results: The gray colorscale shows a top-view slice of the electron density divided by the relativistic gamma factor n_e/γ at 360 fs after the pump-laser peak. The refractive index is calculated by formula 4.1 and inserted into the object plane of an imaging setup in Zemax with similar imaging properties like the experimental setup. The bending of the probe rays in the object plane is visualized by the green lines. The simulated front-side and rear-side shadow radii are retrieved in the image plane and presented together with a horizontal lineout of n_e/γ. The spatial scale of the lineout and the top-view slice are equivalent. **(e)** Evolution of the shadow radii for different pump-probe delays in the experiment (crosses) and ray tracing of the PIC-simulation results (circles, brackets indicate the occurrence of transmitted light within the shadow). **(f)** Temporal evolution of n_e, γ and n_e/γ from the PIC simulation, averaged over the initial target bulk (2.5 µm radius and 1 µm along the target axis).

outer parts of the interaction. While the shadow on the front side shows prominent spikes, the shadow on the rear side is spatially more homogeneous. Thus, the measured rear-side radius reflects the expansion of the plasma bulk, whereas the front-side radius shows the extent of the largest observed spike. In figure 4.4 (e), the front-side and rear-side radii are plotted by blue and orange crosses versus pump-probe delay. The spatial errorbars originate from the limited spatial resolution, the reduced observational accuracy by occasional plasma emission or a faint transition of the shadow into the signal level of the probe illumination. The arrival of the pump-laser peak causes a rapid growth of the shadow radii, with the front-side radius increasing to higher values than the rear-side radius. The maximum velocity of the shadow expansion is consequently observed on the front side and a linear fit gives $(2.3 \pm 0.4) \cdot 10^7$ m/s (dashed-blue line) between 0 ps and 0.4 ps. Subsequently, the growth of the shadow radii first stagnates and then reverses until full transparency of the target is reached at 1.4 ps. The ultra-fast plasma expansion occurs on a timescale close to the probe-laser pulse duration and motional blurring of the individual shadowgrams is expected.

4.2.2. Plasma expansion into vacuum versus relativistically induced transparency

To compare the experimental obervation to the theoretically expected plasma-expansion dynamics and to get more insight to the role of relativistically induced transparency (RIT) to the observed full transparency of the target at 1.4 ps delay, a three-dimensional PIC simulation is conducted via PIConGPU [35, 36] version 0.4.3. The implementation and conduction of the PIC simulation is part of a different thesis project [79] and details about the simulation are presented in Appendix E. For the PIC simulation, the target is initialized as a fully ionized plasma cylinder with a density of solid hydrogen and a diameter of 5 µm. An additional exponential surface scalelength of 100 nm is chosen to fit the experimentally determined pre-expansion at −0.2 ps delay (refer section 4.1.2). The time window of the simulation starts at −110 fs and stops at 1440 fs after the pump-laser peak reaches the target center.
Because of the mass ratio of protons and electrons, light transparency of plasmas is governed by the interaction with electrons. For relativistic laser plasmas, the high velocity of electrons can be considered as a mass increase quantified by the relativistic gamma factor γ [124]. Therefore, a top-view slice of the electron density n_e divided by the local mean of γ from the PIC simulation is shown in gray colorscale in figure 4.4 (d). Because the experimentally measured shadow expansion is maximized at 0.4 ps, the top-view slice shows n_e/γ at 360 fs. It is retrieved by averaging the particles in the three-dimensional simulation box within 1 µm along the target axis and in the plane of the pump-laser maximum. The pump-probe geometry is indicated by the red and green arrow. A lineout of the density n_e/γ along the central-horizontal axis of the top-view slice is shown at the bottom. The values of the lineout are averaged over 1 µm along the vertical axis of the top view.
To compare the PIC simulation to the experiment, the shadowgram formation for a given particle-density distribution needs to be modeled. For this, a dispersion relation of the plasma is required. The refractive index $\tilde{n}$ is commonly calculated from n_e/γ via the formula [124]

$$\tilde{n} = \sqrt{1 - \frac{n_e}{\gamma \cdot n_c}} \tag{4.1}$$

with n_c being the critical density of the probe wavelength. The spatial distribution of the refractive index is inserted into the object plane of a virtual imaging setup in Zemax (*Zemax 13 Release 2 SP6 Professional (64-bit)*) with similar imaging properties like the experimental setup. The bending of the probe rays penetrating the strongly refracting plasma distribution is shown as green lines together with the top-view slice in figure 4.4 (d). The ray tracing allows to retrieve simulated front-side and rear-side shadowradii in the image plane. For the simulated particle density at 360 fs, the retrieved shadowradii are indicated by horizontal arrows in the lineout at the bottom of the figure. Only probe rays that are captured by the numerical aperture of the objective contribute to the shadowgram formation. They propagate the plasma in a way that they do not penetrate densities higher than $0.1\,n_c$. This illustrates that the formation of the shadow is governed by refraction on the density gradients of the plasma and that the dispersive properties of the plasma are of specific importance here.
The simulated front-side and rear-side shadowradii at −110 fs, 360 fs, 720 fs, 960 fs and 1440 fs delay

are plotted together with the experimental data as circular markers in figure 4.4 (e). Comparing the simulated front-side and rear-side radius at 360 fs with the experimental data, the rear-side shadowradius is well matched by the simulation. However, the radius on the front side is underestimated. A possible reason could be the difference in spatial shape of the shadowgrams on the front and on the rear side in the experiment. While the front side shows a more structured contour of the shadow with several spikes and the front radii reflect the extend of the largest spike, the rear-side radii are measured from a spatially more homogeneous expansion. For the ray tracing, a spatial average of the particle density in the PIC simulation (top-view slice in fig. 4.4 (d)) is used to calculate the refractive-index distribution. It follows that the simulated shadow radii represent the expansion of the target bulk rather than small-scale structures. This explains the better congruence of experiment and simulation results for the rear-side radius. The simulated front-side radius at 360 fs reasonably compares to the experimental observation, if the spikes in the experimental shadowgram would be neglected.

More insight to plasma dynamics at times between -110 fs and ~ 360 fs requires a detailed investigation of the simulation results. Because of the comparably long pulse duration of the probe laser, these timescales are at the limit of the experimental capabilities of the current setup. Furthermore, and as described below, the interpretation of the corresponding PIC-simulation results requires a careful treatment of the dispersion relation of the plasma. The pump laser induces a high non-equilibrium state of the plasma, in which the local proton and electron density differ significantly. This is visualized in a 45° slice and a top-view slice of the particles in the three-dimensional simulation box at 120 fs delay in figure 4.5 (a). The green contour lines directly show local quantitative differences of the proton density n_p and electron density n_e. The *initial target bulk* with 5 µm diameter is marked by gray circles in all top-view slices. An asymmetric expansion of the "front" and "rear" side of the plasma is visible in the 45° slice. During the laser-target interaction, the laser heats electrons to relativistic velocities and the local relativistic gamma factor γ of these electrons is much higher than unity. This is apparent by viewing the difference between the electron-density slice and the electron-density-over-gamma slice.
The laser-heated hot electrons induce strong charge-separation fields and dominate the physics of the plasma system on the timescale of the pump-laser pulse up to about 360 fs. The hot electrons initiate the subsequently dominating plasma expansion into vacuum. Line-outs of n_p, n_e and n_e/γ at different simulation-time steps demonstrate the dynamics in figure 4.5 (b) quantitatively. The lineouts at 0 fs, 40 fs and 80 fs delay show that electrons rapidly leave the initial target bulk. The ratio of n_e (orange) and n_e/γ (green) resembles the high velocities, i.e., a high gamma factor. At 160 fs, the gamma factor decreases along the overall lineout and converges to unity at times later than 360 fs, i.e., $n_e \approx n_e/\gamma$. The protons (blue), however, react more slowly and remain at rest during the laser-target interaction (compare -110 fs and 0 fs). At 40 fs, the Debye-sheath of electrons already triggered a movement of the protons and a proton-density front with a sharp cutoff is occurring on the left and on the right side of the initial target bulk. For the lineouts at later times, both cutoffs follow the evolution of the hot electrons into vacuum until they leave the simulation box at about 360 fs.
In general, the lineouts show the spatial anisotropy of the electron and proton densities up to about 360 fs. Furthermore, a high temporal variation of the proton current is initialized during the first 100 fs after the pump-laser peak. All of these observations violate the approximations that are required for the derivation of the usual dispersion relation of equation 4.1. For clarity, a detailed derivation of the dispersion relation is given in Appendix F. It follows that for the timescales between 0 ps and about 360 fs, the usage of formula 4.1 is questionable. The interpretation of corresponding optical-probing data requires a more rigorous treatment via a dedicated solution of the plasma waveequation. However, a more convenient future approach can be the propagation of the probe light within the PIC simulation, for which Maxwell's equations are solved explicitly.
Because of the comparably long pulse duration of the probe laser of 160 fs and the challenging interpretation of small-scale structures especially at timescales close to the pump-laser peak, we limited the comparison between simulation and experiment to the time steps -110 fs, 360 fs, 720 fs, 960 and 1440 fs, for which n_e, n_e/γ and n_p are spatially nearly equally distributed.

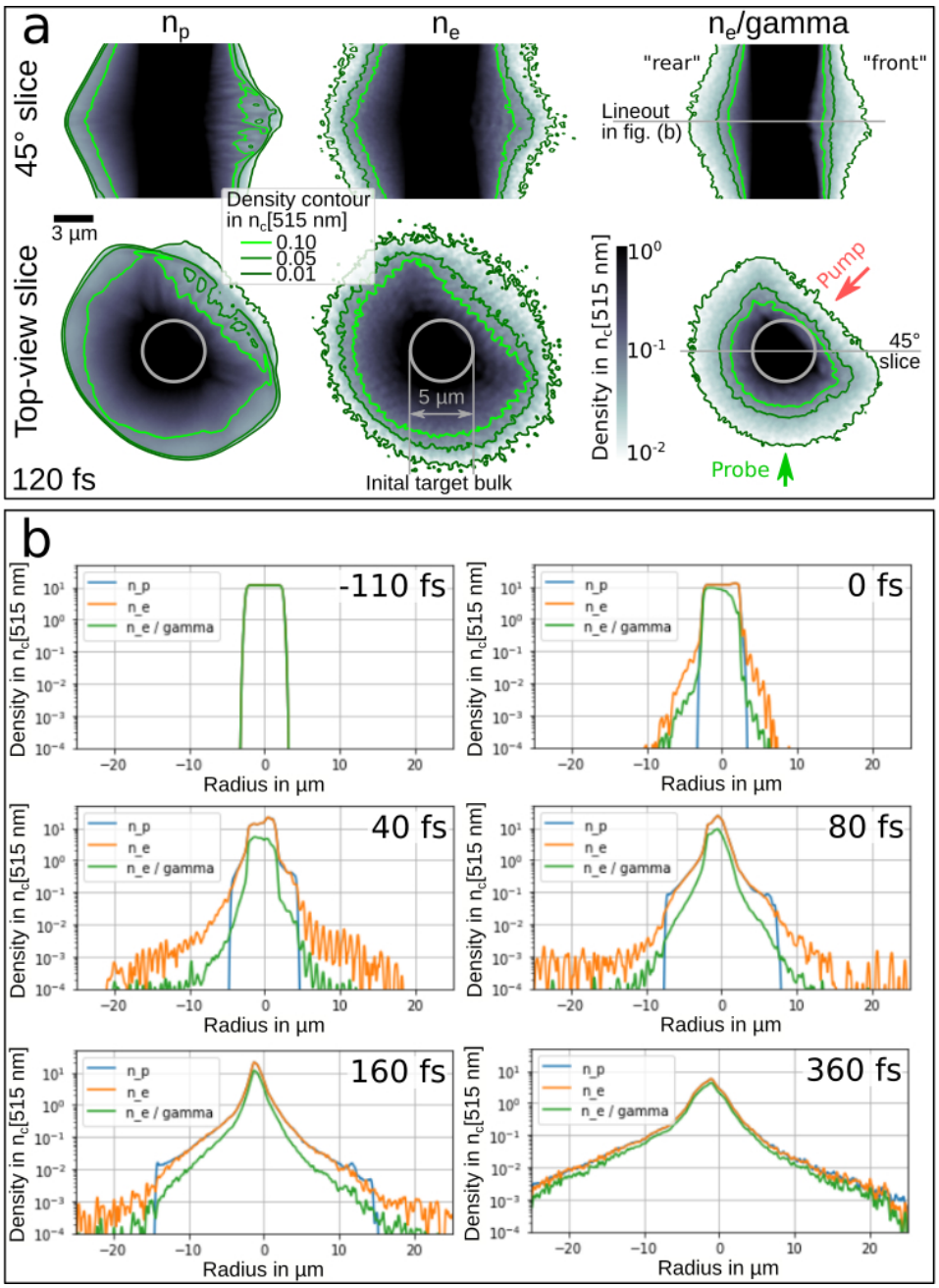

Figure 4.5.: PIC-simulation results: **(a)** Proton density n_p, electron density n_e and electron density over gamma n_e/γ at 120 fs after the pump-laser peak. The upper line shows the 45° slice through the three-dimensional simulation and the lower line shows the top-view slice in the plane of the pump-laser maximum. All slices are averaged over 1 µm into the displayed direction. **(b)** Lineouts of n_p (blue), n_e (orange) and n_e/γ (green) for different delays. The position of the lineout is given in the 45° slice on the right side of figure (a).

A clear experimental observation is the full transparency of the target at 1.4 ps. Although plasma self-emission masks central regions of the shadowgram and the temporal resolution of the time-delay scan is 175 fs, the penetration of probe light through central regions of the target demonstrates that n_e/γ dropped to values lower than n_c along the complete path of propagation. The PIC simulation can be used as a guide to disentangle the contributions of RIT and the density reduction by plasma expansion into vacuum. Figure 4.4 (f) shows the temporal evolution of n_e (orange), γ (blue) and n_e/γ (green). All quantities are volumetric averages over the initial target bulk of 5 µm diameter and 1 µm along the target axis. The evolution of γ shows that significant reduction of n_e/γ by RIT is mainly present in the first 200 fs after the pump-laser peak. The fast increase of γ lowers the average n_e/γ down to about $3\,n_c$ at 40 fs. It follows that, for the discussed target geometry, material and pump-laser intensity, the laser heating of electrons is not sufficient to induce full transparency of the target by RIT right after the pump-laser pulse.
For timescales greater 200 fs, γ converges towards unity and n_e/γ converges to n_e. The evolution of n_e shows the effect of density reduction by plasma expansion into the surrounding vacuum. As expected, n_e drops over time. At 1070 fs, n_e falls below n_c and at 1440 fs n_e has reached $0.64\,n_c$. Although the entire target shows undercritical densities at this time, the gradients of the refractive index are still high and a shadowgram with sharp edges is retrieved by ray tracing (see simulated radii at 1.44 ps in figure 4.4 (e)). The majority of rays close to the central axis is refracted to angles larger than the opening angle of the objective. However, in contrast to the simulated shadowgrams at earlier times, a low amount of transmitted light on the percent level is observed close to the central axis, indicating the onset of transparency of the target. Because of the observation of transmitted light in the ray-tracing simulation, figure 4.4 (e) presents the simulated shadow radii at 1.44 ps delay in brackets. Note that especially at these long timescales the absorbing boundary conditions of the PIC simulation can influence the temporal evolution of the plasma expansion. Electrons with $n_e > 10^{-3}\,n_c$ and protons with $n_p > 10^{-3}\ n_c$ reach the boundaries of the simulation box already at 60 fs and 360 fs, respectively. A possible future improvement of the simulation approach can be a modeling of the plasma expansion subsequent to the laser heating and thermalization of electrons by a two-temperature hydrodynamics simulation with an interconnection point to the PIC simulation subsequent to the pump-laser peak.
In conclusion, the temporal evolution of n_e and γ in the PIC simulation indicate that the experimentally observed full transparency of the target at 1.4 ps is not caused by RIT, but results from the reduction of the bulk-plasma density by plasma expansion into vacuum.

In summary, this chapter demonstrates the application of off-harmonic optical probing to interactions of Petawatt-class high-intensity-laser pulses and the cylindrical hydrogen-jet target. The concept allows to make hitherto impossible observations of the plasma evolution at a pump-laser-peak intensity of $5.4 \cdot 10^{21}\,\mathrm{W/cm^2}$. Three successive characteristic target states are identified: LIB of a volumetric target together with target pre-expansion by the leading edge of the pump laser, the rapid plasma expansion subsequent to the pump-laser peak and full transparency of the target in the single-picosecond timeframe. The measurement of target pre-expansion at $(-0.2 \pm 0.1)\,\mathrm{ps}$ delay allows to restrict the surface scalelength of the plasma density to between $0.06\,\mu\mathrm{m}$ and $0.13\,\mu\mathrm{m}$. This provides realistic initial conditions for a three-dimensional PIC simulation of the ultra-relativistic laser-plasma interaction. A quantitative comparison to the experimentally observed rapid plasma expansion with speeds of up to $(2.3 \pm 0.4) \cdot 10^7\,\mathrm{m/s}$ is enabled by post-processing the particle-density distribution of the PIC simulation by ray-tracing simulations. Full transparency of the target is measured at $(1.4 \pm 0.1)\,\mathrm{ps}$ delay. The PIC simulation suggests that the observation is caused by plasma expansion into vacuum and the contribution of relativistically induced transparency is negligible.

5. Controlled all-optical target-density tailoring

For laser-driven ion-acceleration, the target-density distribution to the arrival of the pump-laser peak is decisive for the ultra-relativistic laser-target interaction. Different particle-acceleration mechanism occur for different target densities and especially densities in the nearcritical-density regime promise superb ion-acceleration performance [81], but are rarely explored in experiments. Active and controlled manipulation of the target's plasma density, i.e., an artificial *target-density tailoring*, is desired to decide on the laser-target-interaction mode and to tune the parameters of the accelerated ion beam. A general overview of the relation between the target density and the mechanism of laser-ion acceleration is given in section 2.1.2.
Several targetry concepts utilize preshaped or layered targets, e.g., reduced-mass targets, cone targets and foam targets [48, 124, 162]. They are manufactured with a specific design before insertion to the experimental chamber. For a high flexibility, however, a target manipulation that provides a variety of different target-density distributions from a single target platform within the experimental chamber is attractive. Furthermore, easy alignment, low production cost and the capability of high-repetition-rate operation are desired to ultimately deliver application-relevant laser-accelerated particle beams from optimized target systems [183].
A convenient way to approach this objective is *controlled all-optical target-density tailoring* via heater beams that artificially pre-expand the target before the arrival of the particle-accelerating ultra-relativistic laser pulse, see Ref. [143] and Rehwald et al. [168]. Because of the accessibility with respect to experimental diagnostics and the high-repetition-rate operation, the cylindrical hydrogen jet constitutes a superior target platform to investigate the prospects of all-optical target-density tailoring. Furthermore, the initially low density of only $30\,n_c[800\,\mathrm{nm}]$ fosters a pre-expansion of the target to the nearcritical-density regime and is thus perfectly suited to explore enhanced laser-proton-acceleration mechanisms in experiments and accompanying simulations.
To ensure a target-density manipulation via the optical heater beam only, target pre-expansion by the leading edge of the ultra-relativistic laser pulse is desired to be small. For the PM-cleaned leading edge of the DRACO-PW laser with $5.4 \cdot 10^{21}\,\mathrm{W/cm^2}$ peak intensity on target, first laser-induced breakdown of the hydrogen-jet target occurs between $-3.9\,\mathrm{ps}$ and $-2.7\,\mathrm{ps}$ before the laser peak (see section 3.2). For the cylindrical jet target, no target pre-expansion is observed at $-0.7\,\mathrm{ps}$ delay and the surface gradient of the plasma density at $-0.2\,\mathrm{ps}$ delay is determined to feature a minor exponential scalelength between $0.06\,\mu\mathrm{m}$ and $0.13\,\mu\mathrm{m}$ (see section 4.1.2). It follows that heater beams at a delay earlier than $-4\,\mathrm{ps}$ interact with the unperturbed target and target-density modifications that exceed a plasma-density surface scalelength of $0.13\,\mu\mathrm{m}$ dominate over the influence of the leading edge of DRACO PW.

The chapter is structured as follows. Sections 5.1.1 and 5.1.2 present the concept and experimental results of target-density tailoring via ultra-short relativistic laser pulses. Section 5.1.3 determines the full evolution of the target-density distribution by a hybrid of hydrodynamics simulations and ray-tracing simulations, which is a contribution to Ref. Rehwald et al. [168]. As already mentioned in the introductory section 2.2.5 about the recent achievements of the overarching project on laser-driven proton acceleration at HZDR, the tunability of the target's density distribution is used to switch between different proton-acceleration mechanisms in an experiment at DRACO PW. Section 5.1.4 explains the relevance of the here presented data of target-density tailoring to the experiment in detail. Section 5.2 presents the concept of utilizing the presented experiments of all-optical target-density tailoring as a testbed platform to experimentally benchmark PIC simulations in the collisional regime of laser intensities between $10^{16}\,\mathrm{W/cm^2}$ and $10^{19}\,\mathrm{W/cm^2}$, which is one of the two limiting intensity regimes that require further investigation to improve start-to-end simulations of high-intensity laser-solid interactions in the future. The realization of the concept for the case of a laser with a dimensionless vector

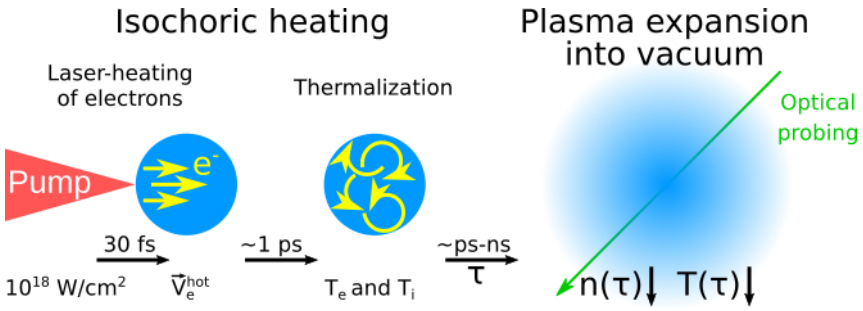

Figure 5.1.: Concept of all-optical target-density tailoring via relativistic ultra-short laser pulses: (1) A laser with $\sim 10^{18}\,\mathrm{W/cm^2}$ heats electrons to relativistic velocities $\vec{V}_e^{\mathrm{hot}}$. (2) Via different collisional processes (see text), the hot electrons thermalize and create an electron and ion temperature T_e and T_i in the target bulk. (3) On the picosecond timescale, both temperatures equilibrate to a single temperature T while the plasma expands into the surrounding vacuum. The plasma expansion leads to a reduction of the peak of the plasma density $n(\tau)$ and a change of the overall density profile, depending on the delay τ.

potential of $a_0 \sim 1$, i.e., an intensity of $\sim 10^{18}\,\mathrm{W/cm^2}$, is published in Ref. Yang et al. [208]. The last section 5.3 is dedicated to an experimental exploration of future prospects of all-optical target-density tailoring. Within a characterization study, femtosecond- and picosecond laser pulses of different peak intensity are used to generate different target shapes that are visualized by time-resolved optical shadowgraphy. The results outline a possible parameter range to realize all-optical target-density tailoring for laser-proton acceleration in the future.

5.1. Experimental demonstration: Isochoric heating via ultra-short relativistic laser pulses

5.1.1. Concept

The approach of all-optical target-density tailoring pursued in this section is *isochoric heating* via ultra-short laser pulses with a normalized vector potential $a_0 \approx 1$. Isochoric heating at similar laser intensities is studied in several experiments, e.g., see references [177, 157, 69]. The physics concept is sketched in figure 5.1. The first step is the *laser-heating of electrons*. A laser pulse with 30 fs duration, 800 nm central wavelength and 0.24 J energy is focused to a FWHM area of $32 \times 19\,\mu\mathrm{m}^2$ and a peak intensity of $1.5 \cdot 10^{18}\,\mathrm{W/cm^2}$. On the front side of the cylindrical hydrogen-jet target, the laser heats electrons to a mean velocity $\vec{V}_e^{\mathrm{hot}}$ (refer to ponderomotive scaling in section 2.1). The hot electrons move into the target bulk and the surrounding vacuum, cause charge separation fields and ionize further electrons either directly by collisions or via field-ionization. During the process of *thermalization*, the hot-electron population transfers it's energy to the colder electrons and ions of the target. On one side, this occurs directly via collisions of the hot electrons with cold electrons (electron-electron), ions (electron-ion) or the solid-state lattice (electron-phonon). On the other side, the generated secondary electrons collectively form return currents that try to balance the charge-separation fields. The return-current electrons undergo the same collision mechanisms like the hot electrons. Because of the energy dependence of the collision frequency [58], however, the return-current electrons with several eV to hundreds of eV kinetic energy induce a more efficient target heating than the laser-heated hot electrons. Within the target bulk, the process of thermalization creates a Maxwellian temperature for all electrons T_e and for all ions T_i. Ultilizing the cryogenic hydrogen-jet target and similar laser parameters like in this study, PIC simulations suggests that the thermalization of the electron population occurs on a timescale below 1 ps [69]. In a next step, the laser-heated plasma starts to expand into the surrounding vacuum. Hereby, the equilibration of T_e and T_i to a single temperature T occurs on a single-picosecond timescale [69]. For time delays τ in the picosecond to nanosecond range, hydrodynamic plasma expansion into the surrounding vacuum

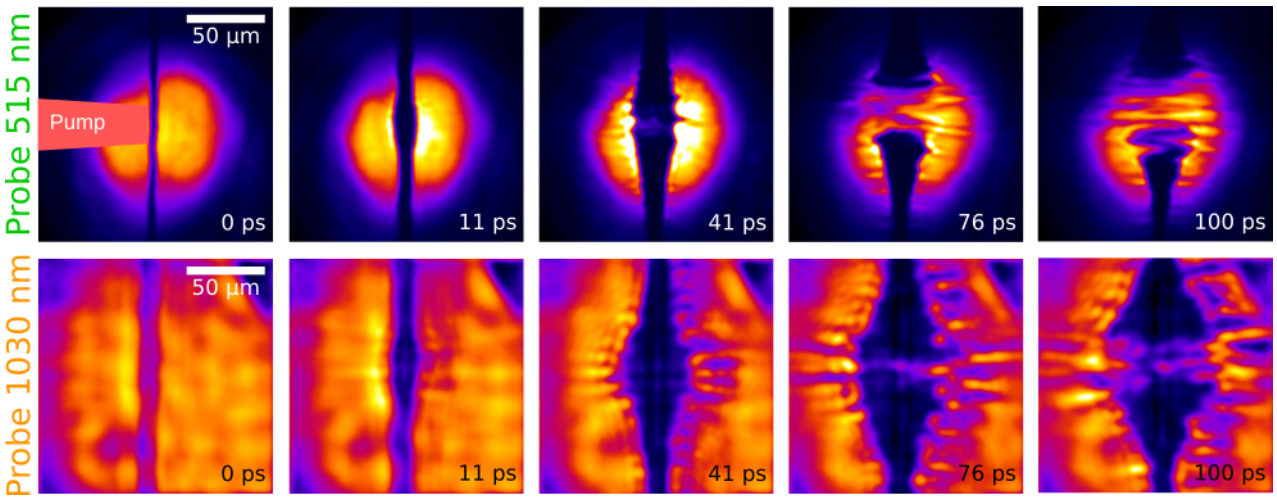

Figure 5.2.: Figure copied from Rehwald et al. [168]. Plasma expansion of the cylindrical hydrogen-jet target after interaction with a 30 fs-pump-laser pulse with a peak intensity of $1.5 \cdot 10^{18}\,\mathrm{W/cm^2}$. Exemplary shadowgraphy images of probe 515 nm and probe 1030 nm are given in the upper and lower line, respectively. The corresponding pump-probe delay is given in the bottom-right corner of each image.

leads to a reduction of the temperature $T[\tau]$ and a reduction of the peak of the plasma density $n[\tau]$.

5.1.2. Discussion of the experimental findings

5.1.2.1. Volumetric transparency

The process of plasma expansion is accessible via time-resolved optical shadowgraphy with the setup that is presented in section 2.2.4. Exemplary shadowgrams of a time-delay scan are presented in figure 5.2. 0 ps delay corresponds to the arrival of the pump-laser pulse on target and the pump-probe delay is given in the lower-right corner of each shadowgram. The two backlighter beams probe 515 nm (upper line) and probe 1030 nm (lower line) allow for simultaneous data acquisition at two different colors and two different angles, with 67 deg spacing. For all images, the shadow of the target appears symmetric around the jet axis. This indicates a radially symmetric expansion, i.e., a spatially homogeneous heating of the target. The target bulk becomes transparent at 41 ps for probe 515 nm and at 76 ps for probe 1030 nm. The observation is equivalent to the *full transparency* of the target in the previous chapter. In the following, however, the observation is termed *volumetric transparency*. The approximately equal transmittivity throughout the whole horizontal plane of the target is an additional argument for a volumetric process, i.e, a volumetric heating of the target. Volumetric transparency indicates that the peak density of the plasma dropped below the critical density of the backlighter wavelength at the respective delay, $n_c[515\,\mathrm{nm}] = 4.21 \cdot 10^{21}\,\mathrm{cm^{-3}}$ at 41 ps and $n_c[1030\,\mathrm{nm}] = 1.05 \cdot 10^{21}\,\mathrm{cm^{-3}}$ at 76 ps.
As discussed in section 4.2, volumetric transparency of the target is also observed at a pump-laser-peak intensity of $5.4 \cdot 10^{21}\,\mathrm{W/cm^2}$ via probe 515 nm. However, it is observed at a much earlier delay of 1.4 ps. The comparison to a PIC simulation in section 4.2 yields that volumetric transparency is caused by plasma expansion into vacuum and not by RIT. The same conclusion applies to the results at $1.5 \cdot 10^{18}\,\mathrm{W/cm^2}$ peak intensity, because the scaling of the mean kinetic energy of hot electons (e.g. ponderomotive scaling, refer to section 2.1) is lower than the rest mass of electrons, i.e., $\gamma \lesssim 1$ even for the fastest electrons.
At $5.4 \cdot 10^{21}\,\mathrm{W/cm^2}$ peak intensity, volumetric transparency is observed 30 times earlier than at $1.5 \cdot 10^{18}\,\mathrm{W/cm^2}$ peak intensity. This means that the average radial-expansion speed V of the plasma approximately fulfills the relation

$$\frac{V[5.4 \cdot 10^{21}\,\mathrm{W/cm^2}]}{V[1.5 \cdot 10^{18}\,\mathrm{W/cm^2}]} \approx 30.$$

The ion sound speed of a collisionless plasma $C_s \propto \sqrt{Zk_BT_e/m_i}$ [54] gives the proportionality

$$C_s \propto \sqrt{T_e}, \tag{5.1}$$

with the ion-charge state Z, Boltzmann's constant k_B, the electron temperature T_e and the ion mass m_i. Assuming a purely hydrodynamic expansion of a quasineutral collisionless plasma, the ion sound speed equals the expansion speed of the plasma $V \approx C_s$, which gives the relation

$$\frac{T_e[5.4 \cdot 10^{21}\,\mathrm{W/cm^2}]}{T_e[1.5 \cdot 10^{18}\,\mathrm{W/cm^2}]} \approx \frac{V^2[5.4 \cdot 10^{21}\,\mathrm{W/cm^2}]}{V^2[1.5 \cdot 10^{18}\,\mathrm{W/cm^2}]} \approx 30^2 = 900. \tag{5.2}$$

Analytical scalings about the laser-heating of electrons estimates the mean kinetic energy of hot electrons E_e^{hot} only. For example, the ponderomotive scaling gives

$$\frac{E_e^{\mathrm{hot}}[5.4 \cdot 10^{21}\,\mathrm{W/cm^2}]}{E_e^{\mathrm{hot}}[1.5 \cdot 10^{18}\,\mathrm{W/cm^2}]} = \frac{17.6\,\mathrm{MeV}}{82.6\,\mathrm{keV}} = 213. \tag{5.3}$$

Although the experiments at both intensity levels are conducted with the same target and the same optical diagnostics, the comparison of the relations 5.2 and 5.3 shows that the increased hot-electron energy is not sufficient to explain the much faster plasma expansion at $5.4 \cdot 10^{21}\,\mathrm{W/cm^2}$ compared to $1.5 \cdot 10^{18}\,\mathrm{W/cm^2}$. However, there are several oversimplifications of the estimation.
First, although the plasma at a peak intensity of $5.4 \cdot 10^{21}\,\mathrm{W/cm^2}$ is quasi collisionless (refer to evolution of the gamma factor in figure 4.4 (f) in section 4.2), the ansatz of a pure hydrodynamic expansion of the target is wrong. The thermalization time of hot electrons to a Maxwell-Boltzmann distribution of kinetic energy of all bulk electrons exceeds the time that it takes to accelerate a significant amount of target ions by the strong non-equilibrium charge-separation fields generated by the laser-heated hot electrons. This becomes clear by comparing the lineouts of electron and proton density of figure 4.5 (b) in section 4.2. High charge separation occurs during the pump-laser-pulse duration (30 fs) up to about 0.4 ps after the laser peak. Thus, the observed volumetric transparency at 1.4 ps shows not only contributions by hydrodynamic expansion, i.e., the conversion of thermal energy into kinetic energy, but also aspects of *Coulomb-explosion* during the first third of the expansion process.
The argumentation shows similarity to the analysis of experiments with peak intensities from $10^{15}\,\mathrm{W/cm^2}$ to $10^{17}\,\mathrm{W/cm^2}$ and nanometer-sized atomic clusters in gas jets from the 1990s [54, 114]. Recently, experiments with laser-heated atomic clusers gained renewed interest, because of the availabilty of x-ray free-electron lasers that enable direct experimental observations of the laser-induced cluster-expansion process via x-ray scattering [155, 80, 142, 140, 154]. The results discussed here with a peak intensity of $5.4 \cdot 10^{21}\,\mathrm{W/cm^2}$ utilize 10^4 to 10^6 higher intensity and targets with about 10^3 times higher diameter. The similarity of the orders of magnitude suggests that similar approaches of the description of the laser-target system can be useful for evaluations in the future. In summary, relation 5.1 accounts for the hydrodynamic-expansion process only and neglects the nonequilibrium particle acceleration that is induced by charge-separation fields after laser heating.
A second reasoning for the non-agreement of the relations 5.2 and 5.3 considers the validity of equation 5.1 for a laser-peak intensity of $1.5 \cdot 10^{18}\,\mathrm{W/cm^2}$. On this intensity level, the plasma is collisional and the negligence of the ion temperature T_i to equation 5.1 is questionable. Here, a convenient approach is the fit of a heuristic average plasma temperature to describe the system after isochoric heating. The approach is discussed in section 5.1.3.

5.1.2.2. Shadow diameter versus delay

Another aspect of the experimental observations is considered in the following. For both lines of figure 5.2, the horizontal shadow diameter is measured as follows. At the position of the pump-laser peak (center of each image) and for every shadowgram, a horizontal lineout is derived by averaging over the vertical extend of the FWHM of the pump-laser focal spot. The shadow diameter is measured by the derived FWHM of the shadow of the lineout. The results are displayed by the cross markers in figure 5.3. For all delays, the shadow diameter of probe 1030 nm is higher than the shadow diameter

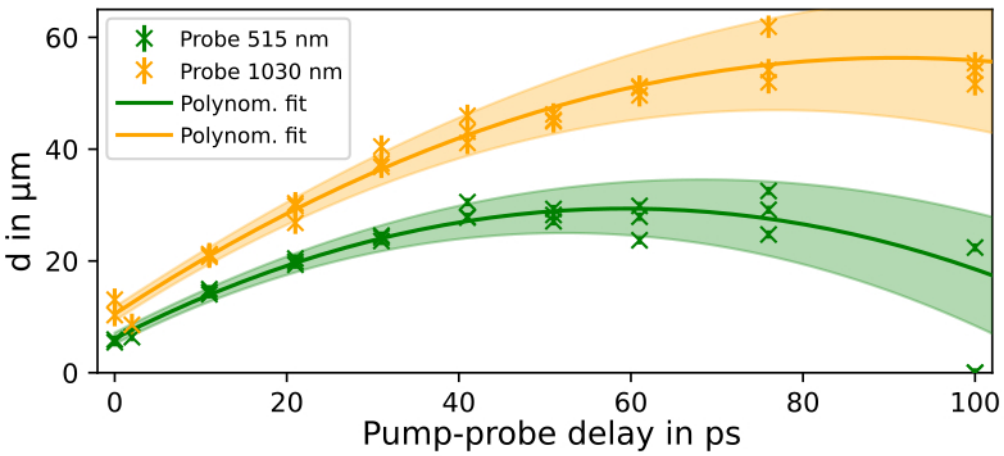

Figure 5.3.: Measured shadow diameter d of both probe beams versus pump-probe delay. The errorbar of each measurement corresponds to the spatial-resolution limit of the diagnostic. The solid lines are second-order polynomial fits to both data sets (equations 5.7 and 5.8).

of probe 515 nm.
The observation is explained by the equation of the critical density

$$n_c = \frac{4\pi^2 \epsilon_0 m_e c^2}{\lambda^2 e^2}$$

and the equation of the refractive index of a plasma

$$\tilde{n} = \sqrt{1 - \frac{n_e}{n_c}} = \sqrt{1 - \frac{\lambda^2 e^2 n_e}{4\pi^2 \epsilon_0 m_e c^2}}. \tag{5.4}$$

As mentioned previously, $\gamma \approx 1$ at all times of this experiment. ϵ_0 is the vacuum permittivity, m_e is the rest mass of an electron, c is the speed of light, e is the elementary charge, λ is the wavelength of the light and n_e is the electron density of the plasma. For the here considered numerical aperture of the optical microscope, probe rays that contribute to image formation are refracted in plasma densities lower than $0.1 n_c$ (refer to section 4.2). A Taylor expansion of equation 5.4 for low plasma densities directly shows that, for a fixed electron density n_e at a specific position of the plasma, the local refractive index quadratically changes with the wavelength:

$$\tilde{n}|_{n_e \ll n_c} = 1 - \frac{1}{2}\frac{n_e}{n_c} = 1 - \frac{e^2 \lambda^2 n_e}{8\pi^2 c^2 \epsilon_0 m_e}.$$

Conversely, this means that by considering a self-similar density distribution of the plasma, e.g., an exponential decrease, and taking into account that both probe beams propagate up to the same refractive index, the maximum-probed plasma density $n_e^{\max}$ differs by a factor of 4:

$$\tilde{n}_{515\,\mathrm{nm}} = \tilde{n}_{1030\,\mathrm{nm}} \iff \frac{515\,\mathrm{nm}^2}{1030\,\mathrm{nm}^2} = \frac{1}{4} = \frac{n_e^{\max}[1030\,\mathrm{nm}]}{n_e^{\max}[515\,\mathrm{nm}]}. \tag{5.5}$$

It follows that the difference of the shadow diameters of the two colors in figure 5.3 constitutes a strong evidence of a surface gradient of the investigated plasma density. Furthermore, the increasing difference of the shadow diameters with time indicates that the plasma gradient is also growing.

Assuming an exponential scalelength L_p of the plasma-density surface and radial symmetry, relation 5.5 is equivalent to

$$4 = \frac{n_0 \exp(-\frac{d[515\,\mathrm{nm}]/2 - R}{L_p})}{n_0 \exp(-\frac{d[1030\,\mathrm{nm}]/2 - R}{L_p})}.$$

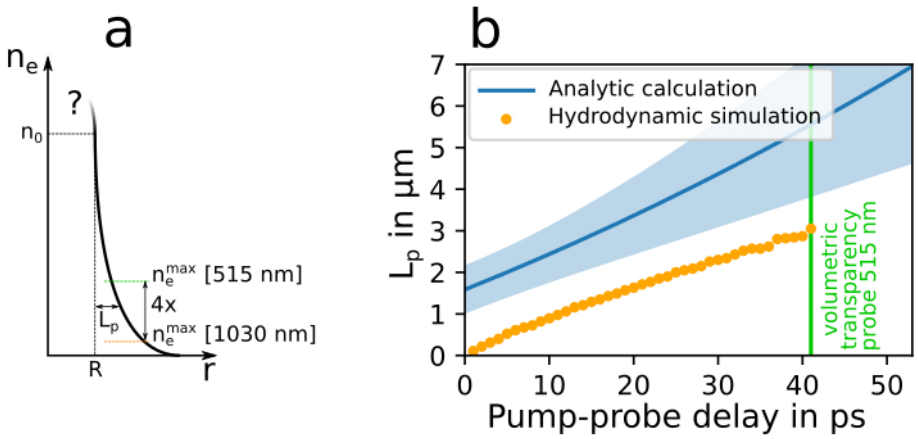

Figure 5.4.: **(a)** Sketch of an heuristic radial density distribution of the expanding plasma. The density distribution for radii $r < R$ is not known. A possible assumption of the density distribution close to the densities that are propagated by the probe-laser pulses $n_e[r] < n_e^{\max} \approx 0.1 n_c[\lambda] < n_0$ is an exponential decrease with the scalelength L_p. **(b)** Surface scalelength of the plasma density L_p versus pump-probe delay. The blue line is calculated via equation 5.6 from the polynomial fit of the measured shadow diameters (equations 5.7 and 5.8). The shaded area shows the propagation of uncertainty from the fits. The orange markers show the scalelength as it is measured from the density profile between $0.1 n_c[800\,\text{nm}]$ and $1/e \cdot 0.1 n_c[800\,\text{nm}]$ of a hydrodynamics simulation with an heuristic initial plasma temperature of 150 eV (figure 5.5 (a)).

d is the measured shadow diameter and n_0 is the plasma density at the radius R, for which the exponential scalelength starts (see sketch in figure 5.4 (a)). The relation directly gives

$$L_p = \frac{d[1030\,\text{nm}] - d[515\,\text{nm}]}{2 \cdot \ln 4}. \tag{5.6}$$

Second-order polynominal fits yield an interpolation of the measured data points of probe 515 nm and probe 1030 nm in figure 5.3

$$d[515\,\text{nm}] = (-6.58 \pm 0.79) \cdot 10^{-3} \cdot \tau^2 + (7.82 \pm 0.62) \cdot 10^{-1} \cdot \tau + (6.1 \pm 1.0), \tag{5.7}$$

$$d[1030\,\text{nm}] = (-5.54 \pm 0.97) \cdot 10^{-3} \cdot \tau^2 + (1.008 \pm 0.076) \cdot \tau + (10.5 \pm 1.3). \tag{5.8}$$

For both equations, the unit of the shadow diameter d and the pump-probe delay τ are µm and ps. With that, a continuous evolution of the scalelength L_p is calculated and displayed as blue line in figure 5.4 (b). The propagation of uncertainty of both polynomial fits is given by the blue-shaded area. The exponential scalelength increases approximately linearly in time with $dL_p/dt \approx 1 \cdot 10^5$ m/s. For comparison, the evolution of the scalelength of the plasma-density surface of a hydrogen plasma with a rod-like initial density distribution of 5 µm diameter and an initial plasma temperature of 150 eV as simulated by a hydrodynamics simulation, which is fitted to the probing data, is given by the orange markers. The expansion speed of the scalelength dL_p/dt is similar in both cases. A discussion is given in section 5.1.3.

5.1.2.3. Experimental uncertainties

Figure 5.3 shows shot-to-shot fluctuations of the shadow diameter for each delay settings and both colors. The fluctuations are caused by a combination of uncertainties from the target and the pump laser. Target uncertainties include local shot-to-shot changes of diameter and aspect ratio of the cross section on the sub-micron scale as well as local bow-like deformations along the jet axis with radii on the micron scale. A high-resolution-microscopy image of the cylindical jet target in figure 2.14 (a1) in section 2.2.2 exemplifies the uncertainties. Furthermore, the rapid evaporative freezing of the jet

at several hundred micrometers below the source introduces compositional and structural variations of the solid hydrogen [110]. The dark-field-microscopy image in figure 2.14 (a3) shows several bright spots within the otherwise transparent and non-scattering target bulk. This indicates translucent regions of the target bulk that could originate from inhomogeneous grain compositions, e.g., crushed hydrogen ice.
Concerning the pump-laser intensity, the primary source of shot-to-shot variation is the peak power with a relative fluctuation of 17 %. A dedicated measurement is presented in Appendix B. The RMS variation of the laser energy is about 1 % and the pointing jitter is negligible compared to the focal-spot size.

Another clear observation of the shadowgraphy data in figure 5.2 are filamentations at the rim of the measured shadows that are visible especially at long timescales. The occurrence of the filaments at laser intensities of about $5 \cdot 10^{20}\,\mathrm{W/cm^2}$ pump-laser-peak intensity is investigated in another thesis project, see Ref. [167]. However, at the end of this chapter, section 5.3.3 presents novel experimental data on the observation of the filaments at laser intensities between $10^{14}\,\mathrm{W/cm^2}$ and $10^{18}\,\mathrm{W/cm^2}$. The driving mechanism of the filament generation is not clarified yet. Compared to the overall expansion of the shadow diameter at delays between 0 ps and 41 ps, the filaments are a secondary effect and are ignored in the following evaluation.

5.1.3. Determination of the full target-density profile

Although several properties of the isochorically heated plasma are already estimated based on analytical relations in the previous section, a complete description of the plasma-density evolution, not only in the outer regions but also close to the center of the plasma, is desired on all time-scales of the experiment. To bypass the modeling of the non-thermal-equilibrium plasma dynamics that originate from isochoric heating by the laser pulse, the heating is approximated by a single heuristic initial temperature of the plasma column before expansion. Subsequently, the plasma expansion into vacuum is calculated utilizing a hydrodynamics simulation. The shadowgraphy observations justify the assumption of radial symmetry around the central vertical axis of the jet.

5.1.3.1. Estimates of the heuristic initial temperature

The heuristic initial temperature of the plasma column, i.e., the plasma temperature after isochoric heating by the laser, is ab initio not known. Three estimates to find the order of magnitude of the heuristic initial temperature from the experimental measurements are considered in the following.
First, the amount of hydrogen atoms in a cylindrical rod with 2.5 µm radius within the FWHM of the elliptical focal spot is given by

$$N = 30 \cdot n_c[800\,\mathrm{nm}] \cdot V = 30 \cdot 1.746 \cdot 10^{21}\,\mathrm{cm^{-3}} \cdot \pi \cdot (2.5\,\mu\mathrm{m})^2 \cdot 32\,\mu\mathrm{m} = 3.3 \cdot 10^{13}.$$

The laser energy incident on the same volume is approximately

$$E \approx \frac{0.24\,\mathrm{J}}{2} \cdot \frac{5\,\mu\mathrm{m} \cdot 32\,\mu\mathrm{m}}{19\,\mu\mathrm{m} \cdot 32\,\mu\mathrm{m}} = 32\,\mathrm{mJ},$$

which corresponds to an energy per atom of

$$E/N = 6\,\mathrm{keV}.$$

Assuming between 90 % and 99 % reflexion of the incident light, the residual energy per hydrogen atom E_H is between

$$E_H = 60\,\mathrm{eV} \text{ to } 600\,\mathrm{eV}.$$

The band gap of solid hydrogen (10.9 eV, [94]) and the ionization potential of atomic hydrogen (13.6 eV) are, in first order, negligible compared to both values. In summary, an initial heuristic temperature of the plasma column of several hundred eV is expected.

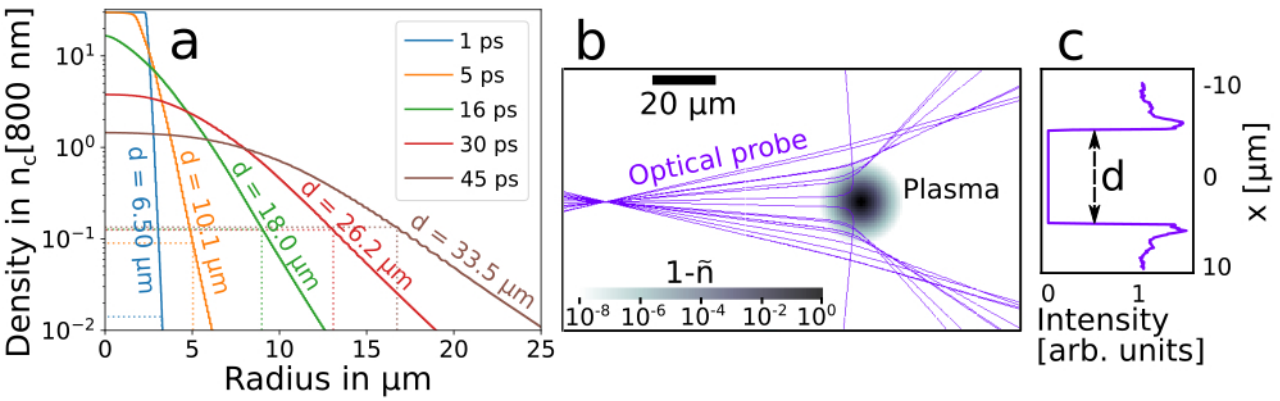

Figure 5.5.: **(a)** Figure copied from Rehwald et al. [168]. A hydrodynamics simulation shows the plasma-density evolution of a hydrogen column with an initial radius of 2.5 µm and an heuristic initial temperature of 150 eV. For each delay, a ray-tracing simulation calculates the shadow diameter d of probe 515 nm (vertical dotted lines). The crossing point of each vertical dotted line and the respective density profile of the plasma gives the maximum-probed density $n_e^{\max}[515\,\mathrm{nm}]$. **(b)** Figure copied from Yang et al. [208]. Exemplary top view of the object plane of the ray-tracing simulation: Each density distribution of fig. (a) is converted to a refractive-index distribution $\tilde{n}$ via equation 5.4 (gray colorscale). The refraction of the probe rays is visualized by purple lines. **(c)** Figure copied from Yang et al. [208]. Light distribution in the image plane of the ray-tracing simulation. The calculated shadow diameter d is measured at half of the unperturbed background intensity (0.5 arb.units).

The second estimate takes the experimental shadowgraphy measurement into account. Considering particle conservation and assuming a box-like plasma expansion, i.e., a box-like distribution of density at 0 ps and a box-like distribution of density to the time of volumetric transparency at 41 ps (probe 515 nm) and 76 ps (probe 1030 nm), the expansion speed is calculated from the initial radius of the target and the shadowradius at the respective delay of volumetric transparency. The shadow diameters are given by the fitted polynomials 5.7 and 5.8. The approximation yields

$$V[515\,\mathrm{nm}] = \frac{27.1\,\mu\mathrm{m} - 5\,\mu\mathrm{m}}{2\cdot(41\,\mathrm{ps} - 0\,\mathrm{ps})} = 2.7\cdot 10^5\,\mathrm{m/s}$$

and

$$V[1030\,\mathrm{nm}] = \frac{55.1\,\mu\mathrm{m} - 5\,\mu\mathrm{m}}{2\cdot(76\,\mathrm{ps} - 0\,\mathrm{ps})} = 3.3\cdot 10^5\,\mathrm{m/s}.$$

Setting $V \approx C_s$ and using the equation $C_s = \sqrt{k_B\,T_e\,Z/m_p}$, the corresponding approximate heuristic initial temperatures are given by

$$k_B\,T_e[515\,\mathrm{nm}] = 760\,\mathrm{eV}$$

and

$$k_B\,T_e[1030\,\mathrm{nm}] = 1140\,\mathrm{eV},$$

with the proton mass m_p and $Z = 1$. Both results are at the upper limit of the first approximation.

The third estimate uses $dL_p/dt \approx 1\cdot 10^5$ m/s as a measure of the ion sound speed C_s. This approach derives a heuristic initial temperature at the lower end of the first approximation

$$k_B T_e \approx \frac{(dL_p/dt)^2\,m_p}{Z} = 105\,\mathrm{eV}. \tag{5.9}$$

5.1.3.2. Hydrodynamics simulation

Several software tools of hydrodynmics simulations are available. For details refer to section 2.1.3.2. In the following, we used *FLASH* with one-dimensional radial symmetry and the implemented EOS

of hydrogen [71]. The simulation is initialized with a plasma column of $30\,n_c[800\,\mathrm{nm}]$ density and a radius of 2.5 µm. The heuristic initial temperature is initialized homogeneously throughout the plasma column.
For a heuristic initial temperature of 150 eV, the density evolution of the plasma column is presented in figure 5.5 (a). The early delays of 1 ps and 5 ps show that the sharp edge of the initial plasma column is smeared out and a density gradient emerges on the plasma surface. Subsequently, the density gradient increases and the density within the initial bulk of the plasma is reduced. At 16 ps delay, the peak density is already significantly decreased below $30\,n_c[800\,\mathrm{nm}]$. Between 30 ps and 45 ps delay, the peak density drops below the critical density of the probing wavelength $n_c[515\,\mathrm{nm}] = 2.4\,n_c[800\,\mathrm{nm}]$.

5.1.3.3. Ray tracing

To compare the results of the hydrodynamics simulation to the experimentally measured shadowgraphy data, the shadowformation of the optical-probe beams is modeled for each plasma-density profile. A step-by-step ray tracing of the probe light through the plasma is needed, as the shadowformation is governed by refraction in the density gradients within the undercritical regions of the plasma (refer section 4.2). Synthetic shadowgrams of each plasma-density distribution are calculated by using the software *ZEMAX* (Zemax 13 Release 2 SP6 Professional (64-bit)). The calculation includes the propagation of probe light through the microscopy system as well as the refraction of the plasma. For every timestep of the hydrodynamics simulation, the dispersive properties of the plasma are derived as follows. Each radial density profile is transformed into a two-dimensional distribution of refractive indices via equation 5.4. The critical density n_c depends on the backlighter wavelength and the refractive indices $\tilde{n}^{515\,\mathrm{nm}}$ and $\tilde{n}^{1030\,\mathrm{nm}}$ are calculated separately. For each backlighter wavelength, the refractive-index distribution is inserted to the object plane of the microscopy system of the ray-tracing simulation. An exemplary top view of the object plane is presented in figure 5.5 (b). The microscope is placed on the right side and the probe rays propagate from left to right. Their refraction in the plasma is illustrated by the purple lines.
The ray-tracing simulation calculates a shadowgram in the image plane of the setup. A lineout of the derived intensity distribution is given in figure 5.5 (c). The graph shows the formation of a shadow with sharp edges around the position of the plasma distribution (central axis at $x = 0$). In congruence to the experimental data, refraction on the plasma-density gradients leads to an increased intensity at the outer rim of the shadow edges. The shadow diameter d is measured at half of the unperturbed background intensity (0.5 arb.units). For each radial density profile of figure 5.5 (a), the expected shadow diameter is given together by a vertical dotted line.
The simulated evolution of the shadow diameter d of probe 515 nm (blue) and probe 1030 nm (red) are presented in figure 5.6 (b). The simulation data is represented by the dot markers. For comparison, the experimental data is given by cross makers. In consistency to the experimental observation, the shadow diameter of probe 1030 nm is larger than the shadow diameter of probe 515 nm for all delays.

5.1.3.4. Fitting the plasma temperature

The combination of hydrodynamics simulations and ray-tracing simulations allows to fit the heuristic initial temperature of the hydrodynamics simulation to the measured shadow diameters at delays before volumetric transparency, i.e., before 41 ps delay. Figure 5.6 shows the results for heuristic initial temperatures between 100 eV and 430 eV. For 430 eV (fig. 5.6 (e)), the simulated shadow diameters (dot markers) of probe 515 nm (blue) and probe 1030 nm (red) increase too fast compared to the experimental data (cross markers). For 100 eV (fig. 5.6 (a)), however, the simulated shadow diameters increase too slow. The best-matching initial temperature is 150 eV, which is displayed in figure 5.6 (b).
For the 150 eV simulation and in agreement to the measurement of volumetric transparency of probe 515 nm at 41 ps and of probe 1030 nm at 76 ps, the simulated peak density of the target n_{peak} is decreased below the critical density of each backlighter wavelength for the corresponding delay:

$$\frac{n_{\mathrm{peak}}[41\,\mathrm{ps}]}{n_c[515\,\mathrm{nm}]} = \frac{1.8 \cdot n_c[800\,\mathrm{nm}]}{2.4 \cdot n_c[800\,\mathrm{nm}]} = 0.75$$

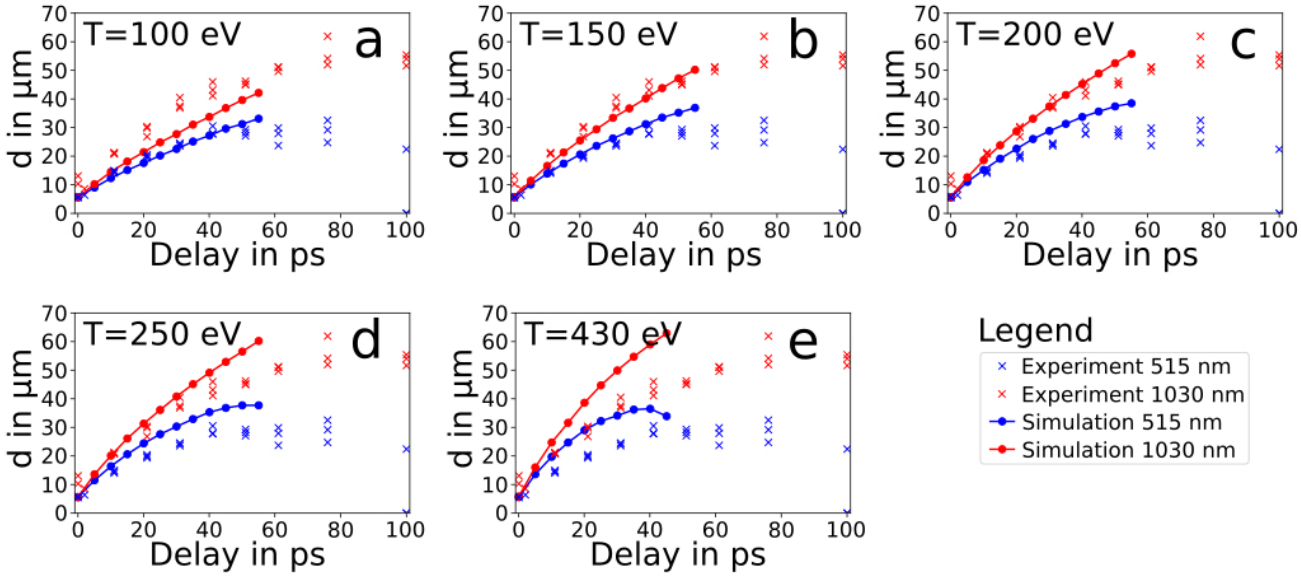

Figure 5.6.: Results of hydrodynamics simulations and ray-tracing simulations with different heuristic initial temperatures between 100 eV and 430 eV (dot markers). For each graph, the experimental data (fig. 5.3) is given for reference (cross markers).

$$\frac{n_{\text{peak}}[76\,\text{ps}]}{n_c[1030\,\text{nm}]} = \frac{0.45 \cdot n_c[800\,\text{nm}]}{0.6 \cdot n_c[800\,\text{nm}]} = 0.75.$$

The consistency of both fractions indicates a similar plasma distribution at 41 ps and 76 ps with respect to the critical density of each wavelength and supports the agreement between simulation and experiment. However, ray-tracing simulations at delays close to volumetric transparency need to be interpreted with caution, as the rays propagate plasma densities between n_c and $0.1 \times n_c$, for which a proper treatment of the dispersion relation of the plasma is needed to include absorption. The simulated peak density of $0.75\,n_c[\lambda]$ at the delay of volumetric transparency is in good agreement to the experimental and simulation results at $5.4 \cdot 10^{21}\,\text{W/cm}^2$ peak intensity in section 4.2. Here, the PIC simulation results at a delay close to the observation of volumetric transparency feature an average electron density within the initial target bulk of $0.64\,n_c[515\,\text{nm}]$.
In future work, an adapted equation of the refractive index beyond equation 5.4 will allow the usage of the point of volumetric transparency as a second boundary condition in addition to the expansion speed of the shadow diameter. Furthermore, more free parameters of the heuristic model of the plasma column that is used as initial condition for the hydrodynamics simulation, i.e., a variation of the initial radius or the inclusion of an initial scalelength on the plasma surface, are needed to improve the fit to the experimental data in the future.

Figure 5.5 (a) shows the simulated shadow diameters as vertical dotted lines. The crossing point of each dotted line with the corresponding plasma-density profile reflects the maximum probed density $n_e^{\text{max}}[515\,\text{nm}]$. Between 5 ps and 45 ps delay, $n_e^{\text{max}}[515\,\text{nm}]$ is around $0.1 \times n_c[800\,\text{nm}] = 0.04 \times n_c[515\,\text{nm}]$. For smaller delays, $n_e^{\text{max}}[515\,\text{nm}]$ is reduced. Rays that contribute to the formation of the shadow propagate the plasma at densities lower than $n_e^{\text{max}}[515\,\text{nm}]$ only. All density profiles in figure 5.5 (a) show that the corresponding densities are exponentially decreasing. The scalelength of the plasma between $0.1\,n_c[800\,\text{nm}]$ and $1/e \cdot 0.1\,n_c[800\,\text{nm}]$ versus delay is shown in figure 5.4 (b) by the orange markers. The simulated evolution of the scalelength is similar to the evolution of the scalelength that is calculated analytically from the experimental data (refer section 5.1.2). An obvious discrepancy is the initial offset of the analytically calculated scalelength of 1.59 µm at 0 ps delay. Taking the uncertainty of the polynomial fit (eq. 5.7 and eq. 5.8) and the spatial resolution limit of both probe beams into account, the uncertainty of the measurement of the initial scalelength is 1.65 µm.
The discrepancy is an indication of initial target pre-expansion by the leading edge of the pump laser or by an intrinsic inhomogeneity of the target surface. Both circumstances are not considered in the

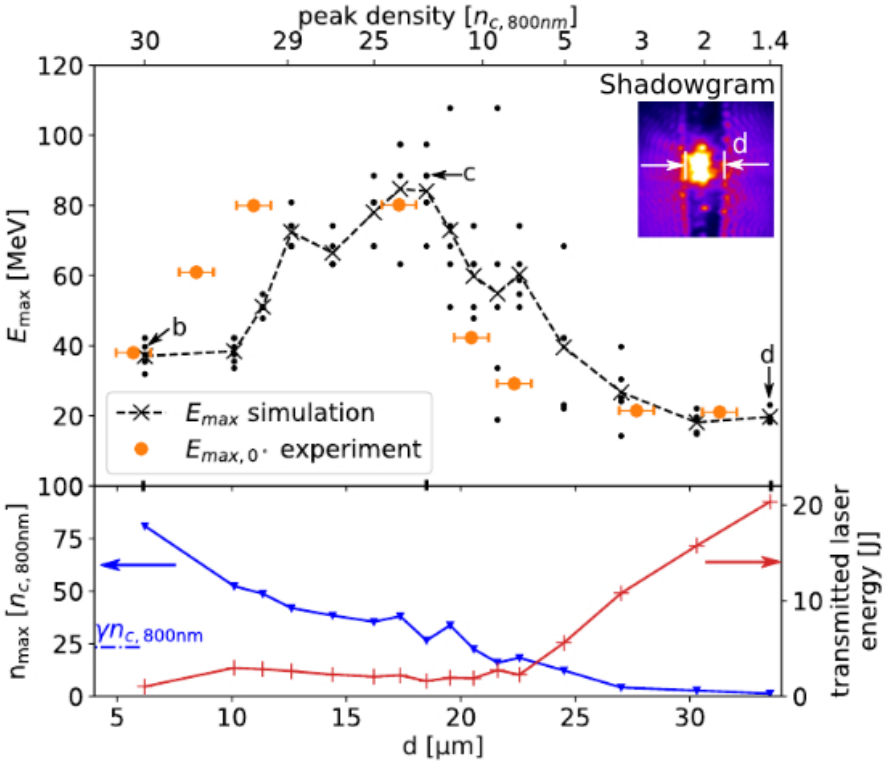

Figure 5.7.: Figure copied from Rehwald et al. [168]. The top panel shows measured maximum proton energy (orange dot markers) versus the measured shadow diameter (bottom x axis) of an experiment of laser-proton acceleration that utilizes all-optical target-density tailoring to switch between different acceleration regimes (for details refer to section 2.2.5). For each high-intensity laser shot, the shadow diameter is measured at 0 ps pump-probe delay, i.e., to the arrival of the pump-laser peak. An exemplary shadowgram is given in the top-right corner. Simulation results (cross markers in the top panel and all data of the bottom panel) are calculated by three-dimensional PIC simulations. The PIC simulations are initialized with targets of different peak density (top x axis) and the corresponding density distribution from fig. 5.5 (a). A mapping of the experimental data (bottom x axis) to the simulation data (top x axis) is enabled by the measured shadow diameter and the hybrid fit of hydrodynamics simulations and ray-tracing simulations that is presented in section 5.1.3.

assumption of a sharp-edged hydrogen column as initial condition of the hydrodynamics simulation. However, the analytic calculation of the initial scalelength from the experimental data yields a high relative error of 104 %. PIC simulations of the isochoric-heating process show that an initial scalelength of the target before the interaction with the laser peak significantly changes the bulk-electron temperature after isochoric heating, see Ref. Yang et al. [208]. Consequently, a precise determination of target pre-expansion and the initial density distribution of the jet target are needed for quantitatively valid simulation approaches. In the future, the best-matching initial scalelength will be introduced as a second free parameter of the hybrid fit of hydrodynamics simulations and ray-tracing simulations to the experimental data.

5.1.4. Utilization for enhanced laser-driven proton acceleration

In the overall project of laser-driven proton acceleration from cryogenic hydrogen-jet targets, all-optical target-density tailoring by ultra-short relativistic laser pulses is utilized to transform the solid-density hydrogen-jet target into a nearcritical-density target. The achieved control over the target system allows to significantly improve the proton-acceleration performance. A detailed explanation of the overall experiment and it's interpretation by PIC simulations is given in section 2.2.5. Target-density

tailoring is realized via a prepulse before the arrival of the ultra-relativistic DRACO-PW-laser pulse. The peak intensity of the prepulse is $5 \cdot 10^{17}\,\mathrm{W/cm^2}$ and the pulse duration is 55 fs, i.e., similar to the ultra-short relativistic laser pulse previously discussed in this section. In the following, the relevance of the presented results to the interpretation of the experiment at ultra-relativistic laser-peak intensities is highlighted.
Figure 5.7 presents the main results of the experiment. For each measured maximum proton energy, the shadow diameter of the target to the time of the arrival of the ultra-relativistic laser peak is measured (see exemplary shadowgram in the top-right corner). This enables a sorting of the measured proton energies (orange dot markers) by the shadow diameter d (lower x axis), independent of shot-to-shot jitters.
The interpretation of the experimental data is provided by a series of PIC simulations. Each PIC simulation, however, requires initial conditions of the target density, as the computable timeframes allow to capture the ultra-relativistic laser-target interaction only. Here, the density profiles shown in figure 5.5 (a) are utilized. They link each measured shadow diameter d to the full target-density distribution and by this provide reasonable initial conditions for the PIC simulations. The hybrid fit of hydrodynamics simulations and ray-tracing simulations from section 5.1.3 provides a conversion of the lower x axis (shadow diameter) of figure 5.7 to the upper x axis (peak density of the target) of figure 5.7. Thus, the results of section 5.1.3 and the time-resolved shadowgraphy data from the experiment at ultra-relativistic peak intensities enable the quantitative comparison of the experimental and simulation data of proton acceleration.
Comparing the simulated and measured maximum proton energies of figure 5.7, the peak of the simulated data is slightly shifted to the right side. This is probably caused by the non-considered initial scalelength of the target, which is discussed in the previous section in the context of figure 5.4 (b). Further investigations are currently performed and details are available in Ref. Yang et al. [208].

In conclusion, the results demonstrate that all-optical target-density tailoring of the cryogenic hydrogen-jet target allows for a controlled manipulation of the plasma density to the nearcritical regime. The combination of proton acceleration with off-harmonic optical-shadowgraphy diagnsotics provides superb control over the laser-target interaction in the regime of ultra-relativistic laser intensities.

5.2. Testbed platform to benchmark PIC simulations

Today, because of the leading-edge-driven target pre-expansion, PIC simulations of ultra-relativistic laser-solid interactions lack of information on the exact initial conditions of the interaction of the target with the final laser peak. The interaction products, e.g., accelerated proton energy, the amount of transmitted light and the energy distribution of electrons, most often have, however, a nonlinear dependency with respect to these initial conditions. Usually, minor modifications of the target parameters or the envelope of the laser pulse generate different properties of the interaction products. Consequently, in a comparison to experimental results, PIC simulations are often used for qualitative explanations only. As introduced in section 2.1.3, start-to-end simulations with quantitative agreement to different experimental boundaries require thorough modeling at all laser-intensity levels of the leading edge.
The modeling capabilities of currently available simulation tools requires further research especially with respect to two different laser-intensity levels. The first one is the starting point of the laser-target interaction at laser intensities below about $10^{14}\,\mathrm{W/cm^2}$ and the second one is target pre-expansion and pre-heating at laser intensities between $10^{16}\,\mathrm{W/cm^2}$ and $10^{19}\,\mathrm{W/cm^2}$. Target pre-expansion at laser intensities between $10^{13}\,\mathrm{W/cm^2}$ and $10^{16}\,\mathrm{W/cm^2}$, however, is comparably well understood and relies on radiation-hydrodynamics simulations.
Investigations about the starting point of the laser-target interaction are discussed in the context of *laser-induced breakdown (LIB)* in chapter 3 of this thesis. However, the presented results of this chapter 5 provide the opportunity to benchmark and improve PIC-simulation tools in the collisional regime between $10^{16}\,\mathrm{W/cm^2}$ and $10^{19}\,\mathrm{W/cm^2}$ via a novel testbed platform that is constituted by the

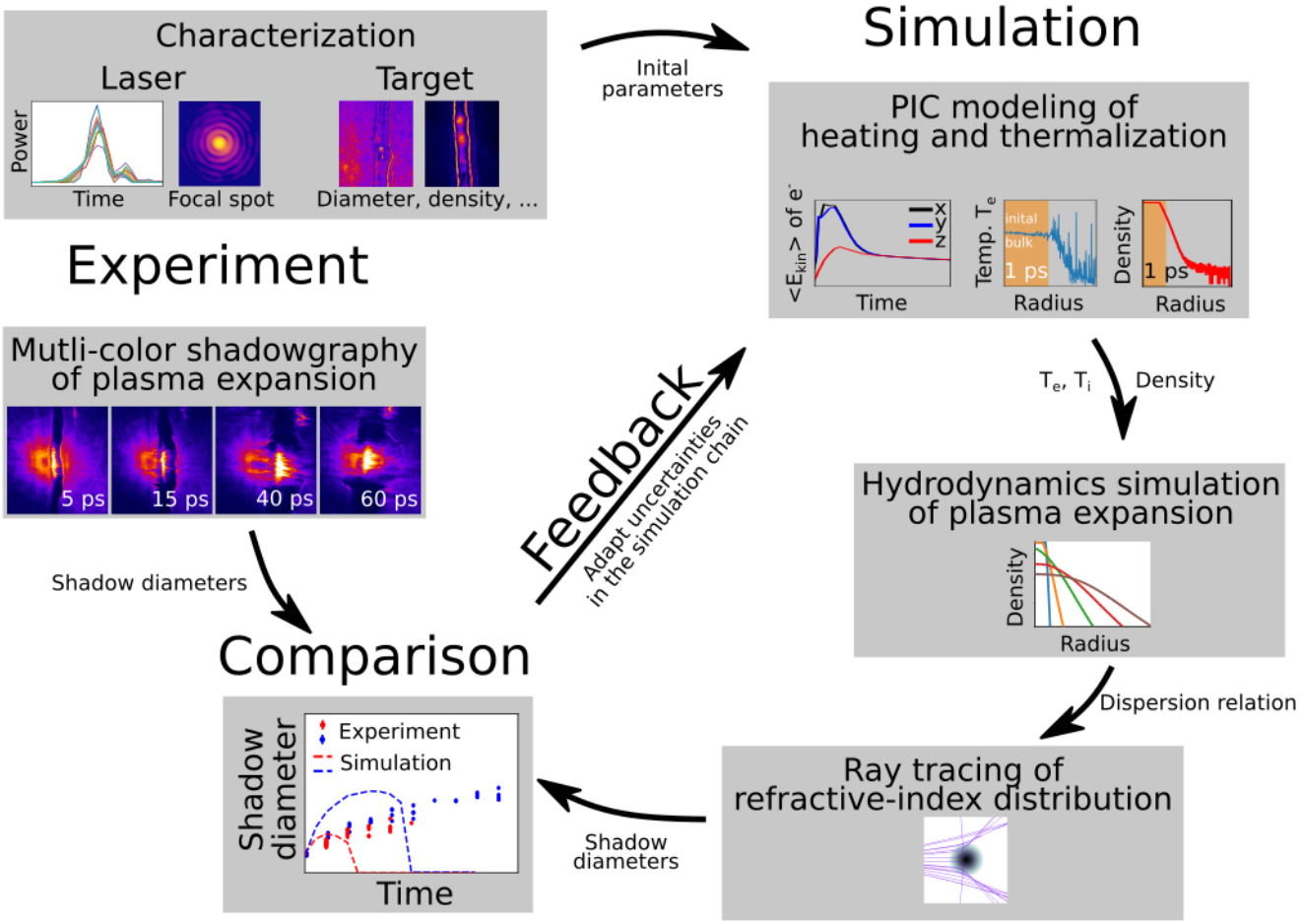

Figure 5.8.: Flow chart of the testbed platform to benchmark PIC simulations in the collisional laser-intensity regime between $10^{17}\,\mathrm{W/cm^2}$ and $10^{19}\,\mathrm{W/cm^2}$ by experiments with the hydrogen-jet target and time-resolved optical shadowgraphy. Several insets of the figure are adapted from Ref. Yang et al. [208].

cryogenic hydrogen-jet target and multi-color optical-shadowgraphy diagnostics.

The cryogenic hydrogen-jet target features ideal properties to benchmark PIC simulations. It provides comparably simple ionization dynamics with only a single bound electron and the low initial plasma density of $30\,n_c[800\,\mathrm{nm}]$ enables PIC simulations in full dimensionality utilizing today's computer resources. Experimentally, the self-replenishing target delivery and the stand-alone target geometry are easily combined with high-repetition-rate diagnostics like time-resolved optical shadowgraphy and enables a statistical approach of data evaluation. Furthermore, testbed experiments at pump-laser intensities between $10^{16}\,\mathrm{W/cm^2}$ and $10^{19}\,\mathrm{W/cm^2}$ do not require a fully amplified Petawatt laser. The operation of DRACO 150TW without a usage of the final laser amplifier provides sufficient pulse energies and a repetition rate of 10 Hz in target chamber I1. This allows for the generation of large data sets and extended parameter scans with hundred thousands of shots in several hours.
A large parameter scan of plasma-expansion dynamics with different pump-laser-peak intensities is presented and discussed in the next section 5.3. In this section 5.2, one particular parameter setting shows an example of the testbed platform to experimentally benchmarking PIC-simulation tools in the regime of $10^{18}\,\mathrm{W/cm^2}$. As the finalization of the results of this project is still ongoing, only the concept of the testbed platform is sketched here. The final results of the project are available in Ref. Yang et al. [208].

The flow chart of the testbed platform, i.e., the experimental measures and the simulation chain to reproduce the experimental data quantitatively, is sketched in figure 5.8. On the experimental side, a statistical evaluation of the target and laser parameters yields the initial conditions of the laser-target interaction with a mean and a standard deviation of the different quantities. For the laser, this includes the variation of the spatial properties, which are minimized by using a large focal spot, in this case an Airy-pattern. The mean and variation of the laser energy is determined by a power meter in the target chamber. The temporal properties, i.e., peak power and laser contrast, are measured with thousands of shots at 10 Hz and at full laser energy (see Appendix B). The mean and standard deviation of the target properties are inferred by high-resolution optical microscopy. The data shows variations of the target diameter, changes of the local geometric properties and it visualizes inner structural changes of the target.
The well-defined initial conditions enable controlled high-intensity laser-plasma interactions at $2.1 \cdot 10^{18}\,\mathrm{W/cm^2}$ peak intensity. Measurements of the plasma expansion are derived by time-resolved multi-color optical shadowgraphy at 258 nm and 515 nm wavelength. A time-delay scan similar to the one described earlier in the chapter is conducted and yields the shadow diameter of both wavelength and for different delays (see *Comparison* in figure 5.8).
The final goal of the testbed platform is the quantitative reproduction of the experimental results purely by using simulation tools and starting conditions in agreement to the measured initial conditions. The simulation chain starts with a PIC simulation of the laser heating of electrons and the subsequent thermalization process. The calculated thermalized, i.e., Maxwellian, temperature of ions T_i and electrons T_e of the target bulk and the corresponding density distribution of the specific timestep, e.g., at 1 ps, is then transfered to a hydrodynamics simulation. On the basis of the equation of state, the hydrodynamics simulation calculates the process of plasma expansion in the timeframe of the pump-probe delays of the experiment, i.e., several tens of picoseconds. In a next step, the dispersion relation allows to convert the electron-density profiles to refractive-index distributions. A simulation of the shadow formation by ray-tracing simulations (e.g. by *Zemax*), which resembles the microscope of the experiment, enables the calculation of the simulated shadow diameters in the image plane. A comparison of the simulated shadow diameters and the measured shadow diameters (see *Comparison* in figure 5.8) allows to quantify the deviation of experiment and simulation.

Discrepancies between experiment and simulation can have two different reasons. On one side, the uncertainties of the initial conditions need to be considered in the simulation chain. As mentioned, high-intensity-laser-plasma interactions are non-linear systems and minor changes of the initial conditions can induce strong changes of the final results. On the other side, if the influences of the initial

conditions is clarified, discrepancies between experiment and simulation are either caused by inadequate simulation settings or imprecise physics models of the simulation tools. It needs to be stressed that *all* three stages of the presented simulation chain feature uncertainties and approximations. However, as explained in the following, the PIC simulation features the highest number of uncertainties.
For the ray-tracing simulations, the validity of the dispersion relation needs to be considered. As mentioned previously, this is especially important in cases where rays propagate plasma densities between $0.1\,n_c$ and $1\,n_c$. The hydrodynamics simulations need to be able to simulate different temperatures of the electron and the ion population. Here, special emphasis needs to be given to the appropriate equation of state and the heat-transfer rate between the two populations. Furthermore, if simulations are performed with reduced dimensionality, the influence of lateral heat transfer needs to be clarified.
The uncertainties of the PIC simulation can be divided into two parts. The first part is the laser-heating of electron and the second part is the thermailzation of hot electrons to a Maxwellian electron- and ion-temperature distribution. For both parts, the influence of the grid size, the number of macro-particles and the dimensionality of the simulation, e.g., three-dimensional or two-dimensional with a circle or a stripe as target model, need to be considered. For two-dimensional simulations, particular attention should be given to the dissipation of energy to regions that lie beyond the boundary conditions of the simulation. The thermalization process in PIC simulations is generally modeled by collision models. As there is no solid-state lattice in a PIC simulation, collisions occur between electrons and electrons, electrons and ions and ions and ions. The colliding species of electrons are either the laser-heated hot electrons or the lower-energetic return current electrons. For both, an appropriate model of the collision frequency of electron-electron and electron-ion collisions is needed. Besides the conventionally used *Spitzer-model* of Coulomb-Coulomb collisions for high electron temperatures and it's sensitivity to the chosen cutoff of the Coulomb-logarithm, an artificial *low-temperature-collision correction* of electron-phonon collisions has proven to be useful at electron temperatures below about 100 eV, for details see references [58] and [156]. Furthermore, energy losses by radiative cooling are usually not captured by PIC simulations and the relevance can be checked via calculation tools like *FLYCHK* [1]. Overall, the comparison of different PIC-simulation tools is convenient and aids to check the reliability of specific results.

In summary, the presented concept of the testbed platform in combination with statistically significant amounts of data will allow to experimentally benchmark and improve the physics models of todays PIC-simulation tools in the laser-intensity regime between $10^{16}\,\mathrm{W/cm^2}$ and $10^{19}\,\mathrm{W/cm^2}$. By this, the platform constitutes an opportunity to improve modeling capabilities of target pre-expansion and pre-heating in start-to-end simulations of ultra-relativistic laser-solid interactions.
In the future, an upgrade of the experiment by additional high-repetition-rate diagnostics like electron and proton spectrometers is readily available and will enable the generation of statistically relevant boundary conditions to benchmark different endpoints of the simulation chain. Furthermore, different target materials and compositions are already commissioned and will enable insight to specific issues of physics models of PIC simulations. For example ionization dynamics of inner-shell electrons can be investigated via cryogenic Argon-jet targets and multi-species effects can be investigated via cryogenic mixtures of hydrogen and deuterium. Finally, the testbed platform are ideally suited to prepare physics cases of high-energy-density experiments at facilities like the *Helmholtz International Beamline for Extreme Fields (HIBEF)* at the european XFEL [3].

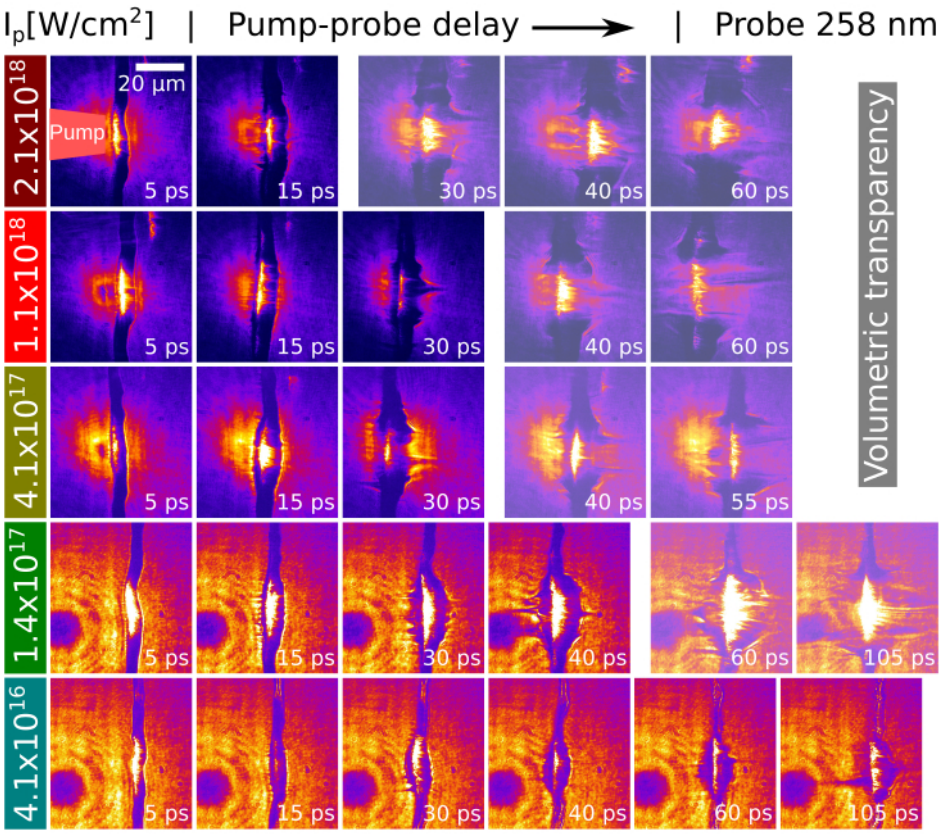

Figure 5.9.: Time-delay scans of shadowgraphy of the cylindrical hydrogen-jet target as captured by probe 258 nm. Each line presents results from a different pump-laser-peak intensity I_p for a constant pump-laser-pulse duration of about 30 fs. Shadowgrams with the observation of volumetric transparency are given with a white shade. Parasitic plasma emission is observed by saturated pixels of the camera (white color) in the center of each shadowgram. The position of the plasma emission is restricted to the front side of the target during the interaction with the pump laser.

5.3. Future possibilities of all-optical target-density tailoring

A Master-thesis project (Ref. [15]) that was supervised within this thesis project explored a large parameter scan of plasma-expansion dynamics of the cylindrical hydrogen-jet target for different pump-laser-peak intensities. The setup and the experimental results are summarized in Appendix G. The following section highlights experimental results that demonstrate the possibilities of all-optical target-density tailoring. The experimental setup utilizes two synchronized optical probe beams with 258 nm and 515 nm wavelength in a 90° geometry to the pump-laser beam. A high-resolution objectives allows for simultaneous acquisition of shadowgrams at both wavelength. The peak intensity of the pump laser is variable by changing the laser-beam energy. The FWHM of the pump-laser focal spot is 14 µm.

5.3.1. Pump-laser intensities between 10^{16} and 10^{18} W/cm^2

Time-delay scans of shadowgraphy captured by probe 258 nm and probe 515 nm for different pump-laser-peak intensities I_p and a pump-laser-pulse duration of about 30 fs are performed and representative data is displayed in figure 5.9. Like in the experiment of section 5.1.2, the evolution of the shadow appears to be mostly symmetric on the front and on the rear side of the target (neglecting filamentations on the front side). Pump-probe delays, for which volumetric transparency is observed, are given with a white shade. We observe that the point of volumetric transparency shifts to earlier delays for an increased pump-laser-peak intensity. The observation is quantified in figure 5.10 (f). The *upper bound* is given by the delay for which volumetric transparency is observed and the *lower*

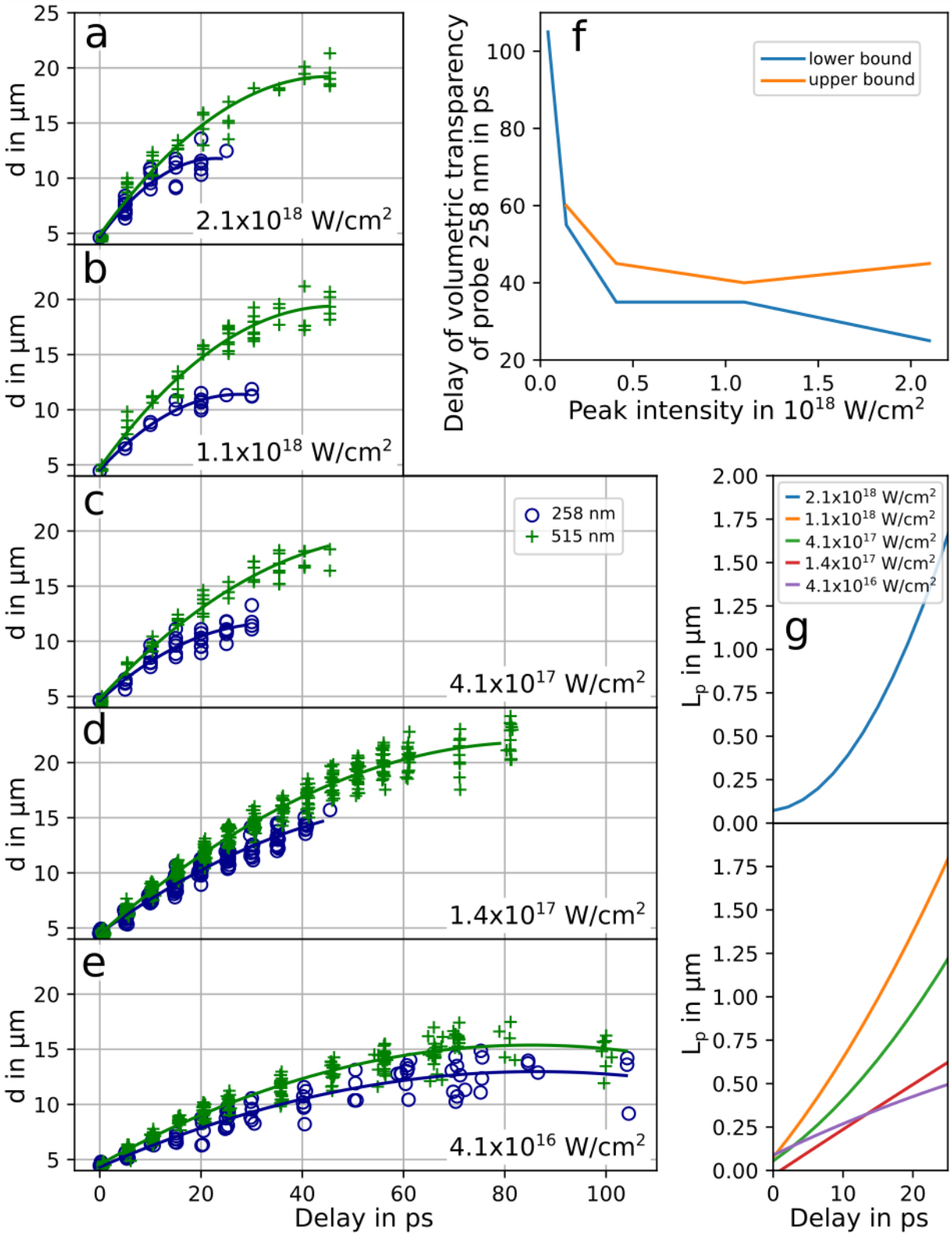

Figure 5.10.: **(a) - (e)** Figures copied from [15]. Shadow diameter d as measured by probe 258 nm and probe 515 nm versus pump-probe delay for different pump-laser-peak intensities (lower-right corner of each graph). The pump-laser-pulse duration is about 30 fs. **(f)** Delay for which volumetric transparency is observed versus pump-laser-peak intensity. **(g)** Figure copied from [15]. Exponential scalelength of the surface-density gradient L_p versus pump-probe delay as calculated from figures (a) to (e) via equation 5.6.

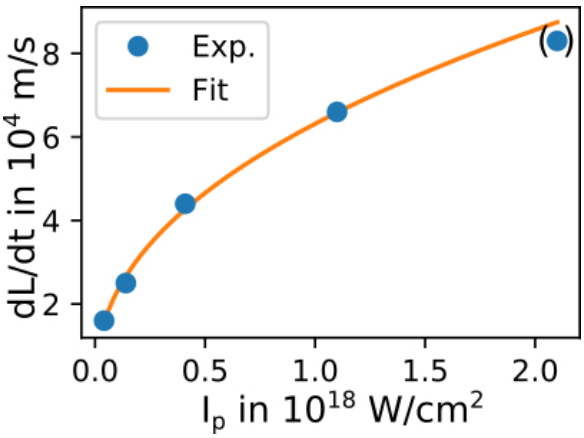

Figure 5.11.: Expansion velocity of the scalelength dL_p/dt versus peak intensity of the pump laser I_p. The fit yields a proportionality of $dL_p/dt \propto I_p^{0.44}$ (equation 5.10).

bound gives the closest delay for which no volumetric transparency is observed. The actual starting point of volumetric transparency is located between the two bounds. The delay of volumetric transparency is approximately constant at intensities between $4.1 \cdot 10^{17}\,\mathrm{W/cm^2}$ and $2.1 \cdot 10^{18}\,\mathrm{W/cm^2}$. For a peak intensity of $1.4 \cdot 10^{17}\,\mathrm{W/cm^2}$, the delay of volumetric transparency shifts to longer delays. The time-delay scan at $4.1 \cdot 10^{16}\,\mathrm{W/cm^2}$ indicates further increase of the delay of volumetric transparency, however, the captured timeframe is not enough to actually observe volumetric transparency. Therefore, only a lower bound is given.
Figures 5.10 (a) to (e) presents the measured shadow diameter of both probe beams versus pump-probe delay for different peak intensities. Quadratic fits to the data (solid lines) enable an interpolation and the identification of trends. As described previously, a difference of the diameter of both probing colors indicates a density gradient on the surface of the plasma. A comparison of the data at different pump-laser-peak intensities shows that the density gradient increases with pump-laser intensity. To demonstrate the observation, we assume an exponential decrease of the plasma density and calculate the respective scalelengths L_p via equation 5.6. Figure 5.10 (g) presents the results. Except for the case of highest peak intensity, all cases show a linear increase of L_p with time. As visualized in figure 5.11, the expansion velocity of the scalelength dL_p/dt increases with pump-laser intensity. A power fit yields

$$\frac{dL_p}{dt}[10^4\,\mathrm{m/s}] = 6.3 \cdot I_p[10^{18}\,\mathrm{W/cm^2}]^{0.44}\,. \tag{5.10}$$

For $2.1 \cdot 10^{18}\,\mathrm{W/cm^2}$ peak intensity, the temporal evolution of L_p in figure 5.10 (g) features a quadratic trend. A linear interpolation between 10 and 25 ps delay yields $dL_p/dt = 8.3 \cdot 10^4\,\mathrm{m/s}$. As the evaluation of dL_p/dt is different than for the lower peak intensities, figure 5.11 shows the data point in brackets. Furthermore, it is not included to the fit in equation 5.10.
For a pump-laser-peak intensity of $1.5 \cdot 10^{18}\,\mathrm{W/cm^2}$, section 5.1.2 derives an expansion velocity of the scalelength of $dL_p/dt = 1 \cdot 10^5\,\mathrm{m/s}$. Compared to the results of figure 5.11, the value is about 30 % higher than what would be expected by the fitted scaling. Conversely, the scaling of equation 5.10 yields $dL_p/dt = 1 \cdot 10^5\,\mathrm{m/s}$ for a peak intensity of $I_p = 2.9 \cdot 10^{18}\,\mathrm{W/cm^2}$. Considering that both experiments are conduced with different probe wavelength and pump-laser beams in different experimental chambers, the disagreement can be considered as small. However, a future evaluation of the here presented data via a hybrid of hydrodynamics simulations and ray-tracing simulations like in section 5.1.3 will enable more conclusive results.

5.3.2. Pump-laser intensities between 10^{14} and $10^{16}\,\mathrm{W/cm^2}$

Pump-laser intensities between $10^{14}\,\mathrm{W/cm^2}$ and $10^{16}\,\mathrm{W/cm^2}$ resembles a transition between the regime of plasma physics and the regime of laser-induced breakdown. The transition regime features laser-heated electron energies in the range of the binding forces of the atoms and perturbative approaches of modeling fail due to the coexistence of strongly-correlated solid-state matter and collective plasmonic

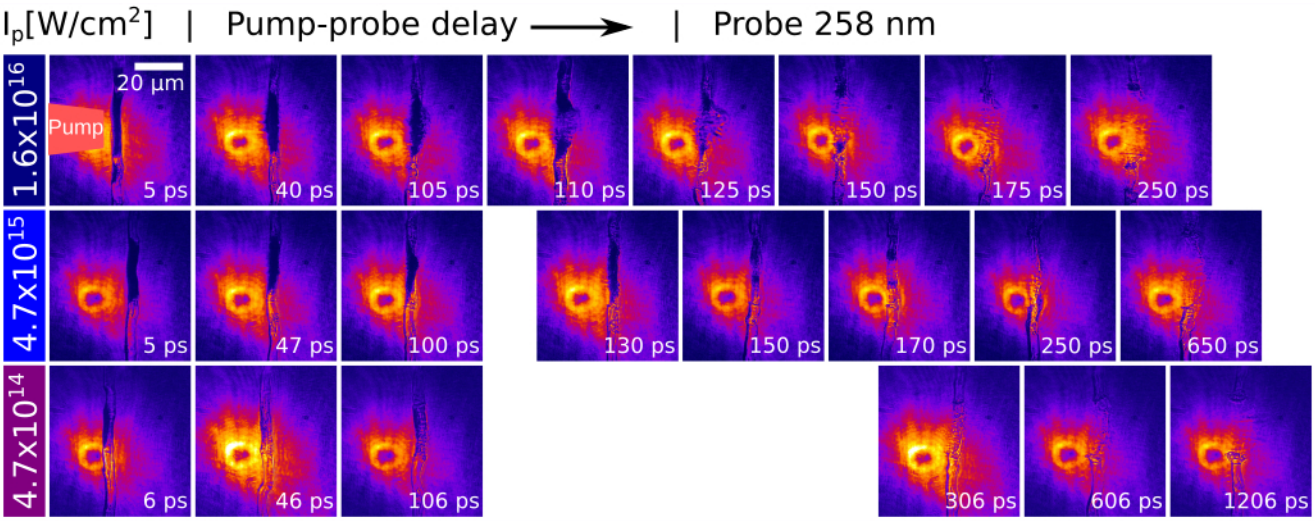

Figure 5.12.: Time-delay scans of shadowgraphy of the cylindrical hydrogen-jet target captured by probe 258 nm. Each line gives a different pump-laser-peak intensity I_p. The pump-laser-pulse duration is about 30 fs.

responses of the ionized material. Figure 5.12 shows time-delay scans of shadowgraphy for pump-laser-peak intensities between $1.6 \cdot 10^{16}\,\mathrm{W/cm^2}$ and $4.7 \cdot 10^{14}\,\mathrm{W/cm^2}$.
For $1.6 \cdot 10^{16}\,\mathrm{W/cm^2}$ and 5 ps delay, the target shows a large area that features LIB. The small island of blackened target area on the bottom of the shadowgram stems from the first side maximum of the Airy-pattern-shaped focal spot. Subsequently, the delays of 40 ps and 105 ps show an expansion of the blackened target area. In contrast to the plasma expansion at higher peak intensities, the shadow edges are dilute. Between 110 ps and 150 ps delay, the bulk of the target becomes transparent and residual material within the original target bulk is visible up to a delay of 250 ps. A possible interpretation of the observation is a fast ionization of the hydrogen target by the pump-laser pulse during the first 5 ps and the generation of a plasma with low temperature. A subsequent plasma expansion of the ionized parts of the target into vacuum on the tens of picosecond timescale accompanied by recombination leads to an increased transparency of the target bulk at about 150 ps. For later times, the residual material is probably constituted by molten hydrogen droplets.
For a peak intensity of $4.7 \cdot 10^{15}\,\mathrm{W/cm^2}$, the observations are similar. However, the whole process is confined within the original target bulk. At long timescales (250 ps and 650 ps), a residual bridge of material is observed on the rear side of the target.
The lowest peak intensity of $4.7 \cdot 10^{14}\,\mathrm{W/cm^2}$ shows that LIB is observed on the target frontside only. Still, on long timescales the dissolution of the target occurs volumetrically. At delays around 300 ps, the original target bulk is filled with hydrogen droplets.

With respect to target-density tailoring, the presented shadowgrams constitute a rich parameter space of different target shapes, e.g., droplet targets and asymmetrically shaped targets with different density gradients on the front and on the rear side.

5.3.3. Occurrence of filamentation

A previous thesis project reported on the observation of filamentations of the shadowedges at pump-laser-peak intensities around $5 \cdot 10^{20}\,\mathrm{W/cm^2}$, see Ref. [167]. Up to now, it was unclear for which range of laser intensities the filamentations occur and why the filaments are observed all along the jet axis within a large field of view, much larger than the FWHM of the focal spot. Therefore, this section explores a large range of laser intensities and, in a second step, utilizes a large focal spot spanning three orders of magnitude of intensity to illustrate that, for the case of $5 \cdot 10^{20}\,\mathrm{W/cm^2}$ peak intensity, the filaments far away from the focal spot probably originate from scattered light and speckles at intensities above $10^{15}\,\mathrm{W/cm^2}$.

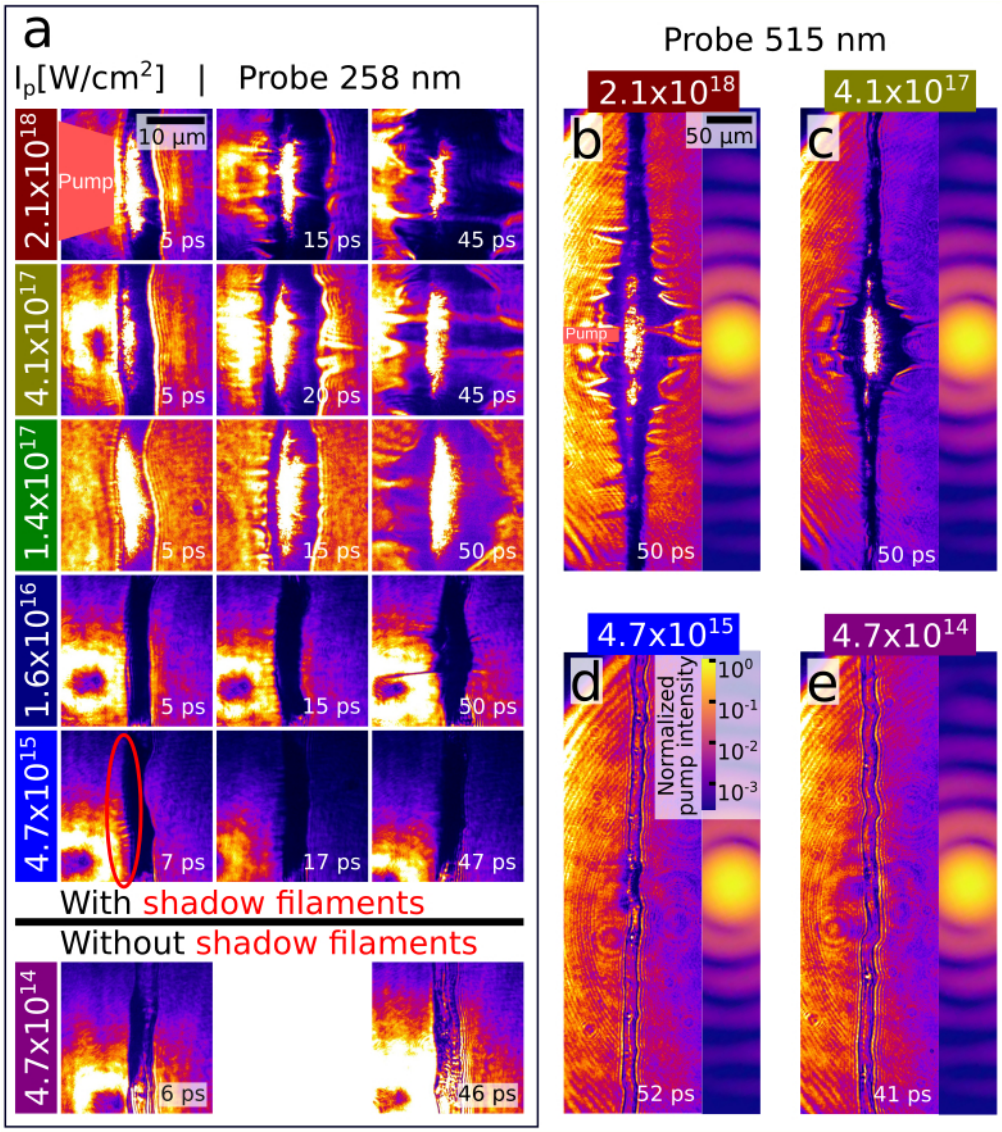

Figure 5.13.: Shadowgrams of **(a)** probe 258 nm and **(b) - (e)** probe 515 nm show the occurrence of filamentations for different timescales and pump-laser-peak intensities. Figure (b) shows the focal spot of the pump laser with the same spatial scale like the shadowgrams.

Figure 5.13 (a) shows shadowgraphy images of probe 258 nm at different levels of the pump-laser-peak intensity. For 5 ps delay, the filaments of the shadowedge are observed on the front side of the target for all intensities between $4.7 \cdot 10^{15}\,\mathrm{W/cm^2}$ and $2.1 \cdot 10^{18}\,\mathrm{W/cm^2}$ (see red circle). For $4.7 \cdot 10^{14}\,\mathrm{W/cm^2}$, however, no filamentation on the front surface is observed. Note that, for pump-probe delays of single picoseconds, i.e., small filaments, the visibility of the filaments is highly sensitive to the position of the jet within the depth of field of the microscopy system. The filament size at 5 ps delay appears to be independent on the pump-laser intensity. At longer timescales, the filaments overlay with volumetric transparency and refraction in the plasma gradients causes strong image distortions of the filaments. The observations suggest that the increased size of the filaments is probably caused by an optical-imaging effect due to refraction in the undercritical regions of the plasma.
Figure 5.13 (b) shows a shadowgram of probe 515 nm with a large field of view next to the intensity distribution of the focal spot. Filamentations are observed all along the jet axis. Considering the absolute intensities of the focal spot, this is expected from the measurements in figure 5.13 (a). The peak of the focus features an intensity of $2.1 \cdot 10^{18}\,\mathrm{W/cm^2}$ and the outermost local maxima of the patter feature intensities of about $10^{-3} \times 2.1 \cdot 10^{18}\,\mathrm{W/cm^2}$, all of which are intensities that enable the generation of filaments.
Further reduction of the peak intensity to $4.1 \cdot 10^{17}\,\mathrm{W/cm^2}$ (figure 5.13 (c)) shifts the outermost local maxima to intensities close to $4.7 \cdot 10^{14}\,\mathrm{W/cm^2}$ and consequently no filaments are observed at the corresponding positions of the jet. Note that the maxima of the intensity pattern are occurring as blackened areas of LIB all along the jet. Areas without LIB occur inbetween. Furthermore, plasma emission indicates the positions of the local maxima of intensity.
For a peak intensity of $4.7 \cdot 10^{15}\,\mathrm{W/cm^2}$ (figure 5.13 (d)), only the central part of the intensity distribution is above the threshold of filament generation and, consequently, no filaments are observed along the jet. The outer maxima of the focal spot generate no LIB of the target. For a peak intensity of $4.7 \cdot 10^{14}\,\mathrm{W/cm^2}$ (figure 5.13 (e)), no filaments are observed, which is in agreement to figure 5.13 (a).

In the case of high-intensity lasers with peak intensities in the range of $5 \cdot 10^{20}\,\mathrm{W/cm^2}$, the usual focal spot shows a Gaussian shape only within one to two orders of magnitude of intensity, e.g., refer to figure 1 (b) in Ref. [211]. Outside this area, the light distribution consists of a more or less random formation of light patterns. The intensities at tens of micrometers away from the focal spot easily exceed $10^{18}\,\mathrm{W/cm^2}$ and the shadowgrams in section 3.2 show that LIB of the target is induced even hundreds of micrometer away from the focal spot. As the threshold of filament generation is located at a low intensity level of about $10^{15}\,\mathrm{W/cm^2}$, figure 5.13 (b) nicely illustrates that the origin of filamentation of the shadowedges of the jet target within a large field of view most likely originates from light of the focal spot, far away from the FWHM of the idealized focal spot. The time-dependent spatial shape of the shadow edges is resulting from plasma expansion and the imaging of refraction on the three-dimensional spatial structure.

6. Conclusion

In summary, this thesis investigates interactions of cryogenic hydrogen-jet targets with the DRACO-PW laser. The experimental implementation of time-resolved optical-probing diagnostics at DRACO PW and the technical innovation of off-harmonic optical probing overcome disturbances by parasitic plasma self-emission and allow for unprecedented observations of the target evolution during interactions with ultra-relativistic laser pulses of up to $6 \cdot 10^{21}\,\mathrm{W/cm^2}$ peak intensity. Together with the scientific framework and the overarching research project, chapter 2 presents the concept of temporal synchronization between the utilized stand-alone probe-laser system and DRACO PW and demonstrates subpicosecond temporal resolution by utilizing a beam-arrival monitor. Measurements of the spectral characteristics of plasma self-emission enable a discussion of the prospects of off-harmonic optical probing in different interaction scenarios that explain details about the choice of spectral filters, wavelength, spectral bandwidth and spectral fluence of the probe beam.
The laser-induced breakdown of solids, i.e., the phase transition from the solid to the plasma state, can be considered as an heuristic starting point of high-intensity laser-solid interactions. As this starting point is highly relevant to the corresponding start-to-end simulations, chapter 3 presents time-resolved measurements of laser-induced breakdown in interactions of dielectric hydrogen jets and the DRACO-PW laser with peak intensities between $0.6 \cdot 10^{21}\,\mathrm{W/cm^2}$ and $5.7 \cdot 10^{21}\,\mathrm{W/cm^2}$. By switching from the lowest to the highest peak intensity, the starting point of laser-induced breakdown shifts from the foot of the steep-rising edge into the picosecond pedestal of the leading edge. The shift is attributed to a lowering of the applicable threshold intensity of laser-induced breakdown well below the appearance intensity of barrier-suppression ionization. The observation demonstrates the relevance of the pulse-duration dependence of laser-induced breakdown and laser-induced damage threshold to the starting point of laser-induced breakdown in high-intensity laser-solid interactions. In addition, the chapter discusses the applicability of laser-induced breakdown as a diagnostic tool for high-power lasers and reports on dielectric breakdown that is caused by relativistic electrons. To apply the results to other laser-target assemblies, chapter 3 closes with a detailed instruction of how to pinpoint the starting point of laser-induced breakdown by comparing a measurement of the laser contrast with a characterization study of the target-specific thresholds of laser-induced breakdown at low laser intensity.
Chapter 4 presents an example of how optical-probing diagnostics are capable of bridging the necessity of simulating target pre-expansion by providing an estimate of initial target parameters for particle-in-cell simulations of the interaction between the target and the ultra-relativistic laser peak. A measurement of the shadow diameter at 200 fs before the DRACO-PW laser peak allows to restrict the surface gradient of the pre-expanded plasma density to an exponential scalelength between 0.06 µm and 0.13 µm. Particle-in-cell simulations compute the subsequent plasma-expansion dynamics that are induced by the ultra-relativistic laser peak. The results are compared to the experimental observations by post-processing of the electron-density evolution with ray-tracing simulations. The comparison yields that the formation of the experimentally measured shadowgrams is governed by refraction in the plasma-density gradients and it suggests that the measured volumetric transparency of the target at 1.4 ps after the laser peak is not caused by relativistically induced transparency but instead by plasma expansion into vacuum.
Leading-edge-driven target pre-expansion on a minimized level enables the precise adjustment of the target density to the arrival of the ultra-relativistic laser peak by all-optical target-density tailoring. In combination with the low solid density of the cryogenic hydrogen-jet target, the approach allows to artificially tune the plasma density of the target to nearcritical-density regime. Chapter 5 presents an experimental demonstration of all-optical target-density tailoring by isochoric heating via ultrashort laser pulses with a dimensionless vector potential of $a_0 \sim 1$. A discussion of the results allows to determine the evolution of the full target-density distribution after isochoric heating by a hybrid of hydrodynamics and ray-tracing simulations. The result enables the quantitative comparison of

particle-in-cell simulations to an experiment of enhanced laser-driven proton acceleration from cryogenic hydrogen jets at DRACO PW. Furthermore, the utilization of all-optical target-density tailoring as a testbed platform to experimentally benchmark collisional PIC simulations in the intensity regime between 10^{17} and $10^{19}\,\mathrm{W/cm^2}$ is proposed and, finally, an experimental exploration of future possibilities of all-optical target-density tailoring is given.

In conclusion, this thesis demonstrates that off-harmonic optical probing enables time-resolved measurements of the target evolution in high-intensity laser-solid interactions. The approach provides quantitative boundary conditions to simulations on all timescales of the interaction. By presenting an heuristic approach to determine the starting point of target pre-expansion, measuring target pre-expansion to the arrival of the ultra-relativistic laser peak and by proposing a testbed platform to experimentally benchmark collisional particle-in-cell simulations, the results foster the simulation of realistic experimental scenarios and will help to to improve the predictive power of simulations of high-intensity laser-solid interactions in the future.

A. Abel transform

The principle of Abel transformation is visualized in figure A.1. The forward-Abel transform AT calculates a projection of a three-dimensional rotational-symmetric object onto a two-dimensional area. The three-dimensional object is given in cylinder coordinates (z,r) and the two-dimensional projection is given in Cartesian coordinates (z,y). The projection is calculated by integration of the three-dimensional object along straight lines along the x axis. The reverse transformation is given by the inverse Abel transform AT^{-1}.
The electron-density distribution $n_e(r, z)$ of a radially symmetric plasma is calculated from the phase-shift map $\Delta\phi(y, z)$ in the following way. The refractive index of a plasma is given by

$$\tilde{n} = \sqrt{1 - \frac{n_e}{n_c}}\,.$$

n_c is the wavelength-dependent critical density of the plasma. The variation of the refractive index with respect to the vacuum is given by

$$\Delta\tilde{n} = 1 - \tilde{n}\,.$$

The phase shift $\Delta\phi(y, z)$ corresponds to a change in optical path length Δs and λ gives the wavelength of the light

$$\frac{\Delta\phi(y,z)}{2\pi} = \frac{\Delta s}{\lambda} = \frac{1}{\lambda}\cdot\int_{-\infty}^{\infty}\Delta\tilde{n}(x,y,z)dx\,,$$

$$\Delta\phi(y,z) = \frac{2\pi}{\lambda}\cdot\int_{-\infty}^{\infty}1-\sqrt{1-\frac{n_e(x,y,z)}{n_c}}dx\,.$$

Here, we assumed a straight line of propagation of the rays through the three-dimensional object. The symmetry of the three-dimensional object allows to reduce the interval of integration to

$$\Delta\phi(y,z) = \frac{2\pi}{\lambda}\cdot 2\cdot\int_{0}^{\infty}1-\sqrt{1-\frac{n_e(x,y,z)}{n_c}}dx\,.$$

A coordinate transformation with $x = \sqrt{r^2 - y^2}$ yields

$$\frac{dx}{dr} = \frac{r}{\sqrt{r^2-y^2}}$$

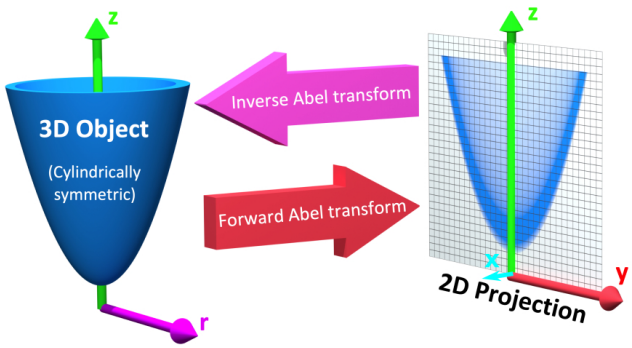

Figure A.1.: Figure copied from [7]. General principle of the Abel transform.

and

$$\Delta\phi(y,z) = 2 \cdot \int_{|x|}^{\infty} dr \cdot \frac{r}{\sqrt{r^2 - y^2}} \cdot \frac{2\pi}{\lambda} \cdot \left(1 - \sqrt{1 - \frac{n_e(r,z)}{n_c}} \right) .$$

The derived integral corresponds to the forward Abel transform AT:

$$\Delta\phi(y,z) = AT\left\{ \frac{2\pi}{\lambda} \cdot \left(1 - \sqrt{1 - \frac{n_e(r,z)}{n_c}} \right) \right\} .$$

Conversely, the radial distribution of electron density $n_e(r,z)$ is calculated by the inverse Abel transform AT^{-1} of the phase map $\Delta\phi(y,z)$:

$$n_e(r,z) = n_c \cdot \left(1 - \left(1 - \frac{\lambda}{2\pi} \cdot AT^{-1}\{\Delta\phi(y,z)\} \right)^2 \right) .$$

For numerical-calulation purposes via the software *python*, a package of Abel transformation is avalable in reference [7].

B. Temporal properties of DRACO PW

B.1. Intrinsic temporal laser contrast

During the high-intensity experiments with DRACO PW and the cryogenic hydrogen-jet target in 2019, a temporal laser-contrast curve with reduced laser energy of about 0.27 J before compression (*diagnostic mode*) was recorded with a third-order autocorrelator (TOAC). The measurement allows to capture thousands of data points and to scan the laser contrast with a high temporal sampling rate. This is not possible at full laser energy (32 J before compression). However, it is known that the amplification of the laser pulse in the final laser amplifiers changes the laser contrast [53, 105]. For DRACO PW, this issue is investigated within another doctoral project, see Ref. [212]. For the project, laser-contrast measurements for different laser-amplification levels were recorded in 2021. The measurements are presented in figure B.1 (a). The blue line shows the measurement in diagnostic mode (0.27 J before compression), the orange line shows the measurement at 4 J laser energy before compression and the black crosses show singular measurements at full amplification (32 J before compression). A comparison of the measurements shows that the laser contrast changes for different stages of amplification. Short pre-pulses, e.g., at −54 ps or −90 ps delay, are effected differently than the more continuous picosecond pedestal. The picosecond pedestal between −90 ps and −2 ps shows negligible changes between the 4 J (orange) and 32 J (black) setting. Significant changes occur by changing from from the 0.27 J (blue) to the 4 J setting (orange). Contrary, the height of singular pre-pulses is changed for all three settings, which is exemplified for the −54 ps pre-pulse in figure B.1 (c).
In this Appendix we calculate a representative *full-energy* laser-contrast curve from the diagnostic-mode measurement in 2019. The calculation utilizes a time-dependent *conversion function*, which is derived from the measurements in 2021. Different conversion functions apply for the more continuous picosecond pedestal, singular pre-pulses, the post-pulse and the amplified spontaneous emission (ASE).

For the picosecond pedestal, the conversion function is derived by division of the contrast curve of the 4 J setting with the contrast curve of the 0.27 J setting. The result is displayed in figure B.1 (b) as blue line. To reduce noise and to take into account changes on the 5 ps timescale only, a rolling average is applied (orange line). The curve shows that the conversion function is varying between about 1 and 20, depending on the delay.
The conversion function of the single short pre-pulses is derived by a different method. For every pre-pulse in figure B.1 (a), the intensity of the pre-pulse in full-energy mode (black) is divided by the intensity of the pre-pulse in diagnostic mode (blue, see exemplary pre-pulse in figure B.1 (c)). The pre-pulse at −54 ps and −90 ps yield a conversion factor of 620 and 540, respectively. The pre-pulse at −160 ps is not differentiable from the ASE level in full-energy mode (black crosses between −160 ps and −100 ps). It is thus neglected in the conversion. The pre-pulse at −67 ps delay is visible in the measurement from 2019 only. Here, the conversion factor is estimated by the mean between the −90 ps and the −54 ps pre-pulse from 2021.
Both, the temporally varying conversion function of the picosecond pedestal in figure B.1 (b) and the individual factors for single short pre-prepulses enable the conversion of the overall diagnostic-mode measurement from 2019 to the full-energy mode in the timeframe between −90 ps and −0.5 ps. The peak of the measurement between −0.5 ps and 0.5 ps is not changed, in agreement to the comparison of the measurements from 2021. The resulting contrast curve in full-energy mode is shown by orange markers in figure B.1 (d).
For the ASE pedestal and the post-pulse, the conversion functions are derived by a different approach, because the measurement of the 4 J setting from 2021 is limited to a time window between −90 ps and 0 ps. The conversion function of the ASE pedestal is derived by averaging the conversion function of

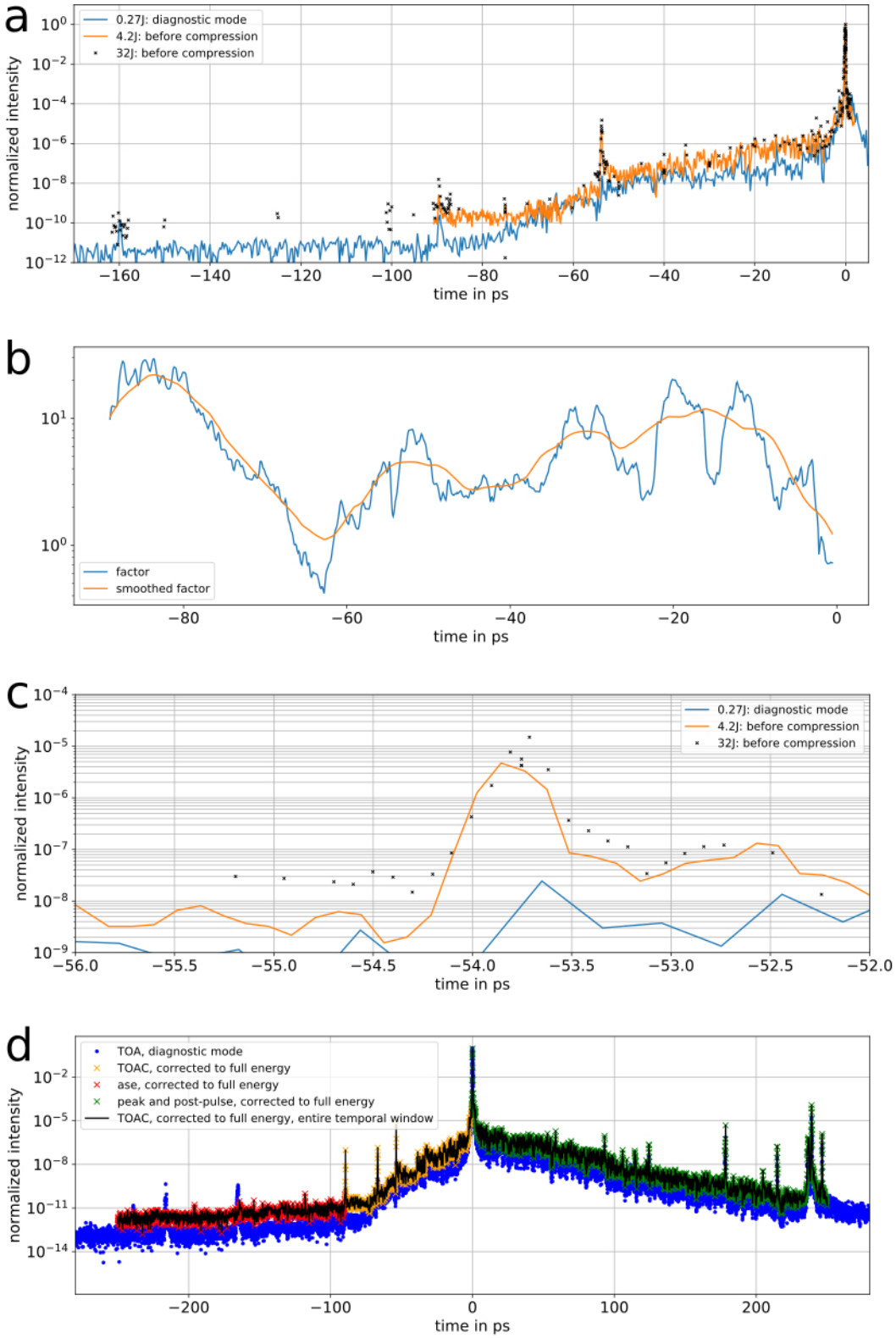

Figure B.1.: **(a)** TOAC measurement of the DRACO-PW-laser contrast in 2021 for different laser-energy levels, from Ref. [212]. **(b)** Conversion function of the picosecond pedestal between −90 ps and −2 ps to calculate the laser contrast in full-energy mode (32 J) from a measurement in diagnostic mode (0.27 J). **(c)** Singular short pre-pulse at −54 ps for different laser-energy levels. **(d)** TOAC measurement of the DRACO-PW-laser contrast in 2019 in diagnostic mode (blue). The black line shows the calculated laser contrast in full-energy mode (32 J) in 2019 (for details see text).

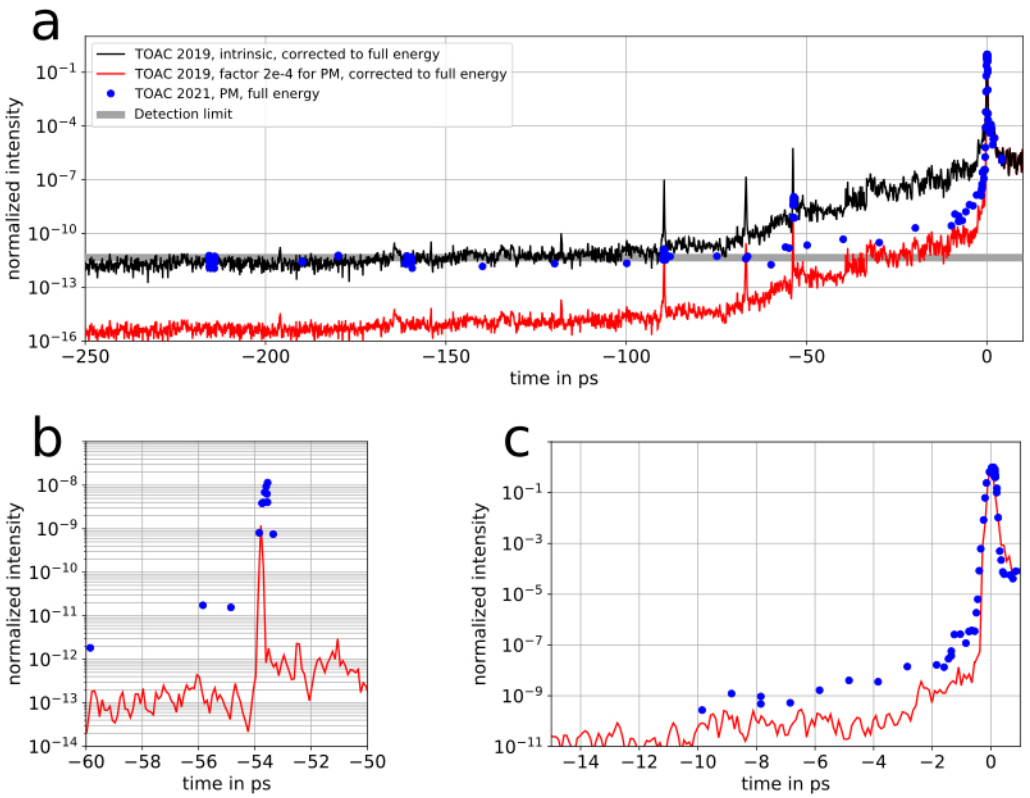

Figure B.2.: **(a)** Calculated contrast in full energy mode (black) from 2019 and the same curve multiplied by the enhancement factor of the plasma mirror (PM, red). For details see text. Blue markers show the TOAC measurement from 2021 of DRACO PW in full energy mode and with PM cleaned contrast (noise level between 10^{-12} and 10^{-11}). **(b)** −54 ps pre-pulse. **(c)** Picosecond pedestal.

the picosecond pedestal (figure B.1 (b)) between −80 ps and −90 ps to a single scalar value, because, viewing the measurements from 2021 in figure B.1 (a), the measurement of the 0.27 J setting (blue) enters the noise level just within this timeframe, while the ASE level of the measurement of the 4 J setting (orange) is still measurable. The derived correction factor of 13.5 is applied in the whole timeframe between −250 ps and −90 ps. The resulting full-energy contrast curve from 2019 is shown as red-cross markers in figure B.1 (d). The curve gives an upper boundary to the expected actual ASE level at full energy. Two pre-pulses at −235 ps and −215 ps delay are identified as an echo of intense short post-pulses and are deleted during conversion.
For the post-pulse between 0.5 ps and 250 ps, the actual trend of the intensity distribution is less important for experimental considerations. However, the overall increased amount of energy in the post-pulse needs to be considered, if energy conservation is required. As an estimate, we take the global mean of the conversion function in figure B.1 (b) of 6.9 and apply it as a conversion factor to the entire post-pulse. The derived contrast curve is shown as green crosses in figure B.1 (d).

The result of the overall conversion of the measurement in diagnostic mode (blue) to the contrast curve in full-energy mode between −250 ps and 250 ps delay is presented in figure B.1 (d) as black line. Both curves are also presented and labeled as *diagnostic mode* and *intrinsic contrast at full energy* in figure 2.16 (a).

B.2. Temporal laser contrast with plasma mirror

In the context of the doctoral project [212], the temporal contrast of DRACO PW with plasma-mirror-enhanced (PM) laser contrast is measured in full-energy mode in 2021 (blue dots in figure B.2 (a)). The noise level of the measurement is between 10^{-12} and 10^{-11}. Laser intensities relevant to the

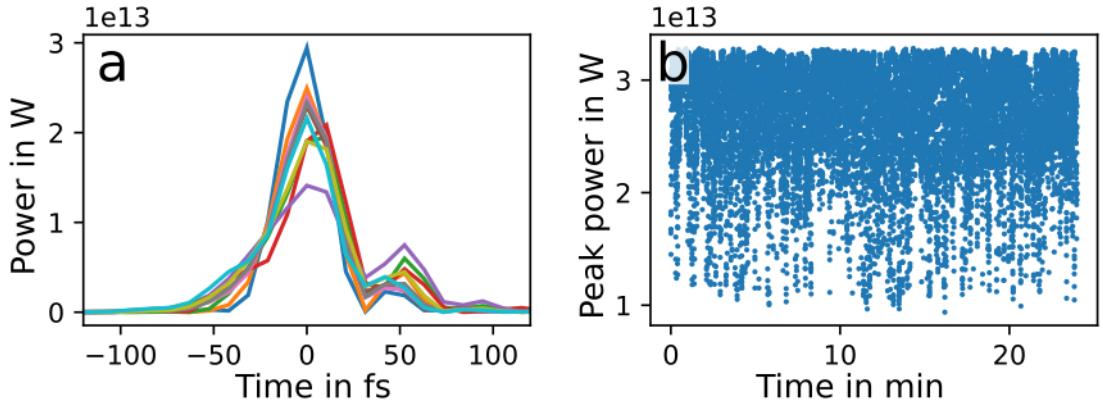

Figure B.3.: Peak-power measurement of the DRACO laser: **(a)** Exemplary measurements of the pulse shape. The area of each trace is normalized to a laser energy of 1 J. **(b)** Peak power versus time over half-an-hour laser operation at 10 Hz.

experiment occur for a short pre-pulse at −54 ps (figure B.2 (b)) and the picosecond pedestal between −10 ps and 0 ps (figure B.2 (c)).
A similar measurement of the PM-enhanced laser contrast is not available for 2019. Based on the considerations above, a synthetic PM-enhanced laser contrast of DRACO PW in full-energy mode from 2019 is derived as follows. Although the absolute signal level of the laser contrast changes over the years and increased by up to a factor of 10 between 2019 and 2021, the contrast-enhancement factor of the PM is expected to stay constant. This is because the setup and substrate coating of the PM did not change over the years. An enhancement factor of $2 \cdot 10^{-4}$ is measured by two methods: First, via a spectrally and angularly resolved absolute-reflectance measurement of the PM-substrate coating and, second, by comparing TOAC measurements in full-energy mode with and without PM, see Ref. [212].
Because of the comparably low temporal resolution of the TOAC, the switching point of the PM is not accessible via this technique. Alternatively, *self-referenced spectral interferometry with extended time excursion* [148] in full-energy mode is used. The measurement locates the PM-switching point at about −0.2 ps delay [211, 212].
It follows that the PM-enhanced contrast curve of the full-energy mode in 2019 is derived by multiplying the intrinsic contrast curve in full-energy mode (black curve in figure B.2 (a)) by a factor of $2 \cdot 10^{-4}$ up to −0.2 ps delay. The result is shown as red line in figures B.2 (a), (b) and (c). The calculated height of the −54 ps pre-pulse (figure B.2 (b)) and of the ∼ 50 ps pedestal (figure B.2 (a)) agree within about one order of magnitude with the measurement from 2021, which is in congruence with the observed degradation of the contrast of about a factor of 10 from diagnostic-mode measurements. Only at around −4 ps relative changes above one order of magnitude are observed (figure B.2 (c)).

B.3. Stability of the peak power

Petawatt-class lasers feature several amplifier stages and a number of alignment-sensitive optical components like stretchers, compressors and non-linear pulse cleaners, e.g., an XPW-crystal. Furthermore, active acousto-optic modulators are implemented for precompensation of spectral-gain narrowing and fine tuning of spectral-phase components, e.g., the *Dazzler* and *Mazzler* devices by *Fastlight*. The ∼ 0.5 km long laser chain of the DRACO PW laser is housed in sealed boxes to keep air turbulences and changes in ambient temperature at a minimum level. For broadband ultra-short laser systems, however, the spectral phase typically shows a variation over time, i.e., from shot to shot. The variation is not chaotic. It occurs as an alternation of different spectral-phase terms. In the temporal domain, this causes a continuous variation of the pulse shape.
For some of the experiments in this thesis, the fluctuation of the peak power on the 10 % level is of relevance. To derive an estimate of the stability, measurements of the pulse shape of the DRACO

laser with an energy of about 400 mJ before compression are conducted at 10 Hz by a *Wizzler* device by *Fastlight*. Exemplary pulse shapes are displayed in figure B.3 (a). The area of each curve is set to 1 J laser energy. As displayed, singular shots show a significant variation of the peak power. The fluctuation of the peak power is displayed in figure B.3 (b) for half-an-hour laser operation. The mean and standard deviation of the measurement is $(26.7 \pm 4.6) \cdot 10^{12}$ W. This gives a relative standard deviation of 17 %.

C. Beam-arrival monitor

Figure C.1 (a) gives a schematic of the setup and alignment procedure of the BAM. The DRACO leakage (red beam) leaves the vacuum chamber with about one mJ of energy by traversing an AR-coated UVFS window with 3.05 mm thickness and one-inch diameter. Via mirrors, it is guided towards a lens with a focal length of 40 mm and creates a filament in the focal plane of the lens. An iris with adjustable aperture size allows to change the laser energy continuously without changing the delay of the pulse. To capture time-resolved shadowgraphy images of the filament, the probe leakage (green beam) is used as backlighter in 90° direction to the DRACO leakage. A long-working-distance finite-conjugate microscope objective images the filament with ten-times magnification onto a camera. An exemplary shadowgraphy image is presented in figure C.1 (c) (DRACO leakage is propagating from bottom to top). The brightness of the background-signal level is adjustable via an iris in the beamline of the probe leakage. Multiple passes over several mirrors accumulate time delay such that the leading edge of the filament is central on the camera when the reference time is reached. The general setup needs to be aligned only once during preparation of an experimental campaign and requires readjustment, if the optical-path length of the DRACO or the probe beam between the pickoff of the BAM leakage and the final laser-plasma interaction point is changed. Thus, it is desired to pick the leakage of both lasers as close as possible to the final interaction point in the target chamber. In this way, devices that enlarge or shorten the optical beampath, e.g., the recollimating PM setup, do not imply a realignment of the BAM. However, small changes of the optical-path length up to multiple centimeters can be compensated by the motorized delay stage in the beam path of the probe leakage. The alignment process of the BAM is sketched in the inset of figure C.1 (a). The first step is the spatial alignment between pump and probe. For this, the tip of a small pin (e.g. 0.5 mm diameter) is placed in the object plane of the objective and the shadow that is produced via illumination by the probe leakage is recorded with the camera. In the next step, the DRACO leakage is switched on and the horizontal and vertical angle of the last folding mirror before the lens is tuned until the scattered light of the DRACO leakage is maximized on the tip of the pin. To match the focal position to the pin position, the lens is shifted along the beam path until the area of scattered light is minimized. In the second step a rough temporal synchronization of the two laser beams is achieved by replacing the pin with a fast photo diode (e.g. *DET025A* by *Thorlabs*, rise time = fall time = 150 ps). Viewing the temporal position of both laser pulses on an oscilloscope, the gate trigger of the probe laser system (second pillar of the temporal synchronization) is shifted until both pulses are within one oscillator bucket (~ 12.8 nm for 78 MHz oscillator frequency). Via the phase-shifter DDS120, the residual time delay of the probe laser is tuned to 200 ps after the pump laser. This ensures that the generated filament in air is visible in the shadowgraphy imaging. Finally, in the third step, the photo diode is removed and a shadowgram of the filament is visible on the camera. Via the phaseshifter, the pump-probe delay is reduced until the leading edge of the filament is centralized in the camera image. The visibility of the filament is maximized by tuning the filament position via the last folding mirror before the lens in the DRACO-leakage beamline.

The derivation of a time delay from the measured raw data of shadowgraphy is done as follows. The field of view of the microscopy setup is calibrated by a resolution test chart. Via the speed of light, the spatial calibration is transformed into a temporal calibration, given on the right side of figure C.1 (e). In a first step, the background signal (B, fig. C.1 (b)) without filament is substracted from the raw signal (S, fig. C.1 (c)). Taking the decadic logarithm of the derived signal $\log(S - B)$ and setting negative values of $S - B$ to zero gives fig. C.1 (d). Figure C.1 (e) presents the central vertical lineout of figure C.1 (d), which shows a clear cut-off (horizonal yellow line). The time at which the signal level of the cut-off drops below 0.5 arb.units is taken as time delay of the specific shot. Evaluating the width of the cut-off, the uncertainty of a BAM measurment is about 50 fs, see Ref. [213].

Checking the filament position on the BAM is part of the daily routine of the experimental preparation

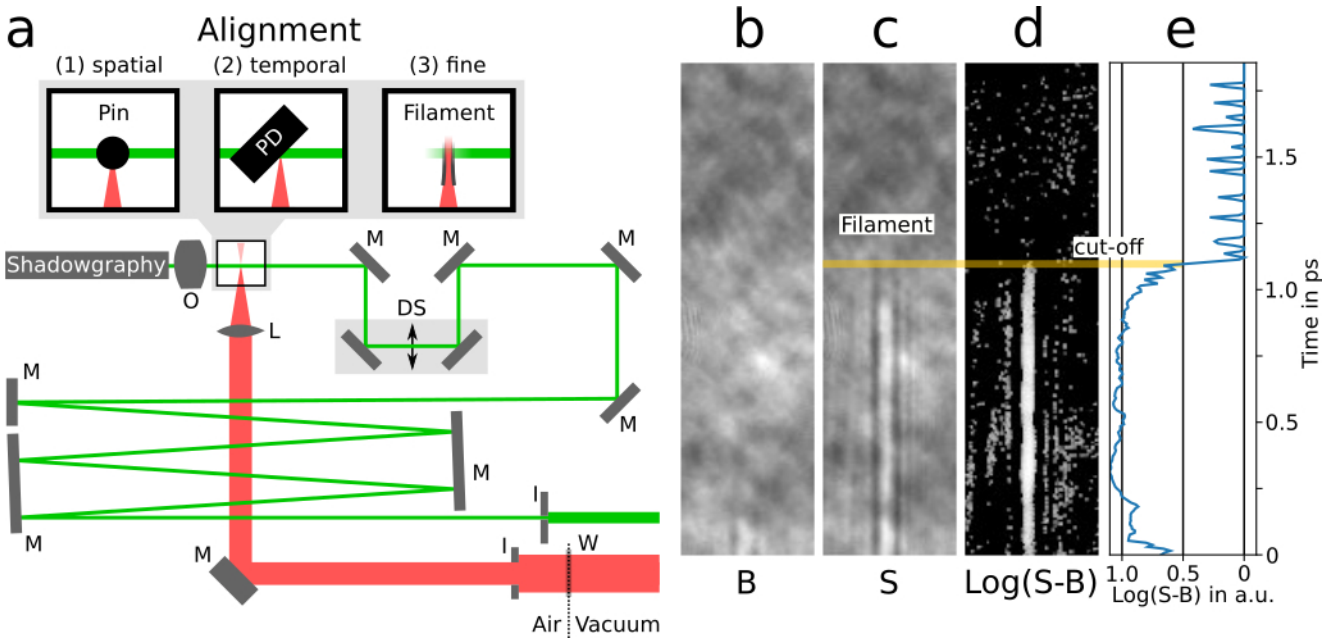

Figure C.1.: *Beam-arrival monitor* (BAM): **(a)** General setup: The DRACO leakage (red beam) is focused outside the experimental chamber and creates a filament in air. The filament is illuminated transversally by the probe leakage (green beam). An objective (O) images the shadow onto a shadowgraphy camera. Optical components: window (W), iris (I), lens (L), mirror (M), photo diode (PD) and a delay stage (DS). The alignment procedure (1), (2), (3) is described in the text. **(b)** Background image (B). **(c)** Signal image (S) with a filament showing a clear cut-off (DRACO leakage is propagating from bottom to top). **(d)** Decadic logarithm of the background-subtracted signal image and **(e)** line-out along the central vertical axis of fig. (d) for signal processing.

and guarantees the temporal synchronization of pump and probe beam at the interaction point in the experimental chamber.

D. Polarization mixing in the final laser amplifier

To estimate the possible origin of a beam with ordinary polarization by polarization mixing in the final laser amplifier, even if the laser is operated in nominal conditions (extraordinary-polarized seed), we compare the peak height of the focal spot labeled "(1)" in figure 3.14 (b) in the extraordinary-polarization setting and the focal spots labeld "(1)" and "(2)" in figure 3.14 (b) in the ordinary-polarization setting. First, the polarization-filter efficiency of the compressor chamber $T^e_{\mathrm{KK}}/T^o_{\mathrm{KK}}$ is estimated by comparing the peak heights of focal spot (1) in the ordinary-polarization and extraordinary-polarization setting I^o_1 and I^e_1. By taking into account the transmission of the wedge attenuator $T^e_{\mathrm{wedge}}/T^o_{\mathrm{wedge}} = 1/150$ we derive

$$\frac{I^e_1}{I^o_1} = \frac{T^e_{\mathrm{KK}}}{T^o_{\mathrm{KK}}} \cdot \frac{T^e_{\mathrm{wedge}}}{T^o_{\mathrm{wedge}}} \cdot \frac{1-\alpha_{\mathrm{mix}}}{1-\alpha_{\mathrm{mix}}} \cdot \frac{I_{\mathrm{seed}}}{I_{\mathrm{seed}}}. \tag{D.1}$$

I_{seed} is the intensity of the seed beam and α_{mix} is the fraction of light that is rotated into the other polarization direction (*mixing fraction*). The ratio $T^e_{\mathrm{KK}}/T^o_{\mathrm{KK}}$ is calculated to be 850/1.
In a second step, the mixing fraction α_{mix} of the overall amplifier, i.e., the fraction of light that is transformed into the unwanted polarization direction, is estimated by comparing the focal spot (1) and (2) in the ordinary-polarization setting. Here, focal spot (1) with a peak intensity of I^o_1 corresponds to the nominal seed beam and focal spot (2) with a peak intensity of I^o_2 corresponds to the parasitically generated spot of perpendicular polarization. For this estimation, again the transmission of the wedge attenuator and the transmission of the compressor chamber need to be taken into account and we approximate that focal spot "(3)" or further conversions are negligible:

$$\frac{I^o_2}{I^o_1} = \frac{T^e_{\mathrm{KK}}}{T^o_{\mathrm{KK}}} \cdot \frac{T^e_{\mathrm{wedge}}}{T^o_{\mathrm{wedge}}} \cdot \frac{\alpha_{\mathrm{mix}}}{1-\alpha_{\mathrm{mix}}} \cdot \frac{I_{\mathrm{seed}}}{I_{\mathrm{seed}}}. \tag{D.2}$$

From the measurements in figure 3.14 (b) a mixing fraction of $\alpha_{\mathrm{mix}} = 18\,\%$ is calculated. Because of the negligence of focal spot (3), the result is an upper limit.
The estimation shows that a significant amount of the ordinary-polarized seed is converted into a beam with extraordinary polarization, just by the inherent properties of the setup and components of the final laser amplifier. The result is qualitatively confirmed by a two-fold increase of ellipticity of the laser beam after propagating the two final multi-pass amplifiers. The value is derived from a measurement of the polarization contrast via the combination of a Glan-Thompson prims and a photodiode. The non-visibility of the polarization mixing in the upper image with respect to the lower image of figure 3.14 (b) is explained by the strong difference of the combined transmission of the wedge attenuator and the compressor for ordinary and extraordinary polarization. Because the extraordinary-polarized nominal beam experiences higher overall transmission, the detection of extraordinary light in the setting with an ordinary-polarized seed beam is easier than in the opposite setting. However, the mixing fraction from one polarized beam into the orthogonally polarized beam within the amplifier should be equivalent.

E. PIC simulation of the interaction between the cylindrical hydrogen-jet target and DRACO PW

This Appendix discusses details of the PIC simulation, which is part of the discussion in section 4.2. The Appendix is published in Ref. Bernert et al. [24]. The implementation and conduction of three-dimensional-PIC simulation is part of a different PhD-thesis project, see Ref. [79]. The PIC cycle uses the Yee field solver, Esirkepov current deposition and Boris particle push. The simulation uses 18 particles per cell. The pump-laser pulse is initialized with p polarization, 800 nm wavelength and a Gaussian shape in all three dimensions. The pulse-duration FWHM is set to 30 fs, the spatial FWHM into the two lateral dimensions is 4.1 µm and the normalized peak of the normalized vector potential is $a_0 = 33$. The overall box size is 20 µm (target axis) $\times 40.6$ µm $\times$ 80 µm (laser propagation direction) and the laser wavelength is isotropically resolved by 24 cells. One timestep of the simulation is 0.064 fs and absorbing boundary conditions are used. The simulation runs on 60 GPUs of the type *NVIDIA® V100* and the overall runtime is 4.5 h.
Although higher spatial resolution of the PIC simulation is desired and would give more robust results, the presented numerical settings are as good as possible for the given computational resources and a balanced choice between resolution and overall box size needs to be considered. A large box size is relevant to simulate the plasma expansion at later delays.

F. Dispersion relation of optical waves in homogeneous plasmas

As a supplement to section 4.2, the following Appendix describes the derivation of the dispersion relation of an optical plane wave in an homogeneous plasma. The result of the derivation is the formula of the refractive index

$$\tilde{n} = \sqrt{1 - \frac{n_e}{n_c}} \tag{F.1}$$

with n_e and n_c being the electron density and the critical density of the specific wavelength of the optical wave, respectively. As detailed in the following, several assumptions about the spatial and temporal variation of the electronic currents, ionic currents and densities of the plasma need to be considered to derive the dispersion relation of equation F.1.

We start with Maxwell's equations

$$\mathrm{div}\vec{E} = \frac{\rho}{\epsilon_0} \tag{F.2}$$

$$\mathrm{div}\vec{B} = 0 \tag{F.3}$$

$$\mathrm{rot}\vec{E} = -\frac{\partial \vec{B}}{\partial t} \tag{F.4}$$

$$\mathrm{rot}\vec{B} = \mu_0 \vec{j} + \mu_0 \epsilon_0 \frac{\partial \vec{E}}{\partial t}. \tag{F.5}$$

$\vec{E}$ is the electric field, $\vec{B}$ is the magnetic field, ρ is the charge density, $\vec{j}$ is the current density, ϵ_0 is the vacuum permittivity and μ_0 is the vacuum permeabiliy. Taking the rotation of equation F.4, switching the temporal and spatial derivative and insertion of equation F.5 gives

$$\mathrm{rot}\,\mathrm{rot}\vec{E} = -\mathrm{rot}\frac{\partial \vec{B}}{\partial t}$$

$$\mathrm{rot}\,\mathrm{rot}\vec{E} = -\mu_0 \frac{\partial \vec{j}}{\partial t} - \mu_0 \epsilon_0 \frac{\partial^2 \vec{E}}{\partial t^2}. \tag{F.6}$$

Taking the gradient of equation F.2 and using the Laplace operator with $\Delta\vec{E} = \mathrm{grad}\,\mathrm{div}\vec{E} - \mathrm{rot}\,\mathrm{rot}\vec{E}$ gives

$$\mathrm{grad}\,\mathrm{div}\vec{E} = \frac{1}{\epsilon_0}\mathrm{grad}\rho$$

$$\Delta\vec{E} + \mathrm{rot}\,\mathrm{rot}\vec{E} = \frac{1}{\epsilon_0}\mathrm{grad}\rho. \tag{F.7}$$

The combination of equations F.6 and F.7 gives the **wave equation**

$$\Delta\vec{E} - \frac{1}{\epsilon_0}\mathrm{grad}\rho = \mu_0 \frac{\partial \vec{j}}{\partial t} + \mu_0 \epsilon_0 \frac{\partial^2 \vec{E}}{\partial t^2}. \tag{F.8}$$

To derive equation F.1, four assumption about the plasma need to be considered:

1. There are no spatial gradients of the electron density n_e and the ion density n_i:

$$\text{grad}\rho = e\,\text{grad}n_e + Ze\,\text{grad}n_i = 0.$$

   Here, Z is the charge state of the ions.

2. There are no magnetic fields:

$$\vec{B} = 0.$$

3. All ionic currents $\vec{j}_i$ do not change in time:

$$\frac{\partial \vec{j}_i}{\partial t} = 0.$$

4. The temporal variation of the electron density is small compared to the absolute electron density:

$$\frac{1}{n_e}\frac{\partial n_e}{\partial t} = 0.$$

To calculate the temporal variation of current $\partial\vec{j}/\partial t$ in the wave equation F.8, the equation of motion is considered:

$$m\frac{\partial \vec{V}}{\partial t} = q(\vec{E} + \vec{V} \times \vec{B}).$$

The charge q is equal to the elementary charge e for electronic currents and $Z \cdot e$ for ionic currents. m corresponds to the particle mass of each species. Together with assumption 2 the equation of motions for electrons and ions reads:

$$m_i\frac{\partial \vec{V}_i}{\partial t} = Ze\vec{E}$$

$$m_e\frac{\partial \vec{V}_e}{\partial t} = -e\vec{E}.$$

From $\vec{j} = nq\vec{V}$ we derive

$$\frac{\partial \vec{V}}{\partial t} = \frac{1}{qn}\frac{\partial \vec{j}}{\partial t} - \frac{\vec{j}}{n^2 q}\frac{\partial n}{\partial t}.$$

Combined with the equation of motion of each species, the temporal variation of the electronic and ionic currents is

$$\frac{\partial \vec{j}_i}{\partial t} = \frac{Ze^2 n_i}{m_i} \cdot \vec{E} + \frac{\vec{j}_i}{n_i} \cdot \frac{\partial n_i}{\partial t}$$

$$\frac{\partial \vec{j}_e}{\partial t} = \frac{e^2 n_e}{m_e} \cdot \vec{E} + \frac{\vec{j}_e}{n_e} \cdot \frac{\partial n_e}{\partial t}.$$

The variation of overall current with time $\partial\vec{j}/\partial t$ is written as the sum of the electronic and the ionic currents

$$\frac{\partial \vec{j}}{\partial t} = \frac{\partial \vec{j}_i}{\partial t} + \frac{\partial \vec{j}_e}{\partial t}.$$

Considering the assumptions 3 and 4, the equation simplifies to

$$\frac{\partial \vec{j}}{\partial t} = \frac{e^2 n_e}{m_e} \vec{E}. \tag{F.9}$$

Using approximation 1 and equation F.9, the wave equation F.8 simplifies to the **wave equation of homogeneous plasmas**:

$$\Delta \vec{E} - \frac{\mu_0 e^2 n_e}{m_e} \vec{E} - \frac{1}{c^2} \frac{\partial^2 \vec{E}}{\partial t^2} = 0. \tag{F.10}$$

Here, the relation $c^2 = (\mu_0 \epsilon_0)^{-1}$ is used.
Using a plane wave $\vec{E} = \hat{e}_x E_0 \exp(i\omega t + ikx)$ with the unit vector $\hat{e}_x$ in x direction, the light frequency ω and the momentum vector k in x direction, equation F.10 gives

$$-k^2 - \frac{\mu_0 e^2 n_e}{m_e} + \frac{\omega^2}{c^2} = 0$$

$$\frac{k^2}{\omega^2} = \frac{1}{c^2}\Big(1 - \frac{e^2 n_e}{\epsilon_0 m_e} \cdot \frac{1}{\omega^2}\Big).$$

Defining the plasma frequency $\omega_p^2 = e^2 n_e / (\epsilon_0 m_e)$ and inversion of the equation yields the phase velocity of the light $V(\omega)$:

$$V^2 = \frac{\omega^2}{k^2} = \frac{c^2}{1 - \frac{\omega_p^2}{\omega^2}}.$$

The refractive index $\tilde{n}(\omega)$, i.e., the **dispersion relation**, is defined by $V^2 = c^2/\tilde{n}^2$. Thus, the refractive index of a homogeneous plasma is given by

$$\tilde{n}(\omega)^2 = 1 - \frac{\omega_p^2}{\omega^2}.$$

The frequency ω of the light defines the critical density of the plasma

$$n_c = \frac{\epsilon_0 m_e \omega^2}{e^2}.$$

For densities higher than n_c, the electrons are able to collectively shield the plasma and prevent propagation of electromagnetic waves. For densities lower than n_c, electromagnetic waves traverse the plasma and the electrons move according to the electromagnetic fields. Given a wavelength λ and a plasma with an electron density n_e, the dispersion relation reads

$$\tilde{n}(\lambda)^2 = 1 - \frac{n_e}{n_c(\lambda)}. \tag{F.11}$$

G. Plasma dynamics of the hydrogen-jet target at subrelativistic pump-laser intensities

G.1. Setup in target chamber I1

To study the plasma dynamics of the cylindrical hydrogen-jet target for subrelativistic pump-laser intensities, a dedicated pump-probe experiment is conducted in experimental chamber I1. The experiment is part of a master-thesis project (Ref. [15]) that was supervised within this thesis project. A part of the DRACO-150TW-laser beam is used as pump laser. The top-view schematic of the setup is shown in figure G.1 (a). A 16 mm-wide circular aperture is placed in the collimated pump beam and the transmitted light is focused by an f/16 OAP to an Airy-pattern focus with a FWHM of 14 µm of the central disk (see fig. G.1 (b)). Two pulse-duration settings of the pump beam are realized by introducing defined dispersion in the beam path before compression (28.5 fs and 12.6 ps). The energy of the pump laser is tunable between 0.16 J and 2.7 µJ. Tuning is achieved by switching off laser amplifiers or by using a waveplate attenuator with a variable transmission between 10 and 100 %. This enables experiments with pump-laser peak intensities between $2.1 \cdot 10^{18}\,\mathrm{W/cm^2}$ and $3.6 \cdot 10^{13}\,\mathrm{W/cm^2}$ for the 28.5 fs pulse-duration setting and with intensities between $5.5 \cdot 10^{15}\,\mathrm{W/cm^2}$ and $1.3 \cdot 10^{12}\,\mathrm{W/cm^2}$ for the 12.6 ps pulse-duration setting. The experiments utilize the cylindrical hydrogen-jet target with a nominal source diameter of 5 µm.
The pump-laser-target interaction is investigated by off-harmonic optical shadowgraphy at 90° angle to the pump-laser-propagation direction. Two copropagating probe pulses with a wavelength of 515 nm and 258 nm are generated by the stand-alone synchronized probe-laser system (section 2.3.1). The *258 nm probe* and the *515 nm probe* feature a pulse energy of 5 µJ and approximately 0.3 µJ and a pulse duration of 260 fs and 160 fs, respectively. The pump-probe delay is variable and the temporal resolution of a time-delay scan is 175 fs. The captured shadowgrams are blurred by the pulse duration. Because of dispersion effects, the 515 nm probe arrives 4.6 ps earlier on target than the 258 nm probe. To increase fluence and to reduce the influence of parasitic plasma emission, the probe beams are focused on target by an f/1 OAP. For more details about the technical implementation, see Ref. [15]. A long-working-distance infinite-conjugate microscope objective (designed for laser operation at 266 nm and 532 nm wavelengths, *M Plan UV 80x* by *Mitutoyo*, alternatively *PFL-50-UV-AG-LC07-A* by *Op-*

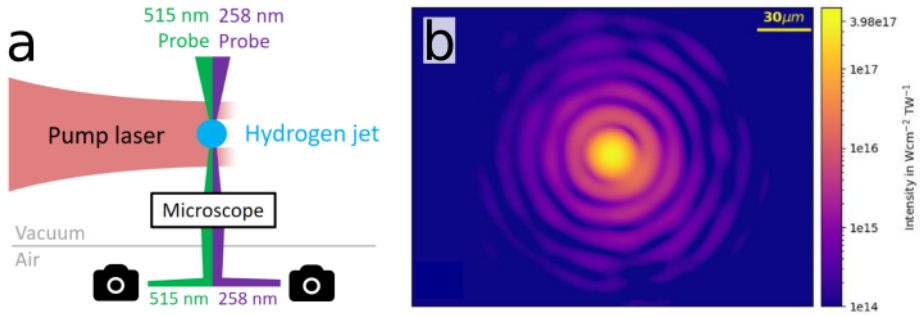

Figure G.1.: **(a)** Figure copied from Yang et al. [208]. Setup of the experiments with subrelativistic pump-laser intensities in target chamber I1. Energy and pulse duration of the pump laser are variable. The shadow of the target is imaged by two synchonized probe beams, each with a different wavelength, and one single microscopy system. A dichroic mirror splits the probe beams and each is recorded by a separate camera. **(b)** Figure copied from [15]. The pump-laser focal spot is an Airy-pattern with 14 µm FWHM of the central disk.

toSigma) is used to image the shadow of the target simultaneously with both probe colors. The images are split by a dichroic mirror behind the objective and each image is recorded by a separate camera, equipped with the corresponding bandpass filters of the probing wavelength. For the 258 nm probe, the magnification of the microscope is $M = 77$ and the measured spatial-resolution limit is better than 500 nm. The utilized camera is a *PCO.ultraviolet* (14bit-CCD sensor with 1392×1040 pixels, each of 4.65 µm size) that provides a total field of view (FoV) of 84 µm × 63 µm. For the 515 nm probe, the microscope features a magnification of $M = 70$ and a measured spatial-resolution limit better than 1 µm. The utilized camera is a *PCO.edge 4.2* (16bit-sCMOS sensor with 2048×2048 pixels, each of 6.5 µm size) that provides a FoV of 190 µm × 190 µm.

G.2. Results

The self-replenishing target delivery and the repetition rate of the pump laser allow for data acquisition of shadowgrams of the laser-target interaction at 1 Hz. Thousands of shadowgrams are recorded for each setting of the pump-laser-pulse duration. A large parameter space of pump-probe delays and pump-laser-peak intensities is scanned. A secondary optical-probing axis at 0 deg angle, which uses the OAP of the pump laser as imaging system, guarantees central overlap of the pump laser and the target. Both probing axis (0 deg and 90 deg) are used to sort out shots for which the target is not within the depth of field of the microscope [15]. For each pump-probe delay, peak intensity and pulse duration setting, a representative shadowgram is presented in the following.

G.2.1. 28.5 fs duration of the pump laser

For a pump-pulse duration of 28.5 fs, figures G.2 and G.3 show time-delay scans that are captured by the 258 nm probe for pump-laser-peak intensities between $2.1 \cdot 10^{18}$ W/cm^2 and $4.7 \cdot 10^{14}$ W/cm^2. Figures G.4 and G.5 show the corresponding data of the 515 nm probe. The shadowgrams of the 258 nm probe and the 515 nm probe correspond pairwise to the same shot, e.g., at $2.1 \cdot 10^{18}$ W/cm^2 peak intensity, the shadowgram of the 258 nm probe with 0 ps pump-probe delay corresponds to the same shot of the 515 nm probe with −5 ps pump-probe delay. Figure G.6 shows shadowgraphy images of the 258 nm probe and the 515 nm probe for the lowest peak intensities between $3.5 \cdot 10^{14}$ W/cm^2 and $3.5 \cdot 10^{13}$ W/cm^2.

G.2.2. 12.6 ps duration of the pump laser

The figures G.7 and G.8 show time-delay scans that are captured by the 258 nm probe at pump-laser-peak intensities between $5.5 \cdot 10^{15}$ W/cm^2 and $4.1 \cdot 10^{13}$ W/cm^2 and a pump-pulse duration of 12.6 ps. Figures G.10 and G.11 show the same data as captured by the 515 nm probe. The figures G.9 and G.12 show time-delay scans captured by the 258 nm probe and the 515 nm probe for pump-laser-peak intensities between $1.3 \cdot 10^{13}$ W/cm^2 and $1.3 \cdot 10^{12}$ W/cm^2. Like in the previous section, the shadowgrams of the 258 nm probe and the 515 nm probe pairwise correspond to the same shot.

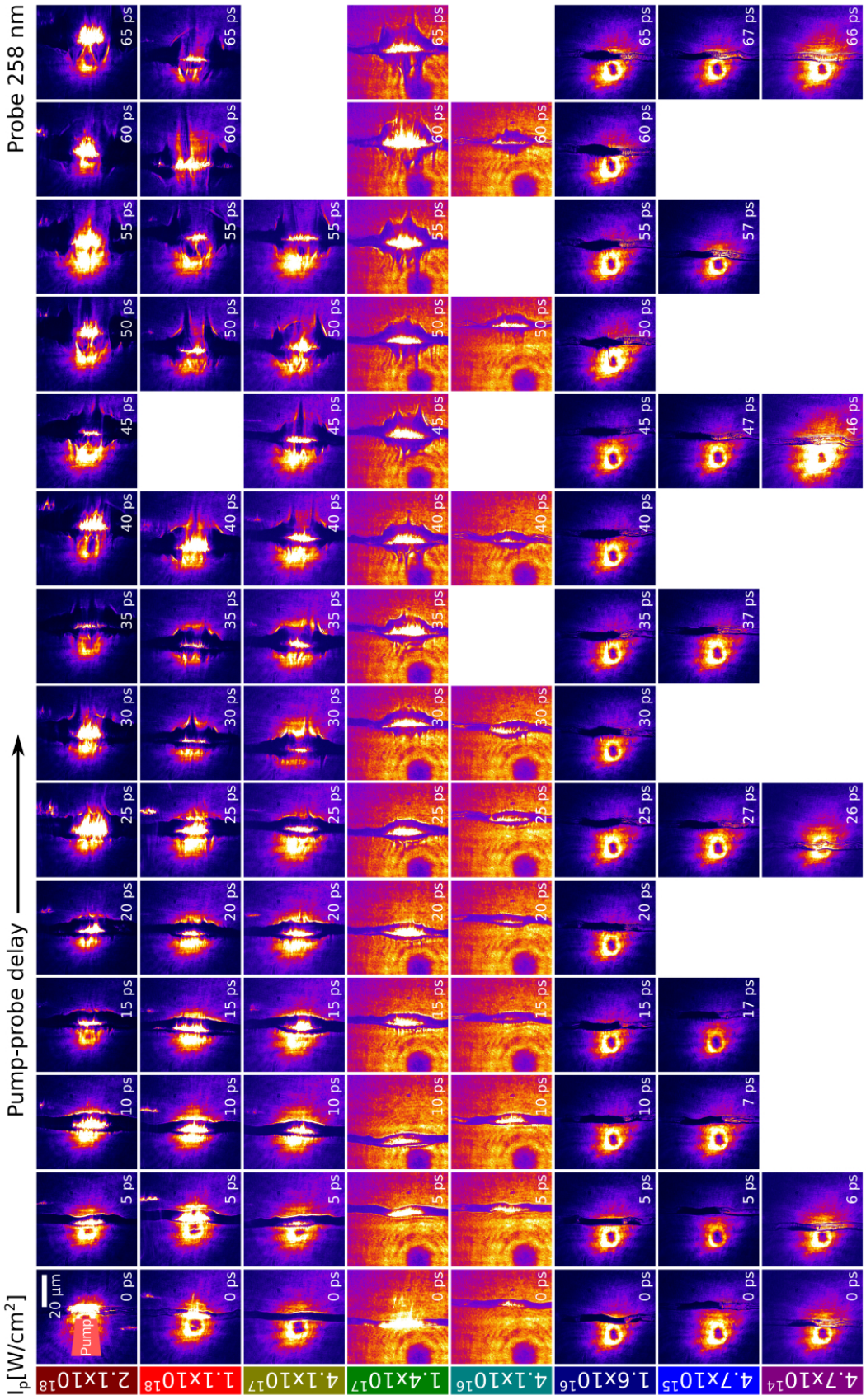

Figure G.2.: Time-resolved shadowgraphy of the plasma expansion of the cylindrical hydrogen-jet target captured by the 258 nm probe for different pump-laser-peak intensities and 28.5 fs pump-laser-pulse duration.

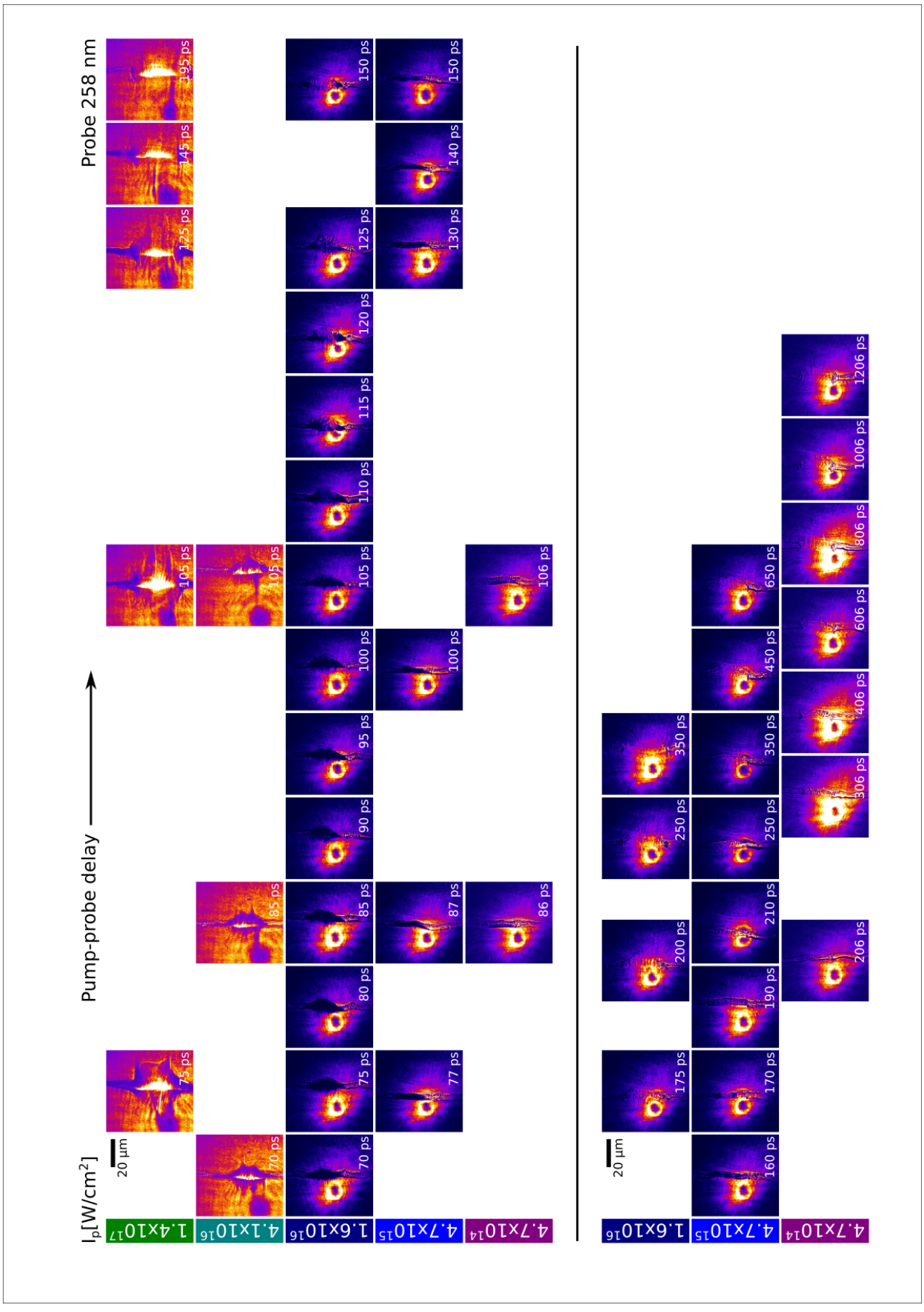

Figure G.3.: Time-resolved shadowgraphy of the plasma expansion of the cylindrical hydrogen-jet target captured by the 258 nm probe for different pump-laser-peak intensities and 28.5 fs pump-laser-pulse duration.

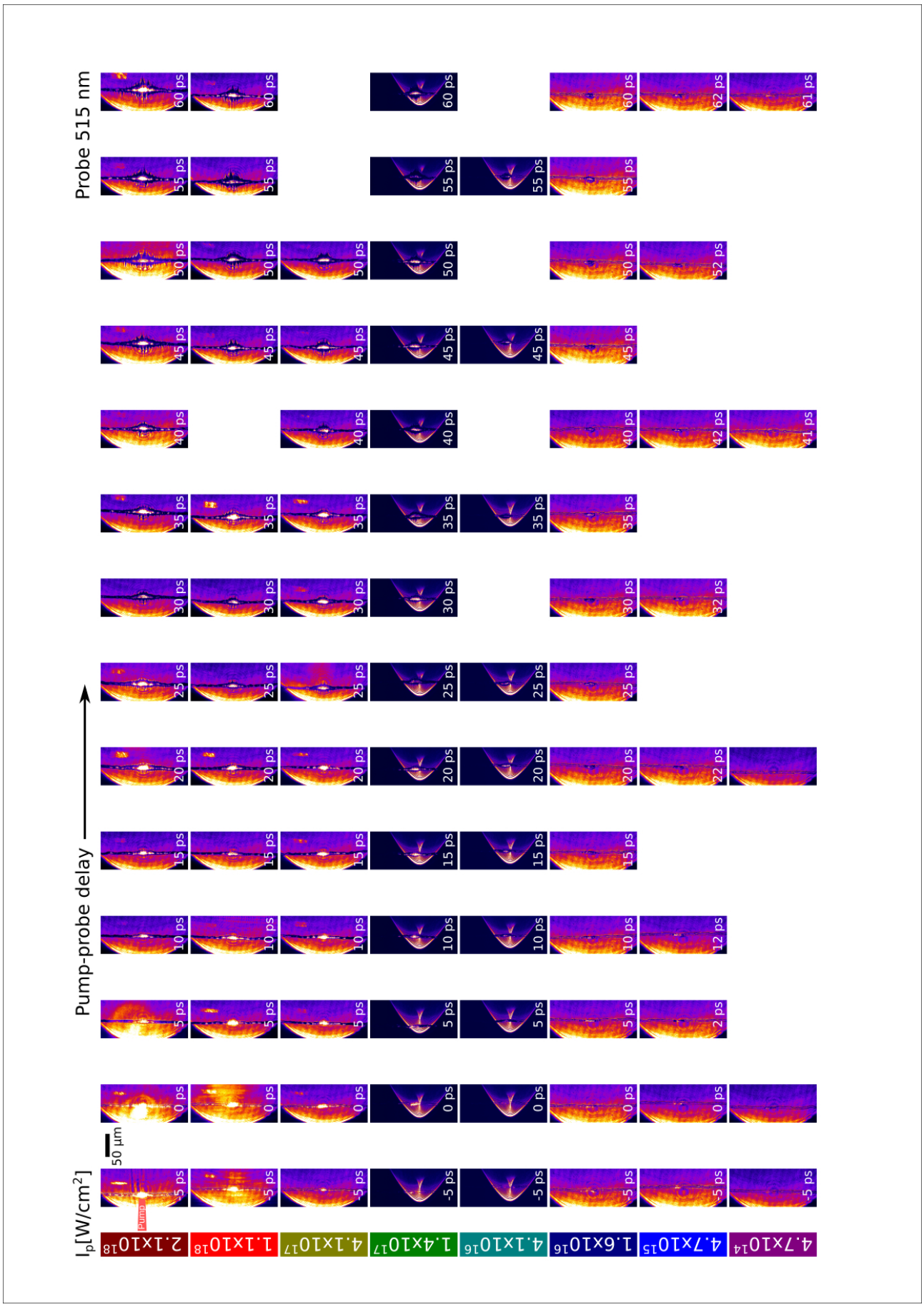

Figure G.4.: Time-resolved shadowgraphy of the plasma expansion of the cylindrical hydrogen-jet target captured by the 515 nm probe for different pump-laser-peak intensities and 28.5 fs pump-laser-pulse duration.

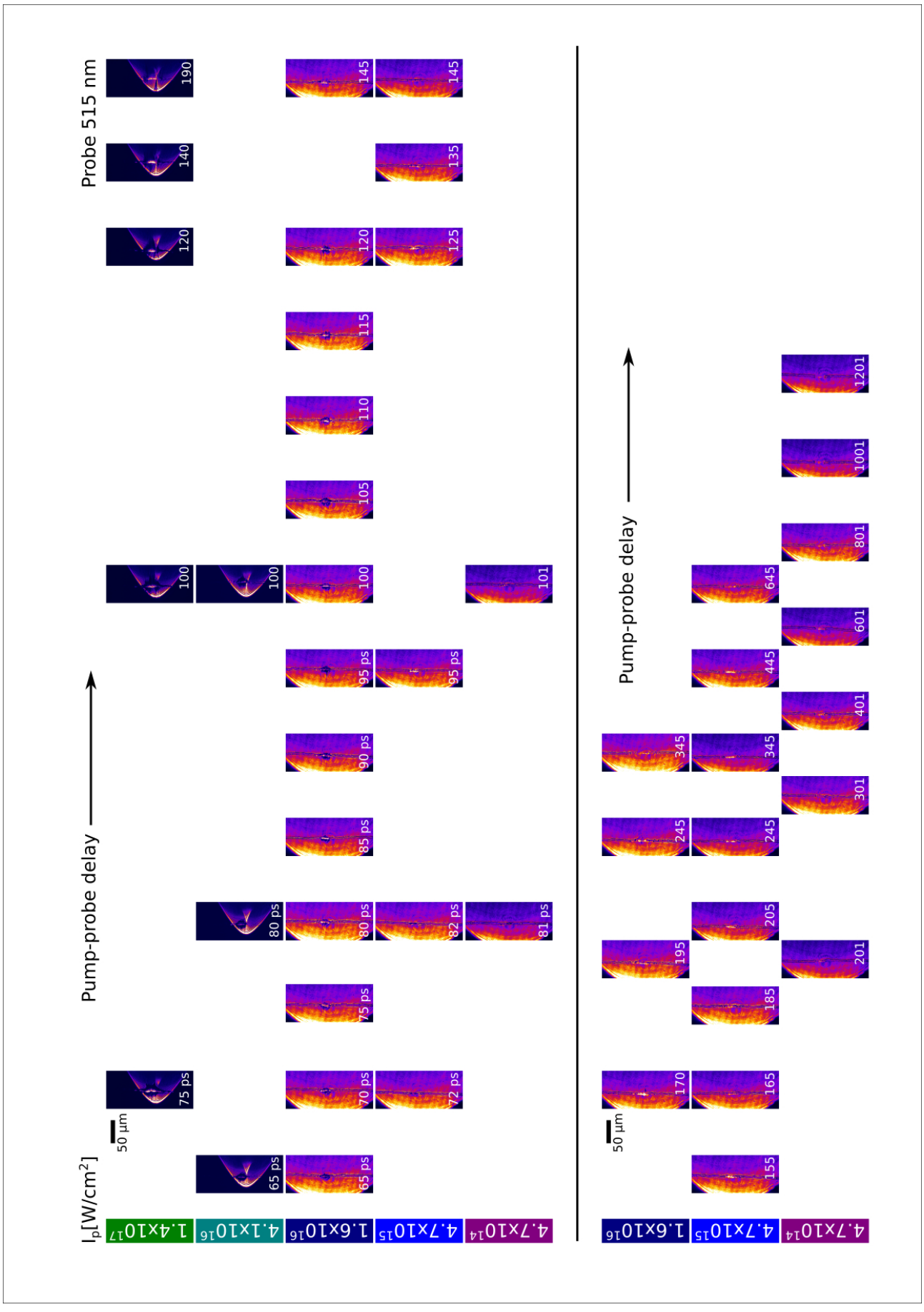

Figure G.5.: Time-resolved shadowgraphy of the plasma expansion of the cylindrical hydrogen-jet target captured by the 515 nm probe for different pump-laser-peak intensities and 28.5 fs pump-laser-pulse duration.

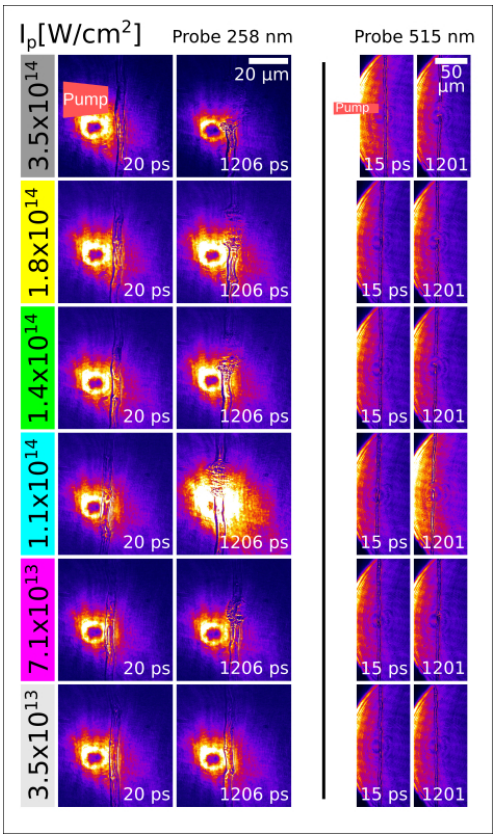

Figure G.6.: Time-resolved shadowgraphy of the plasma expansion of the cylindrical hydrogen-jet target captured by the 258 nm probe and the 515 nm probe for the lowest pump-laser-peak intensities and 28.5 fs pump-laser-pulse duration.

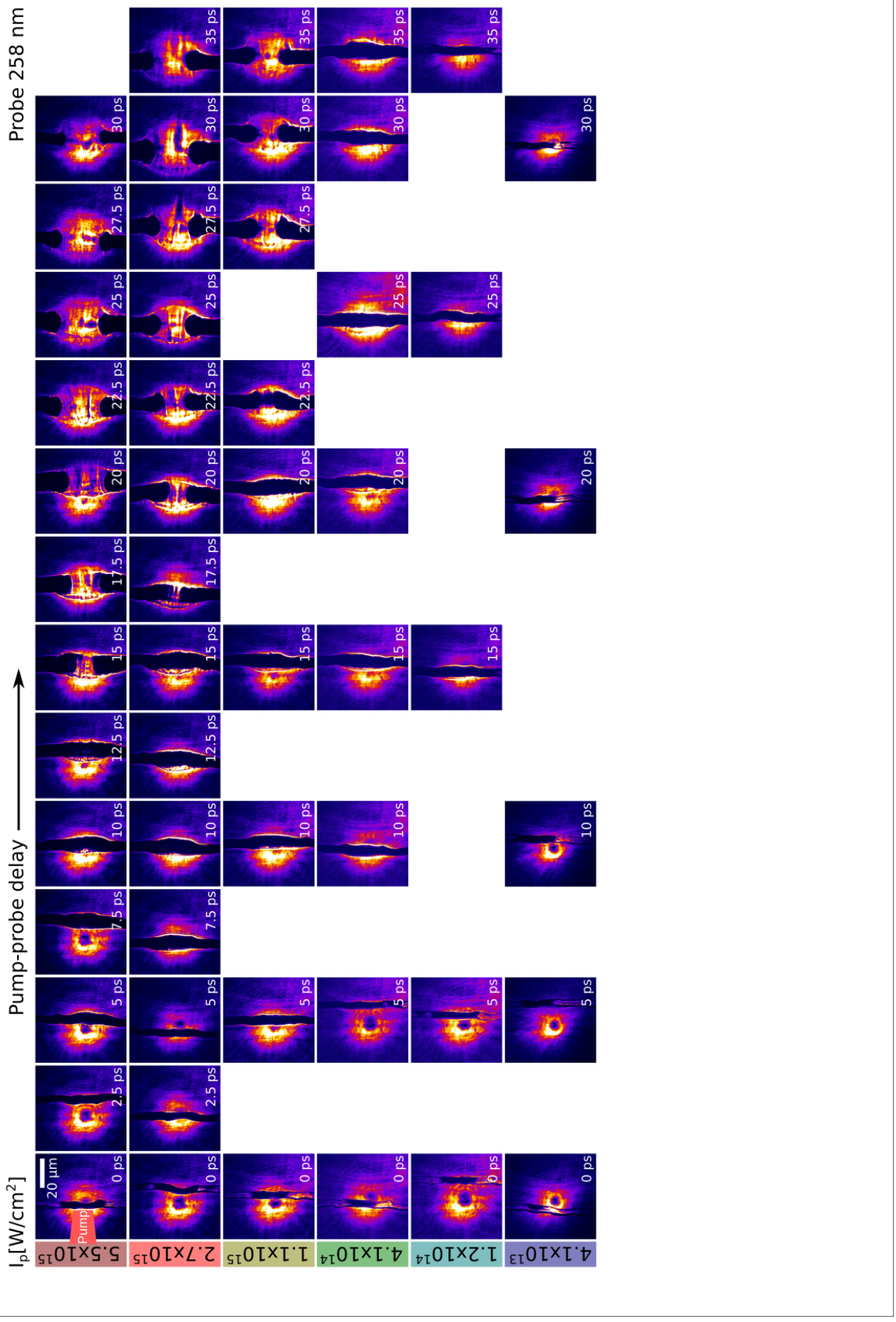

Figure G.7.: Time-resolved shadowgraphy of the plasma expansion of the cylindrical hydrogen-jet target captured by the 258 nm probe for different pump-laser-peak intensities and 12.6 ps pump-laser-pulse duration.

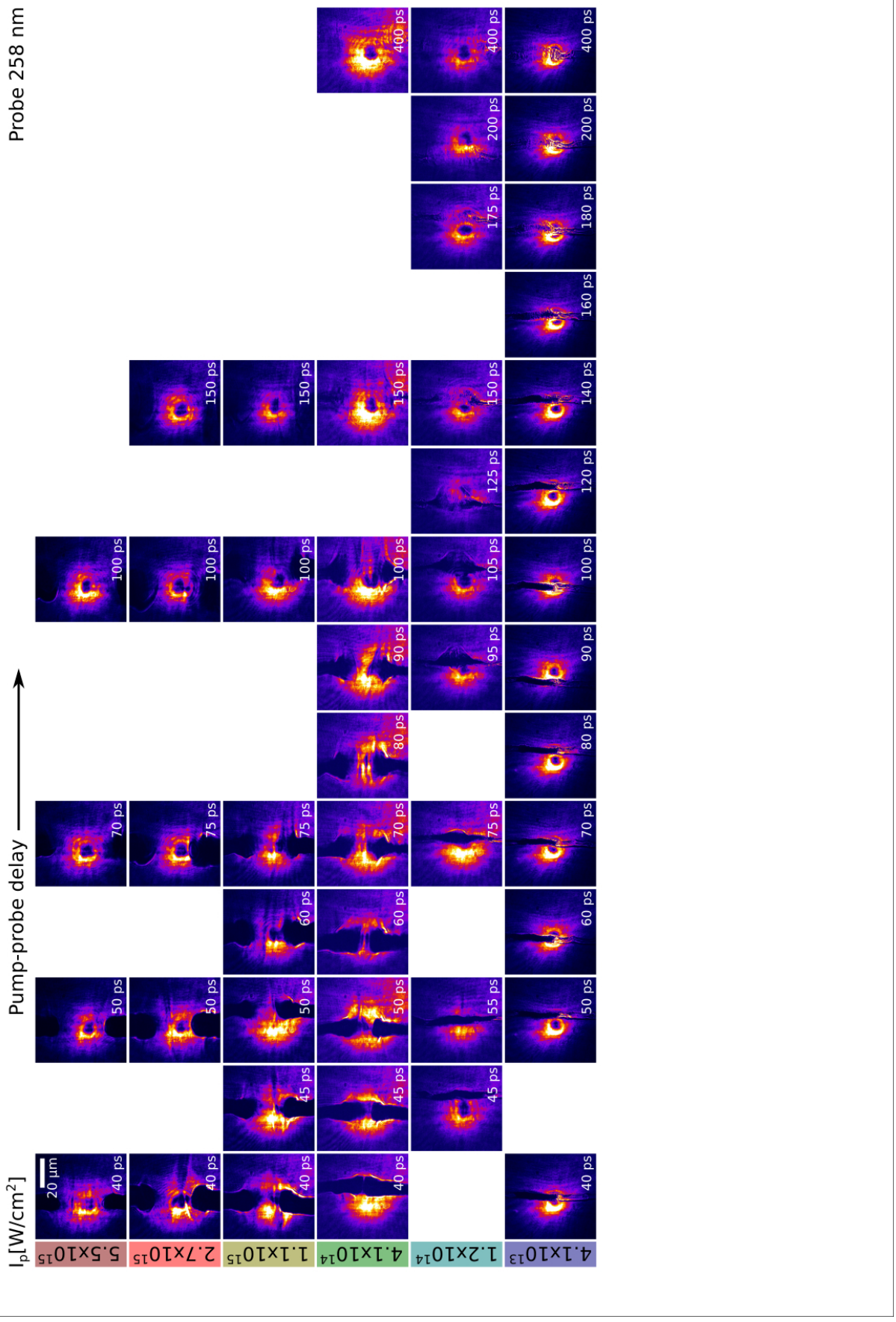

Figure G.8.: Time-resolved shadowgraphy of the plasma expansion of the cylindrical hydrogen-jet target captured by the 258 nm probe for different pump-laser-peak intensities and 12.6 ps pump-laser-pulse duration.

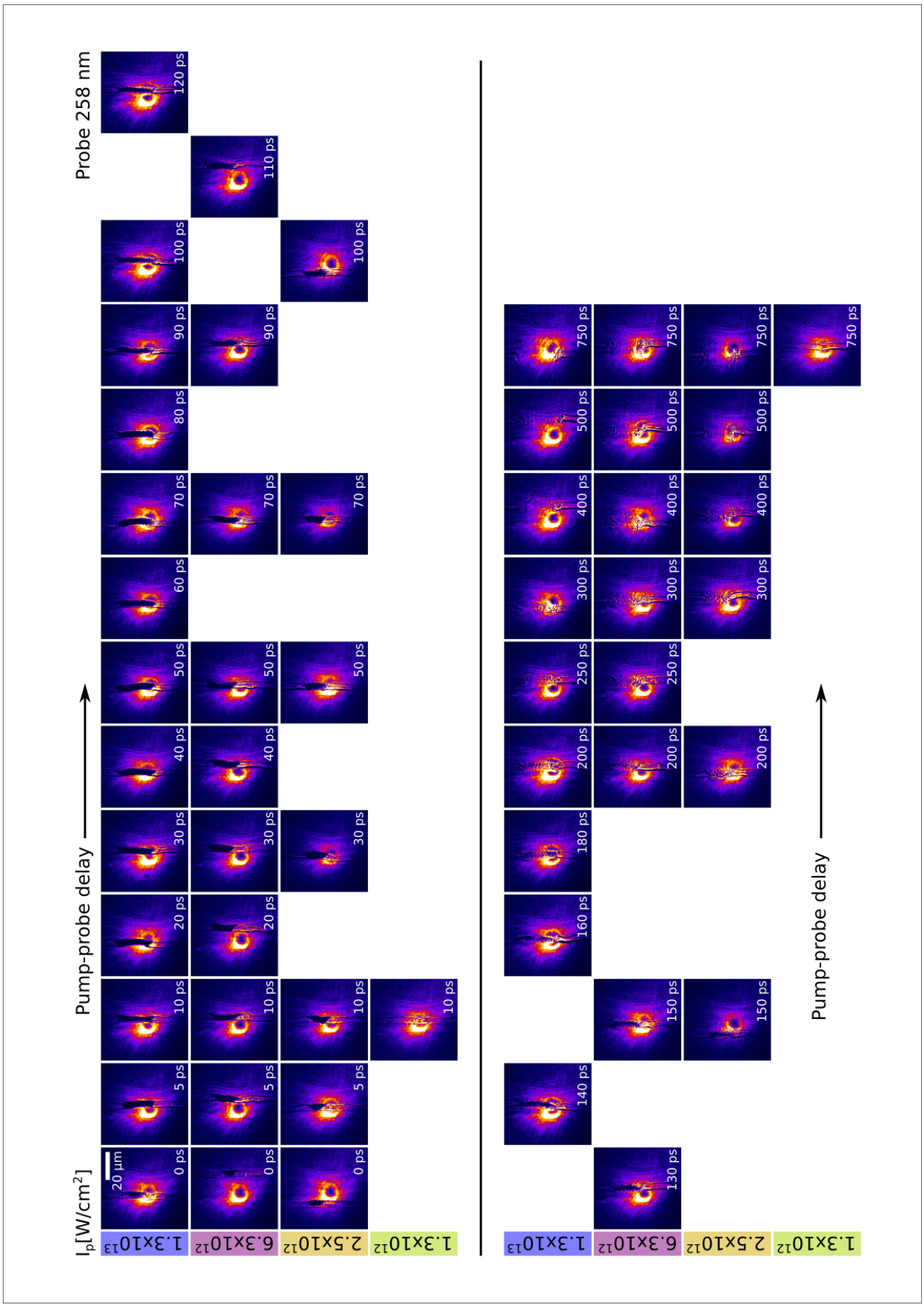

Figure G.9.: Time-resolved shadowgraphy of the plasma expansion of the cylindrical hydrogen-jet target captured by the 258 nm probe for different pump-laser-peak intensities and 12.6 ps pump-laser-pulse duration.

Figure G.10.: Time-resolved shadowgraphy of the plasma expansion of the cylindrical hydrogen-jet target captured by the 515 nm probe for different pump-laser-peak intensities and 12.6 ps pump-laser-pulse duration.

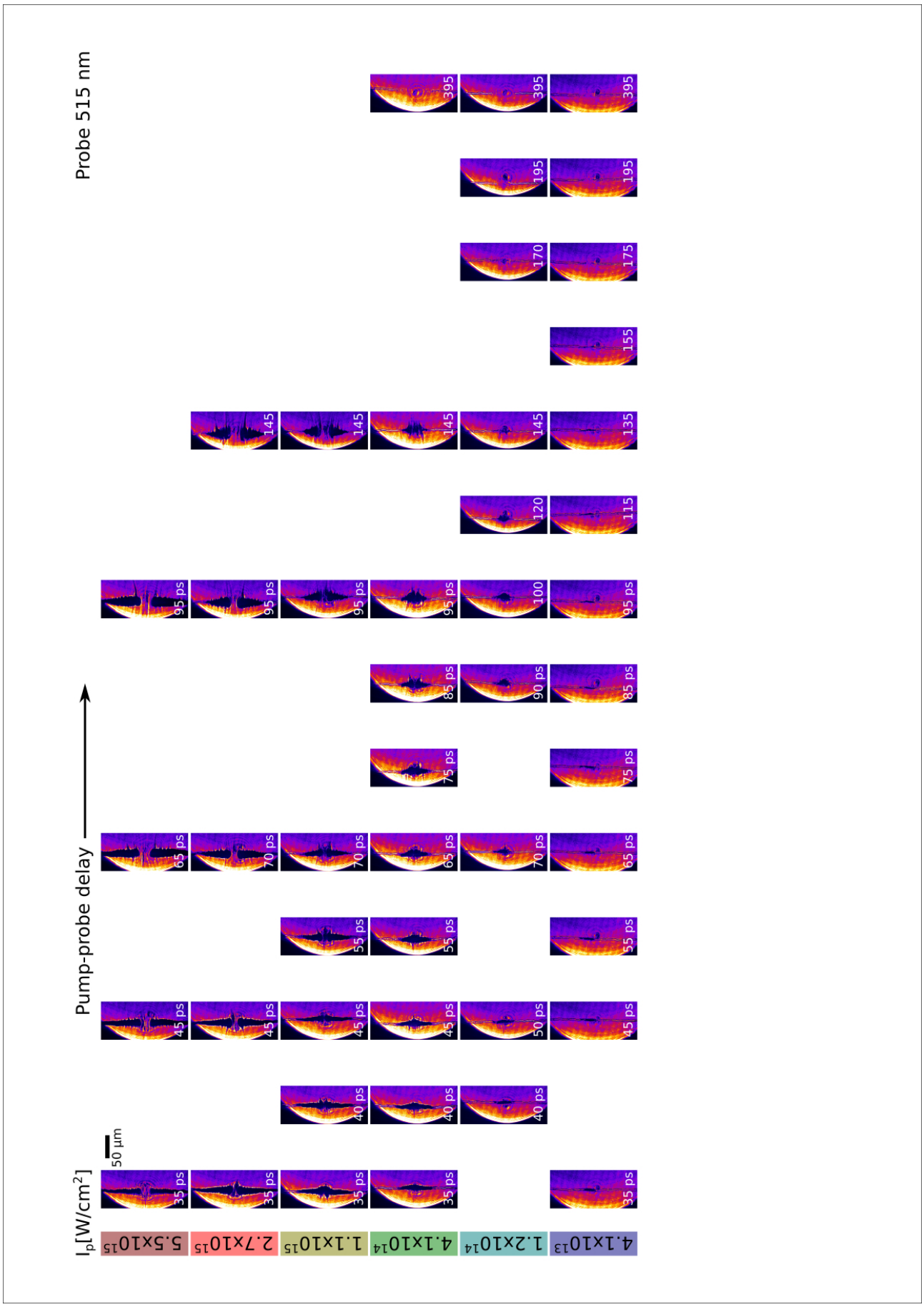

Figure G.11.: Time-resolved shadowgraphy of the plasma expansion of the cylindrical hydrogen-jet target captured by the 515 nm probe for different pump-laser-peak intensities and 12.6 ps pump-laser-pulse duration.

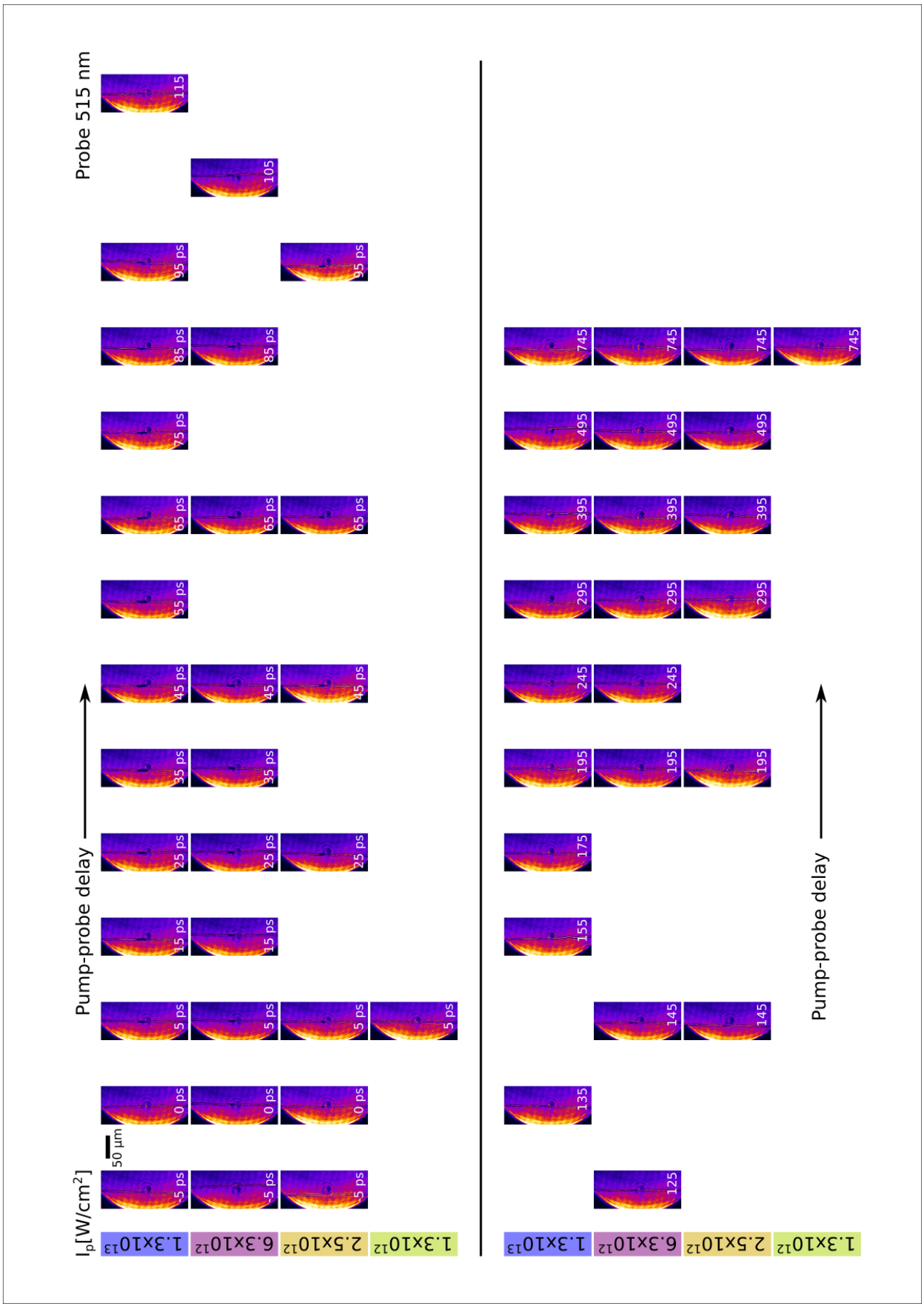

Figure G.12.: Time-resolved shadowgraphy of the plasma expansion of the cylindrical hydrogen-jet target captured by the 515 nm probe for different pump-laser-peak intensities and 12.6 ps pump-laser-pulse duration.

Bibliography

[1] FLYCHK. https://nlte.nist.gov/FLY/. [Accessed: February 21, 2023].

[2] FSWP by Rohde-Schwarz. https://www.rohde-schwarz.com/de/produkte/messtechnik/phasenrauschmessplaetze/rs-fswp-phasenrausch-und-vco-messplatz_63493-120512.html. [Accessed: February 21, 2023].

[3] Helmholtz International Beamline for Extreme Fields (HIBEF). https://www.hzdr.de/db/Cms?pNid=694&pLang=en. [Accessed: February 21, 2023].

[4] High Energy Density division at European XFEL. https://www.xfel.eu/facility/instruments/hed/index_eng.html. [Accessed: February 21, 2023].

[5] High Energy Density Science division at SLAC National Accelerator Laboratory. https://heds.slac.stanford.edu/. [Accessed: February 21, 2023].

[6] ICUIL World map 2020. https://www.icuil.org/pdf/icuil-world-map-2020.pdf. [Accessed: February 21, 2023].

[7] Introduction to PyAble, a package for Python. https://pyabel.readthedocs.io/en/latest/readme_link.html#introduction. [Accessed: February 21, 2023].

[8] Laser ion acceleration at Helmholtz-Zentrum Dresden Rossendorf. https://www.hzdr.de/db/Cms?pNid=2094. [Accessed: February 21, 2023].

[9] Light Conversion. https://www.lightcon.com/. [Accessed: February 21, 2023].

[10] MenloSystems. https://www.menlosystems.com/. [Accessed: February 21, 2023].

[11] NIST Atomic Spectra Database Ionization Energies. https://physics.nist.gov/PhysRefData/ASD/ionEnergy.html. [Accessed: February 21, 2023].

[12] SNLO. https://as-photonics.com/products/snlo/. [Accessed: February 21, 2023].

[13] Félicie Albert, Marie-Emmanuelle Couprie, Alexander Debus, Mike C Downer, Jérôme Faure, Alessandro Flacco, Leonida A Gizzi, Thomas Grismayer, Axel Huebl, Chan Joshi, et al. 2020 roadmap on plasma accelerators. *New J. Phys.*, 23(3):031101, 2021. https://iopscience.iop.org/article/10.1088/1367-2630/abcc62/meta.

[14] TD Arber, Keith Bennett, CS Brady, A Lawrence-Douglas, MG Ramsay, NJ Sircombe, P Gillies, RG Evans, Holger Schmitz, AR Bell, et al. Contemporary particle-in-cell approach to laser-plasma modelling. *Plasma Phys. Control. Fusion*, 57(11):113001, 2015. https://iopscience.iop.org/article/10.1088/0741-3335/57/11/113001/meta.

[15] Stefan Assenbaum. Characterization of a cryogenic hydrogen jet target in the low intensity regime to optimize laser proton acceleration. Master's thesis, TU Dresden, 2020.

[16] S. Augst, D. Strickland, D. D. Meyerhofer, S. L. Chin, and J. H. Eberly. Tunneling ionization of noble gases in a high-intensity laser field. *Phys. Rev. Lett.*, 63:2212–2215, Nov 1989. https://link.aps.org/doi/10.1103/PhysRevLett.63.2212.

[17] P Balling and Jørgen Schou. Femtosecond-laser ablation dynamics of dielectrics: basics and applications for thin films. *Rep. Prog. Phys.*, 76(3):036502, 2013. https://doi.org/10.1088/0034-4885/76/3/036502.

[18] W Bang, BJ Albright, PA Bradley, DC Gautier, S Palaniyappan, EL Vold, MA Santiago Cordoba, CE Hamilton, and JC Fernández. Visualization of expanding warm dense gold and diamond heated rapidly by laser-generated ion beams. *Sci. Rep.*, 5(1):1–7, 2015. https://www.nature.com/articles/srep14318.

[19] D. Bauer and P. Mulser. Exact field ionization rates in the barrier-suppression regime from numerical time-dependent schrödinger-equation calculations. *Phys. Rev. A*, 59:569–577, Jan 1999. https://link.aps.org/doi/10.1103/PhysRevA.59.569.

[20] Georg A Becker, Matthew B Schwab, Robert Lötzsch, Stefan Tietze, Diethard Klöpfel, Martin Rehwald, Hans-Peter Schlenvoigt, Alexander Sävert, Ulrich Schramm, Matt Zepf, et al. Characterization of laser-driven proton acceleration from water microdroplets. *Sci. Rep.*, 9(1):1–8, 2019. https://doi.org/10.1038/s41598-019-53587-3.

[21] FN Beg, AR Bell, AE Dangor, CN Danson, AP Fews, ME Glinsky, BA Hammel, P Lee, PA Norreys, and Ma Tatarakis. A study of picosecond laser–solid interactions up to 10^{19} W cm^{-2}. *Phys. Plasma*, 4(2):447–457, 1997. https://aip.scitation.org/doi/abs/10.1063/1.872103.

[22] R Benattar, C Popovics, and R Sigel. Polarized light interferometer for laser fusion studies. *Rev. Sci. Instrum.*, 50(12):1583–1586, 1979. https://aip.scitation.org/doi/abs/10.1063/1.1135764.

[23] Constantin Bernert, Stefan Assenbaum, Stefan Bock, Florian-Emanuel Brack, Thomas E. Cowan, Chandra B. Curry, Marco Garten, Lennart Gaus, Maxence Gauthier, René Gebhardt, et al. Transient laser-induced breakdown of dielectrics in ultrarelativistic laser-solid interactions. *Phys. Rev. Appl.*, 19:014070, Jan 2023. https://link.aps.org/doi/10.1103/PhysRevApplied.19.014070.

[24] Constantin Bernert, Stefan Assenbaum, Florian-Emanuel Brack, Thomas E. Cowan, Chandra B. Curry, Marco Garten, Lennart Gaus, Maxence Gauthier, Sebastian Göde, Ilja Goethel, et al. Off-harmonic optical probing of high intensity laser plasma expansion dynamics in solid density hydrogen jets. *Sci. Rep.*, 12:7287, 2022. https://doi.org/10.1038/s41598-022-10797-6.

[25] Elke Beyreuther, Michael Brand, Stefan Hans, Katalin Hideghéty, Leonhard Karsch, Elisabeth Leßmann, Michael Schürer, Emília Rita Szabó, and Jörg Pawelke. Feasibility of proton flash effect tested by zebrafish embryo irradiation. *Radiotherapy and Oncology*, 139:46–50, 2019. https://www.sciencedirect.com/science/article/pii/S0167814019329640.

[26] J Bierbach, C Rödel, M Yeung, B Dromey, T Hahn, A Galestian Pour, S Fuchs, A E Paz, S Herzer, S Kuschel, et al. Generation of 10 μW relativistic surface high-harmonic radiation at a repetition rate of 10 Hz. *New J. Phys.*, 14(6):065005, Jun 2012. https://doi.org/10.1088/1367-2630/14/6/065005.

[27] Stefan Bock, Thomas Oksenhendler, Thomas Püschel, René Gebhardt, Uwe Helbig, Richard Pausch, Tim Ziegler, Constantin Bernert, Karl Zeil, Arie Irman, et al. Spectral-temporal measurement capabilities of third-order correlators. *Opt. Express*, 31(6):9923–9934, Mar 2023. https://opg.optica.org/oe/abstract.cfm?URI=oe-31-6-9923.

[28] Paul Bolton, Katia Parodi, and Jörg Schreiber. *Applications of laser-driven particle acceleration.* CRC Press, 2018. https://www.routledge.com/Applications-of-Laser-Driven-Particle-Acceleration/Bolton-Parodi-Schreiber/p/book/9780367571511.

[29] M. Borghesi, D. H. Campbell, A. Schiavi, M. G. Haines, O. Willi, A. J. MacKinnon, P. Patel, L. A. Gizzi, M. Galimberti, R. J. Clarke, et al. Electric field detection in laser-plasma interaction experiments via the proton imaging technique. *Phys. Plasma*, 9(5):2214–2220, 2002. https://doi.org/10.1063/1.1459457.

[30] M Borghesi, AJ Mackinnon, AR Bell, G Malka, C Vickers, O Willi, JR Davies, A Pukhov, and J Meyer-ter Vehn. Observations of collimated ionization channels in aluminum-coated glass targets irradiated by ultraintense laser pulses. *Phys. Rev. Lett.*, 83(21):4309, 1999. https://link.aps.org/doi/10.1103/PhysRevLett.83.4309.

[31] Florian-Emanuel Brack, Florian Kroll, Lennart Gaus, Constantin Bernert, Elke Beyreuther, Thomas E. Cowan, Leonhard Karsch, Stephan Kraft, Leoni A. Kunz-Schughart, Elisabeth Lessmann, et al. Spectral and spatial shaping of laser-driven proton beams using a pulsed high-field magnet beamline. *Sci. Rep.*, 10:9118, 2020. https://doi.org/10.1038/s41598-020-65775-7.

[32] A. V. Brantov, E. A. Govras, V. F. Kovalev, and V. Yu. Bychenkov. Synchronized ion acceleration by ultraintense slow light. *Phys. Rev. Lett.*, 116:085004, Feb 2016. https://link.aps.org/doi/10.1103/PhysRevLett.116.085004.

[33] F. Brunel. Not-so-resonant, resonant absorption. *Phys. Rev. Lett.*, 59:52–55, Jul 1987. https://link.aps.org/doi/10.1103/PhysRevLett.59.52.

[34] SV Bulanov, DV Dylov, T Zh Esirkepov, FF Kamenets, and DV Sokolov. Ion acceleration in a dipole vortex in a laser plasma corona. *Plasma Phys. Rep.*, 31(5):369–381, 2005. https://link.springer.com/article/10.1134/1.1925787.

[35] Heiko Burau, Renée Widera, Wolfgang Hönig, Guido Juckeland, Alexander Debus, Thomas Kluge, Ulrich Schramm, Tomas E Cowan, Roland Sauerbrey, and Michael Bussmann. Picongpu: a fully relativistic particle-in-cell code for a gpu cluster. *IEEE Trans. Plasma Sci.*, 38(10):2831–2839, 2010. https://doi.org/10.1109/TPS.2010.2064310.

[36] M. Bussmann, H. Burau, T. E. Cowan, A. Debus, A. Huebl, G. Juckeland, T. Kluge, W. E. Nagel, R. Pausch, F. Schmitt, et al. Radiative signatures of the relativistic kelvin-helmholtz instability. In *Proceedings of the International Conference on High Performance Computing, Networking, Storage and Analysis*, SC '13, New York, NY, USA, 2013. Association for Computing Machinery. https://dl.acm.org/doi/abs/10.1145/2503210.2504564.

[37] Pankaj Chaudhary, Giuliana Milluzzo, Hamad Ahmed, Boris Odlozilik, Aaron McMurray, Kevin M. Prise, and Marco Borghesi. Radiobiology experiments with ultra-high dose rate laser-driven protons: Methodology and state-of-the-art. *Front. Phys.*, 9:75, 2021. https://www.frontiersin.org/article/10.3389/fphy.2021.624963.

[38] S.N. Chen, S Atzeni, M. Gauthier, D.P Higginson, F. Mangia, J-R Marques, R. Riquier, and J. Fuchs. Proton stopping power measurements using high intensity short pulse lasers produced proton beams. *Nucl. Instrum. Methods Phys. Res., Sect. A*, 740:105–106, 2014. https://www.sciencedirect.com/science/article/pii/S0168900213015027.

[39] SN Chen, M Vranic, T Gangolf, E Boella, P Antici, M Bailly-Grandvaux, P Loiseau, H Pépin, G Revet, JJ Santos, et al. Collimated protons accelerated from an overdense gas jet irradiated by a 1 μm wavelength high-intensity short-pulse laser. *Sci. Rep.*, 7(1):1–12, 2017. https://www.nature.com/articles/s41598-017-12910-6.

[40] B Chimier, O Utéza, N Sanner, M Sentis, T Itina, P Lassonde, F Légaré, F Vidal, and J.C. Kieffer. Damage and ablation thresholds of fused-silica in femtosecond regime. *Phys. Rev. B*, 84(9):094104, 2011. https://journals.aps.org/prb/abstract/10.1103/PhysRevB.84.094104.

[41] B. I. Cho, J. Osterholz, A. C. Bernstein, G. M. Dyer, A. Karmakar, A. Pukhov, and T. Ditmire. Characterization of two distinct, simultaneous hot electron beams in intense laser-solid interactions. *Phys. Rev. E*, 80:055402, Nov 2009. https://link.aps.org/doi/10.1103/PhysRevE.80.055402.

[42] Bjarke Holl Christensen and Peter Balling. Modeling ultrashort-pulse laser ablation of dielectric materials. *Phys. Rev. B*, 79(15):155424, 2009. https://journals.aps.org/prb/abstract/10.1103/PhysRevB.79.155424.

[43] A Compant La Fontaine, C Courtois, and E Lefebvre. Production of multi-mev bremsstrahlung x-ray sources by petawatt laser pulses on various targets. *Phys. Plasmas*, 19(2):023104, 2012. https://doi.org/10.1063/1.3680611.

[44] Fabrizio Consoli, Vladimir T. Tikhonchuk, Matthieu Bardon, Philip Bradford, David C. Carroll, Jakub Cikhardt, Mattia Cipriani, Robert J. Clarke, Thomas E. Cowan, Colin N. Danson, et al. Laser produced electromagnetic pulses: generation, detection and mitigation. *High Power Laser Sci. Eng.*, 8:e22, 2020. https://doi.org/10.1017/hpl.2020.13.

[45] R. S. Craxton, K. S. Anderson, T. R. Boehly, V. N. Goncharov, D. R. Harding, J. P. Knauer, R. L. McCrory, P. W. McKenty, D. D. Meyerhofer, J. F. Myatt, et al. Direct-drive inertial confinement fusion: A review. *Phys. Plasma*, 22(11):110501, 2015. https://doi.org/10.1063/1.4934714.

[46] Brigitte Cros. Laser-driven plasma wakefield: propagation effects. *arXiv preprint arXiv:1705.10566*, 2017. https://arxiv.org/abs/1705.10566.

[47] Chandra B Curry, Christopher Schoenwaelder, Sebastian Goede, Jongjin B Kim, Martin Rehwald, Franziska Treffert, Karl Zeil, Siegfried H Glenzer, and Maxence Gauthier. Cryogenic liquid jets for high repetition rate discovery science. *J. Vis. Exp.*, (159), 2020. https://doi.org/10.3791/61130.

[48] Hiroyuki Daido, Mamiko Nishiuchi, and Alexander S Pirozhkov. Review of laser-driven ion sources and their applications. *Rep. Prog. Phys.*, 75(5):056401, Apr 2012. https://doi.org/10.1088/0034-4885/75/5/056401.

[49] Colin N. Danson, Constantin Haefner, Jake Bromage, Thomas Butcher, Jean-Christophe F. Chanteloup, Enam A. Chowdhury, Almantas Galvanauskas, Leonida A. Gizzi an Joachim Hein, David I. Hillier, et al. Petawatt and exawatt class lasers worldwide. *High Power Laser Sci. Eng.*, 7:e54, 2019. https://doi.org/10.1017/hpl.2019.36.

[50] ZE Davidson, Bruno Gonzalez-Izquierdo, Adam Higginson, Kathryn Louise Lancaster, SDR Williamson, Martin King, D Farley, David Neely, Paul McKenna, and Ross J Gray. An optically multiplexed single-shot time-resolved probe of laser–plasma dynamics. *Opt. Express*, 27(4):4416–4423, 2019. http://www.osapublishing.org/oe/abstract.cfm?URI=oe-27-4-4416.

[51] Jean-Luc Déziel, Louis J Dubé, and Charles Varin. Dynamical rate equation model for femtosecond laser-induced breakdown in dielectrics. *Phys. Rev. B*, 104(4):045201, 2021. https://journals.aps.org/prb/abstract/10.1103/PhysRevB.104.045201.

[52] Emmanuel dHumières, Erik Lefebvre, Laurent Gremillet, and Victor Malka. Proton acceleration mechanisms in high-intensity laser interaction with thin foils. *Phys. Plasma*, 12(6):062704, 2005. https://doi.org/10.1063/1.1927097.

[53] N.V. Didenko, A.V. Konyashchenko, A.P. Lutsenko, and S.Yu. Tenyakov. Contrast degradation in a chirped-pulse amplifier due to generation of prepulses by postpulses. *Opt. Express*, 16(5):3178–3190, Mar 2008. http://opg.optica.org/oe/abstract.cfm?URI=oe-16-5-3178.

[54] T Ditmire, T Donnelly, AM Rubenchik, RW Falcone, and MD Perry. Interaction of intense laser pulses with atomic clusters. *Phys. Rev. A*, 53(5):3379, 1996. https://journals.aps.org/pra/abstract/10.1103/PhysRevA.53.3379.

[55] F Dollar, P Cummings, V Chvykov, L Willingale, M Vargas, V Yanovsky, C Zulick, A Maksimchuk, AGR Thomas, and K Krushelnick. Scaling high-order harmonic generation from

laser-solid interactions to ultrahigh intensity. *Phys. Rev. Lett.*, 110(17):175002, 2013. https://link.aps.org/doi/10.1103/PhysRevLett.110.175002.

[56] N. P. Dover, M. Nishiuchi, H. Sakaki, Ko. Kondo, M. A. Alkhimova, A. Ya. Faenov, M. Hata, N. Iwata, H. Kiriyama, J. K. Koga, et al. Effect of small focus on electron heating and proton acceleration in ultrarelativistic laser-solid interactions. *Phys. Rev. Lett.*, 124:084802, Feb 2020. https://link.aps.org/doi/10.1103/PhysRevLett.124.084802.

[57] Nicholas P. Dover, Tim Ziegler, Stefan Assenbaum, Constantin Bernert, Stefan Bock, Florian-Emanuel Brack, Thomas E. Cowan, Emma J. Ditter, Marco Garten, Lennart Gaus, et al. Enhanced ion acceleration from transparency-driven foils demonstrated at two ultraintense laser facilities. *Light Sci. Appl.*, 2023. https://doi.org/10.1038/s41377-023-01083-9.

[58] K. Eidmann, J. Meyer-ter Vehn, T. Schlegel, and S. Hüller. Hydrodynamic simulation of subpicosecond laser interaction with solid-density matter. *Phys. Rev. E*, 62:1202–1214, Jul 2000. https://link.aps.org/doi/10.1103/PhysRevE.62.1202.

[59] L Englert, M Wollenhaupt, L Haag, C Sarpe-Tudoran, B Rethfeld, and T Baumert. Material processing of dielectrics with temporally asymmetric shaped femtosecond laser pulses on the nanometer scale. *Appl. Phys. A*, 92(4):749–753, 2008. https://link.springer.com/article/10.1007/s00339-008-4584-1.

[60] E. Esarey, C. B. Schroeder, and W. P. Leemans. Physics of laser-driven plasma-based electron accelerators. *Rev. Mod. Phys.*, 81:1229–1285, Aug 2009. https://link.aps.org/doi/10.1103/RevModPhys.81.1229.

[61] T. Esirkepov, M. Borghesi, S. V. Bulanov, G. Mourou, and T. Tajima. Highly efficient relativistic-ion generation in the laser-piston regime. *Phys. Rev. Lett.*, 92:175003, Apr 2004. https://link.aps.org/doi/10.1103/PhysRevLett.92.175003.

[62] T. Esirkepov, M. Yamagiwa, and T. Tajima. Laser ion-acceleration scaling laws seen in multiparametric particle-in-cell simulations. *Phys. Rev. Lett.*, 96:105001, Mar 2006. https://link.aps.org/doi/10.1103/PhysRevLett.96.105001.

[63] Steffen Faik, Anna Tauschwitz, and Igor Iosilevskiy. The equation of state package FEOS for high energy density matter. *Comput. Phys. Commun.*, 227:117–125, 2018. https://doi.org/10.1016/j.cpc.2018.01.008.

[64] Roland Rainer Fäustlin, Th Bornath, Tilo Döppner, Stefan Düsterer, Eckhart Foerster, Carsten Fortmann, SH Glenzer, Sebastian Göde, Gianluca Gregori, Robert Irsig, et al. Observation of ultrafast nonequilibrium collective dynamics in warm dense hydrogen. *Phys. Rev. Lett.*, 104(12):125002, 2010. https://journals.aps.org/prl/abstract/10.1103/PhysRevLett.104.125002.

[65] S Feister, JA Nees, JT Morrison, KD Frische, C Orban, EA Chowdhury, and WM Roquemore. A novel femtosecond-gated, high-resolution, frequency-shifted shearing interferometry technique for probing pre-plasma expansion in ultra-intense laser experiments. *Rev. Sci. Instrum.*, 85(11):11D602, 2014. https://doi.org/10.1063/1.4886955.

[66] J.C. Fernández, B.J. Albright, F.N. Beg, F.N. Foord, B.M. Hegelich, J.J. Honrubia, M. Roth, R.B. Stephens, and L. Yin. Fast ignition with laser-driven proton and ion beams. *Nucl. Fusion*, 54(5):054006, apr 2014. https://doi.org/10.1088/0029-5515/54/5/054006.

[67] J.C. Fernández, B.J. Albright, F.N. Beg, M.E. Foord, B.M. Hegelich, J.J. Honrubia, M. Roth, R.B. Stephens, and L. Yin. Fast ignition with laser-driven proton and ion beams. *Nucl. Fusion*, 54(5):054006, Apr 2014. https://doi.org/10.1088/0029-5515/54/5/054006.

[68] F. Fiuza, A. Stockem, E. Boella, R. A. Fonseca, L. O. Silva, D. Haberberger, S. Tochitsky, C. Gong, W. B. Mori, and C. Joshi. Laser-driven shock acceleration of monoenergetic ion beams. *Phys. Rev. Lett.*, 109:215001, Nov 2012. https://link.aps.org/doi/10.1103/PhysRevLett.109.215001.

[69] L. B. Fletcher, J. Vorberger, W. Schumaker, C. Ruyer, S. Goede, E. Galtier, U. Zastrau, E. P. Alves, S. D. Baalrud, R. A. Baggott, et al. Electron-ion temperature relaxation in warm dense hydrogen observed with picosecond resolved x-ray scattering. *Front. Phys.*, 10, 2022. https://www.frontiersin.org/article/10.3389/fphy.2022.838524.

[70] R. A. Fonseca, L. O. Silva, F. S. Tsung, V. K. Decyk, W. Lu, C. Ren, W. B. Mori, S. Deng, S. Lee, T. Katsouleas, and J. C. Adam. Osiris: A three-dimensional, fully relativistic particle in cell code for modeling plasma based accelerators. In Peter M. A. Sloot, Alfons G. Hoekstra, C. J. Kenneth Tan, and Jack J. Dongarra, editors, *Computational Science — ICCS 2002*, pages 342–351, Berlin, Heidelberg, 2002. Springer Berlin Heidelberg. https://link.springer.com/chapter/10.1007/3-540-47789-6_36.

[71] B. Fryxell, K. Olson, P. Ricker, F. X. Timmes, M. Zingale, D. Q. Lamb, P. MacNeice, R. Rosner, J. W. Truran, and H. Tufo. FLASH: An adaptive mesh hydrodynamics code for modeling astrophysical thermonuclear flashes. *Astrophys. J. Supplement Series*, 131(1):273–334, Nov 2000. https://doi.org/10.1086/317361.

[72] Jian Gao, Boyuan Li, Feng Liu, Huaipeng Cai, Min Chen, Xiaohui Yuan, Xulei Ge, Liming Chen, Zhengming Sheng, and Jie Zhang. Double optimal density gradients for harmonic generation from relativistically oscillating plasma surfaces. *Phys. Plasmas*, 26(10):103102, 2019. https://doi.org/10.1063/1.5097440.

[73] Lennart Gaus, Lothar Bischoff, Michael Bussmann, Eric Cunningham, Chandra B. Curry, Juncheng E, Eric Galtier, Maxence Gauthier, Alejandro Laso García, Marco Garten, et al. Probing ultrafast laser plasma processes inside solids with resonant small-angle x-ray scattering. *Phys. Rev. Research*, 3:043194, Dec 2021. https://link.aps.org/doi/10.1103/PhysRevResearch.3.043194.

[74] M. Gauthier, C. B. Curry, S. Göde, F.-E. Brack, J. B. Kim, M. J. MacDonald, J. Metzkes, L. Obst, M. Rehwald, C. Rödel, et al. High repetition rate, multi-mev proton source from cryogenic hydrogen jets. *Appl. Phys. Lett.*, 111(11):114102, 2017. https://doi.org/10.1063/1.4990487.

[75] M. Gauthier, J. B. Kim, C. B. Curry, B. Aurand, E. J. Gamboa, S. Göde, C. Goyon, A. Hazi, S. Kerr, A. Pak, et al. High-intensity laser-accelerated ion beam produced from cryogenic micro-jet target. *Rev. Sci. Instrum.*, 87(11):11D827, 2016. https://aip.scitation.org/doi/abs/10.1063/1.4961270.

[76] Paul Gibbon. *Short pulse laser interactions with matter: an introduction*. World Scientific, 2005. https://www.worldscientific.com/worldscibooks/10.1142/p116#t=aboutBook.

[77] V N Ginzburg, N V Didenko, Aleksandr V Konyashchenko, V V Lozhkarev, G A Luchinin, Andrei P Lutsenko, S Yu Mironov, Efim A Khazanov, and I V Yakovlev. Third-order correlator for measuring the time profile of petawatt laser pulses. *Quantum Electron.*, 38(11):1027–1032, Nov 2008. https://doi.org/10.1070/qe2008v038n11abeh013833.

[78] S. Göde, C. Rödel, K. Zeil, R. Mishra, M. Gauthier, F.-E. Brack, T. Kluge, M. J. MacDonald, J. Metzkes, L. Obst, et al. Relativistic electron streaming instabilities modulate proton beams accelerated in laser-plasma interactions. *Phys. Rev. Lett.*, 118:194801, May 2017. https://link.aps.org/doi/10.1103/PhysRevLett.118.194801.

[79] Ilja Goethel. PhD thesis, TU Dresden, 2023.

[80] Tais Gorkhover, Sebastian Schorb, Ryan Coffee, Marcus Adolph, Lutz Foucar, Daniela Rupp, Andrew Aquila, John D Bozek, Sascha W Epp, Benjamin Erk, et al. Femtosecond and nanometre visualization of structural dynamics in superheated nanoparticles. *Nat. Photonics*, 10(2):93–97, 2016. https://www.nature.com/articles/nphoton.2015.264.

[81] Ilja Göthel, Constantin Bernert, Michael Bussmann, Marco Garten, Thomas Miethlinger, Martin Rehwald, Karl Zeil, Tim Ziegler, Thomas E Cowan, Ulrich Schramm, and Thomas Kluge. Optimized laser ion acceleration at the relativistic critical density surface. *Plasma Phys. Controlled Fusion*, 64(4):044010, Feb 2022. http://iopscience.iop.org/article/10.1088/1361-6587/ac4e9f.

[82] RJ Gray, DC Carroll, XH Yuan, CM Brenner, Matthias Burza, M Coury, KL Lancaster, XX Lin, YT Li, D Neely, et al. Laser pulse propagation and enhanced energy coupling to fast electrons in dense plasma gradients. *New J. Phys.*, 16(11):113075, 2014. https://iopscience.iop.org/article/10.1088/1367-2630/16/11/113075/meta.

[83] L Gremillet, F Amiranoff, SD Baton, J-C Gauthier, M Koenig, E Martinolli, F Pisani, G Bonnaud, C Lebourg, C Rousseaux, et al. Time-resolved observation of ultrahigh intensity laser-produced electron jets propagating through transparent solid targets. *Phys. Rev. Lett.*, 83(24):5015, 1999. https://link.aps.org/doi/10.1103/PhysRevLett.83.5015.

[84] S. Guizard, A. Semerok, J. Gaudin, M. Hashida, P. Martin, and F. Quéré. Femtosecond laser ablation of transparent dielectrics: measurement and modelisation of crater profiles. *Appl. Surf. Sci.*, 186(1):364–368, 2002. https://www.sciencedirect.com/science/article/pii/S016943320100681X.

[85] MM Günther, ON Rosmej, P Tavana, M Gyrdymov, A Skobliakov, A Kantsyrev, S Zähter, NG Borisenko, A Pukhov, and NE Andreev. Forward-looking insights in laser-generated ultra-intense γ-ray and neutron sources for nuclear application and science. *Nat. Commun.*, 13(1):1–13, 2022. https://www.nature.com/articles/s41467-021-27694-7.

[86] Dan Haberberger, Sergei Tochitsky, Frederico Fiuza, Chao Gong, Ricardo A Fonseca, Luis O Silva, Warren B Mori, and Chan Joshi. Collisionless shocks in laser-produced plasma generate monoenergetic high-energy proton beams. *Nat. Phys.*, 8(1):95–99, 2012. https://www.nature.com/articles/nphys2130.

[87] Daniel Haffa, Jianhui Bin, Martin Speicher, Klaus Allinger, Jens Hartmann, Christian Kreuzer, Enrico Ridente, Tobias M Ostermayr, and Jörg Schreiber. Temporally resolved intensity contouring (tric) for characterization of the absolute spatio-temporal intensity distribution of a relativistic, femtosecond laser pulse. *Sci. Rep.*, 9(1):1–9, 2019. https://doi.org/10.1038/s41598-019-42683-z.

[88] E. Hecht. *Optics*. Boston: De Gruyter, 2018. https://www.degruyter.com/document/doi/10.1515/9783110526653/html?lang=en.

[89] JL Henares, P Puyuelo-Valdes, F Hannachi, T Ceccotti, M Ehret, F Gobet, L Lancia, J-R Marquès, JJ Santos, M Versteegen, et al. Development of gas jet targets for laser-plasma experiments at near-critical density. *Rev. Sci. Instrum.*, 90(6):063302, 2019. https://aip.scitation.org/doi/full/10.1063/1.5093613.

[90] A Higginson, RJ Gray, M King, RJ Dance, SDR Williamson, NMH Butler, R Wilson, R Capdessus, C Armstrong, JS Green, et al. Near-100 mev protons via a laser-driven transparency-enhanced hybrid acceleration scheme. *Nat. Commun.*, 9(1):1–9, 2018. https://www.nature.com/articles/s41467-018-03063-9.

[91] David Hillier, Colin Danson, Stuart Duffield, David Egan, Stephen Elsmere, Mark Girling, Ewan Harvey, Nicholas Hopps, Michael Norman, Stefan Parker, et al. Ultrahigh contrast from

a frequency-doubled chirped-pulse-amplification beamline. *Appl. Opt.*, 52(18):4258–4263, Jun 2013. http://www.osapublishing.org/ao/abstract.cfm?URI=ao-52-18-4258.

[92] L. G. Huang, T. Kluge, and T. E. Cowan. Dynamics of bulk electron heating and ionization in solid density plasmas driven by ultra-short relativistic laser pulses. *Phys. Plasma*, 23(6):063112, 2016. https://doi.org/10.1063/1.4953891.

[93] L. G. Huang, H. Takabe, and T. E. Cowan. Maximizing magnetic field generation in high power laser-solid interactions. *High Power Laser Sci. Eng.*, 7:e22, 2019. https://doi.org/10.1017/hpl.2019.9.

[94] K Inoue, H Kanzaki, and S Suga. Fundamental absorption spectra of solid hydrogen. *Solid State Commun.*, 30(10):627–629, 1979. https://www.sciencedirect.com/science/article/pii/0038109879901108.

[95] O Jäckel, J Polz, S. M. Pfotenhauer, H. P. Schlenvoigt, H Schwoerer, and M. C. Kaluza. All-optical measurement of the hot electron sheath driving laser ion acceleration from thin foils. *New J. Phys.*, 12(10):103027, 2010. https://doi.org/10.1088/1367-2630/12/10/103027.

[96] Antoine Jeandet, Spencer W. Jolly, Antonin Borot, Benoît Bussière, Paul Dumont, Julien Gautier, Olivier Gobert, Jean-Philippe Goddet, Anthony Gonsalves, Arie Irman, et al. Survey of spatio-temporal couplings throughout high-power ultrashort lasers. *Opt. Express*, 30(3):3262–3288, Jan 2022. https://opg.optica.org/oe/abstract.cfm?URI=oe-30-3-3262.

[97] L. Jiang and H.L. Tsai. Energy transport and material removal in wide bandgap materials by a femtosecond laser pulse. *Int. J. Heat Mass Transf.*, 48(3):487–499, 2005. https://doi.org/10.1016/j.ijheatmasstransfer.2004.09.016.

[98] M. P. Kalashnikov, E. Risse, H. Schönnagel, and W. Sandner. Double chirped-pulse-amplification laser: a way to clean pulses temporally. *Opt. Lett.*, 30(8):923–925, Apr 2005. http://www.osapublishing.org/ol/abstract.cfm?URI=ol-30-8-923.

[99] Malte C Kaluza, Marko IK Santala, Jörg Schreiber, George D Tsakiris, and Klaus J Witte. Time-sequence imaging of relativistic laser–plasma interactions using a novel two-color probe pulse. *Appl. Phys. B*, 92(4):475–479, 2008. https://doi.org/10.1007/s00340-008-3150-z.

[100] MC Kaluza, H-P Schlenvoigt, SPD Mangles, AGR Thomas, AE Dangor, H Schwoerer, WB Mori, Z Najmudin, and KM Krushelnick. Measurement of magnetic-field structures in a laser-wakefield accelerator. *Phys. Rev. Lett.*, 105(11):115002, 2010. https://link.aps.org/doi/10.1103/PhysRevLett.105.115002.

[101] Leonhard Karsch, Elke Beyreuther, Wolfgang Enghardt, Malte Gotz, Umar Masood, Ulrich Schramm, Karl Zeil, and Jörg Pawelke. Towards ion beam therapy based on laser plasma accelerators. *Acta Oncologica*, 56(11):1359–1366, 2017. https://doi.org/10.1080/0284186X.2017.1355111.

[102] Jérôme Kasparian and Jean-Pierre Wolf. Physics and applications of atmospheric nonlinear optics and filamentation. *Opt. Express*, 16(1):466–493, Jan 2008. http://opg.optica.org/oe/abstract.cfm?URI=oe-16-1-466.

[103] I Jong Kim, Ki Hong Pae, Il Woo Choi, Chang-Lyoul Lee, Hyung Taek Kim, Himanshu Singhal, Jae Hee Sung, Seong Ku Lee, Hwang Woon Lee, Peter V Nickles, et al. Radiation pressure acceleration of protons to 93 mev with circularly polarized petawatt laser pulses. *Phys. Plasma*, 23(7):070701, 2016. https://aip.scitation.org/doi/full/10.1063/1.4958654.

[104] J. B. Kim, S. Göde, and S. H. Glenzer. Development of a cryogenic hydrogen microjet for high-intensity, high-repetition rate experiments. *Rev. Sci. Instrum.*, 87(11):11E328, 2016. https://aip.scitation.org/doi/abs/10.1063/1.4961089.

[105] Hiromitsu Kiriyama, Yasuhiro Miyasaka, Akito Sagisaka, Koichi Ogura, Mamiko Nishiuchi, Alexander S Pirozhkov, Yuji Fukuda, Masaki Kando, and Kiminori Kondo. Experimental investigation on the temporal contrast of pre-pulses by post-pulses in a petawatt laser facility. *Opt. Lett.*, 45(5):1100–1103, 2020. https://opg.optica.org/ol/fulltext.cfm?uri=ol-45-5-1100&id=427582.

[106] Hiromitsu Kiriyama, Alexander S. Pirozhkov, Mamiko Nishiuchi, Yuji Fukuda, Koichi Ogura, Akito Sagisaka, Yasuhiro Miyasaka, Michiaki Mori, Hironao Sakaki, Nicholas P. Dover, et al. High-contrast high-intensity repetitive petawatt laser. *Opt. Lett.*, 43(11):2595–2598, Jun 2018. https://doi.org/10.1364/OL.43.002595.

[107] T Kluge, T Cowan, A Debus, U Schramm, K Zeil, and M Bussmann. Electron temperature scaling in laser interaction with solids. *Phys. Rev. Lett.*, 107(20):205003, 2011. https://journals.aps.org/prl/abstract/10.1103/PhysRevLett.107.205003.

[108] Florian Kroll, Florian-Emanuel Brack, Constantin Bernert, Stefan Bock, Elisabeth Bodenstein, Kerstin Brüchner, Thomas E. Cowan, Lennart Gaus, René Gebhardt, Uwe Helbig, et al. Tumour irradiation in mice with a laser-accelerated proton beam. *Nat. Phys.*, 18(3):316–322, 2022. https://www.nature.com/articles/s41567-022-01520-3.

[109] W. L. Kruer and Kent Estabrook. Jxb heating by very intense laser light. *Phys. Fluids*, 28(1):430–432, 1985. https://aip.scitation.org/doi/pdf/10.1063/1.865171.

[110] Matthias Kühnel, José M Fernández, Guzmán Tejeda, Anton Kalinin, Salvador Montero, and Robert E Grisenti. Time-resolved study of crystallization in deeply cooled liquid parahydrogen. *Phys. Rev. Lett.*, 106(24):245301, 2011. https://doi.org/10.1103/PhysRevLett.106.245301.

[111] KL Lancaster, JS Green, DS Hey, KU Akli, JR Davies, RJ Clarke, RR Freeman, H Habara, MH Key, R Kodama, et al. Measurements of energy transport patterns in solid density laser plasma interactions at intensities of 5×10^{20} W cm^{-2}. *Phys. Rev. Lett.*, 98(12):125002, 2007. https://link.aps.org/doi/10.1103/PhysRevLett.98.125002.

[112] M. Lenzner and W. Rudolph. *Laser-Induced Optical Breakdown in Solids*, volume 134 of *Springer Series in Optical Sciences - Strong Field Laser Physics*, pages 243–257. Springer, 2008. https://link.springer.com/chapter/10.1007/978-0-387-34755-4_11.

[113] Dan Levy, Constantin Bernert, Martin Rehwald, Igor A Andriyash, Stefan Assenbaum, Thomas Kluge, Eyal Kroupp, Lieselotte Obst-Huebl, Richard Pausch, Alexander Schulze-Makuch, et al. Laser-plasma proton acceleration with a combined gas-foil target. *New J. Phys.*, 22(10):103068, 2020. https://iopscience.iop.org/article/10.1088/1367-2630/abbf6d/meta.

[114] M. Lezius, S. Dobosz, D. Normand, and M. Schmidt. Explosion dynamics of rare gas clusters in strong laser fields. *Phys. Rev. Lett.*, 80:261–264, Jan 1998. https://link.aps.org/doi/10.1103/PhysRevLett.80.261.

[115] Guo-Qian Liao and Yu-Tong Li. Review of intense terahertz radiation from relativistic laser-produced plasmas. *IEEE Trans Plasma Sci IEEE Nucl Plasma Sci Soc*, 47(6):3002–3008, 2019. https://doi.org/10.1109/TPS.2019.2915624.

[116] John Lindl. Development of the indirect-drive approach to inertial confinement fusion and the target physics basis for ignition and gain. *Phys. Plasma*, 2(11):3933–4024, 1995. https://aip.scitation.org/doi/abs/10.1063/1.871025.

[117] Markus Loeser, Constantin Bernert, Daniel Albach, Karl Zeil, Ulrich Schramm, and Mathias Siebold. Compact millijoule Yb^{3+} : CaF^2 laser with 162fs pulses. *Opt. Express*, 29(6):9199–9206, Mar 2021. http://www.opticsexpress.org/abstract.cfm?URI=oe-29-6-9199.

[118] E. Louzon, Z. Henis, S. Pecker, Y. Ehrlich, D. Fisher, M. Fraenkel, and A. Zigler. Reduction of damage threshold in dielectric materials induced by negatively chirped laser pulses. *Appl. Phys. Lett.*, 87(24):241903, 2005. https://doi.org/10.1063/1.2140476.

[119] Xiaoming Lu, Hui Zhang, Jinfeng Li, and Yuxin Leng. Reducing temporal pedestal in a ti: sapphire chirped-pulse amplification system by using a stretcher based on two concave mirrors. *Opt. Lett.*, 46(21):5320–5323, 2021. https://opg.optica.org/ol/fulltext.cfm?uri=ol-46-21-5320&id=460686.

[120] Olle Lundh, Filip Lindau, Anders Persson, C-G Wahlström, P McKenna, and D Batani. Influence of shock waves on laser-driven proton acceleration. *Phys. Rev. E*, 76(2):026404, 2007. https://journals.aps.org/pre/abstract/10.1103/PhysRevE.76.026404.

[121] François Lureau, Ghuillaume Matras, Olivier Chalus, Christophe Derycke, Christophe Radier, Olivier Casagrande, Sandrine Ricaud, and Christophe Simon Boisson. 10 petawatt laser system for extreme light physics. In *Conference on Lasers and Electro-Optics*, page STu4E.2. Optical Society of America, 2020. http://www.osapublishing.org/abstract.cfm?URI=CLEO_SI-2020-STu4E.2.

[122] Jingui Ma, Peng Yuan, Xiaoping Ouyang, Jing Wang, Guoqiang Xie, and Liejia Qian. Demonstration of single-shot measurements of 10^{13} ultrahigh-contrast pulses by manipulating cross-correlation. *Adv. Photonics Res.*, 2(12):2100105, 2021. https://doi.org/10.1002/adpr.202100105.

[123] Jingui Ma, Peng Yuan, Jing Wang, Guoqiang Xie, Heyuan Zhu, and Liejia Qian. Single-shot cross-correlator for pulse-contrast characterization of high peak-power lasers. *High Power Laser Sci. Eng.*, 6:e61, 2018. https://doi.org/10.1017/hpl.2018.57.

[124] Andrea Macchi, Marco Borghesi, and Matteo Passoni. Ion acceleration by superintense laser-plasma interaction. *Rev. Mod. Phys.*, 85(2):751, 2013. https://journals.aps.org/rmp/abstract/10.1103/RevModPhys.85.751.

[125] A. Maksimchuk, S. Reed, S. S. Bulanov, V. Chvykov, G. Kalintchenko, T. Matsuoka, C. McGuffey, G. Mourou, N. Naumova, J. Nees, et al. Studies of laser wakefield structures and electron acceleration in underdense plasmas. *Phys. Plasma*, 15(5):056703, 2008. https://doi.org/10.1063/1.2856373.

[126] Sophia Malko, Witold Cayzac, Valeria Ospina-Bohorquez, Krish Bhutwala, M Bailly-Grandvaux, Christopher McGuffey, Robert Fedosejevs, Xavier Vaisseau, An Tauschwitz, JI Apiñaniz, et al. Proton stopping measurements at low velocity in warm dense carbon. *Nat. Commun.*, 13(1):1–12, 2022. https://www.nature.com/articles/s41467-022-30472-8.

[127] D. Margarone, A. Velyhan, J. Dostal, J. Ullschmied, J. P. Perin, D. Chatain, S. Garcia, P. Bonnay, T. Pisarczyk, R. Dudzak, et al. Proton acceleration driven by a nanosecond laser from a cryogenic thin solid-hydrogen ribbon. *Phys. Rev. X*, 6:041030, Nov 2016. https://link.aps.org/doi/10.1103/PhysRevX.6.041030.

[128] E Martinolli, M Koenig, F Amiranoff, SD Baton, L Gremillet, JJ Santos, TA Hall, M Rabec-Le-Gloahec, C Rousseaux, and D Batani. Fast electron heating of a solid target in ultrahigh-intensity laser pulse interaction. *Phys. Rev. E*, 70(5):055402, 2004. https://journals.aps.org/pre/abstract/10.1103/PhysRevE.70.055402.

[129] A. S. Martynenko, S. A. Pikuz, I. Yu. Skobelev, S. N. Ryazantsev, C. Baird, N. Booth, L. Doehl, P. Durey, A. Ya. Faenov, D. Farley, et al. Effect of plastic coating on the density of plasma formed in si foil targets irradiated by ultra-high-contrast relativistic laser pulses. *Phys. Rev. E*, 101:043208, Apr 2020. https://link.aps.org/doi/10.1103/PhysRevE.101.043208.

[130] AS Martynenko, SA Pikuz, L Antonelli, F Barbato, G Boutoux, L Giuffrida, JJ Honrubia, E Hume, J Jacoby, D Khaghani, et al. Role of relativistic laser intensity on isochoric heating of metal wire targets. *Opt. Express*, 29(8):12240–12251, 2021. https://opg.optica.org/oe/fulltext.cfm?uri=oe-29-8-12240&id=449934.

[131] U Masood, M Bussmann, TE Cowan, W Enghardt, L Karsch, F Kroll, U Schramm, and J Pawelke. A compact solution for ion beam therapy with laser accelerated protons. *Appl. Phys. B*, 117(1):41–52, 2014. https://link.springer.com/article/10.1007/s00340-014-5796-z.

[132] K. Matsukado, T. Esirkepov, K. Kinoshita, H. Daido, T. Utsumi, Z. Li, A. Fukumi, Y. Hayashi, S. Orimo, M. Nishiuchi, et al. Energetic protons from a few-micron metallic foil evaporated by an intense laser pulse. *Phys. Rev. Lett.*, 91:215001, Nov 2003. https://link.aps.org/doi/10.1103/PhysRevLett.91.215001.

[133] P McKenna, DC Carroll, Olle Lundh, F Nürnberg, K Markey, S Bandyopadhyay, D Batani, RG Evans, R Jafer, Saty Kar, et al. Effects of front surface plasma expansion on proton acceleration in ultraintense laser irradiation of foil targets. *Laser Part. Beams*, 26(4):591–596, 2008. https://doi.org/10.1017/S0263034608000657.

[134] J Metzkes, K Zeil, SD Kraft, M Rehwald, TE Cowan, and U Schramm. Reflective optical probing of laser-driven plasmas at the rear surface of solid targets. *Plasma Phys. Control. Fusion*, 58(3):034012, 2016. https://doi.org/10.1088/0741-3335/58/3/034012.

[135] P. Mora. Plasma expansion into a vacuum. *Phys. Rev. Lett.*, 90:185002, May 2003. https://link.aps.org/doi/10.1103/PhysRevLett.90.185002.

[136] Peter Mulser and Dieter Bauer. *High power laser-matter interaction*, volume 238. Springer, 2010. https://link.springer.com/book/10.1007/978-3-540-46065-7.

[137] Tatsufumi Nakamura, Sergei V. Bulanov, Timur Zh. Esirkepov, and Masaki Kando. High-energy ions from near-critical density plasmas via magnetic vortex acceleration. *Phys. Rev. Lett.*, 105:135002, Sep 2010. https://link.aps.org/doi/10.1103/PhysRevLett.105.135002.

[138] Tatsufumi Nakamura and Kunioki Mima. Magnetic-dipole vortex generation by propagation of ultraintense and ultrashort laser pulses in moderate-density plasmas. *Phys. Rev. Lett.*, 100:205006, May 2008. https://link.aps.org/doi/10.1103/PhysRevLett.100.205006.

[139] Gregory K Ngirmang, John T Morrison, Kevin M George, Joseph R Smith, Kyle D Frische, Chris Orban, Enam A Chowdhury, and W Mel Roquemore. Evidence of radial weibel instability in relativistic intensity laser-plasma interactions inside a sub-micron thick liquid target. *Sci. Rep.*, 10(1):1–10, 2020. https://doi.org/10.1038/s41598-020-66615-4.

[140] Akinobu Niozu, Yoshiaki Kumagai, Hironobu Fukuzawa, Naomichi Yokono, Daehyun You, Shu Saito, Yu Luo, Edwin Kukk, Claudio Cirelli, Jonas Rist, et al. Relation between inner structural dynamics and ion dynamics of laser-heated nanoparticles. *Phys. Rev. X*, 11:031046, Aug 2021. https://link.aps.org/doi/10.1103/PhysRevX.11.031046.

[141] M. Nishiuchi, N. P. Dover, M. Hata, H. Sakaki, Ko. Kondo, H. F. Lowe, T. Miyahara, H. Kiriyama, J. K. Koga, N. Iwata, et al. Dynamics of laser-driven heavy-ion acceleration clarified by ion charge states. *Phys. Rev. Research*, 2:033081, Jul 2020. https://link.aps.org/doi/10.1103/PhysRevResearch.2.033081.

[142] Toshiyuki Nishiyama, Yoshiaki Kumagai, Akinobu Niozu, Hironobu Fukuzawa, Koji Motomura, Maximilian Bucher, Yuta Ito, Tsukasa Takanashi, Kazuki Asa, Yuhiro Sato, et al. Ultrafast structural dynamics of nanoparticles in intense laser fields. *Phys. Rev. Lett.*, 123:123201, Sep 2019. https://link.aps.org/doi/10.1103/PhysRevLett.123.123201.

[143] A Stockem Novo, MC Kaluza, RA Fonseca, and LO Silva. Optimizing laser-driven proton acceleration from overdense targets. *Sci. Rep.*, 6:29402, 2016. https://www.nature.com/articles/srep29402.

[144] Lieselotte Obst, Sebastian Göde, Martin Rehwald, Florian-Emanuel Brack, João Branco, Stefan Bock, Michael Bussmann, Thomas E Cowan, Chandra B Curry, Frederico Fiuza, et al. Efficient laser-driven proton acceleration from cylindrical and planar cryogenic hydrogen jets. *Sci. Rep.*, 7(1):10248, 2017. https://doi.org/10.1038/s41598-017-10589-3.

[145] Lieselotte Obst, Josefine Metzkes-Ng, Stefan Bock, Ginevra E Cochran, Thomas E Cowan, Thomas Oksenhendler, Patrick L Poole, Irene Prencipe, Martin Rehwald, Christian Rödel, et al. On-shot characterization of single plasma mirror temporal contrast improvement. *Plasma Phys. Controlled Fusion*, 60(5):054007, 2018. https://iopscience.iop.org/article/10.1088/1361-6587/aab3bb/meta.

[146] Lieselotte Obst-Huebl, Tim Ziegler, Florian-Emanuel Brack, João Branco, Michael Bussmann, Thomas E Cowan, Chandra B Curry, Frederico Fiuza, Marco Garten, Maxence Gauthier, et al. All-optical structuring of laser-driven proton beam profiles. *Nat. Commun.*, 9(1):1–7, 2018. https://doi.org/10.1038/s41467-018-07756-z.

[147] Thomas Oksenhendler. Self-referenced spectral interferometry theory. *arXiv preprint*, 2012. https://arxiv.org/abs/1204.4949.

[148] Thomas Oksenhendler, Pierre Bizouard, Olivier Albert, Stefan Bock, and Ulrich Schramm. High dynamic, high resolution and wide range single shot temporal pulse contrast measurement. *Opt. Express*, 25(11):12588–12600, 2017. https://opg.optica.org/oe/fulltext.cfm?uri=oe-25-11-12588&id=366776.

[149] A. Olle, J. Luce, N. Roquin, C. Rouyer, M. Sozet, L. Gallais, and L. Lamaignère. Implications of laser beam metrology on laser damage temporal scaling law for dielectric materials in the picosecond regime. *Rev. Sci. Instrum.*, 90(7):073001, 2019. https://doi.org/10.1063/1.5094774.

[150] Sasi Palaniyappan, B Manuel Hegelich, Hui-Chun Wu, Daniel Jung, Donald C Gautier, Lin Yin, Brian J Albright, Randall P Johnson, Tsutomu Shimada, Samuel Letzring, et al. Dynamics of relativistic transparency and optical shuttering in expanding overdense plasmas. *Nat. Phys.*, 8(10):763, 2012. https://www.nature.com/articles/nphys2390.

[151] D.N. Papadopoulos, J.P. Zou, C. Le Blanc, G. Chériaux, P. Georges, F. Druon, G. Mennerat, P. Ramirez, L. Martin, A. Fréneaux, et al. The Apollon 10 PW laser: experimental and theoretical investigation of the temporal characteristics. *High Power Laser Sci. Eng.*, 4:e34, 2016. https://doi.org/10.1017/hpl.2016.34.

[152] J. Park, S. S. Bulanov, J. Bin, Q. Ji, S. Steinke, J.-L. Vay, C. G. R. Geddes, C. B. Schroeder, W. P. Leemans, T. Schenkel, and E. Esarey. Ion acceleration in laser generated megatesla magnetic vortex. *Phys. Plasma*, 26(10):103108, 2019. https://doi.org/10.1063/1.5094045.

[153] P. K. Patel, A. J. Mackinnon, M. H. Key, T. E. Cowan, M. E. Foord, M. Allen, D. F. Price, H. Ruhl, P. T. Springer, and R. Stephens. Isochoric heating of solid-density matter with an ultrafast proton beam. *Phys. Rev. Lett.*, 91:125004, Sep 2003. https://link.aps.org/doi/10.1103/PhysRevLett.91.125004.

[154] C Peltz, J A Powell, P Rupp, A Summers, T Gorkhover, M Gallei, I Halfpap, E Antonsson, B Langer, C Trallero-Herrero, et al. Few-femtosecond resolved imaging of laser-driven nanoplasma expansion. *New J. Phys.*, 24(4):043024, Apr 2022. https://doi.org/10.1088/1367-2630/ac5e86.

[155] Christian Peltz, Charles Varin, Thomas Brabec, and Thomas Fennel. Time-resolved x-ray imaging of anisotropic nanoplasma expansion. *Phys. Rev. Lett.*, 113:133401, Sep 2014. https://link.aps.org/doi/10.1103/PhysRevLett.113.133401.

[156] F. Pérez, L. Gremillet, A. Decoster, M. Drouin, and E. Lefebvre. Improved modeling of relativistic collisions and collisional ionization in particle-in-cell codes. *Phys. Plasma*, 19(8):083104, 2012. https://doi.org/10.1063/1.4742167.

[157] F. Perez, L. Gremillet, M. Koenig, S. D. Baton, P. Audebert, M. Chahid, C. Rousseaux, M. Drouin, E. Lefebvre, T. Vinci, et al. Enhanced isochoric heating from fast electrons produced by high-contrast, relativistic-intensity laser pulses. *Phys. Rev. Lett.*, 104:085001, Feb 2010. https://link.aps.org/doi/10.1103/PhysRevLett.104.085001.

[158] GM Petrov and J Davis. Interaction of intense ultra-short laser pulses with dielectrics. *J. Phys. B*, 41(2):025601, 2008. https://iopscience.iop.org/article/10.1088/0953-4075/41/2/025601/meta?casa_token=Va6pwDCbl5wAAAAA:NqaVt6RasHmAE7sgCz-9zpYERPUndmeEiBot54VL8Gpr6KApJL-fd8FMj7NWMdqUgz2ElJaT1qsz.

[159] J. Polz, A. P. L. Robinson, A. Kalinin, G. A. Becker, R. A. Costa Fraga, M. Hellwing, M. Hornung, S. Keppler, A. Kessler, D. Klöpfel, et al. Efficient laser-driven proton acceleration from a cryogenic solid hydrogen target. *Sci. Rep.*, 9:16534, 2019. https://doi.org/10.1038/s41598-019-52919-7.

[160] Vladimir S Popov. Tunnel and multiphoton ionization of atoms and ions in a strong laser field (keldysh theory). *Phys.-Uspekhi*, 47(9):855–885, Sep 2004. https://doi.org/10.1070/pu2004v047n09abeh001812.

[161] SV Popruzhenko. Keldysh theory of strong field ionization: history, applications, difficulties and perspectives. *J. Phys. B*, 47(20):204001, 2014. https://doi.org/10.1088/0953-4075/47/20/204001.

[162] Irene Prencipe, Josefine Metzkes-Ng, Andrea Pazzaglia, Constantin Bernert, David Dellasega, Luca Fedeli, Arianna Formenti, Marco Garten, Thomas Kluge, Stephan Kraft, et al. Efficient laser-driven proton and bremsstrahlung generation from cluster-assembled foam targets. *New J. Phys.*, 23(9):093015, Sep 2021. https://dx.doi.org/10.1088/1367-2630/ac1fcd.

[163] P. Puyuelo-Valdes, J-L. Henares, F. Hannachi, T. Ceccotti, J. Domange, M. Ehret, E. D'Humieres, L. Lancia, J-R. Marquès, J. Santos, and M. Tarisien. Laser driven ion acceleration in high-density gas jets. In *Laser Acceleration of Electrons, Protons, and Ions V*, volume 11037, page 110370B. International Society for Optics and Photonics, SPIE, 2019. https://doi.org/10.1117/12.2520799.

[164] B. Qiao, S. Kar, M. Geissler, P. Gibbon, M. Zepf, and M. Borghesi. Dominance of radiation pressure in ion acceleration with linearly polarized pulses at intensities of 10^{21} W cm^{-2}. *Phys. Rev. Lett.*, 108:115002, Mar 2012. https://link.aps.org/doi/10.1103/PhysRevLett.108.115002.

[165] R. Ramis, K. Eidmann, J. Meyer ter Vehn, and S. Hüller. MULTI-fs – a computer code for laser-plasma interaction in the femtosecond regime. *Comput. Phys. Commun.*, 183(3):637–655, 2012. https://doi.org/10.1016/j.cpc.2011.10.016.

[166] R. Ramis, J. Meyer ter Vehn, and J. Ramírez. MULTI2D - a computer code for two-dimensional radiation hydrodynamics. *Comput. Phys. Commun.*, 180(6):977–994, 2009. https://doi.org/10.1016/j.cpc.2008.12.033.

[167] Martin Rehwald. *Laser-proton acceleration in the near-critical regime using density tailored cryogenic hydrogen jets*. PhD thesis, TU Dresden, 2021. https://nbn-resolving.org/urn:nbn:de:bsz:d120-qucosa2-786267.

[168] Martin Rehwald, Constantin Bernert, Florian-Emanuel Brack, Michael Bussmann, Thomas E. Cowan, Chandra B. Curry, Frederico Fiuza, Marco Garten, Lennart Gaus, Maxence Gauthier, et al. Ultra-short pulse laser acceleration of protons to 80 MeV from cryogenic hydrogen jets tailored to near-critical density. *submitted*, 2023.

[169] Marvin Reimold, Stefan Assenbaum, Constantin Bernert, Elke Beyreuther, Florian-Emanuel Brack, Leonhard Karsch, Stephan D Kraft, Florian Kroll, Markus Loeser, Alexej Nossula, et al. Time-of-flight spectroscopy for laser-driven proton beam monitoring. *Sci. Rep.*, 12(1):21488, 2022. https://www.nature.com/articles/s41598-022-25120-6.

[170] Jieru Ren, Zhigang Deng, Wei Qi, Benzheng Chen, Bubo Ma, Xing Wang, Shuai Yin, Jianhua Feng, Wei Liu, Zhongfeng Xu, et al. Observation of a high degree of stopping for laser-accelerated intense proton beams in dense ionized matter. *Nat. Commun.*, 11(1):1–7, 2020. https://www.nature.com/articles/s41467-020-18986-5.

[171] B Rethfeld, K Sokolowski-Tinten, D Von Der Linde, and SI Anisimov. Timescales in the response of materials to femtosecond laser excitation. *Appl. Phys. A*, 79(4):767–769, 2004. https://link.springer.com/article/10.1007/s00339-004-2805-9.

[172] Baerbel Rethfeld, Dmitriy S Ivanov, Martin E Garcia, and Sergei I Anisimov. Modelling ultrafast laser ablation. *J. Phys. D: Appl. Phys.*, 50(19):193001, 2017. https://iopscience.iop.org/article/10.1088/1361-6463/50/19/193001/meta.

[173] Lorenzo Romagnani, Julien Fuchs, M Borghesi, Patrizio Antici, P Audebert, F Ceccherini, T Cowan, T Grismayer, S Kar, A Macchi, et al. Dynamics of electric fields driving the laser acceleration of multi-mev protons. *Phys. Rev. Lett.*, 95(19):195001, 2005. https://journals.aps.org/prl/abstract/10.1103/PhysRevLett.95.195001.

[174] ON Rosmej, NE Andreev, S Zaehter, N Zahn, P Christ, B Borm, T Radon, A Sokolov, LP Pugachev, D Khaghani, et al. Interaction of relativistically intense laser pulses with long-scale near critical plasmas for optimization of laser based sources of mev electrons and gamma-rays. *New J. Phys.*, 21(4):043044, 2019. https://iopscience.iop.org/article/10.1088/1367-2630/ab1047/meta.

[175] M Roth. Review on the current status and prospects of fast ignition in fusion targets driven by intense, laser generated proton beams. *Plasma Phys. Controlled Fusion*, 51(1):014004, Dec 2008. https://doi.org/10.1088/0741-3335/51/1/014004.

[176] M Roth, I Alber, V Bagnoud, C R D Brown, R Clarke, H Daido, J Fernandez, K Flippo, S Gaillard, C Gauthier, et al. Proton acceleration experiments and warm dense matter research using high power lasers. *Plasma Phys. Controlled Fusion*, 51(12):124039, Nov 2009. https://doi.org/10.1088/0741-3335/51/12/124039.

[177] A. Saemann, K. Eidmann, I. E. Golovkin, R. C. Mancini, E. Andersson, E. Förster, and K. Witte. Isochoric heating of solid aluminum by ultrashort laser pulses focused on a tamped target. *Phys. Rev. Lett.*, 82:4843–4846, Jun 1999. https://link.aps.org/doi/10.1103/PhysRevLett.82.4843.

[178] J. J. Santos, F. Amiranoff, S. D. Baton, L. Gremillet, M. Koenig, E. Martinolli, M. Rabec Le Gloahec, C. Rousseaux, D. Batani, A. Bernardinello, et al. Fast electron transport in ultraintense laser pulse interaction with solid targets by rear-side self-radiation diagnostics. *Phys. Rev. Lett.*, 89:025001, Jun 2002. https://link.aps.org/doi/10.1103/PhysRevLett.89.025001.

[179] V. A. Schanz, F. Wagner, M. Roth, and V. Bagnoud. Noise reduction in third order cross-correlation by angle optimization of the interacting beams. *Opt. Express*, 25(8):9252–9261, Apr 2017. http://www.osapublishing.org/oe/abstract.cfm?URI=oe-25-8-9252.

[180] M. Schollmeier, A. B. Sefkow, M. Geissel, A. V. Arefiev, K. A. Flippo, S. A. Gaillard, R. P. Johnson, M. W. Kimmel, D. T. Offermann, P. K. Rambo, et al. Laser-to-hot-electron conversion limitations in relativistic laser matter interactions due to multi-picosecond dynamics. *Phys. Plasmas*, 22(4):043116, 2015. https://doi.org/10.1063/1.4918332.

[181] U Schramm, M Bussmann, A Irman, M Siebold, K Zeil, D Albach, C Bernert, S Bock, F Brack, J Branco, et al. First results with the novel petawatt laser acceleration facility in dresden. volume 874, page 012028. IOP Publishing, Jul 2017. https://doi.org/10.1088/1742-6596/874/1/012028.

[182] J. Schreiber, F. Bell, F. Grüner, U. Schramm, M. Geissler, M. Schnürer, S. Ter-Avetisyan, B. M. Hegelich, J. Cobble, E. Brambrink, et al. Analytical model for ion acceleration by high-intensity laser pulses. *Phys. Rev. Lett.*, 97:045005, Jul 2006. https://link.aps.org/doi/10.1103/PhysRevLett.97.045005.

[183] Jörg Schreiber, P. R. Bolton, and K Parodi. Invited review article: Hands-on laser-driven ion acceleration: A primer for laser-driven source development and potential applications. *Rev. Sci. Instrum.*, 87(7):071101, 2016. https://doi.org/10.1063/1.4959198.

[184] MB Schwab, A Sävert, O Jäckel, J Polz, M Schnell, T Rinck, László Veisz, M Möller, P Hansinger, GG Paulus, et al. Few-cycle optical probe-pulse for investigation of relativistic laser-plasma interactions. *Appl. Phys. Lett.*, 103(19):191118, 2013. https://doi.org/10.1063/1.4829489.

[185] Luís O. Silva, Michael Marti, Jonathan R. Davies, Ricardo A. Fonseca, Chuang Ren, Frank S. Tsung, and Warren B. Mori. Proton shock acceleration in laser-plasma interactions. *Phys. Rev. Lett.*, 92:015002, Jan 2004. https://link.aps.org/doi/10.1103/PhysRevLett.92.015002.

[186] Prashant Kumar Singh, Vishwa Bandhu Pathak, Jung Hun Shin, Il Woo Choi, Kazuhisa Nakajima, Seong Ku Lee, Jae Hee Sung, Hwang Woon Lee, Yong Joo Rhee, Constantin Aniculaesei, et al. Electrostatic shock acceleration of ions in near-critical-density plasma driven by a femtosecond petawatt laser. *Sci. Rep.*, 10(1):1–10, 2020. https://www.nature.com/articles/s41598-020-75455-1.

[187] S. Steinke, J. H. Bin, J. Park, Q. Ji, K. Nakamura, A. J. Gonsalves, S. S. Bulanov, M. Thévenet, C. Toth, J.-L. Vay, et al. Acceleration of high charge ion beams with achromatic divergence by petawatt laser pulses. *Phys. Rev. Accel. Beams*, 23:021302, Feb 2020. https://link.aps.org/doi/10.1103/PhysRevAccelBeams.23.021302.

[188] R. Stoian, M. Boyle, A. Thoss, A. Rosenfeld, G. Korn, I. V. Hertel, and E. E. B. Campbell. Laser ablation of dielectrics with temporally shaped femtosecond pulses. *Appl. Phys. Lett.*, 80(3):353–355, 2002. https://doi.org/10.1063/1.1432747.

[189] MJV Streeter, PS Foster, FH Cameron, M Borghesi, C Brenner, DC Carroll, E Divall, NP Dover, B Dromey, P Gallegos, et al. Relativistic plasma surfaces as an efficient second harmonic generator. *New J. Phys.*, 13(2):023041, 2011. https://doi.org/10.1088/1367-2630/13/2/023041.

[190] B.C. Stuart, M.D. Feit, S Herman, A.M. Rubenchik, B.W. Shore, and M.D. Perry. Nanosecond-to-femtosecond laser-induced breakdown in dielectrics. *Phys. Rev. B*, 53(4):1749, 1996. https://journals.aps.org/prb/abstract/10.1103/PhysRevB.53.1749.

[191] Jae Hee Sung, Hwang Woon Lee, Je Yoon Yoo, Jin Woo Yoon, Chang Won Lee, Jeong Moon Yang, Yeon Joo Son, Yong Ha Jang, Seong Ku Lee, and Chang Hee Nam. 4.2 PW, 20 fs Ti:sapphire laser at 0.1 Hz. *Opt. Lett.*, 42(11):2058–2061, Jun 2017. http://www.osapublishing.org/ol/abstract.cfm?URI=ol-42-11-2058.

[192] F. Sylla, M. Veltcheva, S. Kahaly, A. Flacco, and V. Malka. Development and characterization of very dense submillimetric gas jets for laser-plasma interaction. *Rev. Sci. Instrum.*, 83(3):033507, 2012. https://doi.org/10.1063/1.3697859.

[193] Cédric Thaury and F Quéré. High-order harmonic and attosecond pulse generation on plasma mirrors: basic mechanisms. *J. Phys. B*, 43(21):213001, 2010. https://iopscience.iop.org/article/10.1088/0953-4075/43/21/213001/meta.

[194] Cédric Thaury, F Quéré, J-P Geindre, A Levy, T Ceccotti, P Monot, M Bougeard, F Réau, P d'Oliveira, et al. Plasma mirrors for ultrahigh-intensity optics. *Nat. Phys.*, 3(6):424–429, 2007. https://www.nature.com/articles/nphys595.

[195] W Theobald, K Akli, R Clarke, JA Delettrez, RR Freeman, S Glenzer, J Green, G Gregori, R Heathcote, N Izumi, et al. Hot surface ionic line emission and cold k-inner shell emission from petawatt-laser-irradiated cu foil targets. *Phys. Plasma*, 13(4):043102, 2006. https://aip.scitation.org/doi/full/10.1063/1.2188912.

[196] A Ting, K Krushelnick, HR Burris, A Fisher, C Manka, and CI Moore. Backscattered supercontinuum emission from high-intensity laser–plasma interactions. *Opt. Lett.*, 21(15):1096–1098, 1996. https://doi.org/10.1364/OL.21.001096.

[197] Franziska Treffert, Chandra B Curry, Todd Ditmire, Griffin D Glenn, Hernan J Quevedo, Markus Roth, Christopher Schoenwaelder, Marc Zimmer, Siegfried H Glenzer, and Maxence Gauthier. Towards high-repetition-rate fast neutron sources using novel enabling technologies. *Instruments*, 5(4):38, 2021. https://www.mdpi.com/2410-390X/5/4/38.

[198] J.-L. Vay, A. Almgren, J. Bell, L. Ge, D.P. Grote, M. Hogan, O. Kononenko, R. Lehe, A. Myers, C. Ng, et al. Warp-x: A new exascale computing platform for beam–plasma simulations. *Nucl. Instrum. Methods Phys. Res., Sect. A*, 909:476–479, 2018. https://www.sciencedirect.com/science/article/pii/S0168900218300524.

[199] L. Veisz, W. Theobald, T. Feurer, H. Schillinger, P. Gibbon, R. Sauerbrey, and M. S. Jovanović. Three-halves harmonic emission from femtosecond laser produced plasmas. *Phys. Plasma*, 9(8):3197–3200, 2002. https://doi.org/10.1063/1.1493794.

[200] V. A. Vshivkov, N. M. Naumova, F. Pegoraro, and S. V. Bulanov. Nonlinear electrodynamics of the interaction of ultra-intense laser pulses with a thin foil. *Phys. Plasma*, 5(7):2727–2741, 1998. https://doi.org/10.1063/1.872961.

[201] F. Wagner, O. Deppert, C. Brabetz, P. Fiala, A. Kleinschmidt, P. Poth, V.A. Schanz, A. Tebartz, B. Zielbauer, M. Roth, et al. Maximum proton energy above 85 MeV from the relativistic interaction of laser pulses with micrometer thick CH2 targets. *Phys. Rev. Lett.*, 116(20):205002, 2016. https://journals.aps.org/prl/abstract/10.1103/PhysRevLett.116.205002.

[202] Dahui Wang, Yinren Shou, Pengjie Wang, Jianbo Liu, Zhusong Mei, Zhengxuan Cao, Jianmin Zhang, Pengling Yang, Guobin Feng, Shiyou Chen, et al. Laser-induced damage thresholds of ultrathin targets and their constraint on laser contrast in laser-driven ion acceleration experiments. *High Power Laser Sci. Eng.*, 8, 2020. https://doi.org/10.1017/hpl.2020.40.

[203] I Watts, M Zepf, EL Clark, M Tatarakis, K Krushelnick, AE Dangor, R Allott, RJ Clarke, D Neely, and PA Norreys. Measurements of relativistic self-phase-modulation in plasma. *Phys. Rev. E*, 66(3):036409, 2002. https://journals.aps.org/pre/abstract/10.1103/PhysRevE.66.036409.

[204] Jonathan A Wheeler, Antonin Borot, Sylvain Monchocé, Henri Vincenti, Aurélien Ricci, Arnaud Malvache, Rodrigo Lopez-Martens, and Fabien Quéré. Attosecond lighthouses from plasma mirrors. *Nat. Photonics*, 6(12):829–833, 2012. https://www.nature.com/articles/nphoton.2012.284.

[205] S. C. Wilks, W. L. Kruer, M. Tabak, and A. B. Langdon. Absorption of ultra-intense laser pulses. *Phys. Rev. Lett.*, 69:1383–1386, Aug 1992. https://link.aps.org/doi/10.1103/PhysRevLett.69.1383.

[206] SC Wilks, AB Langdon, TE Cowan, M Roth, M Singh, S Hatchett, MH Key, D Pennington, A MacKinnon, and RA Snavely. Energetic proton generation in ultra-intense laser–solid interactions. *Phys. Plasma*, 8(2):542–549, 2001. https://aip.scitation.org/doi/abs/10.1063/1.1333697.

[207] S.D.R. Williamson, R. Wilson, M. King, M. Duff, B. Gonzalez-Izquierdo, Z.E. Davidson, A. Higginson, N. Booth, S. Hawkes, D. Neely, et al. Self-referencing spectral interferometric probing of the onset time of relativistic transparency in intense laser-foil interactions. *Phys. Rev. Appl.*, 14:034018, Sep 2020. https://link.aps.org/doi/10.1103/PhysRevApplied.14.034018.

[208] Long Yang, Constantin Bernert, et al. Time-resolved optical shadowgraphy of cryogenic hydrogen jets as a test-bed platform to benchmark particle-in-cell simulations. *in preparation*, 2023.

[209] U Zastrau, P Sperling, M Harmand, A Becker, T Bornath, R Bredow, S Dziarzhytski, T Fennel, LB Fletcher, E Förster, et al. Resolving ultrafast heating of dense cryogenic hydrogen. *Phys. Rev. Lett.*, 112(10):105002, 2014. https://journals.aps.org/prl/abstract/10.1103/PhysRevLett.112.105002.

[210] Karl Zeil, Josefine Metzkes, Thomas Kluge, Michael Bussmann, Thomas E Cowan, S.D. Kraft, R Sauerbrey, and U Schramm. Direct observation of prompt pre-thermal laser ion sheath acceleration. *Nat. Commun.*, 3(1):1–6, 2012. https://www.nature.com/articles/ncomms1883.

[211] T Ziegler, D Albach, C Bernert, S Bock, F-E Brack, TE Cowan, NP Dover, M Garten, L Gaus, R Gebhardt, et al. Proton beam quality enhancement by spectral phase control of a pw-class laser system. *Sci. Rep.*, 11(1):1–7, 2021. https://doi.org/10.1038/s41598-021-86547-x.

[212] Tim Ziegler. PhD thesis, TU Dresden, 2023.

[213] Tim Ziegler, Martin Rehwald, Lieselotte Obst, Constantin Bernert, Florian-Emanuel Brack, Chandra B Curry, Maxence Gauthier, Siegfried H Glenzer, Sebastian Göde, Lev Kazak, et al. Optical probing of high intensity laser interaction with micron-sized cryogenic hydrogen jets. *Plasma Phys. Control. Fusion*, 60(7):074003, 2018. http://stacks.iop.org/0741-3335/60/i=7/a=074003.

Erklärung

Hiermit versichere ich, dass ich die vorliegende Arbeit ohne unzulässige Hilfe Dritter und ohne Benutzung anderer als der angegebenen Hilfsmittel angefertigt habe; die aus fremden Quellen direkt oder indirekt übernommenen Gedanken sind als solche kenntlich gemacht. Die Arbeit wurde bisher weder im Inland noch im Ausland in gleicher oder ähnlicher Form einer anderen Prüfungsbehörde vorgelegt. Die Promotionsordnung, Technische Universität Dresden, Bereich Mathematik und Naturwissenschaften vom 23.02.2011 mit letzten Änderungen vom 23.05.2018 erkenne ich an.

Dresden, 03. April 2023

Constantin Andreas Bernert, M. Sc.

HELMHOLTZ ZENTRUM
DRESDEN ROSSENDORF

Bautzner Landstr. 400
01328 Dresden, Germany
Phone +49 351 260-3365
Fax +49 351 260-33651
Email c.bernert@hzdr.de
http://www.hzdr.de